# The Influence of Infragravity Waves on Overtopping at Coastal Structures with Shallow Foreshores

Lashley, Christopher H.

**DOI**
10.4233/uuid:f93143bc-0214-41ad-af4a-4ad2168a42a5

**Publication date**
2021

**Document Version**
Final published version

**Citation (APA)**
Lashley, C. H. (2021). *The Influence of Infragravity Waves on Overtopping at Coastal Structures with Shallow Foreshores.* [Dissertation (TU Delft), Delft University of Technology]. https://doi.org/10.4233/uuid:f93143bc-0214-41ad-af4a-4ad2168a42a5

**Important note**
To cite this publication, please use the final published version (if applicable).
Please check the document version above.

# The Influence of Infragravity Waves on Overtopping at Coastal Structures with Shallow Foreshores

Christopher H. Lashley

The Influence of Infragravity Waves on Overtopping at Coastal Structures with Shallow Foreshores C. H. Lashley

Propositions belonging to the Dissertation

# The Influence of Infragravity Waves on Overtopping at Coastal Structures with Shallow Foreshores

By Christopher Harold LASHLEY

1. By focusing only on wave height attenuation due to shallow foreshores, we grossly overestimate their flood-risk reduction capabilities. *This proposition pertains to this dissertation*.
2. The spectral wave period ($T_{m-1,0}$) is an unreliable parameter and should not be used in the design of coastal structures with shallow foreshores. *This proposition pertains to this dissertation*.
3. Complex wave models are useless when design is governed by time-averaged wave parameters. *This proposition pertains to this dissertation*.
4. It doesn't take a pandemic for a PhD candidate to experience self-isolation and social distancing.
5. Overcoming "paralysis by analysis" is the most important factor for success as a PhD candidate.
6. It is better to write your research questions after your conclusions.
7. By rewarding incremental research, we discourage ground-breaking research.
8. There should be a mandatory section of each published scientific article where the authors reflect on their own research bias.
9. For the sake of equality, the single-blind peer review should be abandoned.
10. Working out helps you to work it out.

These propositions are regarded as opposable and defendable, and have been approved as such by the promotors: Prof. dr. ir. S.N. Jonkman, Prof. dr. ir. J.W. van der Meer and Dr. ir. J.D. Bricker.

# The Influence of Infragravity Waves on Overtopping at Coastal Structures with Shallow Foreshores

## Dissertation

For the purpose of obtaining the degree of doctor

at Delft University of Technology

by the authority of the Rector Magnificus dr. ir. T.H.J.J. van der Hagen;

Chair of the Board for Doctorates

to be defended publicly on

Wednesday 3rd November 2021 at 10:00 o'clock

by

**Christopher Harold LASHLEY**

Master of Science in Water Science and Engineering – specialisation in Coastal Engineering and Port Development, IHE-Delft Institute for Water Education, the Netherlands,

Born in Bridgetown, Barbados

This dissertation has been approved by the promotors.

Composition of the doctoral committee:

| | |
|---|---|
| Rector Magnificus, | chairperson |
| Prof. dr. ir. S.N. Jonkman, | Delft University of Technology, *promotor* |
| Prof. dr. ir. J.W. van der Meer, | Delft University of Technology; IHE-Delft, *promotor* |
| Dr. ir. J.D. Bricker, | Delft University of Technology; University of Michigan (USA), *co-promotor* |
| *Independent members*: | |
| Prof. dr. ir. A.J.H.M Reniers | Delft University of Technology |
| Prof. dr. ir. M. Kok | Delft University of Technology |
| Prof. dr. ir. P. Troch | Ghent University (Belgium) |
| Dr. R.J. Vos | Rijkswaterstaat (the Netherlands) |
| Prof. dr. ir. S.G.J. Aarninkhof | Delft University of Technology, *reserve member* |

*Keywords*: infragravity waves, dikes, levees, seawalls, flood defences, wave overtopping, numerical modelling, probability of failure, coastal flooding

*Printed by*: Proefschriftmaken

*Front & Back*: King 3D Products



ISBN 000-00-0000-000-0

An electronic version of this dissertation is available at http://repository.tudelft.nl/.

*De sea ain't got nuh back door.*

-Bajan (Barbadian) Proverb

Meaning: the sea can be very dangerous, so be careful.

# ACKNOWLEDGEMENTS

Throughout the PhD and writing of this dissertation, I have received a great deal of support and assistance.

Firstly, I acknowledge that this work is part of the All-Risk project, which is (partly) financed by NWO Domain Applied and Engineering Sciences, in collaboration with the following private and public partners: the Dutch Ministry of Infrastructure and Water Management (RWS); Deltares; STOWA; the regional water authority, Noorderzijlvest; the regional water authority, Vechtstromen; It Fryske Gea; HKV consultants; Natuurmonumenten; and waterboard HHNK.

I thank my supervisors, Jeremy Bricker, Jentsje van der Meer and Bas Jonkman, whose expertise, support and guidance were invaluable. I thank Jeremy for his daily supervision, as he always made time for whatever issue I needed to discuss—technical or otherwise. I thank Jentsje for his mentorship. His expertise and attention to detail meant that my analyses had to be thorough, structured and well presented. This led to an overall improvement in the quality of my work and my approach to research, in general. I thank Bas for his oversight and ability to see not just the details but also the bigger picture. By requesting key meetings, he ensured that important milestones were met throughout the PhD, which allowed me to complete this dissertation within the allotted time.

I also acknowledge the following persons who contributed to the success of this research, either through data sharing, insightful discussions or review of key elements: Corrado Altomare (Universitat Politècnica de Catalunya, Spain); Tomohiro Suzuki (Flanders Hydraulics, Belgium); Barbara Zanuttigh (University of Bologna, Italy); Volker Roeber (Université Pau & Pays Adour, France); Katsuya Hirayama (PARI, Japan); Beatriz Marin Diaz (NIOZ); Celso Ferreira (George Mason University, USA); Bas Hofland (TU Delft); Marion Tissier (TU Delft); Ap van Dongeren (IHE-Delft); Ad Reniers (TU Delft); Robert McCall (Deltares); Robert Vos (RWS); Robert Slomp (RWS); Patrick Oosterlo (TU Delft); Christophe Baron-Hyppolite (TU Delft); Charles Feys (TU Delft); and Akshay Patil (TU Delft).

Last, but by no means least, I thank my family, friends and colleagues for their support, which made the PhD and my life in Delft very enjoyable. I thank my fellow All-Risk'ers, especially those in room 3.58, for their comradery and nice discussions. I thank my colleagues at TU—especially the PSOR crew!—for their support both in and outside of the office. I thank the IHE Caribbean family for keeping the culture alive in Delft. I especially want to thank those that offered me genuine encouragement, reassurance and compassion along the way, namely: Keisha, Sharoma, Dave, Martijn, Alex, Geoff, Üwe, Su and King.

# SUMMARY

Coastal communities across the globe are often protected by structures, such as seawalls, levees or dikes, which allow only a safe volume of water to pass over or "overtop" them due to wave action during storms. The area seaward of these structures is often characterised by shallow, gently sloping beds referred to as foreshores.

As storm waves propagate over the shallow foreshores, two notable processes occur. The first, is the attenuation of high-frequency waves that are collectively referred to as wind-sea and swell (SS), with periods less than 20 seconds. The limited water depth over the foreshore forces the SS waves to shoal and ultimately break. This shoaling and breaking, in turn, results in the second important process: the growth of infragravity (IG) waves, with periods in the order of minutes.

The methods used in current practice to estimate wave overtopping are able to accurately quantify the impact of SS waves. However, they tend to neglect the influence of IG waves, which are known to play a critical role in erosion and flooding along shallow coast lines. In light of this, this dissertation aimed to *develop new methods to estimate the influence of IG waves on the safety of coastal defences with shallow foreshores against wave overtopping*. This aim was ultimately achieved by using state-of-art numerical models, empirical methods and field measurements to develop a suite of tools, that together, provide a framework to accurately quantify the influence of IG waves on wave overtopping.

As data on shallow foreshores was limited, a numerical model (XBeach Non-hydrostatic) was first used to generate a large dataset of wave measurements at the toe of the structure for varying offshore, foreshore and structure slope conditions. The analysis, detailed in Chapter 2, revealed that the influence of IG waves increased for higher, directionally narrow-banded (long-crested) offshore waves; shallower foreshore water depths; milder foreshore slopes; and reduced vegetated cover. The combined effect of the different environmental parameters on the IG waves was then captured in an empirical model, which formed the base of the framework to follow.

For determining wave overtopping, the standard approach requires the use of a wave model (often a phase-averaged model like SWAN) to estimate wave parameters at the toe, which are then used as input to the well-known formulae of the EurOtop design manual. However, this approach largely neglects the impact of IG waves. In Chapter 3, this is rectified by augmenting the traditional approach with the empirical model developed in Chapter 2 to include the effects of the IG waves on the design parameters. Considering accuracy and computational demand, the modified approach proved superior when assessing wave overtopping at dikes with shallow foreshores. This approach formed the first sub-method to estimating wave overtopping in the overall framework.

Nevertheless, it is often difficult to obtain accurate estimates of wave parameters at the toe of structures with shallow foreshores. Chapter 4 offers a solution to this problem by proposing a new set of overtopping formulae that instead rely on deep-water wave parameters as input. This is done by revisiting the old but proven approach of Yoshimi Goda, now with additional data and new trend analysis techniques. The newly-derived formulae proved accurate and can be considered an alternative to the current standard (Chapter 3). Particularly, for dikes and seawalls with very and extremely shallow foreshores, where IG waves tend to dominate. This approach formed the second sub-method to estimating wave overtopping in the overall framework.

Finally, in order to estimate the impact of IG waves on safety, a probabilistic method (FORM) was introduced to the framework in Chapter 5. Using the first sub-method (Chapter 3), the probability of dike failure by wave overtopping with and without IG waves was determined for dikes along the shallow Dutch Wadden Sea coast. Including the IG waves resulted in 1.1 to 1.6 times higher failure probabilities for the Dutch Wadden Sea coast, suggesting that coastal safety may be overestimated when they are neglected. This was attributed to the influence of the IG waves on the wave period and, to a lesser extent, the wave height at the structure toe. Furthermore, the spatial variation in this effect observed for the Dutch Wadden Sea highlighted its dependence on local bathymetric and offshore forcing conditions—with IG waves having greater influence on the failure probability for cases with larger offshore waves and shallower water depths.

The general conclusion of the dissertation is that IG waves can have an important impact on safety. Moreover, findings indicate that the safety of existing coastal defences with shallow foreshores may be overestimated, since IG waves are largely neglected in the current practice for their design and assessment. For the case considered here (the Dutch Wadden Sea), the increase in required crest level due to the IG waves was around 2 dm with a cost in the order of M€1/per km. For shallower coastlines exposed to more energetic wave conditions, the influence of the IG waves and the corresponding safety costs are likely to be greater. This dissertation provides practitioners with a suite of tools to quantify to influence of IG waves on the safety of coastal defences with shallow foreshores against wave overtopping. Thereby, reducing the uncertainty in the overall impact of shallow foreshores and allowing dike managers to make more informed decisions when considering hazard mitigation strategies.

# SAMENVATTING

Wereldwijd worden kustgemeenschappen vaak beschermd door constructies, zoals zeeweringen, “levees” of dijken, die alleen een veilige hoeveelheid water doorlaten of "overslaan" als gevolg van golfslag tijdens stormen. Het gebied zeewaarts van deze constructies, ook wel vooroevers genoemd, wordt vaak gekenmerkt door ondiepe beddingen met een gering verhang.

Terwijl stormgolven zich voortplanten over de ondiepe vooroevers, vinden er twee opmerkelijke processen plaats. Het eerste is de verzwakking van hoogfrequente golven die worden aangeduid als wind-zee en deining, ook bekend als SS-golven, met perioden van minder dan 20 seconden. De beperkte waterdiepte van de vooroever leidt tot ophogen van golven en uiteindelijk tot golfbreking. Dit proces resulteert in het tweede belangrijke proces: de vorming van infragravitatie (IG) golven, met perioden in de orde van minuten.

De hedendaagse methoden die worden gebruikt om golfoverslag in te schatten, zijn ook toepasbaar voor het nauwkeurig kwantificeren van de impact van SS-golven. Echter wordt de invloed van IG-golven verwaarloosd in deze methoden, alhoewel bekend is dat deze golven een cruciale rol kunnen spelen bij erosie en overstromingen langs ondiepe kustlijnen. In het licht hiervan is dit proefschrift gericht op het ontwikkelen van nieuwe methoden voor het kwantificeren van de invloed van IG-golven op de veiligheid van kustverdediging met ondiepe vooroevers tegen golfoverslag. Dit doel werd uiteindelijk bereikt door gebruik te maken van geavanceerde numerieke modellen, empirische methoden en veldmetingen om een reeks instrumenten te ontwikkelen, die samen een raamwerk bieden om de invloed van IG-golven op golfoverslag nauwkeurig te kwantificeren.

Omdat de gegevens over ondiepe vooroevers beperkt waren, werd eerst een numeriek model (XBeach Non-hydrostatic) gebruikt om een grote dataset van golfmetingen te genereren aan de voet van de constructie, waarbij de helling in het gebied offshore, in de vooroevers en van de constructies wordt gevarieerd. De analyse, zoals gedetailleerd omschreven in Hoofdstuk 2, onthulde dat de invloed van IG-golven toenam voor hogere, directioneel smalbandige (lange kuif) offshore-golven; ondiepere vooroeverwaterdiepten; mildere vooroeverhellingen; en verminderde begroeide dekking. Het gecombineerde effect van de verschillende omgevingsparameters op de IG-golven werd vervolgens vastgelegd in een empirisch model, dat de basis vormde van het te volgen raamwerk.

Voor het bepalen van golfoverslag vereist de standaardbenadering het gebruik van een golfmodel (vaak een fasegemiddelde model zoals SWAN) om golfparameters aan de voet in te schatten, die vervolgens worden gebruikt als input voor de bekende formules van de

EurOtop ontwerphandleiding . Deze benadering negeert echter grotendeels de impact van IG-golven. In Hoofdstuk 3 wordt dit verbeterd door de traditionele benadering uit te breiden met het empirische model dat in Hoofdstuk 2 wordt beschreven om de effecten van de IG-golven op de ontwerpparameters op te nemen. Rekening houdend met de nauwkeurigheid en de rekenvraag, bleek de aangepaste benadering het beste toepasselijk bij het beoordelen van golfoverslag bij dijken met ondiepe vooroevers. Deze benadering vormde de eerste submethode voor het inschatten van golfoverslag in het algemene raamwerk.

Toch is het vaak moeilijk om de golfparameters aan de voet van de constructies met ondiepe vooroevers nauwkeurig in te schatten. Hoofdstuk 4 biedt een oplossing voor dit probleem door een nieuwe reeks overslagformules voor te stellen die in de plaats daarvan gebaseerd zijn op diepwatergolfparameters als input. Dit wordt gedaan door de oude maar bewezen aanpak van Yoshimi Goda opnieuw te bekijken, nu met aanvullende gegevens en nieuwe trendanalysetechnieken. De nieuwe afgeleide formules bleken nauwkeurig en kunnen worden beschouwd als een alternatief voor de huidige standaard (Hoofdstuk 3). Met name voor dijken en zeeweringen met extreem ondiepe vooroevers waar IG-golven de neiging hebben te domineren. Deze benadering vormde de tweede submethode voor het inschatten van golfoverslag in het algemene raamwerk.

Tenslotte is in Hoofdstuk 5 een probabilistische methode (FORM) in het raamwerk geïntroduceerd om de impact van IG-golven op de veiligheid in te schatten,. Met behulp van de eerste submethode (Hoofdstuk 3) is de kans op dijkdoorbraak door golfoverslag met en zonder IG-golven bepaald voor dijken langs de ondiepe Nederlandse Waddenzeekust. Het opnemen van de IG-golven resulteerde in 1,1 tot 1,6 keer hogere faalkansen voor de Nederlandse Waddenzeekust, wat suggereert dat kustveiligheid kan worden overschat als ze worden verwaarloosd. Dit werd toegeschreven aan de invloed van de IG-golven op de golfperiode en in mindere mate de golfhoogte bij de voet van de constructie. Bovendien benadrukte de waargenomen ruimtelijke variatie voor de Nederlandse Waddenzee de afhankelijkheid van lokale bathymetrische en diepwater-forceringsomstandigheden - waarbij IG-golven een grotere invloed hebben op de faalkans voor gevallen met grotere diepwater golven en kleinere waterdiepten.

De algemene conclusie van het proefschrift is dat IG-golven een belangrijke impact kunnen hebben op de waterveiligheid. Bovendien wijzen de bevindingen erop dat de veiligheid van bestaande kustverdediging met ondiepe vooroevers mogelijk wordt overschat, aangezien IG-golven in de huidige praktijk grotendeels worden verwaarloosd in hun ontwerp en beoordeling. Voor de case study in dit onderzoek (de Nederlandse Waddenzee) bleek de verhoging van het vereiste crestniveau als gevolg van de IG-golven ongeveer 2 dm met bijkomende kosten in de orde van M€1/km. Voor ondiepere kustlijnen die zijn blootgesteld aan meer energetische golfomstandigheden, is de invloed van de IG-golven en de bijbehorende veiligheidskosten waarschijnlijk groter. Dit proefschrift biedt beoefenaars een

reeks hulpmiddelen om de invloed van IG-golven op de veiligheid van kustverdediging met ondiepe vooroevers tegen golfoverslag te kwantificeren. Daardoor wordt de onzekerheid in de algehele impact van ondiepe vooroevers verminderd en kunnen dijkbeheerders beter geïnformeerde beslissingen nemen bij het overwegen van strategieën voor risicobeperking

# CONTENTS

# 1

# INTRODUCTION

This chapter defines the scope of the dissertation by: describing the societal problem to be addressed (Section 1.1); identifying gaps in current literature (Section 1.2); and describing the approach taken to fill these gaps and address the wider problem (Sections 1.3 and 1.4). An outline of the dissertation is provided in Section 1.5, highlighting connections between chapters and their individual contributions to the overall research aim.

## 1.1 BACKGROUND

To protect coastal communities from wave-driven flooding, structures such as seawalls, levees or dikes (or "dykes") are built to resist the force of extreme water levels and waves—permitting only a safe volume of water to pass over or "overtop" the structure. Along many of the world's coastlines, these structures are fronted by shallow, sometimes vegetated foreshores. Examples include the sandy foreshores along the Belgian coast (Altomare et al., 2016), the wide shelfs of the Mekong Delta, Vietnam (Nguyen et al., 2020), the steep foreshores found in Japan (Mase et al., 2013), the broad saltmarshes of New Orleans (Jonkman et al., 2009) and the intertidal flats of the Wadden Sea along the north coasts of the Netherlands (Figure 1.1) and Germany and the west coast of Denmark.

**Figure 1.1:** *Dike partially covered by asphalt and partially by grass, fronted by a shallow, mildly-sloping foreshore (mudflat) along the Dutch Wadden Sea coast.*

1

As wind-waves (generated by local winds) or swell (generated by distant storms)—referred to collectively as sea and swell (hereafter, SS) waves—propagate over these foreshores, the limited water depth forces the waves to shoal and ultimately break (Figure 1.2). This reduced wave load at the structure is then expected to improve the reliability of the structure by reducing the likelihood of it failing. If vegetation is present, this attenuation effect is further enhanced by the drag forces exerted by stems, branches and leaves.

The efficiency with which the foreshores attenuate the incident wave energy is dependent on their width, slope, properties of their vegetated cover (if present) and how shallow the water depth over the foreshore is compared to the incident wave height. The ability of shallow foreshores, with and without vegetation, to attenuate SS waves has been the subject of many studies, including physical model tests (Möller et al., 2014), numerical simulations (Vuik et al., 2016, Willemsen et al., 2020) and field measurements (Garzon et al., 2019). While these studies assessed the ability of the foreshore to attenuate the height of SS waves, they neglected the influence of infragravity (hereafter, IG) waves, which tend to dominate in shallow water (Figure 1.2).

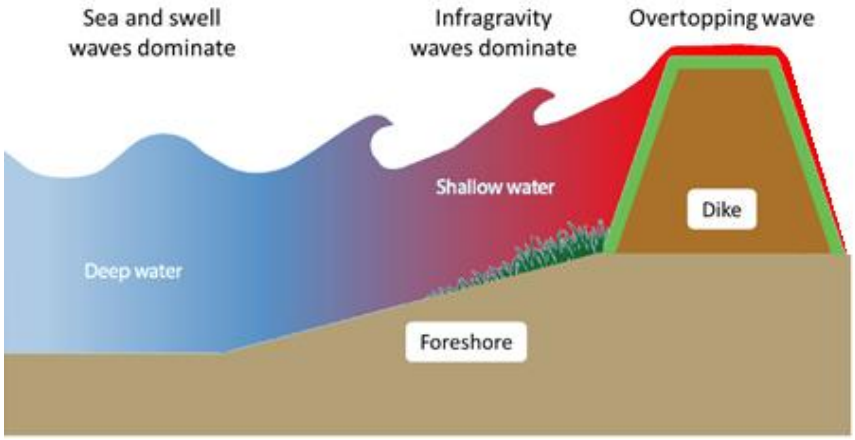


**Figure 1.2:** *Schematic representation of wave overtopping at a dike-foreshore system showing the transition from deep water, where SS waves play a more critical role (or dominate) to shallow water, where IG waves dominate (adapted from: https://kbase.ncr-web.org/all-risk/projects/b2-wave-propagation-over-foreshores/).*

In the deep ocean, these low-amplitude (IG) waves—with periods exceeding 20 s or frequencies lower than 0.05 Hz—are formed through nonlinear interactions of SS-wave components (Longuet-Higgins and Stewart, 1962). This may be visualized in Figure 1.3 by considering a bichromatic wave field (comprising 2 SS waves with discrete frequencies). As the waves travel with different celerities, there are moments where they add up and moments where they cancel each other out. The resulting wave-group pattern, with sequences of higher and lower amplitudes, generates an IG wave which travels phase-locked or "bound" to the wave group. As SS waves approach shallow water, they may experience shoaling over

gently-sloping foreshores and continue to transfer energy to the bound IG wave resulting in amplitude growth. After SS waves break, the wave-group structure disappears and the bound IG wave is freed (released) (Masselink, 1995). Alternatively, IG waves may be generated on steeply-sloping foreshore slopes by the temporal variation in the location of breaking waves. This occurs when alternating groups of higher and lower amplitude wave groups break farther and closer to the shore, respectively. The resulting fluctuations in wave set-up and set-down, with the period of the wave groups, produce both seaward and shoreward propagating IG waves (Battjes, 2004, Symonds et al., 1982).

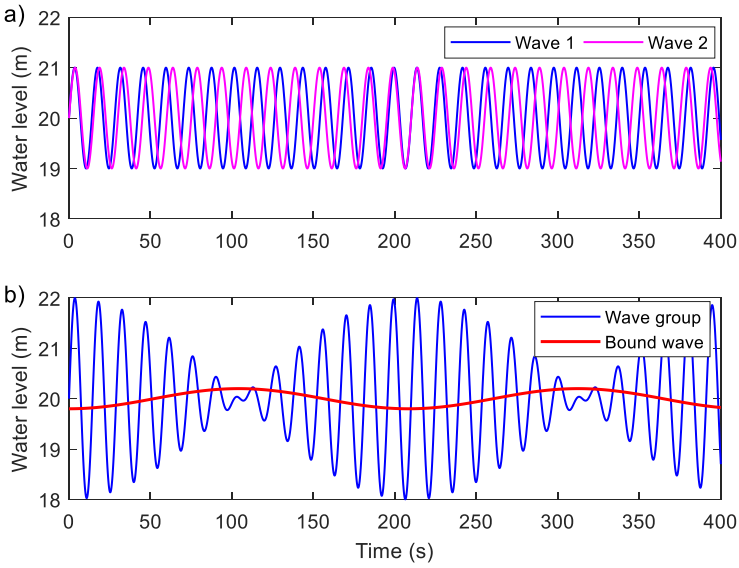


**Figure 1.3**: *Example of a) a bichromatic wave field of two sinusoidal waves with periods 14 s and 15 s propagating over a flat bottom in 20 m water depth; and the b) the resulting wave group pattern and bound IG wave, adapted from Bertin et al. (2018) and Longuet-Higgins and Stewart (1962).*

Recent observations of the impact of IG waves include: unexpectedly high run-up levels observed at the rocky coast of Banneg Island, France (Sheremet et al., 2014); extensive damage and causalities that occurred along a coral reef-lined coast in the Philippines during Typhoon Haiyan (Roeber and Bricker, 2015, Shimozono et al., 2015); and the erosion and overwash of several dunes on the west coast of France (Baumann et al., 2017, Lashley et al., 2019). In each of these cases, the observed extreme water levels and resulting damage have been attributed to the presence or dominance of nearshore IG waves by means of either data analysis or numerical modelling.

Despite evidence of their impact, IG waves are often not considered in the design and flood risk assessment of coastal flood defences, as many of the widely-used methods—such as phase-averaged wave modelling (e.g. SWAN)—tend to exclude them. As a result, the true

efficacy of shallow foreshores in attenuating nearshore waves and reducing the likelihood or probability of dike failure by wave overtopping remains unknown.

## 1.2 KNOWLEDGE GAPS

The following knowledge gaps, organized by the four themes, were identified through a review of relevant literature.

### 1.2.1 IMPORTANCE OF INFRAGRAVITY (IG) WAVES FOR DETERMINING WAVE OVERTOPPING

Previous attempts have been made to relate the magnitude of IG-wave energy, either at the shore (in the form of swash) or near the shore, to parameters that describe the coastal environment; however, to date, the findings have been inconsistent. Guza and Thornton (1982) found that the IG component of wave run-up increased linearly with increasing offshore wave height; while it was later shown to be better predicted using the well-known breaker (Iribarren) parameter which considers deep-water wave length and foreshore slope, in addition to the offshore wave height (Ruessink et al., 1998, Sallenger and Holman, 1985). In contrast, Stockdon et al. (2006) concluded that the IG component was actually independent of the foreshore slope. This was later challenged by studies advocating the importance of the slope parameter (Gomes da Silva et al., 2018, Passarella et al., 2018). At the same time, other authors found clear correlations between IG-wave motions and the local water depth (Cox et al., 2013, Hofland et al., 2017). These contradictory findings reveal that further research on the subject is required and suggest that nearshore IG-wave energy is unlikely a function of any single environmental factor.

### 1.2.2 APPROPRIATE MODELS FOR SIMULATING NEARSHORE WAVES AND OVERTOPPING

Practitioners often employ diverse, though not always thoroughly validated, numerical models to directly or indirectly estimate wave overtopping at sloping structures. These models, broadly classified as either phase-resolving or phase-averaged, each have strengths and limitations owing to the physical schematization of processes within them (Cavaleri et al., 2007, Vyzikas and Greaves, 2018). Phase-resolving models use high-grid resolutions in order to simulate the propagation of individual waves; while phase-averaged models do not treat waves individually but instead describe the evolution of the wave energy spectrum—a phase-averaged quantity.

Previous studies have shown that while phase-averaged models are generally able to accurately reproduce SS waves, they do not account for the interactions that force IG-wave motions (Buckley et al., 2014, Cavaleri et al., 2007); yet these models are often applied in shallow water where IG waves may dominate. Whether or not phase-averaged models can be accurately applied under very shallow conditions requires further investigation.

Several attempts at model comparisons for wave overtopping have been made (St-Germain et al., 2014, Vanneste et al., 2014). However, no study to date has considered the full range of model complexity—from phase-resolving models, which also resolve depth, to phase-

averaged. Likewise, none of these studies successfully quantified the accuracy versus speed of these models under irregular wave forcing.

### 1.2.3 EMPIRICAL MODELS FOR WAVE OVERTOPPING

The state-of-the-art empirical models for wave overtopping of sloping structures (EurOtop, 2018) typically require wave parameters at the toe of the structure as input. Phase-averaged wave models are commonly used to estimate these parameters; however, there is one major drawback of this approach. Under very shallow conditions—where IG waves may play a significant role—phase-averaged models are no longer valid. This means that either costly physical model tests, or more computationally demanding phase-resolving models, must be used to obtain accurate estimates of the required input parameters (Mase et al., 2013).

In light of this drawback, there is need for an empirical method capable of capturing the influence of IG waves but based on deep-water wave characteristics—similar to the early design diagrams of Goda et al. (1975) for vertical walls; thereby removing the need for additional numerical or physical modelling.

### 1.2.4 OVERTOPPING FAILURE PROBABILITY

The probability of failure due to wave overtopping is determined by assessing the likelihood that the actual overtopping discharge ($m^3/s$ or l/s per m) exceeds some critical value, which is dependent on the structures erosion resistance. Vuik et al. (2018) assessed the failure probability of the hybrid flood defences along the Dutch Wadden coast considering the effects of vegetation and an idealized foreshore geometry. While this study proved to be a significant step towards the incorporating the foreshore in assessing coastal flood risk, it was based on phase-averaged wave modelling and only partly considered the influence of IG waves on the wave period at the toe using the empirical model of Hofland et al. (2017)—which has been shown to underestimate the influence of IG waves on very gentle slopes (Nguyen et al., 2020). On the other hand, Oosterlo et al. (2018) carried out a similar probabilistic assessment of a dike with a sandy foreshore but used a more computationally-demanding wave model. The authors found, for the considered case, that accounting for the IG waves resulted in two orders of magnitude higher failure probabilities compared to a simple rule-of-thumb method that neglected them.

There is need for a computationally inexpensive probabilistic method which accurately considers the influence of IG waves on both the wave height and spectral wave period at the dike toe. Likewise, it is necessary to investigate whether the large influence of the IG waves reported by Oosterlo et al. (2018) is also found for other cases, or if it were merely an artefact of the method used or specific case considered.

## 1.3 RESEARCH OBJECTIVES

It is the primary aim of this dissertation to *develop new methods to estimate the influence of IG waves on the safety of coastal defences with shallow foreshores against wave overtopping*. The study is guided by the following four research questions (RQ's), which aim to fill the identified knowledge gaps (Section 1.2):

RQ1. Under what conditions do IG waves dominate wave conditions at the toe of the dike?

RQ2. Is there a trade-off between numerical model accuracy and the computational load required to simulate wave overtopping in IG-wave dominated environments?

RQ3. How can empirical estimates of wave overtopping be improved to account for very shallow foreshores where IG waves dominate?

RQ4. What is the influence of IG waves on the probability of dike failure by wave overtopping along the Dutch Wadden Sea coast?

It should be noted that while the Dutch Wadden Sea coast was considered the central case study of this dissertation, RQ's 1 to 3 were not limited to environmental conditions specific to that area. Likewise, the analytical framework developed in response to RQ4 is also adaptable to other locations. The findings herein may therefore be considered applicable to coastlines within and outside of the Netherlands.

## 1.4 APPROACH AND METHODS

In this dissertation, the above research objectives were achieved by: assessing the influence of these **IG waves** on wave overtopping using state-of-the art **numerical modelling** tools; deriving **empirical methods** to capture this influence; and finally developing a method to estimate **probability of dike failure by wave overtopping**—taking into account the influence of IG waves. The tools used and developed herein were validated as much as possible with physical model and field measurements (Figure 1.4).

As field measurements and laboratory experiments are expensive to implement and typically limited to a narrow range of conditions, numerical models offer a timely and cost-effective alternative to better understand the interaction between waves, the foreshore, and the structure. Once validated, the phase-resolving wave model, XBeach Nonhydrostatic was used to generate a large dataset of IG wave heights at the structure toe, under a wide range of environmental conditions. From this numerical dataset, empirical relations were derived to estimate the magnitude of IG waves for a given set of environmental conditions (RQ1).

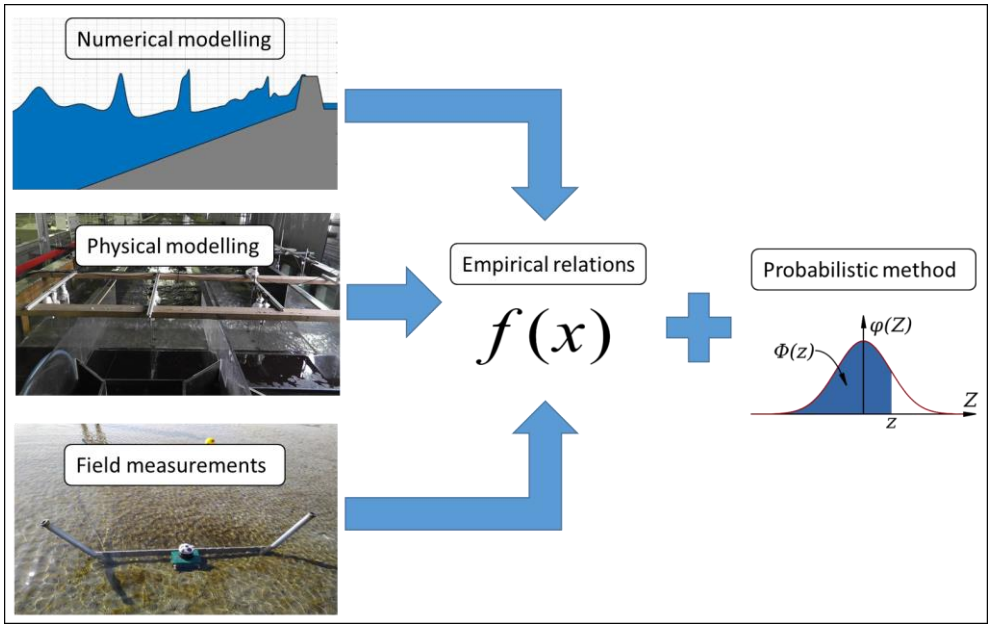


**Figure 1.4** *Overview of the main components of the research approach (adapted from: https://kbase.ncr-web.org/all-risk/projects/b2-wave-propagation-over-foreshores/).*

The newly derived empirical relations are used to augment the phase-averaged wave model, SWAN—which inherently excludes IG waves. The performance of the combined SWAN and empirical approach was assessed against other widely-used numerical models (RQ2).

To account for the effects of IG waves on empirical wave overtopping (RQ3), the Goda et al. (1975) approach was revisited here. In this approach, wave overtopping is determined using deep-water wave parameters; thus, removing the need for additional numerical modelling and avoiding the difficulties of obtaining accurate estimates of nearshore parameters. Using existing physical model tests, a new set of empirical formulae based on this approach were derived.

Finally, a modular probabilistic framework that couples numerical, empirical and probabilistic models, is advanced to estimate the influence of IG waves on the overtopping failure probability. This is done by augmenting the approach of Vuik et al. (2018) with newly derived empirical relations to account for the IG waves. The framework is then applied to the Dutch Wadden Sea coast to assess the overtopping failure probability with and without the influence of IG waves (RQ4).

## 1.5 OUTLINE OF THE DISSERTATION

An overview of the connections between the dissertation chapters, RQ's and the four major themes, as described in Section 1.2, is presented in Figure 1.5.

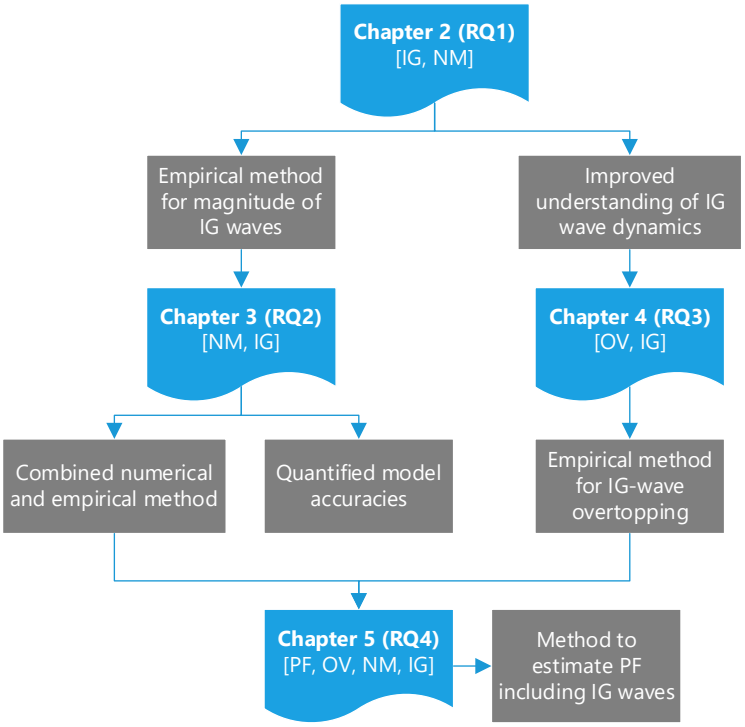


**Figure 1.5:** *Connections between chapters (black), research questions (RQ's), main outputs (grey) and dissertation themes: infragravity waves (IG), numerical modelling (NM), overtopping (OV) and probability of failure (PF).*

This dissertation is organized as follows:

Chapter 2 describes the influence of various environmental parameters on the magnitude of IG waves at the dike toe. In this way, the conditions that result in IG waves dominating wave conditions at the dike toe are identified (RQ1).

Chapter 3 compares the ability of several widely-used numerical wave models to simulate wave propagation and wave overtopping, either directly or indirectly, for dikes with very shallow foreshores. In this way, their speed versus accuracy in very shallow foreshore environments is quantified (RQ2).

In Chapter 4 a new set of formulae to estimate the mean overtopping discharge are derived empirically using deep-water wave characteristics and key foreshore parameters, which accurately describe the influence of the foreshore bathymetry on wave breaking and the growth of IG waves (RQ3).

Chapter 5 demonstrates, by means of a case study of the Dutch Wadden Sea coast, how the probability of dike failure by wave overtopping for cases with shallow foreshores can be

calculated, both with and without considering the influence of IG waves. In this way the influence of IG waves on the probability of failure is quantified (RQ4).

Chapter 6 concludes the thesis by addressing the overall research objectives, highlighting the implications of the findings for current practice, stating limitations and identifying areas for future work.

## 1.6 RESEARCH CONTEXT: THE ALL-RISK PROJECT

This dissertation is part of the wider All-Risk project, which was initiated in 2017 to support the Dutch Flood Protection program (in Dutch, HWBP) in its implementation of a new probabilistic risk-based approach to the management of flood defences. This approach required that multiple failure mechanisms for all flood defence structures be established and then combined to assess the overall probability of flooding. The All-Risk project sought to address this new challenge by providing cutting-edge research in the fields of: A) risk-based design; B) hydraulic loads; C) subsoil heterogeneity; D) flood defence reliability; and E) the legal framework necessary for the implementation and acceptance of the proposed solutions.

The overall project aimed to: i) provide a better understanding of the reliability of flood defences, and ii) provide scientific support for the transition towards the implementation of risk-based flood protection standards. To that end, project B covered three topics:

1. Foreshore ecosystems management
2. **Wave propagation over foreshores and impact on dike design**; and
3. Large-scale uncertainty in river water levels.

This dissertation (sub-project B2, emboldened above) focuses on how the safety of coastal flood defences—specifically, their ability to resist overtopping waves—may be affected by processes occurring over shallow foreshores. The findings herein not only offer insight into the influence of shallow foreshores on wave propagation and overtopping but also provide a suite of tools to quantify that influence. This dissertation may therefore serve the HWBP as guidance for the design and assessment of coastal defences with shallow foreshores, taking into account IG waves; and thereby reducing the uncertainty in hydraulic (wave) loads.

This dissertation is also closely linked to that of sub-project B3 (authored by Beatriz Marin Diaz), focused on the ecological aspects of the shallow, often-vegetated foreshores of the Dutch Wadden Sea. Together, they offer insight into the ability of shallow foreshores improve coastal protection in the face of climate change and other ecological stressors.

# 2

# IMPORTANCE OF INFRAGRAVITY WAVES AT DIKES WITH SHALLOW FORESHORES*


## ABSTRACT

As a first step to achieving the overall research aim (Section 1.3), this chapter seeks to: i) identify the influence of various offshore, foreshore and dike slope conditions on the magnitude of nearshore IG waves; and ii) develop a predictive model for the relative magnitude of IG waves—defined as the ratio of the IG- to SS-wave height at the dike toe. This is achieved using a combined physical and numerical modelling approach. Findings show that higher, directionally narrow-banded incident waves; shallower water depths; milder foreshore slopes; reduced vegetated cover; and milder dike slopes promote IG-wave dominance. Additionally, the empirical model derived—which captures the combined effect of the varied environmental parameters—allows practitioners to quickly estimate the significance of IG waves at the coast, and may also be combined with spectral wave models to extend their applicability to areas where IG waves contribute significantly.


The chapter is organized as follows: Section 2.1 describes the physical processes that result in IG waves in deep and shallow water. Section 2.2 provides descriptions of the numerical and physical models, followed by an overview of the formulae used to carry out the analyses. In Section 2.3, the numerical model is first validated and used—together with the physical experiment—to provide an in-depth discussion on the source of nearshore IG-wave energy. Next, the results of the numerical simulations of varied offshore, foreshore and dike slope conditions are presented and discussed. Section 2.3 ends by quantifying the influence of each parameter and presenting the empirical model to predict the relative magnitude of nearshore IG waves. Section 2.4 concludes the chapter by addressing the objective and identifying specific areas for future work.

*This chapter has been published as: Lashley, C. H., Bricker, J. D., van der Meer, J., Altomare, C., and Suzuki, T.: Relative Magnitude of Infragravity Waves at Coastal Dikes with Shallow Foreshores: A Prediction Tool, Journal of Waterway, Port, Coastal, and Ocean Engineering, 146, 10.1061/(asce)ww.1943-5460.0000576, 2020.

## 2.1 INTRODUCTION

### 2.1.1 BACKGROUND

Infragravity (IG) waves—often referred to as "long", "surfbeat" or "tsunami-like" waves—are now widely recognized as the driving force behind several critical nearshore processes: beach and dune erosion (Roelvink et al., 2009); the development of seiches in harbours (Okihiro et al., 1993); and wave-driven coastal inundation (Stockdon et al., 2006). Recent observations of their impact include: unexpectedly high run-up levels observed at the rocky coast of Banneg island (Sheremet et al., 2014); extensive damage and casualties which occurred along a coral-reef-lined coast in the Philippines during Typhoon Haiyan (Roeber and Bricker, 2015, Shimozono et al., 2015); and on the west coast of France, where several dunes were eroded and "over-washed" (Baumann et al., 2017, Lashley et al., 2019a). In each of these cases, the observed extreme water levels and resulting damage have been attributed to the presence or dominance of nearshore IG waves.

In deep water, these long-period, low-amplitude waves are formed through nonlinear interactions of sea and swell—hereafter referred to as sea-swell (SS)—wave components (Longuet-Higgins and Stewart, 1962), such as: those locally generated by wind (sea); and those generated by distant storms (swell). The resulting wave-group pattern, with sequences of higher and lower amplitudes, generates an IG wave which travels bound to, and $\pi$ radians out of phase with, the wave group.

As SS waves approach shallow mildly-sloping foreshores, they experience shoaling and continue to transfer energy to the bound IG wave, resulting in its amplitude growth. After SS waves break, the wave-group structure disappears and the bound IG wave is either freed (released) (Masselink, 1995) or dissipates together with the SS waves (Baldock, 2012). This enhancement and subsequent freeing of the bound IG wave is considered to be the main generation mechanism of nearshore IG waves on mild slopes ($\beta_b \leq 0.3$, Equation 2.2.1); where the normalized bed-slope parameter ($\beta_b$) is defined as (Battjes, 2004):

$$\beta_b = \frac{\beta}{\omega}\sqrt{\frac{g}{h_b}}, \tag{2.1}$$

where $\beta$ [-] is the bed slope (taken here as foreshore slope, $\tan(m)$); the angular frequency of the IG wave, $\omega = 2\pi f_{low}$ [rad/s], where $f_{low}$ [Hz] is the mean frequency of the IG wave at the breakpoint; $g$ [m/s$^2$] is the gravitational constant of acceleration and $h_b = H_{m0}/\Omega$ [m] is the mean breaker depth, where $\Omega$ [-] is the ratio of local wave height to water depth at the breakpoint.

Alternatively, nearshore IG waves may be generated on steep slopes ($\beta_b \geq 1$) by the temporal variation in the location of breaking waves. This occurs when alternating groups of higher- and lower-amplitude waves break farther and closer to the shore, respectively. The resulting

fluctuations in wave set-up and set-down, with the period of the wave groups, produce both seaward and shoreward propagating IG waves (Battjes, 2004, Symonds et al., 1982) which are out-of-phase and in-phase with the wave groups, respectively (Baldock et al., 2000).

These free IG waves are able to propagate in very shallow water where they either slowly dissipate by: i) bottom friction (Henderson and Bowen, 2002, Pomeroy et al., 2012), ii) IG-wave breaking (De Bakker et al., 2014, Van Dongeren et al., 2007), iii) the nonlinear transfer of energy back to higher frequencies (Henderson et al., 2006); or are reflected off the coast or structure, forming (partially) standing waves (Sheremet et al., 2002). The magnitude of these IG waves at the shoreline can be substantial, exceeding that of waves at SS frequencies. Under these conditions of dominance, IG waves govern wave run-up and consequently, the potential for wave-induced flooding and coastal erosion (Guza and Thornton, 1982, Holman and Sallenger, 1985, Lashley et al., 2018, Ruessink et al., 1998, Ruggiero et al., 2004, Van Gent, 2001).

In the design and assessment of coastal dikes, the extent of wave run-up and the associated volume of water which overtops the dike are typically assessed using empirical formulae that require wave height at the dike toe as input (EurOtop, 2018, Mase et al., 2013, Van Gent, 2001). Given their computational efficiency, spectral wave models—such as SWAN (Booij et al., 1999) and STWAVE (Smith et al., 2001)—are now widely used to estimate wave conditions at the dike toe, including vegetation effects (Suzuki et al., 2012). While these phase-averaged models may accurately estimate the SS-wave height at the toe ($H_{m0,SS,toe}$ [m]), they exclude the nonlinear interactions that force the IG-wave component ($H_{m0,IG,toe}$ [m]) (Nwogu and Demirbilek, 2010). Thus, their applicability to cases with shallow foreshores—where the ratio of local water depth at the dike toe to the offshore (deep-water) wave height, $h_{toe}/H_{m0,deep} < 4$ (Hofland et al., 2017)—is limited; as IG waves tend to be significant under shallow conditions (Hofland et al., 2017, Van Gent, 2001). In light of this, it is the primary aim of the present chapter is to investigate the range of environmental conditions that promote the dominance of IG-wave energy at the toe of coastal dikes; and to provide a tool whereby the magnitude of $H_{m0,IG,toe}$, relative to $H_{m0,SS,toe}$, may be estimated as an indicator for the validity of these models.

Previous attempts have been made to relate the magnitude of IG-wave energy, either at the shore (in the form of swash) or near the shore, to parameters that describe the coastal environment; however, the findings have been inconsistent, to date. Guza and Thornton (1982) found that the IG component of wave run-up increased linearly with increasing offshore wave height ($H_{m0,deep}$ [m]). Holman and Sallenger (1985) and Ruessink et al. (1998) have later shown that it may be better predicted using the well-known breaker parameter ($\xi_0$ [-]), also referred to as the Iribarren number, which considers not only $H_{m0,deep}$ but also the deep-water wavelength ($L_0$ [m]) and foreshore slope angle ($m$ [°]). Contrastingly,

Stockdon et al. (2006)—in their analysis of 6 field sites—concluded that the IG component scaled better with $\sqrt{H_{m0,deep}L_0}$ [m] and was actually independent of $m$. For barred beaches, Cox et al. (2013) found a high correlation between shoreline IG motions and nearshore bar depth, suggesting that local water depth ($h_{toe}$ [m])—or local strong variations in foreshore geometry—plays a significant role. This finding also agrees well with studies on shallow reefs where wave characteristics were better described by relative water depth $\left(h_{toe}/H_{m0,deep}\right)$, compared to $\xi_0$ (Lashley et al., 2018, Yao et al., 2013). Diversely, Inch et al. (2017) have found that nearshore IG waves were best predicted using an offshore forcing parameter that is proportional to the SS-wave energy flux (${H_{m0,deep}}^2 T_p$ [m$^2$s]). Recently, both Gomes da Silva et al. (2018) and Passarella et al. (2018), in disagreement with Stockdon et al. (2006), argue that considering $m$ reduces IG-swash prediction errors. These contradictory findings both reveal that further research on the subject is required and suggest that nearshore IG-wave energy is unlikely a function of any single environmental factor.

Each of the before-mentioned studies aimed at parameterizing IG-wave energy, at or near the shore, were limited to the environmental conditions of the geographic areas and time periods considered. Here, we combine the results of physical modelling and the XBeach phase-resolving numerical model (Smit et al., 2010) to generate a comprehensive dataset of varying: i) offshore forcing conditions (wave height, period and directional spreading); ii) foreshore conditions (initial water depth, slope, vegetated cover and bottom friction); and iii) dike slopes. XBeach, in non-hydrostatic mode, has been successfully used to reproduce nearshore hydrodynamics over a wide-range of coastal environments under varying combinations of deep-water wave heights and periods; these include: shallow, mildly-sloping foreshores (Roelvink et al., 2018); shallow fringing reefs (Lashley et al., 2018, Pearson et al., 2017); vegetated coasts (Van Rooijen et al., 2016); and steeply-sloping gravel beaches (McCall et al., 2015). Therefore, the model is seen here as an appropriate tool to carry out the analysis.

## 2.2 METHODS

### 2.2.1 PHYSICAL MODEL DESCRIPTION

The physical modelling was performed at Flanders Hydraulics Research in a 70-m long, 4-m wide and 1.45-m deep wave flume (Altomare et al., 2016). The experiments simulated the transformation of swell waves—with deep-water wave steepness, $s_0 \leq 0.015$ (Table 2.1)—over a smooth 1:50 sloping foreshore backed by a 1:2 sloping dike (Figure 2.1) with varying offshore significant wave heights ($H_{m0,deep}$), spectral peak periods ($T_p$ [s]) and initial still-water depths ($h_{toe}$). The flume, equipped with second-order wave generation, produced irregular waves which corresponded to a JONSWAP-type spectrum with a peak enhancement factor of 3.3 with a duration equal to 1000 times $T_p$ (~1000 waves). The variations of water-surface elevations were measured using 10 resistance-type gauges, all synchronously sampling at 50 Hz (Figure 2.1). Considering a geometric scaling of 1:25, conditions at the

dike toe were measured 1 m (prototype scale) seaward of the dike base (at gauge 10). A summary of the test conditions is provided in Table 2.1. Note that the depth becomes very shallow and almost zero (Table 2.1).

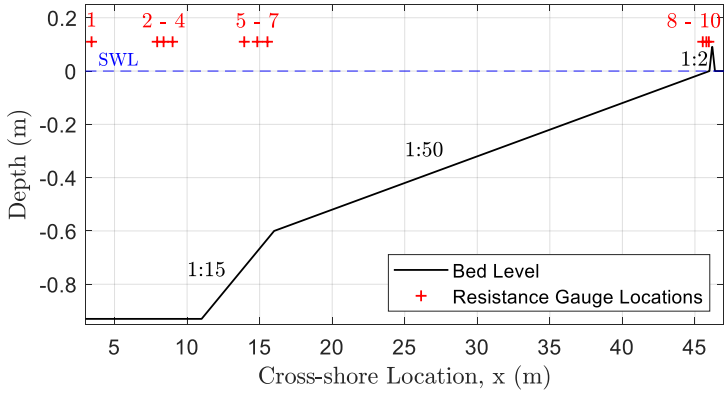


**Figure 2.1**. *Physical model setup showing resistance gauge locations. Reproduced from: Lashley et al. (2019b).*

**Table 2.1**. *Summary of physical model test conditions in prototype scale, with wave steepness ($s_0$), relative water depth ($h_{toe}/H_{m0,deep}$), mean frequency of the IG wave at the breakpoint ($f_{low}$), normalized bed slope ($\beta_b$) and observed relative magnitude of infragravity waves ($\widetilde{H}_{IG}$, Equation 2.22) values.*

| Test No. | Prototype Scale | | | $s_0$ | $\frac{h_{toe}}{H_{m0,deep}}$ | $f_{low}$ (Hz) | $\beta_b$ | $\widetilde{H}_{IG}$ |
|---|---|---|---|---|---|---|---|---|
| | $H_{m0,deep}$ (m) | $T_p$ (s) | $h_{toe}$ (m) | | | | | |
| 1 | 1.675 | 11.50 | 0.757 | 0.008 | 0.452 | 0.06 | 0.50 | 1.05 |
| 2 | 1.425 | 12.65 | 0.025 | 0.006 | 0.018 | 0.06 | 0.53 | 1.43 |
| 3 | 2.125 | 11.60 | 0.020 | 0.010 | 0.009 | 0.05 | 0.47 | 1.74 |
| 4 | 2.500 | 11.60 | 0.025 | 0.012 | 0.010 | 0.05 | 0.48 | 1.82 |
| 5 | 3.025 | 11.50 | 0.025 | 0.015 | 0.008 | 0.05 | 0.42 | 2.01 |
| 6 | 1.700 | 11.40 | 1.250 | 0.008 | 0.735 | 0.07 | 0.41 | 0.85 |
| 7 | 1.475 | 12.40 | 1.262 | 0.006 | 0.856 | 0.06 | 0.48 | 0.70 |
| 8 | 1.625 | 11.40 | 1.250 | 0.008 | 0.769 | 0.06 | 0.48 | 0.82 |
| 9 | 2.850 | 11.55 | 1.250 | 0.014 | 0.439 | 0.05 | 0.41 | 1.20 |
| 10 | 2.875 | 12.65 | 1.250 | 0.012 | 0.435 | 0.05 | 0.42 | 1.12 |
| 11 | 1.500 | 11.45 | 0.787 | 0.007 | 0.525 | 0.06 | 0.49 | 0.96 |
| 12 | 1.300 | 12.40 | 0.050 | 0.005 | 0.038 | 0.06 | 0.55 | 1.39 |

### 2.2.2 NUMERICAL MODEL DESCRIPTION

#### *2.2.2.1 Governing Equations*

For this study, we applied the open-source XBeach numerical model. The non-hydrostatic mode (XB-NH) was selected because it resolves both infragravity and sea-swell wave motions, including the effect of vegetation. It computes depth-averaged flow due to waves and currents using the non-linear shallow water equations, and is less computationally demanding than depth-resolving models (e.g. OpenFOAM (Jasak et al., 2007) or SWASH multi-layer (Zijlema et al., 2011)). The governing equations, in one-dimensional form, follow:

$$\frac{\partial \eta}{\partial t} + \frac{\partial uh}{\partial x} = 0, \tag{2.2}$$

$$\frac{\partial u}{\partial t} + u\frac{\partial u}{\partial x} - v_h\frac{\partial^2 u}{\partial x^2} = -\frac{1}{\rho}\frac{\partial(\bar{q} + \rho g\eta)}{\partial x} - c_f\frac{u|u|}{h} + \frac{F_v}{\rho h}, \tag{2.3}$$

where $x$ [m] and $t$ [s] are the horizontal spatial and temporal coordinates, respectively, $\eta$ [m] is the free surface elevation, $u$[m/s] is the depth-averaged cross-shore velocity, $v_h$ [m$^2$/s] is the horizontal eddy viscosity (Smagorinsky, 1963), $h$ [m] is the water depth, $\rho$ [kg/m$^3$] is the density of water, $c_f$ [-] is the bed friction factor and $F_v$ [N] is the depth-averaged vegetation force (Van Rooijen et al., 2016). The depth-averaged dynamic (non-hydrostatic) pressure normalized by the density, $\bar{q}$ [m$^2$/s$^2$] is computed from the mean of the dynamic pressure at the surface ($q_s$ [m$^2$/s$^2$], assumed to be zero) and the bed ($q_b$ [m$^2$/s$^2$], by assuming a linear change over depth). In order to compute the dynamic pressure at the bed, the contributions of advective and diffusive terms to the vertical momentum balance are considered negligible:

$$\frac{\partial w}{\partial t} + \frac{\partial q}{\partial z} = 0, \tag{2.4}$$

where $w$ [m/s] is the vertical velocity and $z$ [m] is the vertical coordinate. The vertical velocity at the bed is set by the kinematic boundary condition:

$$w_b = u\frac{\partial(\eta - h)}{\partial x}, \tag{2.5}$$

and the vertical momentum balance at the surface follows:

$$\frac{\partial w_s}{\partial t} = 2\frac{q_b}{h} - \frac{\partial w_b}{\partial t}. \tag{2.6}$$

The dynamic pressure at the bed is then solved by combining Equation 2.2.6 and the local continuity equation:

$$\frac{\partial u}{\partial x} + \frac{w_s - w_b}{h} = 0 \tag{2.7}$$

In the present study, we obtain $c_f$ from the Manning's roughness coefficient ($n$ [s/m$^{1/3}$]) as follows (Roelvink et al., 2015):

$$c_f = \frac{n^2 g}{\sqrt[3]{h}}. \tag{2.8}$$

$F_v$ is obtained by integrating the drag force per unit height ($F_D$ [N/m]) over the vegetation height ($h_v$ [m]) (Dalrymple et al., 1984):

$$F_D = \frac{1}{2}\rho C_D b_v N_v \, u|u|, \tag{2.9}$$

where $C_D$ [-] is the drag coefficient, $b_v$ [m] is the vegetation stem diameter and $N_v$ [stems/m$^2$] is the vegetation density. Though not assessed as part of the present study, the performance of XBeach in simulating the effects of vegetation has been previously validated with data from two physical experiments, showing high skill (Van Rooijen et al., 2016). Note that a recent study using SWASH reveals that the effects of porosity and inertia of vegetation can be important for wave propagation in dense vegetation fields (Suzuki et al., 2019). However, those effects were not taken into consideration in this study since the vegetation considered here is not so dense to have a significant influence on the results.

To control the computed location and magnitude of depth-limited wave breaking, a hydrostatic front approximation is applied. The pressure distribution under breaking waves is therefore considered to be hydrostatic once the local surface steepness exceeds a maximum value (Smit et al., 2010). This criterion is controlled by the user-specified *maxbrsteep* parameter.

#### *2.2.2.2 Model Set-up*

The numerical simulations were first configured using a 1D approach to represent actual flume conditions. In the current study, we apply the configuration of Lashley et al. (2018) which obtained reasonably accurate results when applied to similar shallow environments (fringing reefs). As such, the maximum breaking wave steepness (*maxbrsteep*) was set to 0.5 compared to its default value of 0.6. A brief analysis of the sensitivity of the model results to the *maxbrsteep* parameter is provided in the Appendix (Figure A. 1). The Manning's roughness coefficient ($n$) was set to 0.012 s/m$^{1/3}$ to represent a relatively smooth flume bottom (Suzuki et al., 2017). The cross-shore grid spacing ($\Delta x$) applied varied from a maximum of $L_0/100$ (offshore) to a minimum of 1 m (dike toe). This choice of varying $\Delta x$ minimized computation time while ensuring that the waves were accurately resolved. No further tuning of the model was done as part of this study.

For validation, the model was forced at its boundary with time series of velocities derived from the paddle motion observed during the physical experiment, which corresponded to a JONSWAP-type spectrum and included the generation of second-order bound waves.

Likewise, the extent of numerical model domain corresponded to that of the physical flume (Figure 2.1).

While assessing the influence of the varied environmental parameters (described in Section 2.2.4), the model domain was allowed to vary depending on the water depth and foreshore slope (Figure 2.2). These simulations were forced with irregular waves generated using parametric (JONSWAP-type) spectra with a peak enhancement factor of 3.3. For the numerical simulations where directional spreading was considered, a 2DH approach was adopted with cyclic lateral boundaries. This approach assumed alongshore uniformity and used an alongshore grid spacing, $\Delta y = 2\Delta x$, which was found to be optimal considering both accuracy and computational demand. All other model parameters were set to match the 1D simulations.

It should be noted that the numerical model, like the physical experiments, assumes bound IG waves at its boundary and does not consider potentially free IG waves arriving at the boundary from distant sources. Likewise, neither the physical experiment nor the 1D numerical simulations contain (two-dimensional) trapped IG waves, which might have an effect in the field. They do, however, consider the generation of free IG waves resulting from the shoaling and breaking of the SS-wave groups within the model domain.

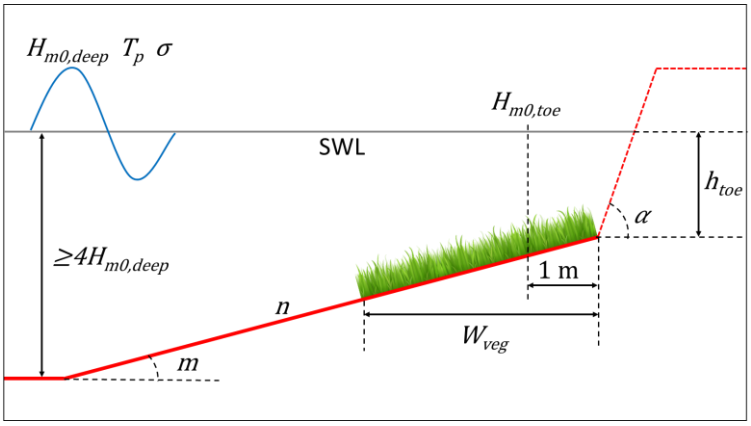


**Figure 2.2**. *Schematic representation of dike-foreshore system indicating the relevant environmental parameters.*

### *2.2.2.3 Validation Metrics*

In order to assess the performance of XB-NH, we applied the following objective functions: Scatter Index ($SCI$ [-]), as a normalized measure of error (Equation 2.10); and Relative Bias ($Rel.bias$ [-]), as an indicator of prediction bias (Equation 2.11).

$$SCI_{\Psi} = \frac{\sqrt{\frac{1}{n}\sum_{i=1}^{N}\left(\Psi_{XB}^{i} - \Psi_{Obs}^{i}\right)^{2}}}{\frac{1}{n}\sum_{i=1}^{N}\Psi_{Obs}^{i}}, \tag{2.10}$$

and

$$Rel.bias_{\Psi} = \frac{\sum_{i=1}^{N}(\Psi_{XB}^{i} - \Psi_{Obs}^{i})}{\sum_{i=1}^{N}\Psi_{Obs}^{i}}, \tag{2.11}$$

where $\Psi$ represents the parameter being evaluated, in a sample size $N$ [-]; and subscripts $XB$ and $Obs$ refer to XBeach predictions and observations during the physical experiment, respectively. Lower $SCI$ values (< 0.15) indicate accurate model predictions (Roelvink et al., 2018); while a positive or negative $Rel.bias$ estimate indicates a systematic over- or under-prediction, correspondingly.

### 2.2.3 DATA PROCESSING AND ANALYSIS

#### *2.2.3.1 Mean Water Level*

The mean water level ($\bar{\eta}$ [m]) was calculated by taking the mean of the surface elevation time series, $\eta(t)$ [m] at each instrument location, relative to the base of the dike (unless otherwise stated).

#### *2.2.3.2 Separation of Sea-swell and Infragravity Waves*

The time series of $\eta(t)$ were further analysed using the Welch's average periodogram method and a Hann filter with a 50% maximum overlap. The resulting one-dimensional spectra of wave energy density, $C_{\eta\eta}(f)$ [m$^2$/Hz], with ~43 degrees of freedom and a frequency resolution of ~0.008 Hz, were then used to determine the significant wave heights in both the SS ($H_{m0,SS}$) and IG ($H_{m0,IG}$) bands, as follows:

$$H_{m0,SS} = 4\sqrt{\int_{f_p/2}^{1} C_{\eta\eta}df}, \tag{2.12}$$

and

$$H_{m0,IG} = 4\sqrt{\int_{0.008}^{f_p/2} C_{\eta\eta}df}, \tag{2.13}$$

where half the peak frequency ($f_p/2 = 1/2T_p$ [Hz]) is taken as the cut-off to separate SS and IG motions (Roelvink and Stive, 1989). This choice of cut-off frequency is based on the

tendency that, in deep water, the majority of SS-wave energy is found at frequencies > $f_p/2$ while the majority of IG-wave energy lies at frequencies <$f_p/2$.

#### 2.2.3.3 *Infragravity-wave Generation Mechanisms*

To investigate the generation of IG waves by either: i) shoaling of the bound wave; or ii) breakpoint forcing, a cross-correlation analysis was carried out between the envelope of the SS waves, $A(t)$ and the low-pass filtered ($< f_p/2$) surface elevation time series , $\eta^{IG}(t)$ [m], which represents IG motions. Following Janssen et al. (2003), $A(t)$ [m] was calculated as:

$$A(t) = |\eta^{SS}(t) + i\Gamma\{\eta^{SS}(t)\}|^{IG}, \tag{2.14}$$

where $\eta^{SS}(t)$ is the high-pass filtered ($> f_p/2$) surface elevation time series which represents SS motions, and $\Gamma$ denotes the Hilbert transform operator.

The correlation between $A(t)$ (offshore) and $\eta^{IG}(t)$ was then determined using the following cross-correlation function:

$$R_{\eta A} = \frac{\langle \eta^{IG}(t) A(t+\tau) \rangle}{\sigma_\eta \sigma_A}, \tag{2.15}$$

where $\langle ... \rangle$ denotes a time averaging operator; $\tau$ denotes a time shift; and $\sigma_\eta$ and $\sigma_A$ are the standard deviations of $\eta^{IG}(t)$ and $A(t)$, respectively; and $-1 \leq R_{\eta A}[-] \leq 1$ .

This approach has been found to successfully identify both bound incoming (negative $R_{\eta A}$) and outgoing free IG waves (positive/negative $R_{\eta A}$) (e.g. Janssen et al., 2003, List, 1992); incoming break-point generated IG waves (positive $R_{\eta A}$ ); and outgoing break-point generated IG waves (negative $R_{\eta A}$) (e.g. Baldock and Huntley, 2002, Pomeroy et al., 2012).

#### 2.2.3.4 *Separation of Incoming and Outgoing Infragravity Waves*

The total low-pass filtered surface elevation signal was then separated into incoming, $\eta_{in}(t)$ [m], and outgoing, $\eta_{out}(t)$ [m], components as follows (Guza et al., 1984):

$$\eta^{IG}(t) = \eta^{IG}_{in}(t) + \eta^{IG}_{out}(t), \tag{2.16}$$

$$\eta^{IG}_{in}(t) = \frac{\eta^{IG}(t) \cdot c_{in} + u^{IG}(t) \cdot h}{c_{in} + c_{out}}, \tag{2.17}$$

and

$$\eta^{IG}_{out}(t) = \frac{\eta^{IG}(t) \cdot c_{out} - u^{IG}(t) \cdot h}{c_{in} + c_{out}}, \tag{2.18}$$

where

$$c_{in} = \begin{cases} c_g & x < x_b \\ \sqrt{gh} & x \geq x_b \end{cases}, \tag{2.19}$$

$$c_{out} = \sqrt{gh}, \tag{2.20}$$

$h$ is the water depth at the location (including wave-induced setup); and $u(t)$ is the horizontal velocity time series. Here, the incoming waves seaward of the breakpoint ($x_b$) are assumed to be bound—propagating with celerity ($c$) equal to the group velocity ($c_g$); while those shoreward of the breakpoint and those outgoing are assumed to be free waves travelling with $\sqrt{gh}$. This method, initially developed for normally-incident, shallow-water (long) waves, requires co-located pressure gauges and current meters—to obtain $\eta(t)$ and $u(t)$, respectively—in order to decompose the total signal into seaward (outgoing) and shoreward (incoming) propagating components (Guza et al., 1984). These signals were then used to calculate the incoming and outgoing significant wave heights in the IG frequency bands ($H_{m0,IG,in}$ and $H_{m0,IG,out}$) using Equation 2.13.

#### *2.2.3.5 Identification of Standing Wave*

Inshore of the forcing zone (shoreward of the breakpoint), the superposition of the incoming wave and that reflected at the structure form a standing-wave (List, 1992). This standing wave is then characterized by areas of maximum energy (antinodes)—where the total energy is approximately the sum of the incoming and outgoing waves—and areas of minimum energy (nodes)—where the total energy is approximately equal to the difference between the incoming and outgoing waves.

For a given cross-shore location ($x$), the frequencies at which nodes in a standing wave occur were identified as follows (Buckley et al., 2018, Nwogu and Demirbilek, 2010):

$$f_{node} = \frac{1}{4}(2m_{node} - 1)\left(\int_{x}^{x_{dike}} \frac{1}{\sqrt{gh}} dx\right)^{-1}, \tag{2.21}$$

where $x_{dike}$ [m] is the dike location (point of reflection) and $m$ is the number of nodes from the reflection point ($m_{node} = 1$ corresponds the fundamental mode of the dike-foreshore system. This equation considers the dike-foreshore system to be an open-ended basin of variable depth. It is based on the formation of a node at a distance from the structure equal to one-quarter the wavelength of a wave propagating with speed, $c = \sqrt{gh}$ [m/s]. By calculating this wave speed at discrete points across the foreshore, $f_{node}$ may be obtained for the sloping bathymetry (Roeber and Bricker, 2015).

#### *2.2.3.6 Relative Magnitude of Infragravity Waves*

We defined the relative magnitude of nearshore IG waves ($\widetilde{H}_{IG}$ [-]) as the ratio of $H_{m0,IG}$ to $H_{m0,SS}$, at the toe of the structure:

$$\widetilde{H}_{IG} = \frac{H_{m0,IG,toe}}{H_{m0,SS,toe}}, \tag{2.22}$$

and IG-wave dominance where $\widetilde{H}_{IG} > 1$.



### 2.2.4 ENVIRONMENTAL PARAMETERS FOR NUMERICAL SIMULATIONS

Following validation, XBeach was used to simulate a range of environmental parameters, specifically those related to hydrodynamic forcing conditions: $H_{m0,deep}$, $T_p$ and directional spreading width ($\sigma$ [°]); foreshore conditions: $h_{toe}$, foreshore slope angle ($m$), width of vegetated cover ($W_{veg}$ [m]) and bottom friction ($n$); and dike slope angle ($\alpha$ [°]).

#### *2.2.4.1 Selection Criteria for Parameter Values*

The range of each parameter was selected to extend the analysis as far as possible while adhering to the limits of both nature and the reliability of the numerical model. The criteria applied to the selection of parameter values follow:

- $0.005 < s_0 < 0.036$ at the model boundary, where $s_0$[-] is the deep-water wave steepness;
- The water depth at the model boundary $\geq 4H_{m0,deep}$ to ensure that no depth-induced breaking occurred offshore (Hofland et al., 2017);
- $kh \leq 1$ [-] at the model boundary to minimise the relative dispersion and celerity errors associated with the nonlinear shallow water equations; where wave number, $k = 2\pi/L$ [m$^{-1}$];
- $\sigma$ values of 0°, 10° and 24° to represent wave flume, swell and wind sea conditions, respectively (Roelvink et al., 2018). This parameter may also be characterized by the user-defined spreading factor $s$ [-] in XBeach (Equation 2.23);

$$\sigma = \frac{180}{\pi}\sqrt{\frac{2}{s+1}}. \tag{2.23}$$

- $W_{veg}$, measured as horizontal distance from the dike, ranged from 0 to 800 m which is typical of salt marshes found in the Netherlands (Vuik et al., 2016). A summary of the parameter values simulated is provided in Table 2.2 and the properties of the vegetation considered in Table 2.3. Note that a relative vegetation submergence depth ($h/h_v$) of 3.33 is considered here.
- $n$ values of 0.012, 0.02 and 0.03 s/m$^{1/3}$ to represent smooth wave flume, muddy foreshore and sandy foreshore conditions, respectively. This parameter is then converted to a dimensionless friction coefficient ($c_f$) in XBeach (Equation 2.2.8).
- For the foreshore slope ($m$), the steepest and mildest slopes considered were 1:10 and 1:1000 respectively. Slopes steeper that 1:10 are considered part of the structure and slopes gentler than or equal to 1:1000 are all treated as (near) flat.

Following a one-[factor]-at-a-time (OAT) approach, each environmental parameter was varied while all others remained constant. For example, in the assessment of the influence of initial water depth, $h_{toe}$ was varied from 0 m to 5 m while $\sigma$, $\cot(m)$, $W_{veg}$, $n$ and $\cot(\alpha)$ were kept constant at their reference values. For each parameter value, 24 combinations of $H_{m0,deep}$ and $T_p$ ($0.005 < s_0 < 0.036$)—based on Table 2.2 and the above criteria—were simulated at the model boundary. As a result, a total of 672 XBeach simulations were carried out.

**Table 2.2**. *Summary of values (prototype scale) for offshore significant wave height ($H_{m0,deep}$), peak period ($T_p$), directional spreading ($\sigma$), initial water depth ($h_{toe}$), foreshore slope ($\cot(m)$), width of vegetated cover ($W_{veg}$), bottom friction ($n$) and dike slope ($\cot(\alpha)$).*

| $H_{m0,\mathrm{deep}}$ (m) | $T_p$ (s) | $\sigma$ (°) | $h_{\mathrm{toe}}$ (m) | $\cot(m)$ | $W_{veg}$ (m) | $n$ (s/m$^{1/3}$) | $\cot(\alpha)$ |
|---|---|---|---|---|---|---|---|
| 1 | 5 | 0 | 0.5 | 10 | 0 | 0.012 | 2 |
| 3 | 6 | 10 | 1.0 | 25 | 200 | 0.020 | 4 |
| 5 | 7 | 24 | 1.5 | 50 | 400 | 0.030 | 6 |
| 7 | 8 | | 2.0 | 100 | 600 | | 10 |
| 9 | 9 | | 2.5 | 250 | 800 | | ∞[a] |
| 11 | 11 | | 3.0 | 500 | | | |
| | 13 | | 3.5 | 1000 | | | |
| | 15 | | 5.0 | | | | |
| | 17 | | | | | | |

[a] No-dike scenario.

**Table 2.3**. *Vegetation properties representative of salt marshes in the Netherlands (Vuik et al., 2016).*

| Parameter | Value |
|---|---|
| Drag coefficient, $C_D$ | 0.4 |
| Stem diameter, $b_v$ | 0.003 m |
| Density, $N_v$ | 1200 stems/m$^2$ |
| Height, $h_v$ | 0.3 m |

### *2.2.4.2 Quantifying the Influence of Environmental Parameters*

Influence factors ($\bar{\gamma}$ [-], Equation 2.24), which describe the effect of each environmental parameter on $\widetilde{H}_{IG}$, were obtained by analysing the mean response of $\widetilde{H}_{IG}$ to variations in each environmental parameter, relative to a reference case—where $h_{toe} = 1$ m, $\sigma = 0°$, $\cot(m) = 50$, $W_{veg} = 0$ m, $n = 0.012\ s/m^{1/3}$ and $\cot(\alpha) = 2$ —for the 24 different combinations of $H_{m0,deep}$ and $T_p$.

$$\bar{\gamma}_{\psi} = \frac{1}{24}\sum_{i=1}^{24}\frac{\widetilde{H}_{IG,i}}{\widetilde{H}_{IG,ref,i}}, \tag{2.24}$$

where the subscript $\psi$ represents the environmental parameter being evaluated and subscript $ref$ refers to the simulation with reference parameter values.

## 2.3 RESULTS AND DISCUSSIONS

### 2.3.1 XBEACH VALIDATION

Before using XB-NH to generate the synthetic dataset, we first verify that it accurately simulates the hydrodynamics of shallow foreshore environments by comparing it to the observations of the physical experiment. The mean water levels ($\bar{\eta}$) predicted by XB-NH compare well with those observed during the physical experiment (Figure 2.3), with minor $SCI$ (0.069) and $Rel.bias$ (0.053) error values. In particular, the location and magnitude of wave-induced setup (the rise in $\bar{\eta}$ ), shoreward of the breakpoint—where $h_b = H_{m0}/\Omega$—is well represented (Figure 2.4a). Here, the ratio of breaking waves to local water depth ($\Omega$) is taken as 0.5; this value was found to best represent the onset of wave breaking (Figure 2.4b).

Likewise, Figure 2.4b shows good agreement between the modelled and observed $H_{m0,IG}$ and $H_{m0,SS}$. These cross-shore profiles show the growth of $H_{m0,SS}$ during shoaling (seaward of the breakpoint) and its subsequent dissipation by depth-induced breaking. Conversely, $H_{m0,IG}$ is enhanced during shoaling but continues to grow as SS waves break, resulting in IG-wave dominance at the dike toe. This is further seen in the transformation of wave spectra (Figure 2.5), shows that XB-NH accurately captures the shift in spectral density, $C_{\eta\eta}(f)$ from SS to IG frequencies. This apparent transfer of energy to lower frequencies is due to the dissipation of SS waves by depth-induced breaking and the concurrent enhancement of IG waves. It should be noted that the results here differ from those in Lashley et al. (2019b), as the observed surface elevation time series are used here as model input and not parametric spectra, for increased accuracy.

Considering the validation metrics, both $H_{m0,IG}$ and $H_{m0,SS}$ show little bias ($Rel.bias$ values of 0.021 and -0.01, respectively); while $H_{m0,IG}$ predictions—though still considered accurate ($SCI = 0.111$, Figure 2.6a)—show more scatter than predictions of $H_{m0,SS}$ ($SCI = 0.04$, Figure 2.6b). That said, note that this difference in scatter is related to the low values of $H_{m0,IG}$ observed. The $SCI$ is defined as the root-mean-square error (RMSE) between the model and observations, normalized by the mean of the observations (Equation 2.10). Both predictions of $H_{m0,IG}$ and $H_{m0,SS}$ have similar RMSE values: 0.002 m and 0.003 m, respectively; however, the lower mean of the observed $H_{m0,IG}$ results in a larger $SCI$ value. Nevertheless, both SCI values are considered to be well within acceptable values—$SCI <$ 0.15 or within 15% error (Roelvink et al., 2018).

To investigate the sensitivity of the predicted $\bar{\eta}$, $H_{m0,IG}$ and $H_{m0,SS}$ to the random wave components imposed at the model boundary, each XBeach simulation was run ten times with a new random-wave time series. However, the effects were found to be negligible (< 3% variation in $H_{m0,IG}$ and < 1% in both $\bar{\eta}$ and $H_{m0,SS}$).

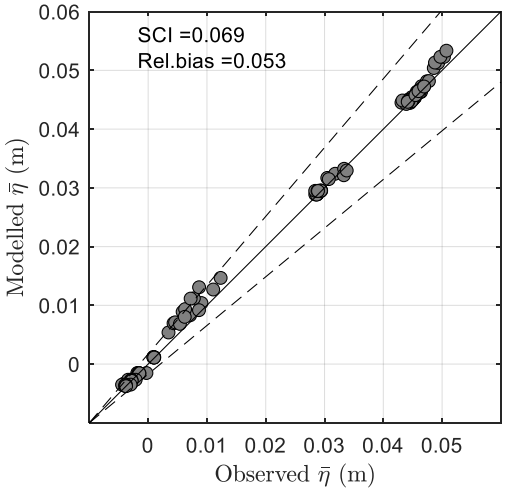


**Figure 2.3**. *Modelled and observed comparison of $\bar{\eta}$ (model scale).*

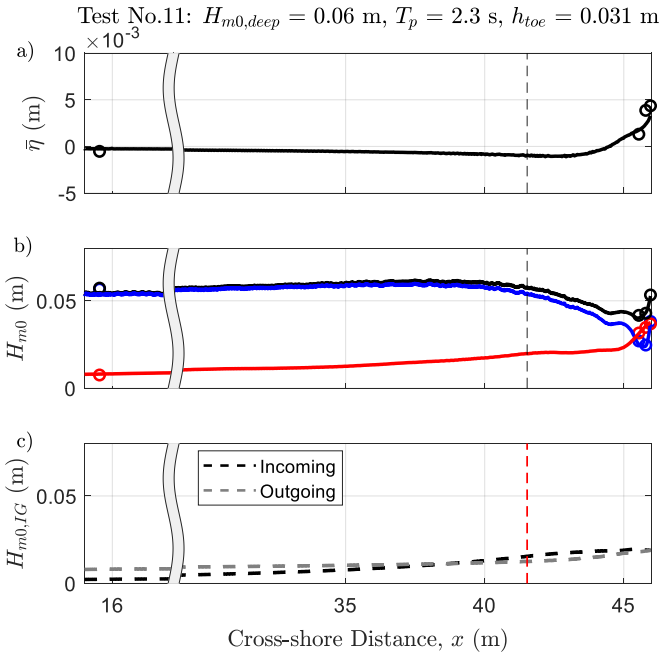


**Figure 2.4**. *Cross-shore profiles of modelled (solid lines) and observed (circles): a) $\bar{\eta}$ ; b) $H_{m0}$, showing the total (black), SS (blue) and IG (red) signals; and c) modelled incoming and outgoing $H_{m0,IG}$, for Test No. 11 (model scale). Dashed vertical lines indicate mean breakpoint.*

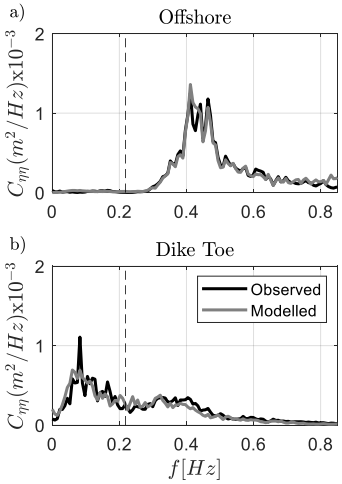


**Figure 2.5.** *Comparison of modelled and observed wave spectra: (a) offshore, at gauge 1; and (b) at the dike toe, at gauge 10, for Test No. 11 (model scale). Dashed lines represent the frequency separating SS and IG motions.*

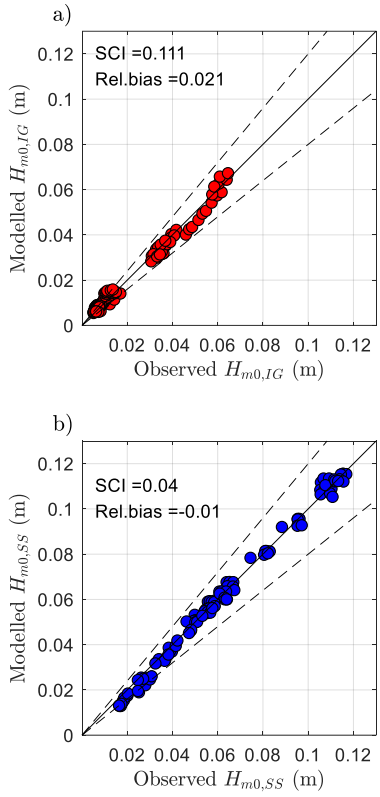


**Figure 2.6.** *Modelled and observed comparison of a) $H_{m0,IG}$ and b) $H_{m0,SS}$ (model scale).*

### 2.3.2 REFLECTION OF INFRAGRAVITY-WAVES AT THE DIKE

The cross-shore evolution of the total, incoming and outgoing $H_{m0,IG}$ for Test No. 11 are shown in Figure 2.4c. The incoming IG waves gain energy over the shallow foreshore as SS waves shoal ($x > 28\ m$) and break ($x \geq 41.5\ m$), before finally experiencing near-complete reflection at the dike ($x = 46\ m$, Figure 2.4c). The superposition of the incoming and the reflected outgoing IG signals results in a maximum total signal at the dike (Figure 2.4b). Following reflection, the outgoing waves experience inverse shoaling—also referred to as de-shoaling (Battjes, 2004)—where they reduce in amplitude with increasing water depth; that is, as the wave celerity increases (Figure 2.4c).

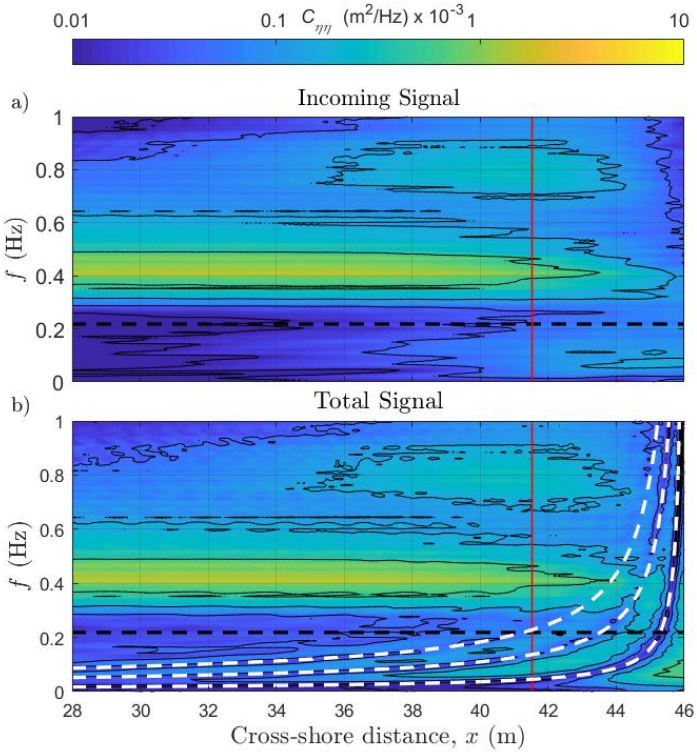


**Figure 2.7**. *Spatial evolution of wave spectral density for Test No. 11 based on a) the incoming and b) the total surface elevation signals. Dashed white curves show the predicted standing wave nodes ($f_{node}$, Equation 2.21 for $m_{node}$ = 1, 2 and 3). Dashed black line shows cut-off frequency separating SS and IG motions. Vertical red line indicates break-point location.*

To investigate the presence of a standing wave, we analyse the evolution of wave spectral density at each cross-shore location, resulting in the spatial plot shown in Figure 2.7. This was done first considering only the incoming signal (Figure 2.7a)—obtained by running the simulation without the dike, to exclude the effects of reflection—and then for the total signal where reflection from the dike is included (Figure 2.7b). A pattern of curved spectral ridges and troughs is clearly visible at low frequencies in Figure 2.7b but absent in Figure 2.7a. These locations of minimum and maximum $C_{\eta\eta}(f)$ correspond to nodes and antinodes in a standing wave (Buckley et al., 2018, Klopman and Van der Meer, 1999, Symonds et al., 1982). This is further corroborated using Equation 2.21, as the predicted $f_{node}$ line corresponds well with the minima in $C_{\eta\eta}(f)$.

### 2.3.3 INFRAGRAVITY-WAVE GENERATION MECHANISM

The high spatial resolution of the numerical model allows the presentation of the sequence of cross-correlations ($R_{\eta A}$ [-]) between the modelled local $\eta^{IG}(t)$ and $A(t)$ offshore ($x =$

0 $m$), at each cross-shore location, as a continuous spatial plot with ridges of positive and negative correlations (Figure 2.8). The slight negative correlation seen at zero time lag ($\tau = 0\ s$) corresponds to the trough of a bound IG wave that is out of phase with the incident wave groups (Longuet-Higgins and Stewart, 1962).

At $x{\sim}10\ m$, both this negative signal and a bar of positive correlation—which represents the crest of the bound wave—becomes more visible. Shoreward of this point ($x > 10\ m$), the positive/negative form of the cross-correlation becomes stronger; this is consistent with an incident bound wave developing an asymmetric form during shoaling (Baldock and Huntley, 2002, List, 1992). Concurrently, the lag between the wave group—travelling with velocity ($c_g$), based on *linear wave theory* (black dashed line in Figure 2.7a and b)—and the trough of the bound wave increases. This phase shift allows the transfer of energy between the wave group and the bound wave, resulting in IG wave growth (Van Dongeren and Svendsen, 1997).

Shoreward of the breakpoint ($x_b = 41.5\ m$), the ridge of positive correlation is strongly enhanced, suggesting the contribution of an incoming break-point generated IG wave. The now-enhanced IG wave is reflected at the dike ($x = 46\ m,\ \tau{\sim}23\ s$) and propagates to the offshore boundary ($x = 0\ m,\ \tau{\sim}53\ s$) as a free long wave; that is, a wave propagating with celerity equalled to $\sqrt{gh}$ (dashed black and white line in Figure 2.7a and b).v

Theoretically, breakpoint forcing would result in both incoming and outgoing IG waves propagating away from the breakpoint. However, this is not immediately evident in Figure 2.7a as the outgoing signal is dominated by that reflected at the dike. To investigate this further, the simulation was re-run with the dike removed and the landward boundary set to absorbing-generating (weakly reflective). In the absence of a reflective boundary, a negatively correlated ridge may be seen extending from the breakpoint ($x_b = 41.5\ m$, $\tau{\sim}30\ s$) to offshore ($x = 0\ m,\ \tau{\sim}49\ s$) (Figure 2.8b). This negative cross-correlation corresponds to a seaward propagating free IG-wave, generated by SS-wave breaking (Baldock, 2006, Contardo and Symonds, 2013, Pomeroy et al., 2012). Thus, the incoming IG waves shoreward of the breakpoint ($x > 41.5\ m$, Figure 2.8a) are the combined result of enhanced bound waves and the shoreward propagating component of breakpoint forced waves. Accordingly, the IG waves propagating seaward (outgoing) are the combined result of the wave reflected at the dike and the wave radiated seaward directly from the breakpoint.

This finding is further supported by the normalized bed-slope parameter analysis, where $\beta_b$ ranged from 0.41 to 0.55 for the 12 physical model tests (Table 2.1). These values are over the threshold for bound-wave shoaling as the main generation mechanism ($\beta_b \leq 0.3$) but still under the threshold for break-point forcing to dominate ($\beta_b \geq 1$). This suggests that both generation mechanisms do indeed contribute to $H_{m0,IG,toe}$.

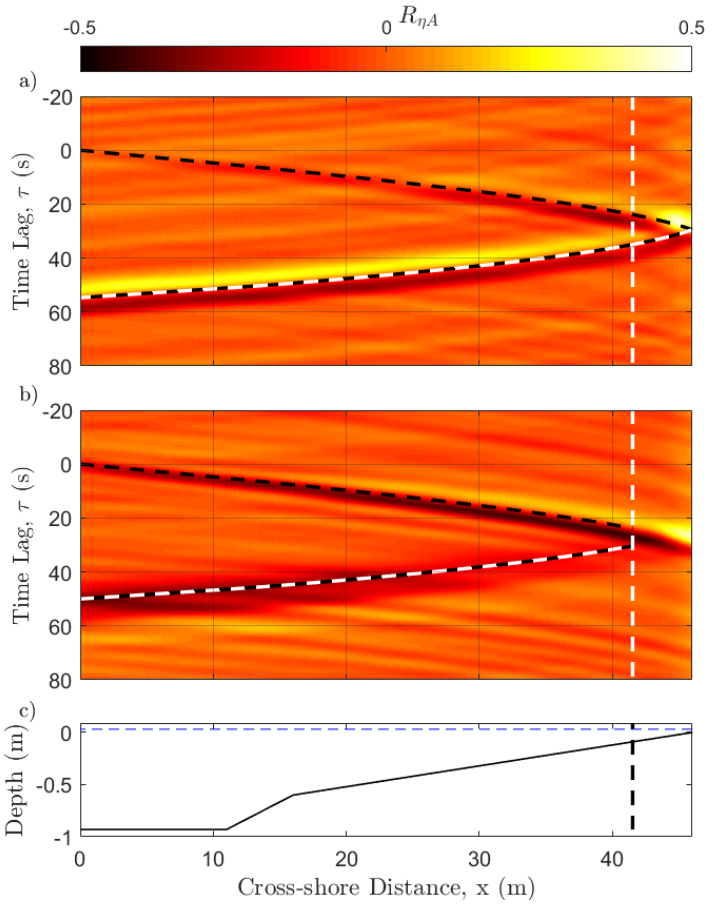


**Figure 2.8**. *Cross-correlation functions ($R_{\eta A}$) between $A(t)$ at $x = 0$ and $\eta^{IG}(t)$ at all cross-shore locations—as modelled in XBeach—for Test No.11 both (a) with and (b) without the dike. Dashed black lines correspond to an incoming wave group propagating with celerity, $c_g$; dashed black and white lines represent an outgoing wave propagating with celerity $\sqrt{gh}$. Dashed vertical lines indicate the breakpoint.*

### 2.3.4 INFLUENCE OF ENVIRONMENTAL PARAMETERS

#### *2.3.4.1 Deep-water Significant Wave Height and Peak Period*

Given that $H_{m0,deep}$ and $T_p$ are known to be correlated, we jointly assess their influence on nearshore wave conditions. Figure 2.9 shows the variation in $H_{m0,IG,toe}$, $H_{m0,SS,toe}$ and $\widetilde{H}_{IG}$ with changes in $H_{m0,deep}$ and $T_p$ at the offshore boundary, while all other parameters were held constant: $h_{toe} = 1\text{ m}$ , $\sigma = 0°$ , $\cot(m) = 50$ , $W_{veg} = 0\text{ m}$ , $n = 0.012\ s/m^{1/3}$ and $\cot(\alpha) = \infty$. Both $H_{m0,IG,toe}$ (Figure 2.9a) and $H_{m0,SS,toe}$ (Figure 2.9b) increase linearly with increasing $H_{m0,deep}$ and, to a much lesser extent, $T_p$; made evident by the

minimal scatter displayed. Likewise, Figure 2.9c displays a clear positive relationship between $H_{m0,deep}$ and $\widetilde{H}_{IG}$ with minor scatter associated with variations in $T_p$.

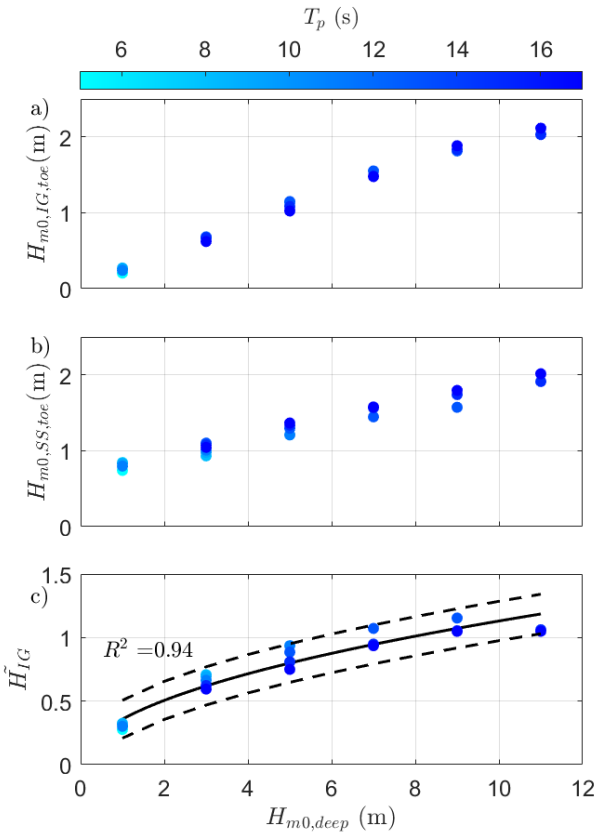


**Figure 2.9**. *Scatterplots of a) $H_{m0,IG,toe}$ b) $H_{m0,SS,toe}$ and c) $\widetilde{H}_{IG}$ against $H_{m0,deep}$ under reference conditions ($\sigma = 0°$, $h_{toe} = 1\ m$, $cot\ \alpha_{fore} = 50$, $W_{veg} = 0\ m$, $n = 0.012\ s/m^{1/3}$ and $cot\ \alpha_{dike} = \infty$), for each of the 24 combinations of $H_{m0,deep}$ and $T_p$ simulated. Solid black line indicates model fit; dashed black lines indicate +/- 95% confidence intervals.*

This relationship is well described (coefficient of determination, $R^2 = 0.94$) by the following expression, obtained using the linear least-squares method:

$$\widetilde{H}_{IG} = a \cdot {H_{m0,deep}}^{0.5}, \tag{2.25}$$

where the fitted coefficient $a = 0.358\ (0.344, 0.371)\ \mathrm{m}^{-0.5}$ for the above-mentioned reference parameter values; numbers in parentheses indicate the lower and upper 95% confidence bounds, respectively.

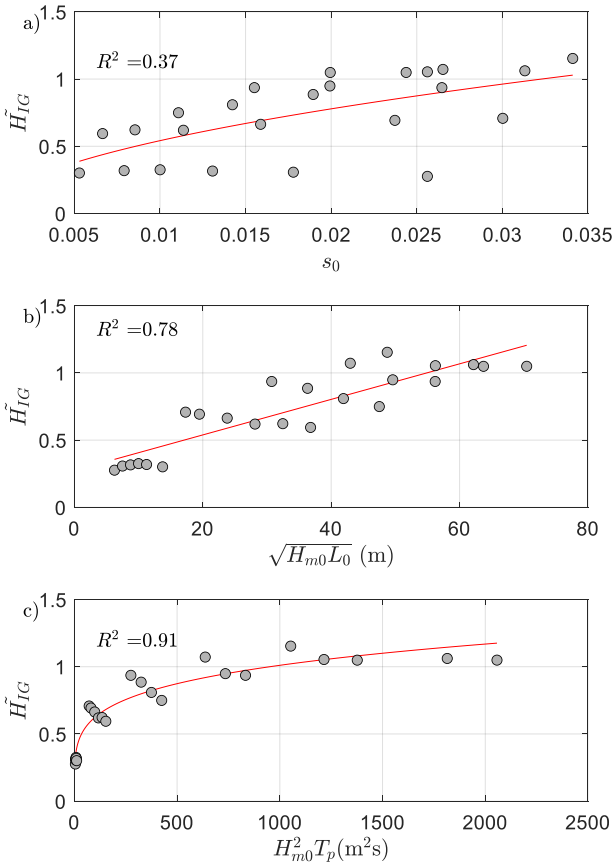


**Figure 2.10**. *Scatterplots of $\tilde{H}_{IG}$ against a) $s_0$, b) $\sqrt{H_{m0,deep}L_0}$ and c) $H_{m0,deep}^2 T_p$ under reference conditions ($\sigma$ = 0°, $h_{toe}$ = 1 $m$, $cot(m)$ = 50, $W_{veg}$ = 0 $m$, $n$ = 0.012 $s/m^{1/3}$and $cot(\alpha) = \infty$), for each of the 24 combinations of $H_{m0,deep}$ and $T_p$ simulated.*

The strong dependence of both $H_{m0,IG,toe}$ and $H_{m0,SS,toe}$ on $H_{m0,deep}$ indicates an unsaturated surf zone, typical of steeper foreshore slopes (Power et al., 2010, Stockdon et al., 2006), where the inner surf zone wave heights are equally dependent on the local water depth ($h_{toe}$) and the offshore wave height ($H_{m0,deep}$). This dependence also justifies the relationship obtained between $\tilde{H}_{IG}$ and $H_{m0,deep}$ (Equation 2.25); that is, $\tilde{H}_{IG}$ exhibits a negative exponential (or negative power) relationship with $h_{toe}/H_{m0,deep}$, as shown in (Lashley et al., 2019b), and hence a positive power relationship with $H_{m0,deep}/h_{toe}$. This ratio of offshore wave height to local water depth has been found to accurately describe both the intensity (Hofland et al., 2017, Lashley et al., 2018) and location of wave breaking (Yao et al., 2013)—which in turn determine the magnitude of nearshore waves. Thus, for the

constant water depth simulated here ($h_{toe} = 1$ m), the above power law holds. The influence of variations in $h_{toe}$ is assessed, separately, in Section 2.3.4.3.

We also assessed the influence of additional parameters that combine $H_{m0,deep}$ and $T_p$: $s_0$ (Figure 2.10a); $\sqrt{H_{m0,deep}L_0}$ (Figure 2.10b), as recommended by Stockdon et al. (2006); and ${H_{m0,deep}}^2 T_p$ (Figure 2.10c), as proposed by Inch et al. (2017). However, while these parameters may describe the individual components ($H_{m0,IG,toe}$ and $H_{m0,SS,toe}$) well—as shown in their respective studies—they yielded lower $R^2$ values here, compared to Equation 2.25. This suggests that $T_p$ has only a minor influence on $\widetilde{H}_{IG}$.

#### *2.3.4.2 Deep-water Directional Spreading*

Considering wave flume ($\sigma = 0°$), typical swell ($\sigma = 10°$) and typical wind-sea ($\sigma = 24°$) conditions, a total of 72 estimates of $H_{m0,IG,toe}$ and $H_{m0,SS,toe}$ were obtained. Both parameters show negative relationships with $\sigma$ (Figure 2.11). However, $H_{m0,IG,toe}$ experiences 2.6 times more dissipation (on average) than $H_{m0,SS,toe}$ for the same increase in $\sigma$, suggesting that wave energy at IG frequencies is significantly more sensitive to variations in $\sigma$. A change in $\sigma$ from wave flume conditions to a typical wind sea results in a 36% reduction in $H_{m0,IG,toe}$ compared to an 16% reduction in $H_{m0,SS,toe}$. This finding emphasizes the need to consider directional spreading in the offshore forcing; as the assumption of unidirectionality leads to unrealistically high estimates of $H_{m0,IG,toe}$ (Van Dongeren et al., 2003). Note that these findings are specific to the large wave height to water depth ratios simulated here, where heavy wave breaking results in an increase in the directional spread of wave energy (Herbers et al., 1999). The effect of directional spreading is expected to be less for deeper conditions.

As $H_{m0,IG,toe}$ is more sensitive to changes in $\sigma$ than $H_{m0,SS,toe}$, $\bar{\gamma}_\sigma$ decreases linearly with increasing $\sigma$ (Figure 2.12):

$$\bar{\gamma}_\sigma = 1 - 0.01 \cdot \sigma \tag{2.26}$$

where $\bar{\gamma}_\sigma = 1$ corresponds to the reference case.

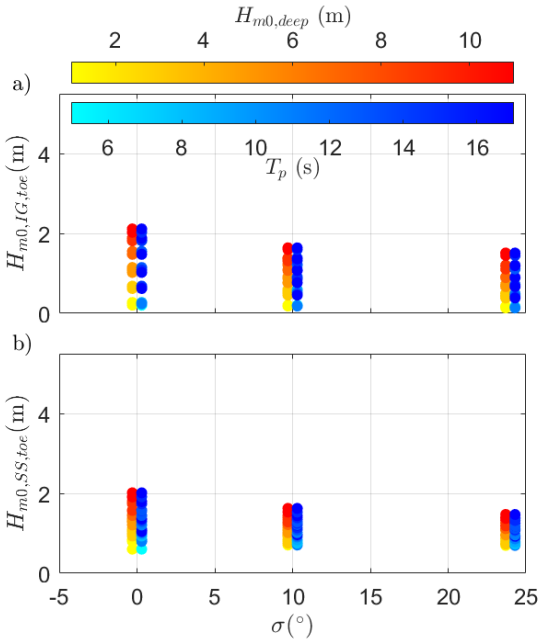


**Figure 2.11**. *Scatterplots of a) $H_{m0,IG,toe}$ and b) $H_{m0,SS,toe}$ against $\sigma$ ($h_{toe} = 1\ m$, $cot(m) = 50$, $W_{veg} = 0\ m$, $n = 0.012\ s/m^{1/3}$ and $cot(\alpha) = \infty$). Each data point is represented by two markers with colormaps indicating the magnitude of $H_{m0,deep}$ (hot) and $T_p$ (cold).*

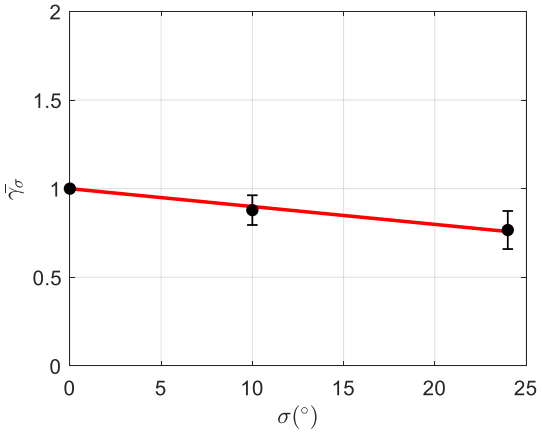


**Figure 2.12**. *Mean response of $\widetilde{H}_{IG}$ to variations in $\sigma$, relative to the reference case ($\sigma = 0°$). Red line indicates the model fit (Equation 2.26). Vertical error bars represent the standard deviation of each mean.*

### *2.3.4.3 Initial Water Depth at the Dike Toe*

Each of the ten values of $h_{toe}$ simulated (Table 2.2) was exposed to the 24 different combinations of $H_{m0,deep}$ and $T_p$, resulting in 240 estimates of $H_{m0,IG,toe}$ (Figure 2.13a) and $H_{m0,SS,toe}$ (Figure 2.13b) for analysis. In addition to the influence of $h_{toe}$, the combined

influence—if any—of $H_{m0,deep}$ or $T_p$ may be observed in the colormaps presented in Figure 2.13. Both $H_{m0,IG,toe}$ and $H_{m0,SS,toe}$ appear to decrease as the initial water depth becomes shallower (Figure 2.13); however, this reduction is more notable in $H_{m0,SS,toe}$, where a clear linear trend is observed. The points in Figure 2.13b which appear to deviate from the general trend, at $h_{toe} = 1.5$ m and $h_{toe} = 3.5$ m, correspond to simulations with $H_{m0,deep} = 1$ m and $H_{m0,deep} = 3$ m, respectively. In these simulations, the relative water depth, $h_{toe}/H_{m0,deep} > 1.0$ and $H_{m0,SS,toe}$ is not yet depth-limited.

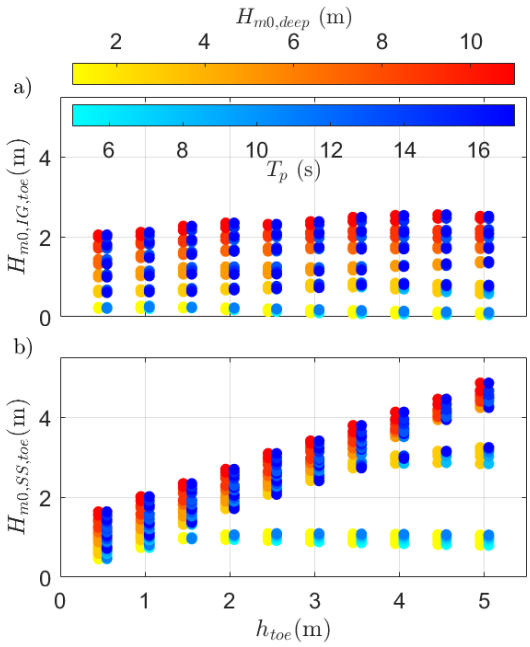


**Figure 2.13**. *Scatterplots of a) $H_{m0,IG,toe}$ and b) $H_{m0,SS,toe}$ against $h_{toe}$ ($\sigma = 0°$, $cot(m) = 50$, $W_{veg} = 0$ m, $n = 0.012\ s/m^{1/3}$ and $cot(\alpha) = \infty$). Each data point is represented by two markers with colormaps indicating the magnitude of $H_{m0,deep}$ (hot) and $T_p$ (cold).*

To quantify the influence of $h_{toe}$, we analyse the average response of $\widetilde{H}_{IG}$ to variations in $h_{toe}$, relative to that obtained for the reference case ($\bar{\gamma}_h$, Equation 2.24)—where $h_{toe} = 1$ m. Figure 2.14 shows that $\bar{\gamma}_h$—and thus $\widetilde{H}_{IG}$, on average—increases exponentially with decreasing water depth. This observation is in line with the findings of Hofland et al. (2017), which showed that the spectral wave period ($T_{m-1,0}$) at the dike toe—which also represents the relative contribution of lower frequency (IG) waves—increased exponentially with shallower water depths. By fitting a curve to the data, we obtain the following expression for the influence of $h_{toe}$:

$$\bar{\gamma}_h = 1.04 \cdot e^{-1.4 \cdot h_{toe}} + 0.9 \cdot e^{-0.19 \cdot h_{toe}}, \tag{2.27}$$

where $\bar{\gamma}_h = 1$ corresponds to the reference case.

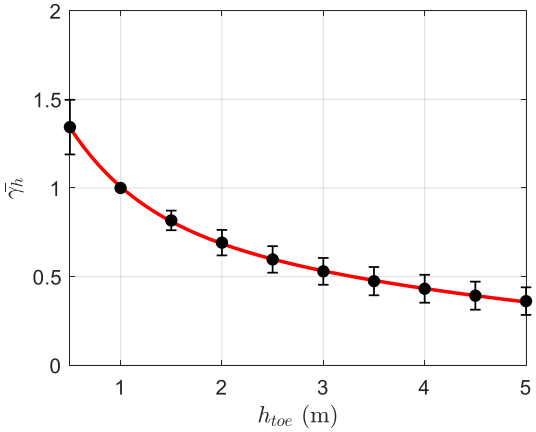


**Figure 2.14**. *Mean response of $\widetilde{H}_{IG}$ to variations in $h_{toe}$, relative to the reference case ($h_{toe} = 1$ m). Red line indicates the model fit (Equation 2.27). Vertical error bars represent the standard deviation of each mean.*

#### 2.3.4.4 *Influence of Foreshore Slope*

$H_{m0,IG,toe}$ initially increases as $\cot(m)$ increases, reaching a maximum value at $\cot(m) = 50$ (Figure 2.15a). This is due to the combination of both the bound-IG wave shoaling and breakpoint generation mechanisms ($0.3 < \beta_b < 1$), as described in Section 2.3.3. However, as the foreshore becomes milder—as $\cot(m)$ increases further— $H_{m0,IG,toe}$ decreases exponentially (note the log scale of the x-axis). $H_{m0,SS,toe}$, on the other hand, shows a consistent negative exponential relationship with $\cot(m)$ (Figure 2.15b). As SS waves begin to break further offshore with increasing $\cot(m)$, the surf zone becomes wider and results in increased dissipation.

These trends lend support to the arguments of Lara et al. (2011) and Baldock (2012) which suggest that the bound IG wave may not be released during SS-wave breaking, but remains locked and therefore dissipates in the surf zone concurrently with the SS-waves that force it. This dissipation is less evident for steeper slopes (Figure 2.16a and b), as the bound wave may indeed experience some dissipation but break-point forcing is strong inside the relatively narrow surf zone; thus, leading to higher values of $H_{m0,IG,toe}$. However, as the foreshore becomes milder ($\cot(m) > 100$; $\beta_b < 0.3$) and the surf zone wider, breakpoint forcing becomes weak—since its forcing (breaking) region becomes large in comparison to the wave-group motion (Baldock and Huntley, 2002). This absence of breakpoint forcing and the dissipation of the bound-IG wave in the surf zone results in lower values of $H_{m0,IG,toe}$ (Figure 2.16c).

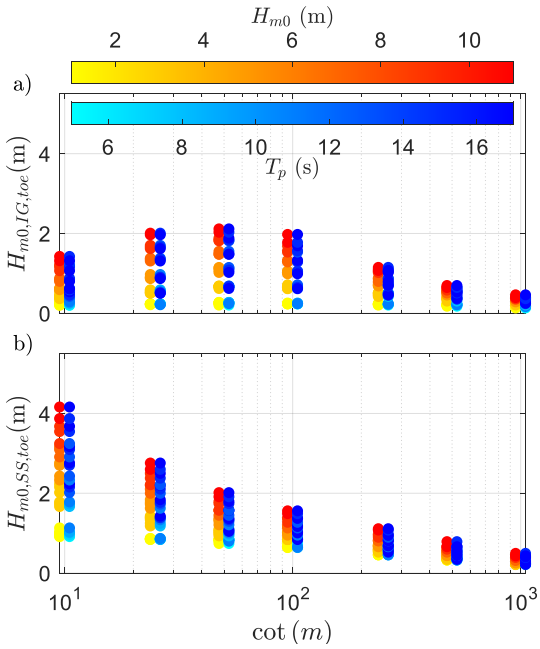


**Figure 2.15.** *Scatterplots of a) $H_{m0,IG,toe}$ and b) $H_{m0,SS,toe}$ against $cot(m)$ ($\sigma = 0°$, $h_{toe} = 1\ m$, $W_{veg} = 0\ m$, $n = 0.012\ s/m^{1/3}$ and $cot(\alpha) = \infty$). Each data point is represented by two markers with colormaps indicating the magnitude of $H_{m0,deep}$ (hot) and $T_p$ (cold).*

The mean response of $\widetilde{H}_{IG}$ to variations in $\cot(m)$, relative to the reference case ($\bar{\gamma}_f$, Equation 2.28) shows three distinct trends (Figure 2.17), dependent on the characteristics of wave breaking (represented here by $\cot(m)$ and the relative water depth, $h_{toe}/H_{m0,deep}$). For steeper slopes ($\cot(m) < 100$), $\bar{\gamma}_f$ increases logarithmically with increasing values of $\cot(m)$ (red line in Figure 2.17). This growth continues for milder slopes ($\cot(m) > 100$) when $h_{toe}/H_{m0,deep} \geq 0.2$; however, for lower values of $h_{toe}/H_{m0,deep}$, the surf zone becomes very wide and $\bar{\gamma}_f$ decreases (blue line in Figure 2.17). The relatively large variation in $\bar{\gamma}_f$ (magenta line) for $\cot(m) = 500$ and $\cot(m) = 1000$—shown by the length of the error bars—is due to the increased influence of $T_p$ on the breakpoint location and the overall surf zone width for very mild slopes.

$$\bar{\gamma}_f = \begin{cases} 1.56 - 3.09 \cdot \cot(m)^{-0.44} & \cot(m) \leq 100 \\ 0.51 \cdot \cot(m)^{0.18} & \cot(m) > 100, h_{toe}/H_{m0} \geq 0.2 \\ 1.62 \cdot \cot(m)^{-0.08} & \cot(m) > 100, h_{toe}/H_{m0} < 0.2 \end{cases} \quad (2.28)$$

where $\bar{\gamma}_f = 1$ corresponds to the reference case ($\cot(m) = 50$).

Additionally, we examined how $\widetilde{H}_{IG}$ relates to the well-known normalized bed slope parameter ($\beta_b$), proposed by Battjes (2004). In Figure 2.18a, $\widetilde{H}_{IG}$ shows a negative

exponential relationship with $\beta_b$ ; with scatter further highlighting the influence of $h_{toe}/H_{m0,deep}$. By combining the two parameters, the scatter is reduced significantly in Figure 2.18b. Therefore, in addition to describing the IG-wave generation mechanism, $\beta_b$ also describes—to some extent—the relative magnitude of the IG waves.

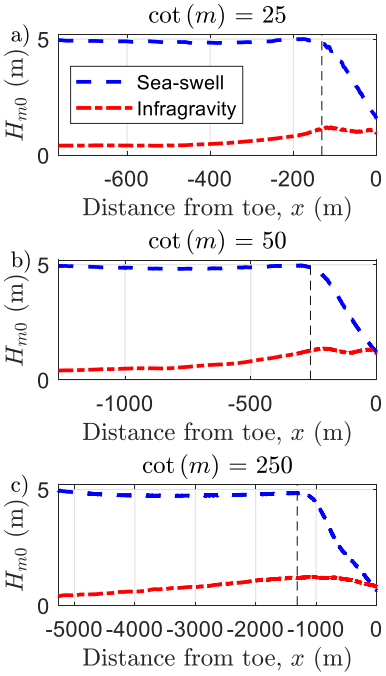


**Figure 2.16**. *Cross-shore profiles of $H_{m0,SS}$ and $H_{m0,IG}$ for (a) $cot(m) = 25$; (b) $cot(m) = 50$; and (c) $cot(m) = 250$ ($H_{m0,deep} = 5m$, $T_p = 11s$, $\sigma = 0°$, $h_{toe} = 1\ m$, $W_{veg} = 0\ m$ and $cot(\alpha) = \infty$). Vertical lines represent the mean break-point location, where $h_b = H_{m0}/0.8$.*

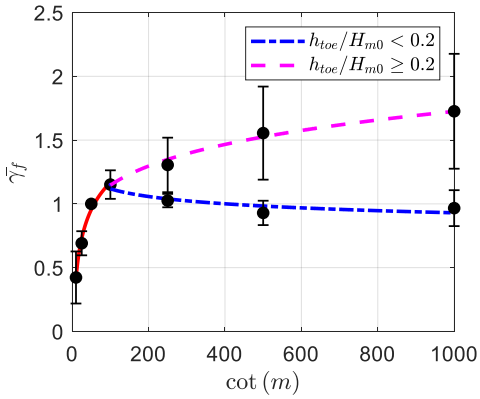


**Figure 2.17**. *Mean response of $\tilde{H}_{IG}$ to variations in $cot(m)$, relative to the reference case ($cot(m) = 50$). Solid lines indicate the model fits (Equation 2.28). Vertical error bars represent the standard deviation of each mean.*

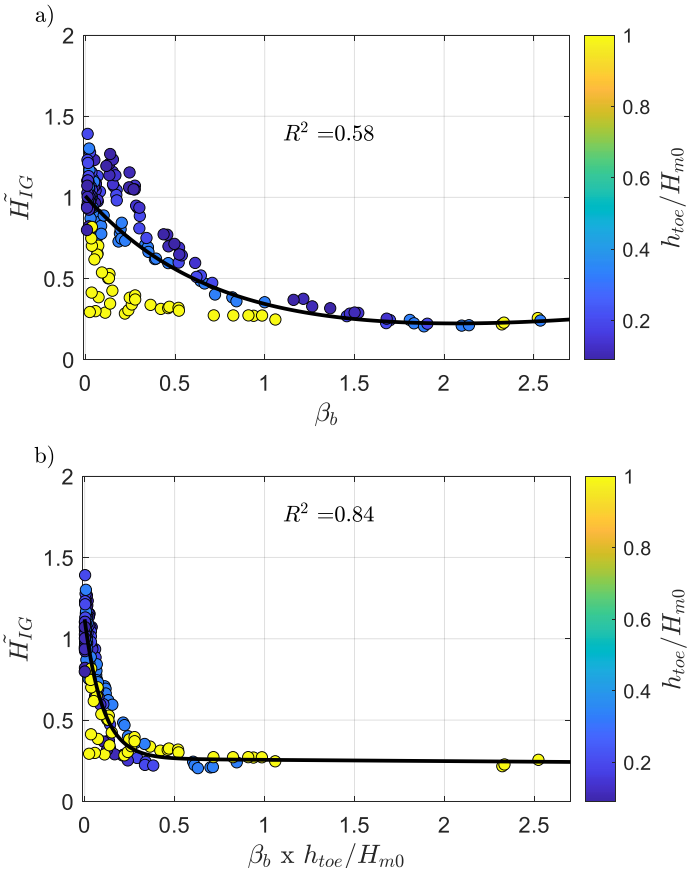


**Figure 2.18**. *Relationship between $\tilde{H}_{IG}$ and $\beta_b$ for the 7 different foreshore slopes simulated ($\sigma = 0°$, $h_{toe} = 1\ m$, $W_{veg} = 0\ m$, $n = 0.012\ s/m^{1/3}$ and $cot(\alpha) = \infty$). Colourmap shows influence of relative water depth ($h_{toe}/H_{m0,deep}$).*

### *2.3.4.5 Vegetated Cover*

$H_{m0,IG,toe}$ (Figure 2.19a) and $H_{m0,SS,toe}$ (Figure 2.19b) both show negative exponential relationships with $W_{veg}$. The presence of vegetation—from $W_{veg} = 0\ m$ to $W_{veg} = 200$ m—notably reduces the wave heights at the dike toe; however, the effect is more significant for $H_{m0,IG,toe}$ than $H_{m0,SS,toe}$ with 60% and 46% reduction (on average), respectively. As a larger portion of the water column is under wave motion for longer-period (IG) waves, vegetation is able to more effectively reduce flow velocities. Therefore, submerged vegetation—also referred to as canopies—attenuates IG wave components more than shorter-period (SS) components, as reported by Lowe et al. (2007) and Koftis et al. (2013).

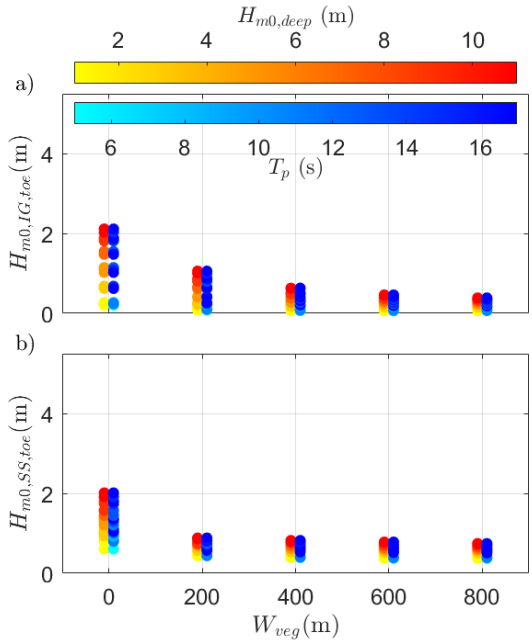


**Figure 2.19**. *Scatterplots of a) $H_{m0,IG,toe}$ and b) $H_{m0,SS,toe}$ against $W_{veg}$ ($\sigma = 0°$, $h_{toe} = 1\ m$, $cot(m) = 50$, $n = 0.012\ s/m^{1/3}$ and $cot(\alpha) = \infty$). Each data point is represented by two markers with colormaps indicating the magnitude of $H_{m0,deep}$ (hot) and $T_p$ (cold).*

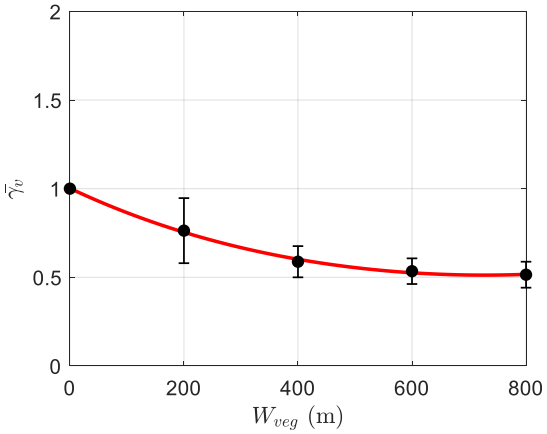


**Figure 2.20**. *Mean response of $\tilde{H}_{IG}$ to variations in $W_{veg}$, relative to the reference case ($W_{veg} = 0\ m$). Red line indicates the model fit (Equation 2.29). Vertical error bars represent the standard deviation of each mean.*

Though the initial attenuation effect between non-vegetated ($W_{veg} = 0\ m$) and some vegetation ($W_{veg} = 200\ m$) is striking, a further increase in the width of vegetated cover does not significantly affect either $H_{m0,IG,toe}$ or $H_{m0,SS,toe}$ (Figure 2.19). A similar response is

seen in the average response of $\widetilde{H}_{IG}$ to variations in $W_{veg}$ ($\bar{\gamma}_v$) where the inclusion of 400 m of vegetation reduces $\bar{\gamma}_v$ by 40%, compared to the non-vegetated (reference) case; while a further increase in $W_{veg}$ has only a minor effect Figure 2.20). This relationship may be described by the following exponential expression:

$$\bar{\gamma}_v = 0.94 \cdot e^{-W_{veg}/500} + 0.06 \cdot e^{W_{veg}/500}, \tag{2.29}$$

where $\bar{\gamma}_v = 1$ corresponds to the reference case ($W_{veg} = 0$ m).

While the vegetation formulations in XBeach were not validated here, it is important to note that the majority of the wave steepness ($s_0$) and relative submergence depth ($h/h_v$) conditions simulated here fall within the range of conditions previously validated by Van Rooijen et al. (2016) using laboratory experiments: $0.006 \leq s_0 \leq 0.028$; and $h/h_v \leq 4.11$ (to emergent). However, caution should be taken when applying Equation 2.29 outside of this range. Furthermore, the $W_{veg}$ values considered here are much wider than those previously considered; therefore the validity of Equation 2.29 for very wide marshes is unknown.

#### *2.3.4.6 Bottom Friction*

With respect to bottom friction, we assessed three general bed conditions: smooth concrete (wave flume, $n = 0.012\ s/m^{1/3}$), mud ($n = 0.020\ s/m^{1/3}$) and sand ($n = 0.03\ s/m^{1/3}$). However, both $H_{m0,IG,toe}$ and $H_{m0,SS,toe}$ were found to be insensitive to $n$, experiencing only minor dissipation (< 2%) with increasing $n$ (not shown here). This finding is in-line with previous studies which found that the dissipation of nearshore waves was governed by depth-induced wave-breaking (Henderson et al., 2006, Thomson et al., 2006, Van Dongeren et al., 2007) and attenuation by vegetation (Baron-Hyppolite et al., 2018), but was insensitive to bottom friction. Thus, the influence of $n$ on $\widetilde{H}_{IG}$ can be considered negligible.

#### *2.3.4.7 Dike Slope*

The presence of a dike increases $H_{m0,IG,toe}$ by a factor of 2.1 (on average) compared to the no-dike ($\cot(\alpha) = \infty$) scenario (Figure 2.21a). This is due to the constructive inference of the incoming and reflected IG-waves at the dike toe (as described in Section 2.3.2). This occurs for dike slopes as mild as $\cot(\alpha) = 10$, though a minor reduction in $H_{m0,IG,toe}$ is seen as the dike slope becomes milder (as $\cot(\alpha)$ increases). $H_{m0,SS,toe}$ experiences a similar increase in amplitude for $\cot(\alpha) = 2$ compared to the no-dike scenario (Figure 2.21b); however, this increase is only by a factor of 1.3 (on average). This difference in amplification is due to the frequency-dependence of wave reflection—that is, lower-frequency (longer-period) waves experience greater reflection than those at higher frequencies. Furthermore, as the dike slope becomes milder ($\cot(\alpha) > 2$), the influence of the dike on $H_{m0,SS,toe}$ quickly becomes negligible (Figure 2.21b).

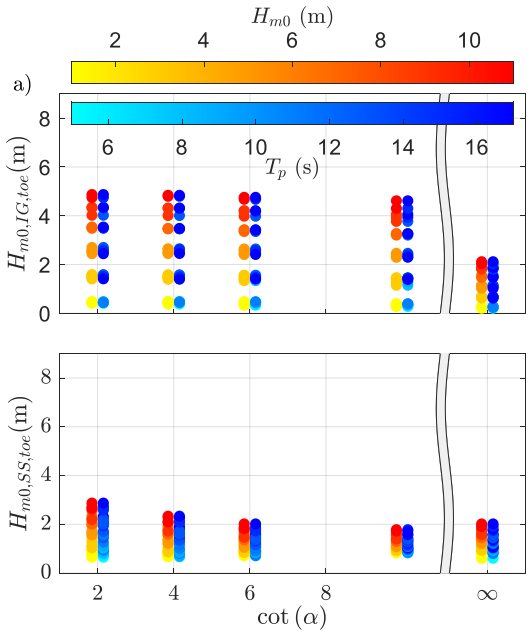


**Figure 2.21**. *Scatterplots of a) $H_{m0,IG,toe}$ and b) $H_{m0,SS,toe}$ against $cot(\alpha)$ ($\sigma = 0°$, $h_{toe} = 1\ m$, $cot(m) = 50$, $W_{veg} = 0\ m$ and $n = 0.012\ s/m^{1/3}$). Each data point is represented by two markers with colormaps indicating the magnitude of $H_{m0,deep}$ (hot) and $T_p$ (cold).*

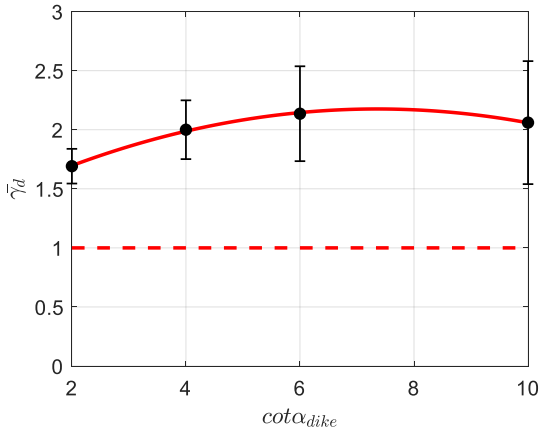


**Figure 2.22**. *Mean response of $\widetilde{H}_{IG}$ to variations in $cot\,\alpha_{dike}$, relative to the reference case (no-dike scenario). Red line indicates the model fit (Equation 2.30). Vertical error bars represent the standard deviation of each mean. Dashed red line indicates the mean response obtained for the "no dike" scenario.*

As a result, the mean response of $\widetilde{H}_{IG}$ to variations in $\cot(\alpha)$ ($\bar{\gamma}_d$) shows an initial positive relationship with $\cot(\alpha)$ where it increases as the dike slope becomes milder, up to $\cot(\alpha) = 6$; but then decreases slightly for $\cot(\alpha) = 10$ (Figure 2.22). The increased variation in $\bar{\gamma}_d$ for larger values of $\cot(\alpha)$ is due to the influence of $T_p$ on wave reflection; where longer-period waves experience greater reflection at the dike, resulting in a larger $\widetilde{H}_{IG}$ values.

$$\bar{\gamma}_d = 1.3 - 0.02 \cdot \cot(\alpha)^2 + 0.24 \cdot \cot(\alpha), \tag{2.30}$$

where $\bar{\gamma}_d = 1$ corresponds to the reference case (no-dike scenario).

While the above expression holds, $\bar{\gamma}_d$ may be approximated as 2 for $\cot(\alpha) > 4$, based on the scatter observed in Figure 2.22.

### 2.3.5 PREDICTING NEARSHORE INFRAGRAVITY-WAVE DOMINANCE

By combining Equations 2.25 to 2.30, we may estimate $\widetilde{H}_{IG}$ based on prior knowledge of offshore forcing ($H_{m0,deep}$ and $\sigma$), foreshore conditions ($h_{toe}$, $\cot(m)$ and $W_{veg}$) and dike slope ($\cot(\alpha)$) using the following empirical model:

$$\widetilde{H}_{IG} = 0.36 \cdot {H_{m0,deep}}^{0.5} \cdot \bar{\gamma}_\sigma \cdot \bar{\gamma}_h \cdot \bar{\gamma}_f \cdot \bar{\gamma}_v \cdot \bar{\gamma}_d, \tag{2.31}$$

where subscripts $\sigma$, $h$, $f$, $v$ and $d$ represent initial water depth, directional spreading, foreshore slope, vegetated cover, bottom friction and dike slope, respectively. To consider only incident wave conditions (no reflection), $\bar{\gamma}_d$ takes a value of 1. For conditions where $\widetilde{H}_{IG} > 1$ (IG-wave dominance), the magnitude of nearshore IG waves exceeds that of SS waves and governs wave-driven processes such as wave run-up and overtopping; thus, under such conditions IG waves should not be neglected.

The combined results of $\widetilde{H}_{IG}$ for the physical modelling—observations obtained from 12 simulations and numerical modelling—672 XBeach simulations—are presented in Figure 2.23. The proposed empirical model (Equation 2.31), developed using XBeach simulations alone, not only describes the entire dataset well ($R^2 = 0.94$) but also shows good agreement with the observations made during the physical experiment ($SCI = 0.098$ and $Rel.bias = -0.07$).

It should be noted that conditions with little to no breaking ($h_{toe}/H_{m0,deep} \geq 1$ and $\widetilde{H}_{IG} < 0.5$) had the largest scatter, where the predictions (Equation 2.32) varied between 0.6 and 2.3 times the observed value (numerical simulations) with a mean of 1.2 times the observed. This suggests that the reliability of Equation 2.33 decreases for cases where $h_{toe}/H_{m0,deep} \geq 1$; therefore, it is recommended that the formulae be applied to these cases with caution. Even with these discrepancies, Equation 2.34 shows reasonable agreement with the numerical simulations ($SCI = 0.18$ and $Rel.bias = 0.01$, Figure 2.23).

To verify the validity of the OAT approach taken here (Section 2.2.4.2)—where the influence of each parameter was assessed independently—a test case scenario, where multiple parameter values differed from the reference case, was simulated in XB-NH and the results compared to Equation 2.31. This test case, with $H_{m0,deep} = 9$ m, $T_p = 15$ s, $\sigma = 0°$, $h_{toe} = 0.5$ m, $\cot(m) = 100$, $W_{veg} = 200$ m and $\cot(\alpha) = 6$, was also well represented by Equation 2.31, shown by the blue marker in Figure 2.23. This shows that the approach taken here does indeed take into account the interaction between environmental parameters.

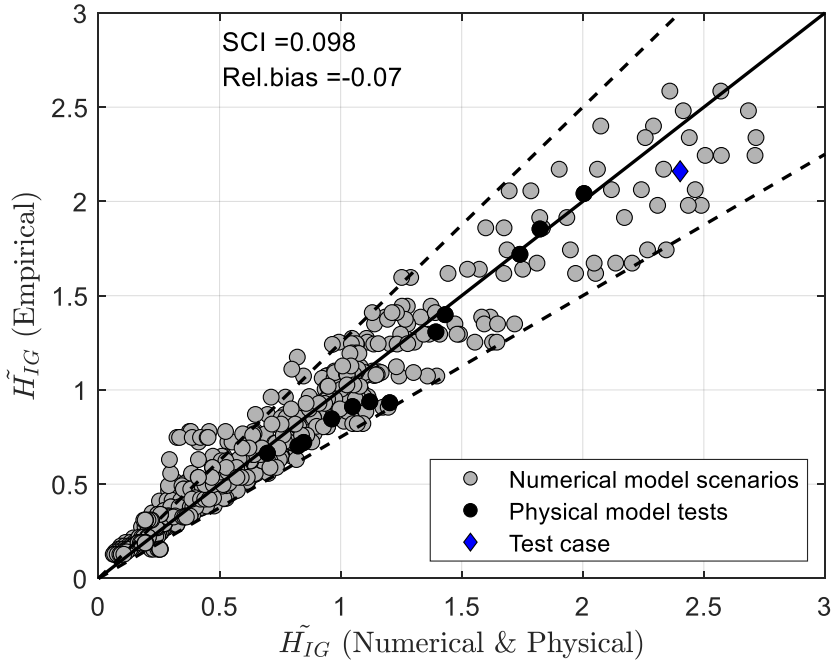


**Figure 2.23**. *Modelled (empirically, Equation 2.31) and observed comparison for the 12 physical model tests (red) and 672 numerical model scenarios (grey). Solid line indicates perfect agreement between empirical model and observations. Dashed lines indicate +/- 25% error. Blue marker indicates test case to where*

## 2.4 CONCLUSIONS

A combination of physical and numerical modelling was applied to assess the range of offshore ($H_{m0}$, $T_p$ and $\sigma$), foreshore ($h_{toe}$, $\cot(m)$, $W_{veg}$ and $n$) and sea-dike ($\cot(\alpha)$) conditions that promote the growth of nearshore IG waves. In particular, the exact conditions that result in the dominance of IG waves over SS waves ($\tilde{H}_{IG} > 1$) were identified. XBeach showed high skill in predicting $\bar{\eta}$, $H_{m0,SS}$ and $H_{m0,IG}$ when compared to physical observations, thereby laying a foundation of confidence in its performance. XBeach was then

used to simulate a wide range of conditions; and thus, to extend the analysis. Both the physical experiment and numerical simulations show that higher, directionally narrow-banded offshore waves; shallower water depths; milder foreshore slopes; reduced vegetated cover; and milder dike slopes give rise to IG-wave dominance. Both $T_p$ and $n$ were found to have minor influence on $\widetilde{H}_{IG}$, for the reference slope ($\cot(m) = 50$). However, this influence may increase for very mild slopes ($\cot(m) \geq 500$), evident by the scatter displayed in Figure 2.17.

XBeach simulations also reveal that, under shallow conditions, nearshore IG-wave energy is the result of both bound-wave shoaling and IG waves generated at the breakpoint. Likewise, reflection from the dike slope (as mild as $\cot(\alpha) = 10$) is shown to result in significant amplitude growth of IG waves at the dike toe. This is due to the interference of the incoming and the almost completely reflected signals which forms a standing wave with a node in the surf zone and an antinode at the shoreline.

The empirical model derived here (Equation 2.31)—which captures the combined effect of the varied environmental parameters—would allow practitioners to quickly estimate the significance of IG waves at a given coast. This is particularly useful as it indicates whether or not using a spectral wave model is sufficient (where $\widetilde{H}_{IG}$ is minor), or whether a more cumbersome phase-resolving model is required (where $\widetilde{H}_{IG}$ is significant). Furthermore, the empirical model may be combined with spectral wave models to extend their applicability to areas where the IG waves contribute significantly, as is often the case with shallow foreshore environments. Future work should verify the applicability of the proposed approach to field sites—considering the influence of alongshore variability and non-uniform foreshore morphologies—and investigate the influence of $\widetilde{H}_{IG}$ on processes such as wave impact, run-up or overtopping. Finally, the approach adopted here independently assessed the influence of each environmental parameter; therefore, future work should also consider the dependencies, if any, among parameters.

# 3

# NUMERICAL MODELLING OF DIKE OVERTOPPING IN INFRAGRAVITY-WAVE DOMINATED ENVIRONMENTS*


## ABSTRACT

Practitioners often employ diverse, though not always thoroughly validated, numerical models to directly or indirectly estimate wave overtopping ($q$ [$m^3$/s/m]) at sloping structures. These models, broadly classified as either phase-resolving or phase-averaged, each have strengths and limitations owing to the physical schematization of processes within them. Models which resolve the vertical flow structure or the full wave spectrum (i.e. sea-swell (SS) and infragravity (IG) waves) are considered more accurate, but more computationally demanding than those with approximations. This chapter assesses the speed-accuracy trade-off of six well-known models for estimating $q$, under shallow foreshore conditions. The results demonstrate that: i) $q$ is underestimated by an order of magnitude when IG waves are neglected; ii) using more computationally-demanding models does not guarantee improved accuracy; and iii) phase-averaged models like SWAN can perform on par, if not better than, phase-resolving models but with far less computational effort. This is achieved by combining SWAN with the empirical formulae developed in Chapter 2 to incorporate IG waves.


This chapter is organized as follows: Section 3.1 gives an overview of the different approaches to nearshore wave modelling with popular examples. Section 3.2 provides overviews of the physical and numerical models applied, followed by descriptions of key parameters and empirical formulae used in the analysis. It ends with a description of the metrics used to quantify model accuracy. In Section 3.3, the results of the model-data comparisons and the overall influence of IG waves on overtopping are presented and

*This chapter has been published as: Lashley, C. H., Zanuttigh, B., Bricker, J. D., Van der Meer, J., Altomare, C., Suzuki, T., Roeber, V., and Oosterlo, P. (2020). "Benchmarking of numerical models for wave overtopping at dikes with shallow mildly sloping foreshores: Accuracy versus speed." *Environmental Modelling & Software*, 130, 104740.

discussed. Section 3.4 concludes the chapter by summarising the findings, acknowledging the limitations of the approach and identifying specific areas for future work.



## 3.1 INTRODUCTION

### 3.1.1 BACKGROUND

Coastal engineers often employ numerical modelling in the design, assessment and rehabilitation of coastal structures to accurately forecast nearshore waves and currents, sometimes including the consequences (Akbar and Aliabadi, 2013, Sierra et al., 2010, Smith et al., 2012, Suzuki et al., 2017). Of particular interest is the extent to which waves reach and pass over the crest of a structure, referred to as wave overtopping. Extreme overtopping events are characterized by considerable flow velocities which impose serious hazards to both people and infrastructure; with flooding or coastal inundation as the most critical consequence.

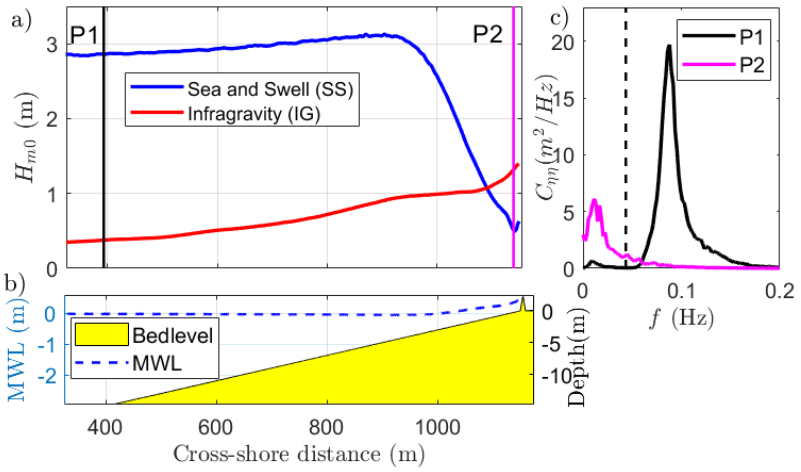


**Figure 3.1** *Schematic representation of wave transformation over a shallow foreshore (from an XBeach model simulation), showing a) the growth of IG waves; b) the increase MWL at the dike toe; and c) the shift in the peak in energy density to lower frequencies from offshore (P1) to the dike toe (P2). Vertical line in panel 'c' indicates the separation between SS and IG frequencies.*

The integration of numerical modelling in estimating wave overtopping and the design of coastal structures is becoming increasingly more attractive given the progress in available computing power and the ability of numerical models to incorporate both unconventional structure configurations and extreme environmental conditions. Furthermore, as many of the empirical overtopping models (e.g. EurOtop (2018)) require the incident significant wave height ($H_{m0,toe,in}$ [m]) and spectral wave period ($T_{m-1,0,toe,in}$ [s]) at the toe of the structure as input, numerical models are often needed to accurately capture the nonlinear effects associated with the shoaling and breaking of high-frequency sea-swell (SS) waves in shallow

water (Altomare et al., 2016, Mase et al., 2013). Such effects include a rise in mean water level—known as wave-induced setup—and the growth of low-frequency infragravity (IG) waves (Figure 3.1) which not only contribute to $H_{m0,toe,in}$ but also result in higher values of $T_{m-1,0,toe,in}$ (Hofland et al., 2017).

A variety of numerical models, which may be broadly classified as phase-resolving or phase-averaged, have been developed for such applications; each with strengths and limitations owing to the physical parameterization of processes and the numerical schemes incorporated within them (Cavaleri et al., 2007, Vyzikas and Greaves, 2018). Models which attempt to resolve the vertical flow structure and those that consider the full frequency range of nearshore waves (i.e. both SS and IG waves) are considered not only more accurate, but also more computationally demanding than those which make use of approximations.

Within the phase-resolving class of wave models, those that resolve the vertical flow structure and solve the fully nonlinear, time-averaged Navier-Stokes (NS) equations—often referred to as Computational Fluid Dynamics (CFD) or depth-resolving models—have the least theoretical limitations and are generally considered the most accurate. CFD models, such as the mesh-based Eulerian approach OpenFOAM (Jasak et al., 2007) or mesh-less Lagrangian approach DualSPHysics (Crespo et al., 2015), are able to simulate complex wave problems, such as: nonbreaking and breaking waves, wave-current interaction and wave-structure interaction from deep to shallow water conditions, including the overturning (Lowe et al., 2019) and roller formation of breaking waves (Higuera et al., 2013). However, these models require a significant amount of computational effort (unless a coupling method is applied (Altomare et al., 2015, Altomare et al., 2018, Verbrugghe et al., 2018)); thus, limiting their application so far to very local phenomena—for example, wave overtopping.

As depth-resolved (fully 3D or 2DV) models are generally considered too computationally expensive for operational use, the problem may be further simplified by depth-averaging. These models, in which the vertical structure is not directly resolved but only modelled parametrically, are referred to as two-dimensional in the horizontal (2DH), or 1DH where only a cross-shore transect is simulated (Brocchini and Dodd, 2008). As a result of depth-averaging, processes such as wave overturning, air-entrainment and wave generated turbulence are not directly solved. Those that simulate the amplitude and phase variation of SS waves are often referred to as phase-resolving. Within this type of model, there are generally two main sets of governing equations: i) the Non-linear shallow water (NLSW) equations; and ii) the Boussinesq type.

While the Boussinesq-type models (e.g. FUNWAVE (Kirby et al., 1998), MIKE21-BOUSS (Warren and Bach, 1992) and BOSZ (Roeber and Cheung, 2012)) directly account for the dispersive properties of waves in deeper water, the NLSW models assume that waves are non-dispersive and are therefore limited to shallow-water applications (Brocchini and Dodd,

2008, Zijlema and Stelling, 2008). This limitation can be removed by taking a SS-wave averaged approach; however, at the cost of decreased accuracy (due to exclusion of SS-wave motions). The high-frequency waves are averaged, resulting in only motions at the scale of the wave group; thus, reducing the computational demand (e.g. XBeach Surfbeat (XB-SB) model (Roelvink et al., 2009, Roelvink and Costas, 2019)).

In order to use the NSLW equations for phase-resolving simulation of SS-wave motions, Stelling and Zijlema (2003) proposed another method to account for dispersion (a result of non-hydrostatic pressure) whereby the pressure is decomposed into non-hydrostatic and hydrostatic pressure components (e.g. SWASH (Zijlema et al., 2011), NHWAVE (Ma et al., 2012) and XBeach Non-hydrostatic (XB-NH) (Smit et al., 2010) numerical models). This approach improves the dispersive properties without neglecting the higher-frequency motions; however, at the expense of more computational demand. The accuracy and range of applicability of the non-hydrostatic models may be further enhanced by coarsely dividing the model domain into a fixed number of vertical layers ($K \leq 3$); thereby, improving the frequency dispersion (e.g. SWASH, NHWAVE or XB-NH in multi-layered mode (De Ridder, 2018)). By further increasing the number of vertical layers ($K \geq 10$), models like SWASH may be extended to the depth-resolving class. This approach increases the computational demand but allows processes, such as undertow and the shoreward flow near the surface, to be resolved.

Given that phase-resolving models require a grid resolution high enough to resolve the individual SS-wave components, they are generally computationally feasible only for areas of limited size. For large-scale modelling of wave motion, a phase-averaged approach is most commonly used. This type of model is constructed on the assumption that a random sea-state is composed of a superposition of linear waves whose height is a function of their frequency and direction of propagation. For an individual wave train the rate of change of wave energy (or action) flux is balanced by the wave energy transfer among different wave components in different directions and different frequencies, as well as energy input and dissipation. With the phase information filtered out, these models can use much courser computational grids and therefore be applied to large areas. However, as individual waves are not resolved, these models must be combined with empirical formulae to estimate wave run-up and overtopping (Oosterlo et al., 2018, Sierra et al., 2010). Commonly used spectral models in nearshore applications include SWAN (Booij et al., 1999) and STWAVE (Smith et al., 2001). These models are generally able to accurately reproduce higher harmonics (SS waves); however, they do not account for the interactions that force IG-wave motions (Cavaleri et al., 2007), which tend to dominate in shallow water.

With respect to previous model comparisons in shallow coastal environments, Buckley et al. (2014) assessed the performance of SWASH, SWAN and XB-SB in predicting SS wave heights ($H_{m0,\mathrm{SS}}$ [m]), IG wave heights ($H_{m0,\mathrm{IG}}$ [m]) and setup ($\bar{\eta}$ [m]) across a steep

laboratory fringing reef profile (varying from 1:5 to 1:18.8). Results showed that each model was capable of accurately predicting $H_{m0,SS}$; however, SWAN failed to simulate the transformation of energy to lower frequencies and thus, failed to predict $H_{m0,IG}$. Likewise, SWAN showed considerably more error in its prediction of $\bar{\eta}$ compared to SWASH and XB-SB. On the other hand, XB-SB performed comparably well to its phase-resolving counterparts in the prediction of nearshore wave heights; and surprisingly the extent of wave run-up, particularly when IG-waves dominated at the shoreline (Lashley et al., 2018). From these previous studies, the points of discussion that naturally arise are:

i) Can phase-averaged models like SWAN be accurately applied under very shallow conditions, where IG waves dominate and $\bar{\eta}$ is significant?
ii) Given that IG waves dominate, are models of increasing complexity needed or is a short-wave averaged but IG-wave resolving approach all that is required?
iii) While attempts at model comparisons for wave overtopping have been made (St-Germain et al., 2014, Vanneste et al., 2014), no study to date has the full range of model complexity (from depth-resolving to phase-averaged) or successfully quantified the accuracy versus speed of these models under irregular wave forcing .

### 3.1.2 OBJECTIVE

In the present study, it is our primary aim to quantify the accuracy versus speed of computation of six commonly-used nearshore wave models (Table 3.1) in their prediction of irregular wave overtopping at sea dikes with very shallow mildly-sloping foreshores—where IG waves and setup contribute significantly.

**Table 3.1** *Overview of the numerical models considered for comparative analysis.* [a]*Does not resolve wave overturning or wave roller formation.* [b]*Does not include SS-wave overtopping..*

| **Model** | **Model Type** | | **Wave Propagation** | | **Overtopping** |
|---|---|---|---|---|---|
| | | | **SS Waves** | **IG Waves** | |
| OpenFOAM | Phase-resolving | Depth-resolving | Directly | | Directly |
| SWASH[a] | | | | | |
| BOSZ | | Depth-averaged | | | |
| XB-NH | | | | | |
| XB-SB | IG-wave resolving; SS-wave averaged | | Action-balance | Directly | Directly for IG waves[b] |
| SWAN | Phase-averaged | | Action-balance | Excluded | Empirically |

## 3.2 METHODS

This section begins with a description of the physical model tests under consideration. After which it describes the six numerical models under evaluation, including their governing equations and setup details. A description on the parameters and metrics used to assess model accuracy and computation speed is then provided. Finally, the additional numerical simulations for comparative analysis are described.

### 3.2.1 DESCRIPTION OF THE PHYSICAL MODELS

In the present study, we consider two specific test cases that were both performed at Flanders Hydraulics Research in a smooth, 1-m wide section of their 70-m long and 1.45-m deep wave flume (Altomare et al., 2016) with different deep water wave heights ($H_{m0,deep}$ [m]), peak periods ($T_p$ [s]), foreshore slopes ($m$ [°]), initial water depths at the toe ($h_{toe}$ [m]), dike slopes ($\alpha$ [°]) and dike freeboards ($R_c$ [m]) (Table 3.2). These cases were selected to cover a wide range of deep-water wave steepness ($s_0$ [-]), from very mild ($s_0$ = 0.007, typical of swell conditions) to very steep ($s_0$ = 0.047, typical of wind-sea conditions). With relative water depths ($h_{toe}/H_{m0,deep}$) < 1, these conditions are considered very shallow (Hofland et al., 2017). Both experiments simulated irregular spilling waves (with breaker parameter based on $m$, $\xi_{0,fore}$ < 0.5) with a duration approximately equal to 500 waves to obtain accurate and comparable estimates of the mean overtopping discharge ($q$) (Romano et al., 2015).

**Table 3.2** *Summary of test conditions for both the mild- and steep-wave cases.*

| Case | $H_{m0,deep}$ (m) | $T_p$ (s) | $\cot(m)$ | $s_0$ | $kh$ | $h_{toe}$ (m) | $\frac{h_{toe}}{H_{m0,deep}}$ | $\cot(\alpha)$ | $R_c$ (m) |
|---|---|---|---|---|---|---|---|---|---|
| Mild swell | 0.06 | 2.29 | 50 | 0.007 | 0.98 | 0.032 | 0.53 | 2 | 0.06 |
| Steep wind-wave | 0.21 | 1.70 | 35 | 0.047 | 1.45 | 0.025 | 0.12 | 3 | 0.08 |

For the mild swell-wave case, the variations of water-surface elevations were measured using 10 resistance-type gauges, all synchronously sampling at 50 Hz (Figure 3.2a); while 6 gauges with a sample frequency of 20 Hz were used in the steep-wave case (Figure 3.2b). In the analysis to follow, the term “offshore” is used to refer to gauges 1 to 7 and 1 to 3 of the mild swell and steep-wind wave cases, respectively; and the term “nearshore” to refer to gauges 8 to 10 and 4 to 6, respectively. In either case, the term “toe” refers to the last wave gauge (gauge 10 and gauge 6 of the mild swell and steep wind-wave cases, respectively).

In both cases, the instantaneous overtopping was measured using two Balluff “Micropulse” water sensors situated inside the overtopping box; and $q$ was then obtained by dividing the total volume of water collected at the end during the test by the total test duration.

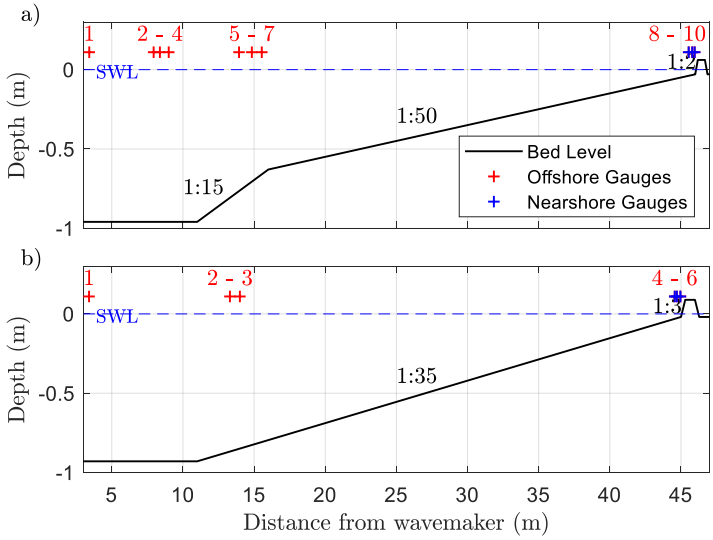


**Figure 3.2** *Physical model setups showing gauge locations for both the: a) mild swell; and b) steep wind-wave cases.*

### 3.2.2 DESCRIPTION OF NUMERICAL MODELS

In this study, six widely-used open-source numerical wave models are considered for comparative analysis. Each model is forced at its boundary with still water levels and parametric spectra (JONSWAP) to match those observed at the most offshore wave gauge during each physical experiment. Likewise, the smooth flume bottom was represented as either a Manning coefficient ($n$) of 0.01 s/m$^{1/3}$ or a Nikuradse geometrical roughness ($k_s$) of 0.3 x 10$^{-3}$ m (in the case of SWAN). A general description of each model is provided in the sections that follow. As we investigate two extremes: very mild swell and very steep wind waves, it is reasonable that some calibration was required for the depth-averaged models (BOSZ, XB-NH and XB-SB). Therefore, a description of the main calibration parameters, their optimum values and impact on model results is also provided. In general, calibration was aimed at reducing the error in $\overline{\eta}$ and $H_{m0}$.

#### *3.2.2.1 OpenFOAM*

The software OpenFOAM is an Open Source object-oriented library, composed by solvers and utilities (Jasak et al., 2007). The formers are designed to numerically solve continuum mechanics problems, while the latter perform tasks involving data manipulation. For the present study, the library *waves2Foam*, a toolbox capable of generating and absorbing free surface water waves, has been adopted. Currently, the method applies the relaxation zone technique (active sponge layers) and supports a large range of wave theories (Jacobsen et al.,

2012). The governing equations for the combined flow of air and water are given by the Reynolds Averaged Navier–Stokes equations (Equations 3.1 and 3.2):

$$\frac{\partial \rho u}{\partial t} + \nabla \cdot [\rho u u^T] = -\nabla p^* - g \cdot x \nabla \rho + \nabla \cdot [\mu \nabla u + \rho \tau] + \sigma_T \kappa_\gamma \nabla \gamma, \quad (3.1)$$

coupled with the continuity equation (2) for incompressible flow:

$$\nabla \cdot u = 0, \quad (3.2)$$

where $u$ [m/s] is the velocity field, $p^*$ [kg/m/s$^2$] is the dynamic pressure component, $\rho$ [kg/m$^3$] is the density, $g$ [m/s$^2$] is the acceleration due to gravity and $\mu$ [kg/m/s] is the dynamic molecular viscosity. The Reynolds stress tensor $\tau$ is defined as:

$$\tau = \frac{2}{\rho}\mu_t S - \frac{2}{3}k^* I, \quad (3.3)$$

where $\mu_t$ [kg/m/s] is the dynamic eddy viscosity, $S$ is the strain rate tensor, $k^*$ is the turbulent kinetic energy per unit mass and $I$ is the identity matrix. The last term in Equation 3.1 is the effect of surface tension, where $\sigma_T$ [kg/s$^2$] is the surface tension coefficient and $\kappa_\gamma$ is the surface curvature (Jacobsen et al., 2012). The track of the free surface is performed by using the VOF method (Hirt and Nichols, 1981), where the scalar field ($\gamma$) is 0 for air, 1 for water and any intermediate value is a mixture of the two fluids.

For the mild and the steep cases, two regular slightly different meshes have been generated, to account for the differences between the two wave conditions. The numerical domains of the mild and steep cases are respectively composed by 49021 and by 70316 cells, with a graded mesh both in the *x* (0.3-0.005 m for the mild, 0.1-0.01 m for the steep) and in the *y* (0.05-0.005 m for the mild, 0.1-0.01 m for the steep) directions. In both cases, the selected regular and constant mesh allowed for a fair compromise between the computational effort and the accuracy of the results.

Note that the OpenFOAM simulations were carried out by Dr. Barbara Zanuttigh (University of Bologna, Italy).

#### 3.2.2.2 SWASH

SWASH is a time domain model for simulating non-hydrostatic, free-surface and rotational flow. It solves the NLSW equations with an added non-hydrostatic pressure correction term (Smit et al., 2013):

$$\frac{\partial \eta}{\partial t} + \frac{\partial uh}{\partial x} = 0, \quad (3.4)$$

$$\frac{\partial u}{\partial t} + \frac{\partial uu}{\partial x} + \frac{\partial wu}{\partial z} = -\frac{1}{\rho}\frac{\partial (p_h + p_{nh})}{\partial x} + \frac{\partial \tau_{xx}}{\partial x} + \frac{\partial \tau_{xz}}{\partial z}, \quad (3.5)$$

$$\frac{\partial w}{\partial t}+\frac{\partial uw}{\partial x}+\frac{\partial ww}{\partial z}=-\frac{1}{\rho}\frac{\partial p_{nh}}{\partial z}+\frac{\partial \tau_{zz}}{\partial z}+\frac{\partial \tau_{zx}}{\partial x}, \tag{3.6}$$

$$\frac{\partial u}{\partial x}+\frac{\partial w}{\partial z}=0, \tag{3.7}$$



where $\eta$ [m] is the free surface elevation; $u(x,z,t)$ [m/s] and $w(x,z,t)$ [m/s] are the horizontal and vertical velocities, respectively; $h$ is the water depth; $\rho$ is the density of water; $p_h$ and $p_{nh}$ are the hydrostatic and non-hydrostatic pressures, respectively; and $\tau_{xx}$, $\tau_{xz}$, $\tau_{zz}$ and $\tau_{zx}$ are the turbulent stresses.

The model exhibits good linear dispersion up to $kh \approx 8$ and $kh \approx 16$ with two and three equidistant (sigma) vertical layers ($K$), respectively; its frequency dispersion is further improved by increasing $K$.

Here, the model was applied with $K$ = 20, which is sufficient for the phase velocity at the breaking wave front to be computed accurately. As such, no additional control is required to initiate or terminate wave breaking. The vertical pressure gradient was discretized by the standard central differencing scheme with the ILU pre-conditioner. The standard k-ε turbulence model is applied to take into account vertical mixing.

A cross-shore grid spacing ($\Delta x$) of 0.025 m was specified for the mild swell cases, while a coarser resolution ($\Delta x$ = 0.04 m) was needed for the steep wind-wave case to maintain model stability. This resulted in approximately 330 and 110 grid cells per deep-water wavelength ($L_0/\Delta x$) for the mild swell and steep wind-wave cases, respectively. For phase-resolving models, $L_0/\Delta x$ is typically kept between 50 and 100 (by rule of thumb) to ensure that the wave components are accurately resolved; however, as waves propagate in very shallow water, the local wavelength becomes much shorter than $L_0$. Thus, in order to maintain a reasonable number of grid cells per local wave length, these higher-than-typical grid resolutions ($L_0/\Delta x$ = 330 and 110) were specified. It should also be noted that while $H_{m0,T}$ in the mild swell case showed convergence (~3% change compared to higher resolutions) at $\Delta x$ = 0.04 m, the resulting $\bar{q}$ increased by a factor of 6 with $\Delta x$ = 0.025 m. This suggests that wave run-up and overtopping at the dike were particularly sensitive to the grid resolution.

Rijnsdorp et al. (2017) proposed a sub-grid approach to improve model efficiency, where vertical accelerations and non-hydrostatic pressures are resolved on a relative course grid while the horizontal velocities and turbulent stresses are resolved on a much finer sub-grid. This approach was attempted here, however, the simulations failed due to instabilities.

#### *3.2.2.3 BOSZ*

The BOSZ wave model—which is freely-available upon request from the developers—computes hazardous free surface flow problems ranging from near-field tsunamis to extreme

swell ranges generated by hurricanes. It solves the following re-formulated, depth-integrated Boussinesq equations of Nwogu (1993), in conservative form:

$$H_t + (HU)_x + \left[\left(\frac{\bar{z}_\alpha{}^2}{2} - \frac{h^2}{6}\right) \cdot hU_{xx} + \left(\bar{z}_\alpha + \frac{h}{2}\right) \cdot h(hU)_{xx}\right]_x = 0 \tag{3.8}$$

$$\begin{aligned}(HU)_t + \left(HU^2 + \frac{1}{2}gH^2\right)_x - gHh_x \\ + U\left[\left(\frac{\bar{z}_\alpha{}^2}{2} - \frac{h^2}{6}\right) \cdot (hU)_{xx} + \left(\bar{z}_\alpha + \frac{h}{2}\right) \cdot h(hU)_{xx}\right]_x \\ + H\left[\bar{z}_\alpha\left(\frac{\bar{z}_\alpha}{2}U_{txx} + (hU_t)_{xx}\right) + \tau\right] = 0,\end{aligned} \tag{3.9}$$

where $H = h + \eta$ is the flow depth, $U$ is the horizontal flow velocity defined at a reference depth $\bar{z}_\alpha$= -0.55502$h$ (Simarro et al., 2013) and $\tau$ the bottom shear in terms of the Manning coefficient.

The governing equations exhibit good dispersion accuracy up to $kh \approx \pi$. Given the difficulty of Boussinesq equations in handling flow discontinuities (such as with breaking waves), the model deactivates the dispersion terms during wave breaking and makes use of the underlying NLSW equations where the breaking wave is then approximated as a bore or hydraulic jump. Wave breaking—and the deactivation of the dispersion terms—occurs in the model based on the momentum gradient:

$$(h + \eta)\frac{\partial u}{\partial x} > B\sqrt{g(h + \eta)}, \tag{3.10}$$

where $B$ is a calibration coefficient (by default = 0.5). Here, $B$ = 0.8 produced the best agreement between model and observations for both cases. This suggests that under these particularly shallow conditions, the wave face becomes very steep prior to breaking. For a detailed overview of the model's sensitivity to this parameter, the reader is pointed to (Roeber et al., 2010). All other model parameters were kept at their default values.

The grid resolution ($L_0/dx$) was set as 200 for the mild swell-wave case but was reduced to 60 for the steep wind-wave case to ensure model stability. For the steep-wave case, higher grid resolutions and lower $B$ values led to instabilities in the form of strong oscillations in surface elevation in the breaking region. This phenomenon, explored extensively by Kazolea and Ricchiuto (2018), is due to the model's hybrid approach to handling wave breaking; that is, where the Boussinesq equations are reduced to the NLSW equations during wave breaking. It should be noted that Boussinesq wave models which take a different (eddy viscosity) approach to wave breaking reportedly show less sensitivity to the grid size (Kazolea and Ricchiuto, 2018); however, this was not evaluated here.

#### 3.2.2.4 XBeach Non-hydrostatic

Like SWASH, XB-NH solves the NLSW equations with a non-hydrostatic pressure correction term (Equations 3.4 to 3.7). Here, XBeach version 1.235527 (also known as the "XBeachX" release) is applied in reduced (simplified) two-layer mode, where the non-hydrostatic pressure is assumed constant in the lower (first) layer (De Ridder, 2018). The water depth is divided into two layers with heights $z_1 = \alpha h$ and $z_2 = (1-\alpha)h$, where $\alpha$ is the layer distribution. The resulting layer-averaged velocities ($u_1$ and $u_2$) are transformed to a depth-averaged velocity ($U$) and a velocity difference ($\Delta u$). Due to the simplified non-hydrostatic pressure in the lower layer, the vertical velocity between layers is neglected. Therefore, only the continuity relation for the upper (second) layer is required:

$$\frac{\partial}{\partial x}[(1+\alpha)hU + (1-\alpha)h\alpha\Delta u] + 2w_2 - u_2\frac{\partial \eta}{\partial x} - u_1\frac{\partial z_1}{\partial x} = 0, \tag{3.11}$$

where $w_2$ is the vertical velocity in the upper (second) layer. To determine the water elevation, the global continuity equation is applied:

$$\frac{\partial \eta}{\partial t} + \frac{\partial hU}{\partial x} = 0, \tag{3.12}$$

In order to control the computed location and magnitude of depth-limited wave breaking, a hydrostatic front approximation is applied. With this, the pressure distribution under breaking waves is considered hydrostatic when the local surface steepness exceeds a maximum prescribed value ($\lambda$ = 0.4, by default):

$$\frac{\partial \eta}{\partial t} > \lambda, \tag{3.13}$$

Here, $\lambda$ = 0.9 and 0.7 produced the best agreement between the model and observations for the mild- and steep-wave cases, respectively. This further supports the statement that for very shallow foreshores, the waves become particularly steep before breaking. All other model parameters were kept at their default values. Additionally, the grid resolution ($L_0/\Delta x$) was set to ~200 and ~180 for the two respective cases.

#### 3.2.2.5 XBeach Surfbeat

XB-SB solves SS-wave motions using the wave-action equation with time-dependent forcing, similar to that of the HISWA model (Holthuijsen et al., 1989). The model represents the SS-wave frequency spectrum by a single frequency ($f_{rep}$) and the wave-action equation is applied at the timescale of the wave group:

$$\frac{\partial A}{\partial t} + \frac{\partial c_{gx}A}{\partial x} = -\frac{D_w}{\sigma}, \tag{3.14}$$

$$A(x,t) = \frac{S_w(x,t)}{\sigma(x,t)} \tag{3.15}$$

$$\sigma = \sqrt{gk\tanh kh} \tag{3.16}$$

where $A$ is the wave action, $S_w$ is the wave energy density, $\sigma$ is the intrinsic wave frequency, $k$ is the wave number, $D_w$ is a dissipation term to account for wave breaking and $c_{gx}$ is the wave-action propagation speed in the cross-shore direction. To simulate wave breaking, XB-SB applies a dissipation model (Roelvink, 1993), by default, for use with SS-wave groups; and a roller model (Nairn et al., 1990, Svendsen, 1984) to represent momentum stored in surface rollers which results in a shoreward delay in wave forcing. The radiation stress gradients that result from these variations in wave action exert forces on the water column and drive IG waves and unsteady currents which are solved by the NLSW equations (Equations 3.4 to 3.7). Therefore, the model directly simulates wave-driven currents and the run-up and overtopping of IG waves.

$$\bar{D}_w = 2\frac{\alpha}{T_{rep}} Q_b E_w \frac{H_{rms}}{h}, \tag{3.17}$$

$$Q_b = 1 - \exp\left(-\left(\frac{H_{rms}}{H_{max}}\right)^{10}\right) \tag{3.18}$$

where $\bar{D}_w$ is the total (directionally-integrated) wave energy dissipation due to breaking, $T_{rep} = 1/f_{rep}$ is the representative wave period and $Q_b$ is the fraction of breaking waves; the root-mean-square SS-wave height, $H_{rms} = \sqrt{8E_w/\rho g}$; the maximum wave height, $H_{max} = \gamma_r h$; $E_w$ is the wave-group varying SS-wave energy; $\alpha$ is a dissipation (by default = 1) and $\gamma_r$ is the ratio of breaking waves to local water depth (by default = 0.55 but typically used for calibration).

Here, $\gamma_r$ = 0.45 and 0.65 provided the best agreement between the model and observations for the mild swell and steep wind-wave cases, respectively.

XB-SB does not directly produce the SS-wave component of the energy density spectrum, instead it computes the change in SS-wave energy as a change in the bulk $H_{rms}$ parameter, as described above. In order to produce a complete energy density ($C_{\eta\eta}$) spectrum at each gauge location, a JONSWAP distribution was assumed around the peak-frequency ($f_p$), where $\sqrt{8\int_{f_p/2}^{2} C_{\eta\eta}\, df} = H_{rms}$. This SS-wave spectrum (Figure 3.3b) was then combined with the IG-wave spectrum (Figure 3.3a)—obtained directly from the computed surface elevation—to produce the complete spectrum (Figure 3.3c).

For the mild swell-wave case, the grid resolution was varied such that it increased shoreward. This reduced computation time while ensuring that the steep dike slope was accurately captured. As such, $L_0/\Delta x$ varied from ~25 (offshore) to ~160 (at the dike) in the mild-wave case; and from ~45 to ~90 in the steep-wave case.

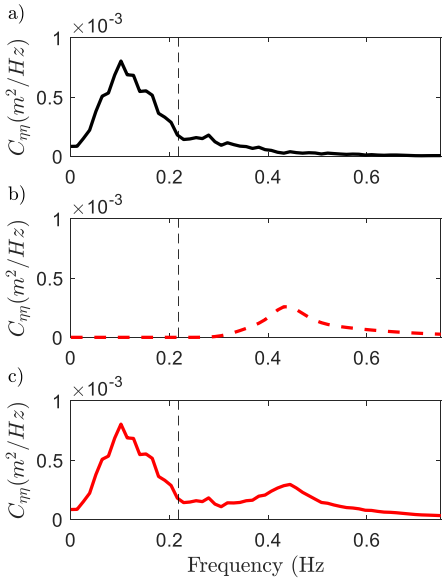


**Figure 3.3** *Example of a) the IG-wave spectrum based on the computed surface elevation; b) an assumed SS-wave spectrum (JONSWAP shape) based on the computed root-mean-square SS-wave height ($H_{rms}$); and c) the total combined spectrum, for XB-SB at the dike toe (steep wind-wave case).*

### 3.2.2.6 SWAN

SWAN is a third-generation, phase-averaged wave model used to estimate the generation (by wind), propagation and dissipation (by depth-induced breaking and bottom friction) of waves from deep water to the surf zone. This includes wave-wave interactions, in both deep and shallow water, and wave-induced setup; but neglects wave-induced currents and the generation or propagation of IG waves. Like XB-SB, SWAN computes the spectral evolution of $A$ in space and time. This is done in a manner similar to Equation 3.14; however, unlike XB-SB which makes use of a single representative frequency, SWAN takes the frequency distribution of action density into account. To simulate depth-limited wave breaking, SWAN uses the following parametric dissipation model, by default (Battjes and Janssen, 1978):

$$\overline{D}_w = \frac{\alpha}{4}\rho g f_{mean} Q_b H_{max}^2, \tag{3.19}$$

and $Q_b$ is estimated as:

$$\frac{1-Q_b}{\ln Q_b} = -8\frac{E_{tot}}{H_{max}^2}, \tag{3.20}$$

where $f_{mean}$ is the mean wave frequency, $H_{max} = \gamma_{bj} h$ and $E_{tot}$ is the total wave-energy variance. Here, $\gamma_{bj}$ = 0.73 (default value) provided good agreement between the model and observations for both the mild swell and steep wind-wave cases. For both wave cases, a

constant grid spacing of 0.25 m was applied. This corresponded to $L_0/\Delta x \approx 30$ for the mild-wave case and $L_0/\Delta x \approx 20$ for the steep-wave case.



### 3.2.3 DATA PROCESSING AND ANALYSIS

#### *3.2.3.1 Mean water level*

The mean water level ($\bar{\eta}$) was calculated by taking the average of the surface elevation, $\eta(t)$, at each gauge location, relative to the elevation of the dike toe. The wave-induced setup, $<\eta>$, was then obtained as the difference between $\bar{\eta}$ at each gauge location and $\bar{\eta}$ at the most offshore gauge.

#### *3.2.3.2 Separation of infragravity and sea-swell waves*

The time series of $\eta(t)$ were further analysed using the Welch's average periodogram method and a Hann filter with a 50% maximum overlap. The resulting one-dimensional spectra of wave energy density, $C_{\eta\eta}(f)$—with ~43 degrees of freedom and a frequency resolution of ~0.008 Hz—were then used to determine $H_{m0,T}$, $H_{m0,SS}$ and $H_{m0,IG}$, as follows:

$$H_{m0} = 4\sqrt{\int_{0.008}^{2} C_{\eta\eta}\, df}, \tag{3.21}$$

$$H_{m0,SS} = 4\sqrt{\int_{f_p/2}^{2} C_{\eta\eta}\, df}, \tag{3.22}$$

and

$$H_{m0,IG} = 4\sqrt{\int_{0.008}^{f_p/2} C_{\eta\eta}\, df}, \tag{3.23}$$

where half the peak frequency ($f_p/2 = 1/2T_p$) is taken as the cut-off to separate SS and IG motions (Roelvink and Stive, 1989). This choice of cut-off frequency is based on the tendency that, in deep water, the majority of SS-wave energy is found at frequencies > $f_p/2$ while the majority of IG-wave energy lies at frequencies <$f_p/2$.

#### *3.2.3.3 Spectral Wave Period*

In addition to wave heights, the spectral wave period ($T_{m-1,0}$) at each gauge location was calculated as follows:

$$T_{m-1,0} = \frac{m_{-1}}{m_0}, \tag{3.24}$$

where,

$$m_n = \sqrt{\int_{0.005}^{2} C_{\eta\eta} \cdot f^n \, df}. \tag{3.25}$$

#### 3.2.3.4 Empirical Estimate of the Incident Infragravity Waves

As SWAN neglects the contribution of IG waves to the total wave incident height at the dike toe ($H_{m0,toe,in}$) we apply an empirical correction, proposed in Chapter 2 (Lashley et al., 2020). Using a dataset of 672 XBeach simulations, an empirical formula for the relative magnitude of the IG waves ($\widetilde{H}_{IG}$) was derived with influence factors to account for variations in offshore wave directional spreading ($\bar{\gamma}_\sigma$), $h_{toe}$ ($\bar{\gamma}_h$), $\cot m$ ($\bar{\gamma}_f$), vegetation ($\bar{\gamma}_v$) and $\cot \alpha$ ($\bar{\gamma}_d$):

$$\widetilde{H}_{IG} = 0.36 \cdot {H_{m0,deep}}^{0.5} \cdot \bar{\gamma}_\sigma \cdot \bar{\gamma}_h \cdot \bar{\gamma}_f \cdot \bar{\gamma}_v \cdot \bar{\gamma}_d, \tag{3.26}$$

For an incident waves analysis (i.e. without the influence of the dike slope) with no directional spreading (1D flume conditions) or vegetation, $\bar{\gamma}_\sigma$, $\bar{\gamma}_v$ and $\bar{\gamma}_d$ = 1; while,

$$\bar{\gamma}_h = 1.04 \cdot \exp(-1.4 \cdot h_{toe}) + 0.9 \cdot \exp(-0.19 \cdot h_{toe}) \tag{3.27}$$

and

$$\bar{\gamma}_f = 1.56 - 3.09 \cdot \cot m^{-0.44}. \tag{3.28}$$

As $\widetilde{H}_{IG}$ represents the ratio of IG to SS waves, $H_{m0,IG,toe,in}$ can be obtained from a SWAN estimate of $H_{m0,SS,toe,in}$:

$$H_{m0,IG,toe,in} = \widetilde{H}_{IG} \cdot H_{m0,SS,toe,in}. \tag{3.29}$$

Finally, a corrected estimate of $H_{m0,toe,in}$ was obtained as follows:

$$H_{m0,toe,in} = \sqrt{{H_{m0,SS,toe,in}}^2 + {H_{m0,IG,toe,in}}^2}. \tag{3.30}$$

#### 3.2.3.5 Empirical Wave Overtopping

While the fully phase-averaged models like SWAN are—to some extent—able to estimate nearshore wave conditions, they cannot directly simulate wave overtopping, as this requires that the individual waves be resolved. In order to estimate wave overtopping, these models can be (and are often) combined with well-established empirical models that require wave parameters at the dike toe as input. In the present study, the EurOtop (2018) formulae based on the work of Van Gent (1999) and Altomare et al. (2016) for (very) shallow foreshores are applied in combination with SWAN. For smooth dikes under perpendicular wave attack with $h_{toe}/H_{m0,deep} < 1.5$:

$$\frac{q}{\sqrt{g \cdot H_{m0,toe,in}^3}} = 10^{-0.79} \cdot \exp\left(-\frac{R_c}{H_{m0,toe,in} \cdot \left(0.33 + 0.022 \cdot \xi_{m-1,0}\right)}\right), \tag{3.31}$$

with

$$\xi_{m-1,0} = \frac{\tan\alpha_{sf}}{\sqrt{H_{m0,toe,in} / L_{m-1,0}}}, \tag{3.32}$$

$$L_{m-1,0} = \frac{g \cdot T_{m-1,0,toe,in}^2}{2\pi}, \tag{3.33}$$

$$\tan\alpha_{sf} = \frac{1.5H_{m0,toe,in} + R_{u2\%}}{\left(1.5H_{m0,toe,in} - h_{toe}\right) \cdot m + \left(h_{toe} + R_{u2\%}\right) \cdot \cot\alpha}, \tag{3.34}$$

$$\frac{R_{u2\%}}{H_{m0,toe,in}} = 4 - \frac{1.5}{\sqrt{\xi_{m-1,0}}}, \tag{3.35}$$

where $g$ is the gravitational constant of acceleration, $\alpha$ is the dike slope, $\alpha_{sf}$ is an equivalent slope (to account for waves breaking on the foreshore) and $T_{m-1,0,toe,in}$ is the spectral wave period at the dike toe based on the incident waves (i.e. without the influence of waves reflected at the dike). It should be noted that $\xi_{m-1,0}$ and $R_{u2\%}$ are obtained iteratively (until $R_{u2\%}$ converges), with a first estimate of $R_{u2\%} = 1.5H_{m0,toe,in}$.

Additionally, as SWAN excludes the contribution of IG waves, corrected estimates of $T_{m-1,0,toe}$ are typically obtained using Equations 3.36 and 3.37 (Hofland et al., 2017), as outlined in the EurOtop (2018) manual:

$$\frac{T_{m-1,0,toe,in}}{T_{m-1,0,deep}} - 1 = 6 \cdot \exp\left(-4\tilde{h}\right) + \exp\left(-\tilde{h}\right), \tag{3.36}$$

where,

$$\tilde{h} = \frac{h_{toe}}{H_{m0,deep}} \left(\frac{\cot m}{100}\right)^{0.2}. \tag{3.37}$$

### 3.2.3.6 Error Metrics

In order to compare the performance of the numerical models, we assess the mean relative accuracy in an approach similar to that of Lynett et al. (2017):

$$Mean\ Ratio_{\Psi} = \frac{1}{n} \sum_{i=1}^{N} \frac{\Psi_{mod}^i}{\Psi_{obs}^i}, \tag{3.38}$$

where $\Psi$ is a stand-in for the parameter under consideration ( $\bar{\eta}$ , $H_{m0}$ , $H_{m0,SS}$ , $H_{m0,IG}$ and $T_{m-1,0}$) for the $N$ wave-gauge locations; and subscripts $mod$ and $obs$ refer to model predictions and observations made during the physical experiment, respectively. Here we make a distinction between gauges offshore and nearshore (Figure 3.2). A mean ratio of 1 suggests perfect agreement between the model and observations, while values higher or lower than one indicate over- or under-predictions, respectively. It should be noted that all wave gauges (offshore and at the dike toe, see Figure 3.2) are considered in Equation 3.38. While the focus of this study is primarily at the dike toe, it is important to assess the model

performance offshore to ensure that: i) the boundary conditions are correctly modelled; and ii) that no (significant) numerical dissipation occurs in deep water, as a result of a coarse grid resolution for example.

Finally, the performance of each model for wave overtopping was assessed by comparing the simple ratio of modelled to observed $q$ and the absolute relative error in the prediction of mean overtopping discharge:

$$Absolute\ Relative\ Error_q = \left|1 - \frac{q_{mod}}{q_{obs}}\right|. \tag{3.39}$$

#### 3.2.3.7 Computation Speed

Two work stations (WS) were used to carry out this research (Table 3.3). Given the required computational effort, the OpenFOAM simulations were performed on WS-A, while the other models were run on WS-B. To assess computation speed, the duration of each simulation (in wall clock time) was recorded.

**Table 3.3** *Overview of work stations used to carry out the numerical simulations.*

| Work Station (WS) | A | B |
|---|---|---|
| Operating System | Ubuntu 14.04 LTS | Windows 10 |
| Memory | 31.2 GB | 16 GB |
| Processor | Intel Xeon® CPU ES-2690 v3 @ 2.60 GHz x 16 | Intel® Core™ i7-6600 CPU @ 2.60GHz, 2.81 GHz x 4 |
| Graphics | Gallium 0.4 on NVE7 | Intel® HD Graphics 520 |
| Type | 64-bit | 64-bit |
| Disk | 1.9 TB | 239 GB |

## 3.3 RESULTS AND DISCUSSIONS

In this section, the results of the model-data comparisons are presented and discussed. As wave overtopping is the end result of wave propagation, the performance of each model for the prediction of mean water levels, wave heights and periods is first assessed. For the models where calibration was carried out (BOSZ, XB-NH and XB-SB), both default and calibrated results are presented. Note that no parameter tuning was done for the depth-resolving models (OpenFOAM and SWASH) as wave breaking is intrinsically resolved. Likewise, SWAN with default settings showed reasonable agreement and was therefore not calibrated. Lastly, it should be noted that the BOSZ simulation of the steep wind-wave case with default settings resulted in instabilities (see Section 3.2.2.3) and is therefore not included in the analysis.

### 3.3.1 MEAN WATER LEVEL

Each model, excluding OpenFOAM, is able to accurately (within 15% error) and consistently reproduce $\overline{\eta}$ for both the mild swell (Figure 3.4a) and steep wind-wave (Figure 3.4b) cases. This includes the increase in $\overline{\eta}$ nearshore, referred to as wave-induced setup ($<\eta>$), highlighted in Figure 3.5 with the XB-NH results representing the general behaviour of the

numerical models. Note that the vertical axes limits of Figure 3.4 are set for an easy comparison with the other modelled versus observed plots that follow. While OpenFOAM agrees well with the observations for the mild swell case, it overestimates <$\eta$> offshore (gauges 2 and 3) and underestimates <$\eta$> nearshore (gauges 4 to 6) for the steep wind-wave case (Figure 3.5). This may be indicative of premature wave breaking in OpenFOAM.

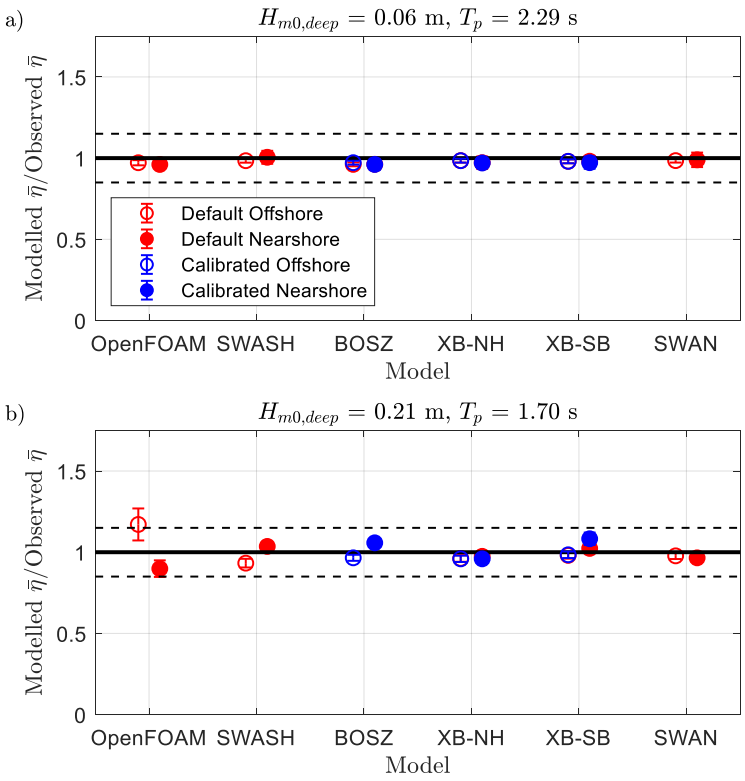


**Figure 3.4** *Mean ratio of modelled to observed $\bar{\eta}$ (markers) for both the a) mild swell and b) steep wind-wave cases, with error bars representing the standard deviation. Solid horizontal lines represent perfect agreement between model and observations. Dashed lines correspond to +/- 15% error.*

The satisfactory performance of BOSZ and XB-NH observed here (Figure 3.4) is in contrast with previous studies (Lashley et al., 2018, Zhang et al., 2019), which found that depth-averaged models were unable to accurately estimate <$\eta$> due to their lack of vertical resolution and exclusion of wave roller dynamics. However, the difference in model performance here is likely due to the spilling nature of the waves ($\xi_{0,fore}$ = 0.23 and 0.13 for the mild swell and steep wind-wave cases, respectively) compared to the plunging waves and steep fore-reef slopes assessed by Lashley et al. (2018) ($\xi_{0,fore}$ > 1.1) and Zhang et al. (2019)

($\xi_{0,fore}$ = 1.29). That is, while resolving the vertical structure of flow may be critical for plunging breakers, depth-averaged models are able to perform well under spilling waves.

There is also a notable difference in the observed maximum $<\eta>$ between the mild swell ($<\eta>$ = 0.004 m) and steep wind-wave ($<\eta>$ = 0.015 m) cases (Figure 3.5). This substantial increase in $<\eta>$ as $h_{toe}/H_{m0,T,deep}$ decreases agrees with the findings of Gourlay (1996) on shallow reefs, and suggests that $<\eta>$—which contributes to wave run-up (Stockdon et al., 2006) and, by extension, overtopping—increases proportionally as foreshores become more shallow, or as deep water wave conditions become more energetic.

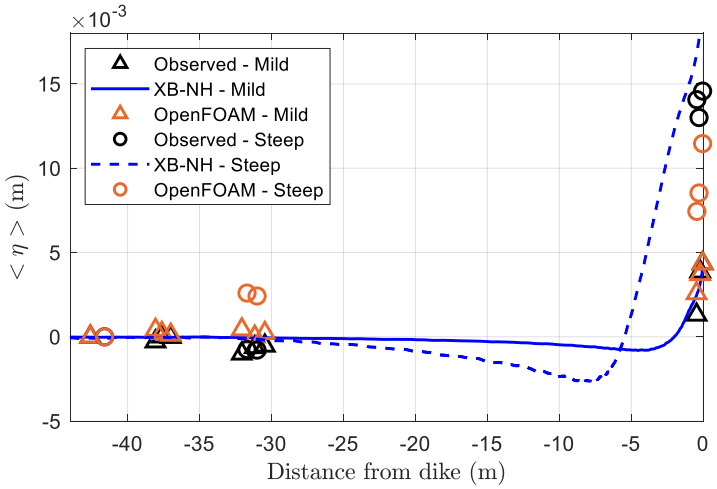


**Figure 3.5** *Cross-shore profiles of modelled (XB-NH and OpenFOAM) and observed $<\eta>$ for both the mild swell and steep wind-wave cases.*

### 3.3.2 SIGNIFICANT WAVE HEIGHT

SWASH, BOSZ, XB-NH and XB-SB are able to reproduce $H_{m0,T}$, both offshore and nearshore, within 15% error for two cases (Figure 3.6). On the other hand, OpenFOAM and SWAN both show notable differences; with SWAN consistently and considerably underestimating $H_{m0,T}$ nearshore.

While SWAN is able to accurately simulate the propagation of high-frequency waves ($H_{m0,SS}$, Figure 3.7), it does not compute the low-frequency waves ($H_{m0,IG}$, Figure 3.8) and therefore underestimates $H_{m0,T}$ nearshore, where the contribution of IG waves is significant (Figure 3.6). The relatively high standard deviation associated with SWAN's nearshore $H_{m0,SS}$ estimates is due to its exclusion of wave reflection. In the physical model, the superposition of the incident and reflected waves results in a nodal/anti-nodal pattern with a maximum at the dike (outsets in Figure 3.9a and Figure 3.10a). As SWAN excludes the reflected component, the model underestimates $H_{m0,SS}$ immediately in front of the dike,

where the incident and reflected waves add up. On the other hand, this shortcoming makes SWAN especially suitable for use with the empirical overtopping models that require incident-wave conditions as input.

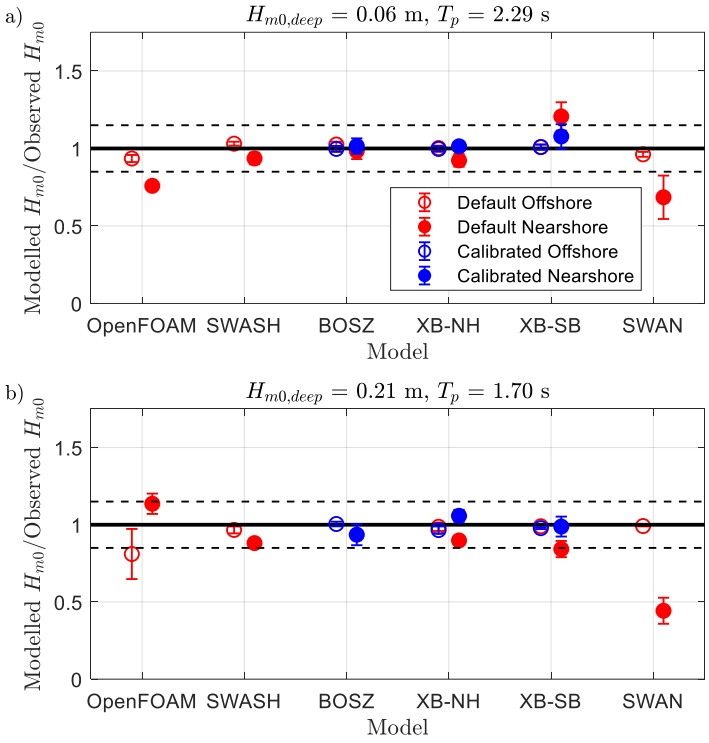


**Figure 3.6** *Mean ratio of modelled to observed $H_{m0}$ (markers) for both the a) mild swell and b) steep wind-wave cases, with error bars representing the standard deviation. Solid horizontal lines represent perfect agreement between model and observations. Dashed lines correspond to +/- 15% error.*

SWAN also predicts a higher and lower maxima in $H_{m0,SS}$ (just before breaking) than XB-NH, for the mild swell (Figure 3.9a) and steep wind-wave (Figure 3.10a) cases, respectively. This is likely due to the dissipation model employed by SWAN (Equation 3.19). Tuning $\gamma_{bj}$—the parameter which controls the maximum wave height to water depth ratio in SWAN—would yield better agreement between the two models; however as there were no wave gauges in this region it is difficult to ascertain which model is correct here.

With respect to OpenFOAM, the model shows inconsistent results between the two cases. Under the mild swell conditions, OpenFOAM underestimates $H_{m0,T}$ nearshore (Figure 3.6a); however for the steep wind-wave case, the model overestimates $H_{m0,T}$ nearshore (Figure

3.6b). In both cases, the model appears to be too dissipative, resulting in a reduction in $H_{m0,SS}$ offshore.

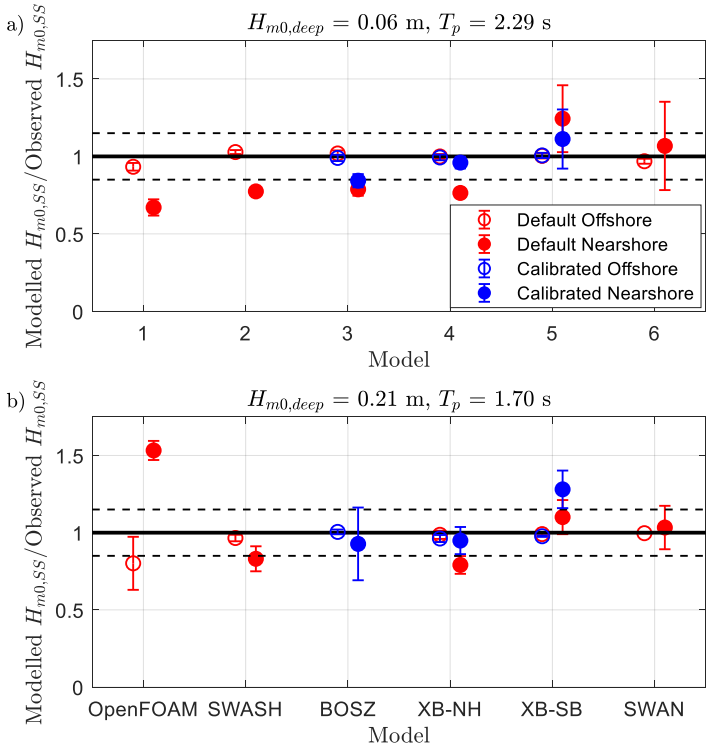


**Figure 3.7** *Mean ratio of modelled to observed $H_{m0,SS}$ (markers) for both the a) mild swell and b) steep wind-wave cases, with error bars representing the standard deviation. Solid horizontal lines represent perfect agreement between model and observations. Dashed lines correspond to +/- 15% error.*

For the mild swell case, this dissipation is minor resulting in a consistent under-prediction of $H_{m0,SS}$ (Figure 3.7a and Figure 3.9a) and $H_{m0,IG}$ (Figure 3.8a and Figure 3.9b). Under the steep wind-wave conditions, however, the dissipation is significant. This observation, combined with the overestimation of $<\eta>$ offshore (Figure 3.5), indicates premature wave breaking in OpenFOAM. This reduction in $H_{m0,SS}$ offshore results in unbroken SS-waves reaching the dike and the overestimation of $H_{m0,SS}$ nearshore (Figure 3.7b and Figure 3.10a). XB-NH also shows some numerical dissipation offshore but this is negligible compared to that of OpenFOAM (Figure 3.10a). The wave damping along the flume by OpenFOAM was already found by other authors (Conde, 2019a, Conde, 2019b) and is popular among the user community. Previous works (Larsen et al., 2019) and this contribution suggest that a more refined mesh by increasing the number of cells per wave height may improve the wave form

modelling during the wave propagation. However, a reduction in grid size for the steep wind-wave case here did not significantly improve the OpenFOAM model results.

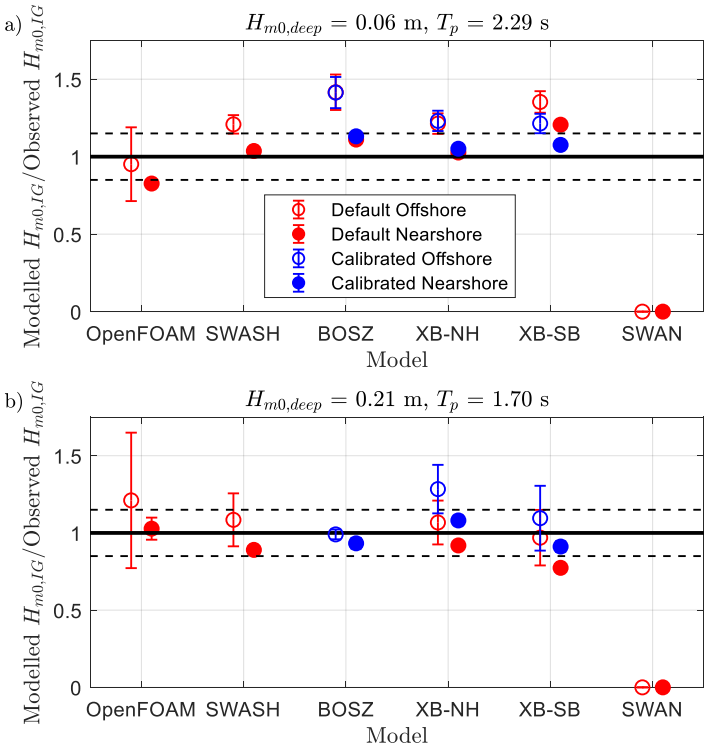


**Figure 3.8** *Mean ratio of modelled to observed $H_{m0,IG}$ (markers) for both the a) mild- and b) steep-wave cases, with error bars representing the standard deviation. Solid horizontal lines represent perfect agreement between model and observations. Dashed lines correspond to +/- 15% error.*

Though SWASH is able to accurately predict $H_{m0,IG}$ it underestimated $H_{m0,SS}$ nearshore in both cases. This is possibly due to the standard k-ε turbulence model applied in multi-layered mode, which may overestimate the turbulent (vertical) viscosity. Similar to OpenFOAM, a reduction in grid size from 0.04 m to 0.025 m did not significantly improve the estimates (~3% change in $H_{m0,SS}$). While calibration generally improved model performance for $\overline{\eta}$ (Figure 3.4), $H_{m0,T}$ (Figure 3.6) and $H_{m0,IG}$ (Figure 3.8), it resulted in the overestimation of $H_{m0,SS}$ nearshore by XB-SB (Figure 3.7). This is as a result of tuning $\gamma_r$ (Equation 3.18) which affects both the maximum $H_{m0,SS}$ and $H_{m0,IG}$. Perhaps a different approach, where $\alpha$ (Equation 3.17)—the parameter that controls the magnitude of dissipation—is calibrated (Lashley et al., 2018) would yield better results. However, as XB-SB predicts IG-wave overtopping only, the loss in accuracy for $H_{m0,SS}$ to improve $H_{m0,IG}$ predictions was considered acceptable.

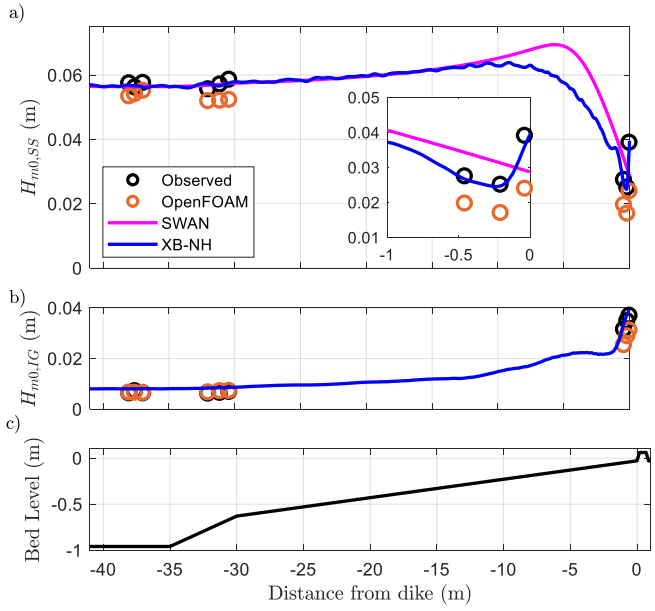


**Figure 3.9** *Cross-shore profiles of modelled and observed: a) $H_{m0,SS}$ and b) $H_{m0,IG}$ for the mild-swell case; with c) bed level, for reference. Outset in panel 'a' magnifies the plot area between -1 and 0 m away from the dike.*

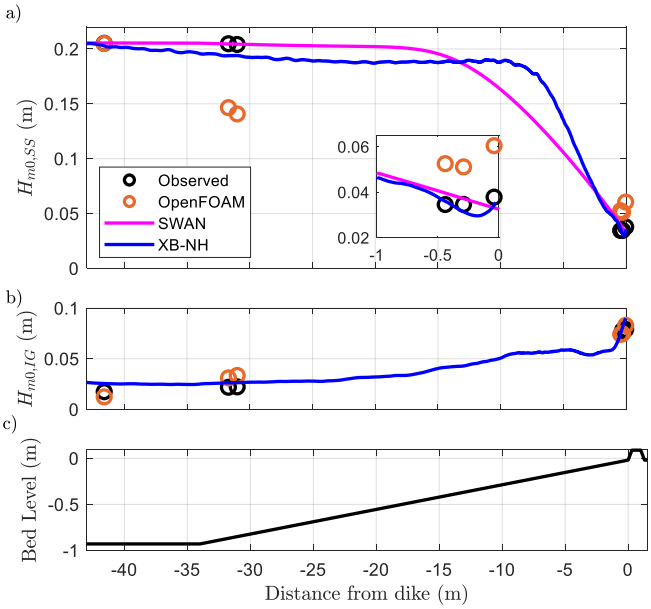


**Figure 3.10** *Cross-shore profiles of modelled and observed: a) $H_{m0,SS}$ and b) $H_{m0,IG}$ for the steep wind-wave case; with c) bed level, for reference. Outset in panel 'a' magnifies the plot area between -1 and 0 m away from the dike.*

### 3.3.3 SPECTRAL WAVE PERIOD

SWASH, XB-NH and XB-SB show good agreement between modelled and observed $T_{m-1,0}$ predictions; while SWAN, OpenFOAM and BOSZ show notable deviations (Figure 3.11). As the accurate prediction of $T_{m-1,0}$ requires the models to correctly represent the distribution of wave energy by frequency (Equation 3.25), we assess the modelled versus observed wave spectra (Figure 3.12 and Figure 3.13). SWASH, BOSZ, XB-NH and XB-SB correctly capture the shift in peak energy density ($C_{\eta\eta}$) from the SS-wave (Figure 3.12a and Figure 3.13a) to the IG-wave band (Figure 3.12b and Figure 3.13b); however BOSZ overestimates the magnitude of the IG peak and shows it at slightly lower frequencies than observed. This, coupled with a minor underestimation of the SS-wave energy—most evident for the mild swell case (Figure 3.12b)—results in an overestimation of $T_{m-1,0}$.

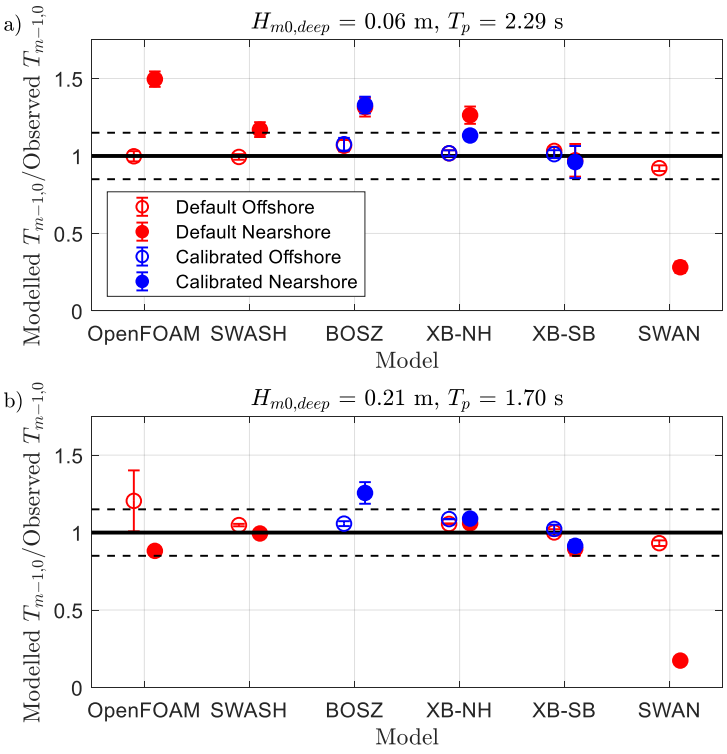


*Figure 3.11 Mean ratio of modelled to observed $T_{m-1,0}$ (markers) for both the a) mild swell and b) steep wind-wave cases, with error bars representing the standard deviation. Solid horizontal lines represent perfect agreement between model and observations. Dashed lines correspond to +/- 15% error.*

The consistent underestimation of $T_{m-1,0}$ by SWAN is expected due to its exclusion of $C_{\eta\eta}$ at IG frequencies (Figure 3.12b and Figure 3.13b). OpenFOAM, on the other hand, does show a shift in energy from offshore to the dike toe; however, it shows two distinct IG peaks

(Figure 3.12b and Figure 3.13b), not present in the observations. In the mild swell case, this misrepresentation of $C_{\eta\eta}$ at IG frequencies couple with the underestimation of $C_{\eta\eta}$ in the SS-wave band resulted in the significant overestimation of $T_{m-1,0}$ nearshore (Figure 3.11a). Under the steep wind-wave conditions, OpenFOAM also shows considerable $C_{\eta\eta}$ in the SS-wave band (nearshore) while the observed spectra shows very little (Figure 3.13b). This further supports the argument that due to premature wave decay in the model, some unbroken SS waves are able to reach the dike.

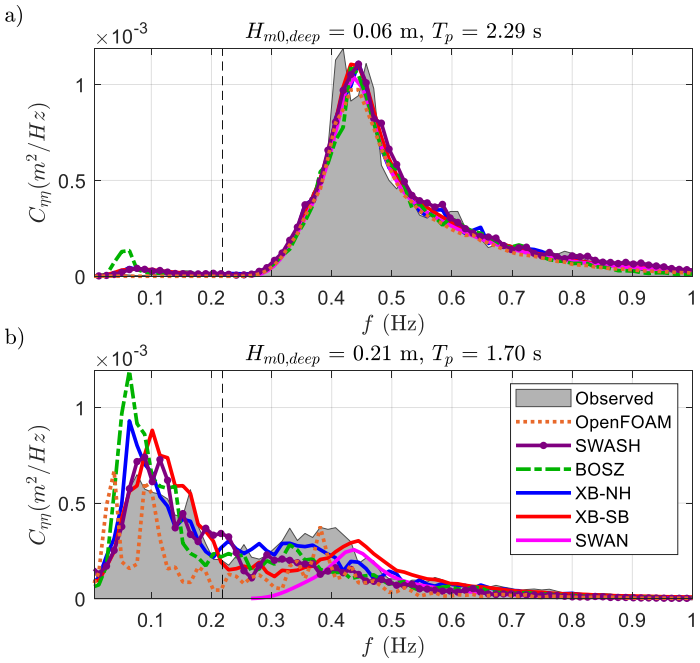


**Figure 3.12** *Model-data comparison of wave spectra: a) offshore (at gauge 1) and b) nearshore (at gauge 10) for the mild swell case. Dashed vertical lines indicate the frequency separating SS- and IG-wave motions.*

### 3.3.4 WAVE OVERTOPPING

#### *3.3.4.1 General*

An important remark is the difference in the observed $q$ between the mild swell (0.094 l/s per m) and steep wind-wave (0.205 l/s per m) cases. Despite having similar $H_{m0,SS,toe}$ values—0.039 m (Figure 3.9) and 0.038 m (Figure 3.10a) for the mild swell and steep wind-wave cases, respectively—the steep-wave case with a higher $R_c$ and lower $h_{toe}$ (Table 3.2), produces double the $q$. This observation suggests that the nonlinear effects of wave breaking—that is, the generation of IG-waves and wave-induced setup—contribute significantly to the resulting overtopping discharge. While the effects of vegetation are not considered here, this observation highlights a potential limitation in studies that assess the

effectiveness of shallow foreshores but focus only on the attenuation of $H_{m0,SS}$ and neglect the contribution of $H_{m0,IG}$ (Vuik et al., 2016, Yang et al., 2012).

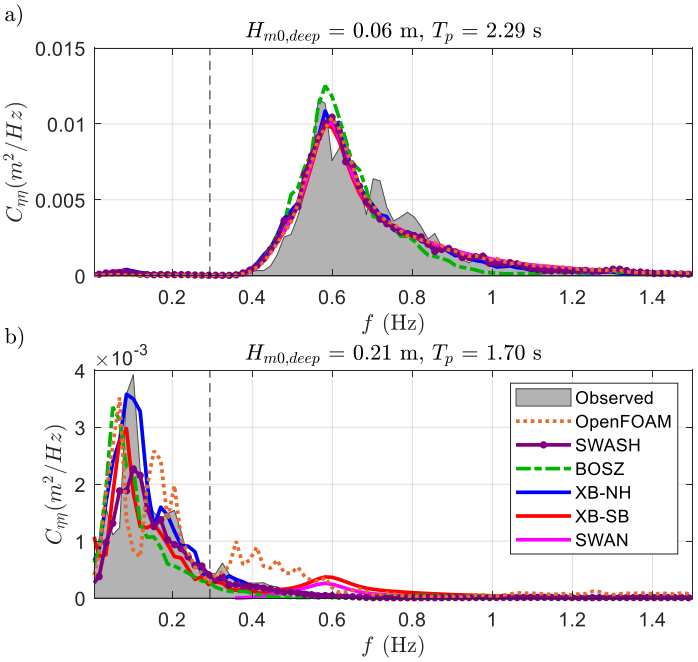


**Figure 3.13** *Model-data comparison of wave spectra: a) offshore (at gauge 1) and b) nearshore (at gauge 6) for the steep wind-wave case. Dashed vertical lines indicate the frequency separating SS- and IG-wave motions.*

To further investigate the influence of the IG-waves, we compare the overtopping estimated using SWAN and EurOtop (2018) with and without the corrections to $H_{m0,IG,toe,in}$ and $T_{m-1,0,toe,in}$ obtained through Equations 3.29 and 3.36, respectively:

**Table 3.4** *SWAN results with and without the empirial corrections for $H_{m0,IG,toe,in}$ (Equation 3.29) and $T_{m-1,0,toe,in}$ (Equation 3.36).*

| Case | SWAN | $H_{m0,SS,toe,in}$ (m) | $H_{m0,IG,toe,in}$ (m) | $H_{m0,toe,in}$ (m) | $T_{m-1,0,toe,in}$ (s) | $q$ (l/s per m) | |
|---|---|---|---|---|---|---|---|
| | | | | | | Modelled | Observed |
| Mild swell | Original | 0.029 | 0 | 0.029 | 2.17 | 0.014 | 0.094 |
| | Corrected | 0.029 | 0.014 | 0.032 | 5.38 | 0.053 | |
| Steep wind wave | Original | 0.033 | 0 | 0.033 | 1.67 | 0.003 | 0.205 |
| | Corrected | 0.033 | 0.03 | 0.045 | 8.37 | 0.089 | |

Under the mild swell-wave conditions, the ratio $\widetilde{H}_{IG}$ = 0.5 (Equation 3.29) and the contribution of $H_{m0,IG,toe,in}$ to $H_{m0,toe,in}$ is minor (Table 3.4). On the other hand, including the IG waves resulted in a 2.5-fold increase in $T_{m-1,0,toe,in}$ and magnitude 4-fold increase in

the predicted $q$, compared to the original SWAN estimates. The difference is more striking for the steep-wave case where the IG waves dominate at the dike toe ($\widetilde{H}_{IG}$ = 0.92). The inclusion of the IG waves resulted in 36% increase in $H_{m0,T,toe,in}$, a 5-fold increase in $T_{m-1,0,toe,in}$ and an order of magnitude increase in the predicted $q$. Furthermore, the original SWAN estimates—without any corrections to $T_{m-1,0,toe,in}$ and $H_{m0,T,toe,in}$—erroneously show a decrease in $q$ between the mild swell and steep wind-wave cases, while the observations show a notable increase. These results further emphasize the danger of neglecting the IG-wave contribution—demonstrated here by the correction of input to the empirical formulae—in the design and assessment of coastal structures with very shallow foreshores. Considering the wider model comparison, each model—with the exception of BOSZ—fails to reproduce the overtopping for the mild swell case (Figure 3.14). This is particularly evident for XB-SB which significantly underestimates $q$ for both wave cases. This suggests that while XB-SB may estimate wave run-up accurately in IG-wave dominant environments (Lashley et al., 2018), it's exclusion of the SS-wave component considerably limits its performance for wave overtopping.

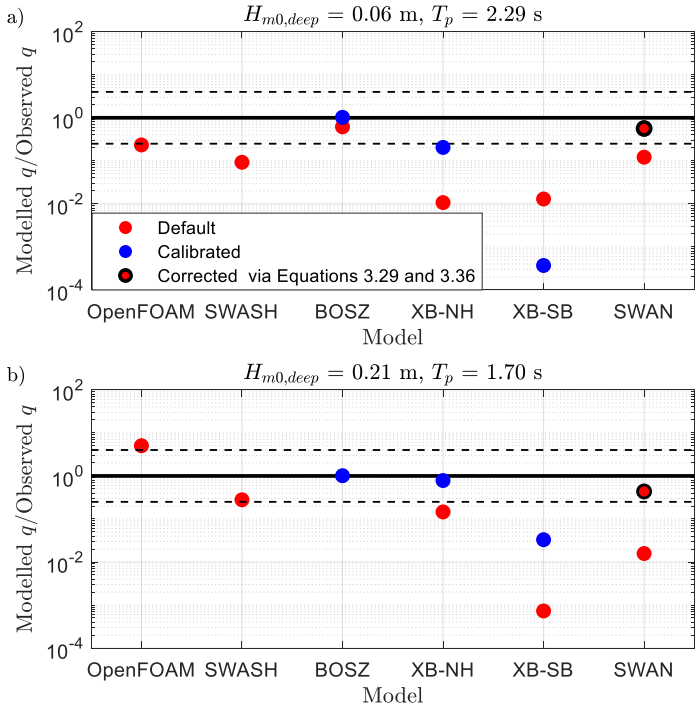


**Figure 3.14** *Ratio of modelled to observed q (markers) for both the a) mild swell and b) steep wind-wave cases. Solid horizontal lines represent perfect agreement between model and observations. Dashed lines correspond to a factor of 4 larger and lower than the observations.*

Compared to the depth-resolving models (XB-NH and BOSZ), both SWASH and OpenFOAM show larger errors in wave overtopping predictions (Figure 3.14). While the performance of OpenFOAM may be attributed to its misrepresentation of nearshore waves and periods (Sections 3.3.2 and 3.3.3), the performance of SWASH—particularly under mild-swell conditions—is somewhat surprising since it performed reasonably well in the prediction of $\overline{\eta}$, $H_{m0}$ and $T_{m-1,0}$ in both cases here and has been previously successful in one-layered mode (Suzuki et al., 2017). However, Suzuki et al. (2017) focused on obtaining good agreement at the toe (the last wave gauge only) and the resulting $\bar{q}$ in their tuning of SWASH; therefore $q$ was not assessed unless wave heights and periods at the toe were within a certain accuracy range, regardless of the input (offshore) conditions. Whereas here, we assess the model's general performance for wave propagation (both offshore and nearshore), in addition to $q$. The models do, however, perform considerably better for the steep-wave case. This is consistent with the findings of Roelvink et al. (2018) and Suzuki et al. (2017) who showed that XB-NH and SWASH, respectively, were more accurate for higher overtopping rates, but suffered for rates below 0.08 – 0.16 l/s per m (in model scale).

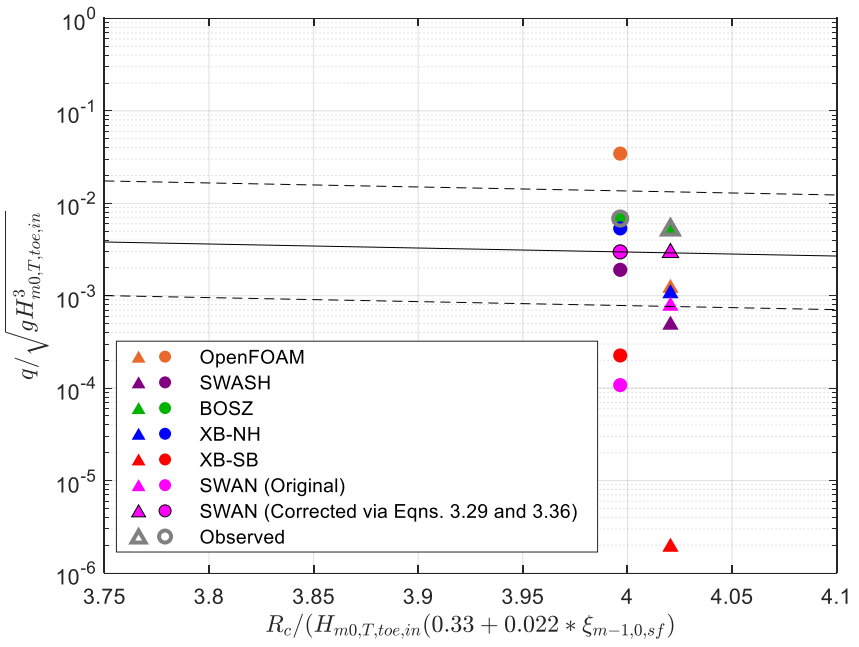


**Figure 3.15** *Relative overtopping discharge versus relative freeboard with triangles and circles representing the mild swell and steep wind-wave cases, respectively. Solid line corresponds to Equation 3.31 with dashed lines representing +/- 5% exceedance. Note that where applicable q corresponds to the calibrated model results.*

The improvement in SWAN with the corrections is most evident for the steep-wave case, with the estimated $q$ now on par with that of BOSZ and outperforming the other more

physically-complex models. Figure 3.15 shows the modelled relative overtopping discharge ($q/\sqrt{gH_{m0,T,toe,in}^3}$) versus the relative freeboard ($R_c/(H_{m0,T,toe,in}(0.33+0.022\xi_{m-1,0,sf})$), where $H_{m0,T,toe,in}$ and $T_{m-1,0}$ (to compute $\xi_{m-1,0,sf}$) are taken from Table 3.4. If we take the +/5 % exceedance lines of the EurOtop (2018) formula (Equation 3.31, Figure 3.15) as the general range of acceptable overtopping predictions, OpenFOAM (mild swell case), SWASH (steep wind-wave case) BOSZ, XB-NH and SWAN (with corrections) are all reasonable.

As most of the models performed reasonably well for wave propagation, the excellent agreement between BOSZ and the observed $q$ is likely not dependent on underlying governing equations (Boussinesq versus NLSW) but more to do with how the shoreline and wave run-up are treated numerically. However, an in-depth analysis of the various numerical schemes implemented in each numerical model was beyond the scope of this study.

### 3.3.4.2 Accuracy versus Speed

In contrast with the general assumption that models of increasing physical complexity produce more accurate results, Figure 3.16 shows no clear relationship between computational demand (simulation time) and the absolute relative error in overtopping.

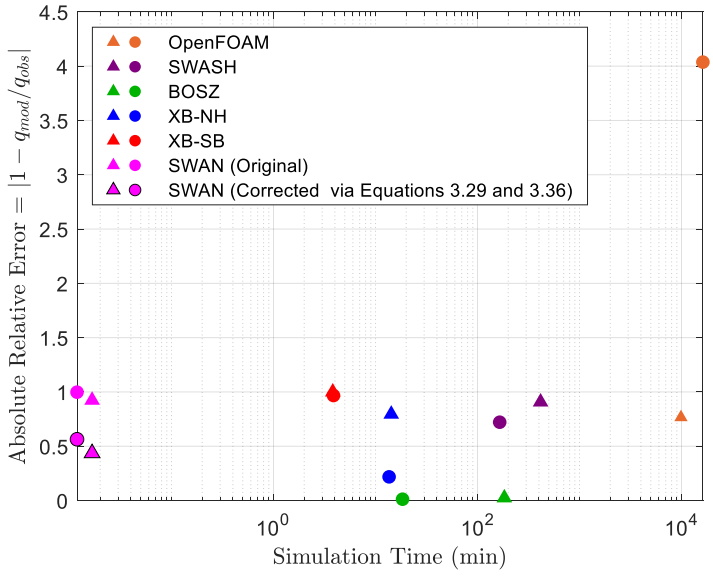


**Figure 3.16** *Accuracy versus speed of the numerical wave models for wave overtopping with triangles and circles representing the mild swell and steep wind-wave cases, respectively.*

Furthermore, the depth-resolving models (SWASH and OpenFOAM), which have significantly higher simulation times show larger errors than the depth-averaged models (XB-NH and BOSZ). The phase-averaged models (XB-SB and SWAN (original)), despite their

considerable speed advantage, significantly underestimated the overtopping discharge due to their exclusion of higher- and lower-frequency wave components, respectively. However, by including the IG-waves empirically, SWAN's performance improved significantly; now within acceptable limits and on par with those of XB-NH and BOSZ but at little to no computational cost (Figure 3.16). It should be noted that the use of SWAN with Equation 3.36 is already the recommended approach in EurOtop (2018); the novelty here is the further improvement in results offered by Equation 3.29.

## 3.4 CONCLUSION

In the present study we assess the ability of 6 widely used numerical models to simulate waves overtopping steep dikes with mildly-sloping shallow foreshores. However, with the exception of OpenFOAM and to some extent SWASH ( $K \geq 10$ ), the above (phase-resolving) models were originally developed to simulate wave evolution over mildly-sloping foreshores; and not specifically for wave run-up and overtopping of steep structure slopes. Since their development, the phase-resolving models have each been successfully applied to simulate wave propagation over steep reefs and run-up of relatively steep beaches. Likewise, depth-resolving models like OpenFOAM and SWASH ($K \geq 10$) were originally developed to simulate wave-structure interaction and not specifically for wave propagation. In the present study we tested the ability of these models in both applications: i) wave evolution over a shallow mildly-sloping foreshore; and ii) the resulting overtopping discharge.

Overall, BOSZ and XB-NH (under steep wind-waves) showed high skill in both applications with a reasonable computational demand; while OpenFOAM, with a much higher computational demand—showed difficulty in performing both functions. The broad implication of the present work is that higher-resolution, more computationally-demanding wave models may simply not be needed; specifically where the analysis is focused on bulk, time-averaged physical quantities ($H_{m0}$, $T_{m-1,0}$ and $q$), as shown here. Should more detail be required—for example, estimates of the vertical velocity profile or turbulence—then a depth-resolving model such as SWASH ( $K \geq 10$ ) or OpenFOAM should be applied. Moreover, SWASH ( $K \geq 10$ ) and OpenFOAM are likely to perform well if the computational domain begins at the dike toe and ends at the overtopping box; i.e., where simulating wave propagation over a large distance is not required.

In addition, our results showed that with simple empirical corrections, phase-averaged models like SWAN can perform on par—if not better than—phase-resolving models, with much less computational effort. Importantly, our work emphasizes the importance of including IG waves in the design and assessment of coastal dikes; as neglecting their contribution to $H_{m0,T,toe}$ and $T_{m-1,0,toe}$ can lead to under-predictions in $q$ of up to two orders of magnitude.

Given the scope of the model comparison, including both phase-resolving and phase-averaged, a detailed wave-by-wave comparison of the higher-resolution models was not carried out. Future work should address this and investigate the influence of the various numerical schemes implemented in the respective numerical models, as this was not within the scope of the present work. Additionally, Equations 3.31 and 3.36 were developed (in part) using the wider dataset from which these cases were taken; therefore their performance under different conditions is still to be confirmed. Despite these limitations, the findings here can aid practitioners in their decision making; specifically in deciding which numerical model should be applied based on the level of accuracy required.

# 4

# EMPIRICAL OVERTOPPING FORMULATION FOR INFRAGRAVITY-WAVE DOMINATED SHORELINES*


## ABSTRACT

The state-of-the-art formulae for mean wave overtopping ($q$ [m$^3$/s/m]) assessment typically require wave conditions at the toe of the structure as input. However, for structures built either on land or in very shallow water, obtaining accurate estimates of wave height and period at the structure toe often proves difficult and requires the use of either physical modelling or high-resolution numerical wave models. In this chapter, the approach of Goda et al. (1975) is applied to establish accurate prediction formulae for both vertical and sloping structures based entirely on deep-water characteristics—where the influence of the foreshore is captured by directly incorporating the foreshore slope and the relative water depth at the structure toe ( $h_{toe}/H_{m0,deep}$ ). Findings show that $q$ decreases exponentially with $h_{toe}/H_{m0,deep}$ due to the decrease of the incident wave energy; however the rate of reduction in $q$ decreases for structures built on land or in extremely shallow water ($h_{toe}/H_{m0,deep} \leq$ 0.1) due to the increased influence of wave-induced setup and infragravity waves—which act as long-period fluctuations in mean water level—generated by wave shoaling and breaking over the foreshore.


This chapter is organized as follows: Section 4.1 describes the standard approach to formulating wave overtopping and the challenges therein when applied to very shallow foreshore—where infragravity waves play a significant role (Chapters 2 and 3). Section 4.2 provides an overview of the existing empirical methods for wave transformation and

*This chapter has been published as: Lashley, C. H., van der Meer, J., Bricker, J. D., Altomare, C., Suzuki, T., and Hirayama, K.: Formulating Wave Overtopping at Vertical and Sloping Structures with Shallow Foreshores Using Deep-Water Wave Characteristics, Journal of Waterway, Port, Coastal, and Ocean Engineering, 147, 10.1061/(asce)ww.1943-5460.0000675, 2021.

overtopping under very shallow conditions, followed by descriptions of the numerical and physical model datasets considered. Section 4.2 also describes the performance metrics used to carry out the analyses. In Section 4.3, the influence of the foreshore on nearshore wave conditions—and by extension the importance of $h_{toe}/H_{m0,deep}$ and $\tan(m)$—is presented and discussed. Following this, new empirical formulae for both vertical and sloping structures fronted by shallow foreshores are derived and compared to existing approaches. Section 4.4 concludes the paper by addressing the overall research objective, stating limitations and identifying areas for future work.



## 4.1 INTRODUCTION

### 4.1.1 BACKGROUND

Coastal engineers rely on empirical formulae to predict the volume of water that passes over the crest of coastal structures due to wave action during storms. This process, known as wave overtopping, can result in damage to critical infrastructure and even loss of life. Despite recent studies which suggest that the flow properties of individual overtopping events are equally important (Altomare et al., 2020a, Sandoval and Bruce, 2018, Suzuki et al., 2020), coastal structures worldwide are typically designed to resist a mean overtopping discharge per meter width of structure, $q$ ($m^3/s$ or l/s per m)—which is often estimated using empirical formulae, in practice.

The state-of-the-art empirical models for wave overtopping of sloping structures (EurOtop, 2018), including that of Altomare et al. (2016) and Van Gent (1999) developed specifically for shallow foreshores, typically require wave parameters at the toe of the structure as input—namely significant wave height ($H_{m0,toe}$) and spectral wave period ($T_{m-1,0,toe}$). The general assumption is that if the wave heights and periods at the toe are known, then the influence of directional spreading (Altomare et al., 2020b), local wind and the foreshore—irregular or uniform—on wave characteristics is already accounted for. However, one major drawback is that for very shallow conditions—with heavy wave breaking—obtaining accurate estimates at the toe typically requires either physical model tests or high-resolution numerical models capable of capturing the nonlinear effects of wave transformation over the foreshore (Mase et al., 2013).

In addition to a rise in mean water level known as wave-induced (static) setup ($\bar{\eta}$), the shoaling and subsequent breaking of incident wind-sea and swell (SS) waves result in the generation and release of much longer waves, referred to as infragravity (IG) waves (or dynamic setup). These waves with periods exceeding 25 s not only contribute to $H_{m0,toe}$ but also result in higher values of $T_{m-1,0,toe}$ (Hofland et al., 2017). Lashley et al. (2020b) showed that the relative magnitude of IG waves at the structure is largely dependent on the foreshore slope ($\tan m$) and the ratio of initial water depth at the toe to the offshore wave height ($h_{toe}/H_{m0,deep}$), with a large amount of IG-wave energy expected under very shallow

conditions ($0.3 < h_{toe}/H_{m0,deep} < 1$) and IG-wave dominance expected under extremely shallow conditions ($h_{toe}/H_{m0,deep} < 0.3$)—as defined by Hofland et al. (2017). Therefore, any numerical model applied to such shallow-water conditions must be capable of resolving both SS and IG-wave motions. This means that the typical approach of using spectral wave models (e.g. SWAN) is no longer valid and that more computationally-demanding, phase-resolving models are required (e.g. SWASH, XBeach or BOSZ) (Chapter 3 (Lashley et al., 2020a)).

Noting these challenges, Mase et al. (2013) developed a set of unified run-up and overtopping formulae, recently improved by Yuhi et al. (2020), for sloping structures under very shallow conditions with the deep-water wave height ($H_{m0,deep}$ [m]) and deep-water peak period ($T_p$ [s]) as main input. However, the approach has two notable drawbacks: firstly, the formulae directly relate wave overtopping to wave run-up. While this is physically justified, it requires the user to first accurately estimate wave run-up before estimating $q$. Secondly, the formulae are highly sensitive to the estimated water depth at the onset of wave breaking—which may vary depending on the wave transformation model or method used to estimate it. In light of this, Tamada et al. (2015) proposed a set of formulae to estimate the water depth at the onset of breaking, which were empirically derived with numerical model tests using a hybrid frequency-domain KdV equation developed by Mase and Kirby (1993).

For vertical structures fronted by very shallow foreshores, the design diagrams of Goda et al. (1975)—which use "equivalent" deep-water wave parameters—are considered the technical standard for the design of port and harbour facilities in Japan. Ultimately, the drawn curves were the combined result of: a basic equation of wave overtopping (Goda, 1970); a wave deformation model for random waves; and engineering judgement, considering the effects of wave setup and IG waves (Goda et al., 1975). As a result, no empirical formula was developed to match the drawn curves. The significant advantage of this approach is that no additional wave transformation model (numerical or empirical) is required and the foreshore's influence is directly taken into account by its relative water depth and slope—which is assumed to be uniform. This uniform slope in the method is a drawback compared to the EurOtop (2018) method. While this approach is widely-recognized and respected, graphical methods are typically more time-consuming, susceptible to human error and difficult to automate for large-scale application than formulae. In light of this, a set of semi-theoretical formulae which approximate the Goda et al. (1975) design diagrams, proposed by Takayama et al. (1982), is sometimes applied in Japan.

In the present study, we aim to resolve these challenges by establishing empirical overtopping formulae for both vertical and sloping structures with very shallow foreshores ($h_{toe}/H_{m0,deep} \leq 1$); formulae which are based entirely on deep-water characteristics and therefore do not require the use of any additional empirical or numerical models. This is

achieved by revisiting the approach of Goda et al. (1975) which suggests that $q$ can be accurately modelled as a function of relative water depth ($h_{toe}/H_{m0,deep}$), foreshore slope ($m$ [°]) and deep-water wave steepness ($s_{op}$ [-]).



## 4.2 METHODS

### 4.2.1 EXISTING EMPIRICAL METHODS FOR VERY SHALLOW WATER

#### *4.2.1.1 Goda's Empirical Wave Model*

Goda et al. (1975) applied the following empirical expression to estimate the amplitude of IG waves (surfbeat)—also referred to as dynamic wave setup—within the surf zone ($\zeta_{rms}$ [m]). This expression corresponds to Equation 3.24 in Goda (2000), published as the book's second edition. It should be noted that the first edition was published in Goda (1985) and the third edition later in Goda (2010):

$$\zeta_{rms} = \frac{0.01 \cdot H_{m0,deep}}{\sqrt{s_{op}\left(1 + \frac{h_{toe}}{H_{m0,deep}}\right)}}. \tag{4.1}$$

In Japanese research, reference is often made to an equivalent deep-water wave ($H_0'$ [m]) to describe deep-water waves which have been adjusted to account for the effects of refraction, diffraction and other transformations—excluding wave shoaling and breaking (Goda, 2000). In the present study, considering 1D numerical and physical model tests with long-crested waves, $H_0'$ and $H_{m0,deep}$ are considered to be the same quantity.

Here, we assume that the IG wave height is twice the IG wave amplitude and thus,

$$H_{m0,IG} = \sqrt{2} \cdot 2 \cdot \zeta_{rms}\,. \tag{4.2}$$

Note that $\sqrt{2}$ is used to convert the root-mean-square wave height to the significant wave height. Despite it being a significant advancement at that time—with the original work published in Goda (1975a)—Goda (2000) acknowledged that Equation 4.1 was an engineering estimate and expected that future random-wave-breaking models would directly include the effects of IG waves for more accurate and rational predictions in the surf and swash zones.

While other random-wave transformation models at the time completely neglected the influence of IG waves (Battjes and Stive, 1985, Dally, 1992). Goda (1975b)—and later Goda (2000)—was able to account for the effects of IG waves on SS-wave transformation in the surf zone, assessed as the change in $H_{1/3}$ [m], by expressing the IG waves as an increase in the local water depth by $\zeta_{rms}$ (Equation 4.1) which, in turn, controls the breaker height:

$$H_{\frac{1}{3}} =$$

$$\begin{cases} K_s \cdot H_{m0,deep} : \dfrac{h_{toe}}{L_0} \geq 0.2 \\ \min\left\{\left(\beta_0 \cdot H_{m0,deep} + \beta_{max} \cdot h_{toe}\right), \beta_{max} \cdot H_{m0,deep}, K_s \cdot H_{m0,deep}\right\} : \dfrac{h_{toe}}{L_0} < 0.2 \end{cases} \quad (4.3)$$



where $H_{1/3}$ is considered the mean of the highest one-third of SS waves; $K_s$ [-] is the shoaling coefficient and,

$$\beta_0 = 0.028 \cdot {s_{op}}^{-0.38} \exp(20 \cdot \tan(m)^{1.5}) , \quad (4.4)$$

$$\beta_1 = 0.52 \cdot \exp(4.2 \cdot \tan(m)) , \quad (4.5)$$

and

$$\beta_{max} = \max\{0.92, 0.32 \cdot {s_{op}}^{-0.29} \cdot exp(2.4\, tan(m))\}. \quad (4.6)$$

Note that Equation 4.3 corresponds to Equation 3.25 in Goda (2000). It is also worth noting that while Goda (2000) looked at $H_{1/3}$—obtained using a zero-crossing analysis of the surface elevation time series—we focus on $H_{m0}$—obtained using spectral analysis—in the present study. In deep-water, $H_{1/3} \approx H_{m0}$ when wave refraction and diffraction are negligible; however, the two quantities can differ significantly for breaking waves in the surf zone. Our choice to focus on $H_{m0}$ here is consistent with the current European standard (EurOtop, 2018) and is based on the fact that most operational forecast models provide $H_{m0}$ as output.

#### *4.2.1.2 Wave Overtopping*

In general, there are two approaches to estimating wave overtopping. The first, which is adopted by EurOtop (2018) for sloping structures, uses wave parameters at the toe of the structure as input. The second approach—proposed by Goda et al. (1975)—uses deep-water parameters to estimate $q$. In this approach, the effects of the foreshore are represented by two foreshore parameters: $h_{toe}/H_{m0,deep}$ and $m$.

##### 4.2.1.2.1 EurOtop (2018) Approach

EurOtop (2018), with the work of Van Gent (1999) and Altomare et al. (2016) for sloping structures in shallow water, makes use of the following formulae:

$$\frac{q}{\sqrt{g \cdot {H_{m0,toe}}^3}} = 0.16 \cdot \exp\left(-\frac{R_c}{H_{m0,toe}} \cdot \frac{1}{\left(0.33 + 0.022 \cdot \xi_{m-1,0}\right)}\right), \quad (4.7)$$

where $R_c$ is the crest freeboard and $\xi_{m,-1,0}$ is the breaker parameter. For shallow foreshores with $h_{toe}/H_{m0,deep} < 1$,

$$\xi_{m,-1,0} = \frac{\tan(\delta)}{\sqrt{s_{om-1,0}}}, \tag{4.8}$$

where $s_{om-1,0} = H_{m0,toe}/L_{m-1,0}$ and,



$$L_{m-1,0} = \frac{g \cdot T_{m-1,0,toe}{}^2}{2\pi}. \tag{4.9}$$

For cases where $T_{m-1,0,toe}$ is unknown, it may be estimated by its deep-water equivalent using the empirical formulae of Hofland et al. (2017).

The "equivalent slope" ($\delta$ [-]), used to calculate the breaker parameter, $\xi_{m-1,0}$ [-], is given by:

$$\tan(\delta) = \frac{1.5 \cdot H_{m0,toe} + R_{u2\%}}{\left(1.5 \cdot H_{m0,toe} - h_{toe}\right) \cdot \cot(m) + \left(h_{toe} + R_{u2\%}\right) \cdot \cot(\alpha)}, \tag{4.10}$$

where $\alpha$ is the structure slope and,

$$\frac{R_{u2\%}}{H_{m0,toe}} = 4 - \frac{1.5}{\sqrt{\xi_{m-1,0}}}. \tag{4.11}$$

Note that $\xi_{m-1,0}$ and $R_{u2\%}$ [m] must also be obtained iteratively (until $R_{u2\%}$ converges), with a first estimate of $R_{u2\%} = 1.5 \cdot H_{m0,toe}$. It should also be noted that the data used by Altomare et al. (2016) and Hofland et al. (2017) were mainly based on foreshores with very mild slopes ($m$ ranging from 1:250 to 1:35). Therefore, the applicability of Equations 4.7 to 4.11 to steeper slopes is yet to be confirmed.

#### *4.2.1.3 Goda et al. (1975) Approach*

Goda et al. (1975) developed design diagrams (Figures 28 and 29 in Goda et al. (1975)) for smooth vertical walls (without roughness elements) and walls covered with sloping rubble-mound (made of armour blocks) with steep foreshores ($m$ = 1:10 and 1:30), which were later published as Figures 5.1, 5.2, 5.4 and 5.5 in Goda (2000). These design diagrams were based on Equation 4.12:

$$\frac{q}{\sqrt{2 \cdot g \cdot H_{m0,deep}{}^3}} = \mathrm{f}\left(\frac{h_{toe}}{H_{m0,deep}}, \frac{R_c}{H_{m0,deep}}, s_{op}, m\right). \tag{4.12}$$

In the present study, we focus on the smooth structures under very shallow conditions; therefore, we focus on the diagrams developed for vertical walls with $h_{toe}/H_{m0,deep} < 1$. Note that digitized sections of the Goda et al. (1975) design diagrams are shown in Figure 4.7 and Figure 4.8 as part of the analysis (Section 4.3.2.1).

### 4.2.2 DESCRIPTION OF DATASETS

A comprehensive collection of physical and numerical model datasets with different foreshore slopes, structure slopes, offshore wave conditions and relative water depths were

considered in this study. Datasets with measurements both offshore and at the structure toe were used to assess the influence of the foreshore on incident wave conditions; while datasets with overtopping measurements for normally incident waves over smooth sloping or vertical structures that met the criteria for very shallow conditions ($h_{toe}/H_{m0,deep} \leq 1$) were used in the development of new overtopping formulae.

The reference, identifier (ID), number of tests and range of parameters for each dataset is provided in Table 4.1, Table 4.2 and Table 4.3. Each of the selected datasets followed Figure 4.1, in terms of layout, with uniformly sloping foreshore slopes under irregular, long-crested and shore-normal wave attack. Rather than provide a lengthy and exhaustive description here, we focus on two datasets: i) the Goda et al. (1975) dataset (DS-802)—which makes up the bulk of the available vertical wall data; and ii) the Lashley et al. (2020b) dataset (XB) developed in Chapter 2—which, unlike the others, is comprised of purely numerical model results. For detailed descriptions of the other datasets, the reader is pointed to the references listed in Table 4.1, Table 4.2 and Table 4.3 for the details related to each individual test set up. The datasets with an ID prefix "DS" refer to tests obtained from the CLASH-project (Crest Level Assessment of Coastal structures by full scale monitoring, neural network prediction and Hazard Analysis on permissible wave overtopping) database, see also EurOtop (2007) and EurOtop (2018). Note that some of the tests within the CLASH database were listed as confidential, therefore no references for these tests were available. Additionally, it should be noted that 1:1000 foreshore slope in the CLASH database refers to a completely flat foreshore in reality.

**Table 4.1.** *Summary of parameter ranges for the datasets used to assess the effect of the foreshore on incident waves.*

| Reference | ID | No. tests | $s_{m-1,0}$ | $\frac{h_{toe}}{H_{m0,deep}}$ | $\cot(m)$ |
|---|---|---|---|---|---|
| - | Sal | 13 | 0.018-0.039 | 1.53-5.19 | 30 |
| (Smith et al., 2003) | Smith | 114 | 0.017-0.052 | 0.36-5.96 | 30; 100 |
| (Lashley et al., 2020b) | XB | 384 | 0.006-0.041 | 0.05-5 | 10; 25; 50; 100; 250; 500; 1000 |
| (Coates et al., 1997) | HR | 161 | 0.008-0.058 | 0.46-4.63 | 10; 20; 30; 50 |
| - | DS-005 | 15 | 0.016-0.028 | 1.4-1.67 | 100 |
| - | DS-111 | 81 | 0.002-0.036 | 1.27-5.08 | 50 |
| (Van der Meer and De Waal, 1993) | DS-221 | 148 | 0.011-0.059 | 0.97-6.87 | 100; flat |
| - | DS-307 | 18 | 0.042-0.043 | 0.98-2.28 | 250 |
| - | DS-330 | 12 | 0.046-0.062 | 1.87-3.38 | 100 |
| (Pullen and Allsop, 2004) | DS-509 | 18 | 0.048-0.09 | 1.08-1.60 | 50 |
| - | DS-916 | 47 | 0.015-0.048 | 1.34-2.65 | 30 |

It is important to note that by using datasets collected from different facilities around the world, additional differences may arise due to model effects and different measurement techniques. Therefore, a certain degree of spread in the compiled dataset is to be expected and accepted as inherent in the approach taken.



**Table 4.2.** *Summary of parameter ranges for the datasets used to assess the effect of the foreshore on incident waves and wave overtopping for sloping structures. The number of tests with $h_{toe}/H_{m0,deep} \leq 0.1$ is parenthesised.*

| Reference | ID | No. tests | $s_{om-1,0}$ | $\frac{h_{toe}}{H_{m0,deep}}$ | $\cot m$ | $\cot \alpha$ | $\frac{R_c}{H_{m0,deep}}$ |
|---|---|---|---|---|---|---|---|
| (Altomare et al., 2016) | 13-116 | 90 (60) | 0.015-0.063 | -0.06-0.22 | 35 | 3 | 0.40-0.82 |
| | 00-025 | 21 (17) | 0.039-0.041 | -0.14-0.25 | 35 | 2 | 0.24-0.67 |
| | 00-142 | 17 | 0.013-0.036 | 0.25-0.5 | 35 | 3 | 0.22-0.52 |
| | 13-168 | 42 (15) | 0.007-0.018 | 0 - 0.86 | 50 | 2 | 0.26-2.55 |
| (Goda, 2009, Tamada et al., 2002) | Tam | 198 (37) | 0.019-0.049 | 0-0.71 | 10; 30 | 3; 5; 7 | 0.31-1.50 |
| (Van Gent, 1999) | DS-226 | 97 | 0.018-0.053 | 0.32 -2.56 | 100; 250 | 2.5; 4 | 1.1 -2.9 |

**Table 4.3**. *Summary of parameter ranges for the datasets used to assess wave overtopping for vertical structures. The number of tests with $h_{toe}/H_{m0,deep} \leq 0.1$ is parenthesised.*

| Reference | ID | No. tests | $s_{om-1,0}$ | $\frac{h_{toe}}{H_{m0,deep}}$ | $\cot m$ | $\frac{R_c}{H_{m0,deep}}$ |
|---|---|---|---|---|---|---|
| (Goda et al., 1975) | DS-802 | 127 (44) | 0.005-0.044 | -0.75-1 | 10; 30 | 0.40-1.92 |
| (Herbert, 1993) | DS-028 | 24 | 0.018-0.049 | 0.49-0.97 | 10; 100 | 0.48-2.07 |
| (Bruce et al., 2002) | VOWS | 10 | 0.027-0.072 | 0.81-0.99 | 10; 50 | 0.76-1.65 |

#### *4.2.2.1 Goda et al. (1975) Dataset*

Goda et al. (1975) carried out a series of experiments in 1973 and 1974 with irregular waves (Bretschneider-Mitsuyasu type spectrum), with $H_{1/3}$ = 0.15 m and $T_{1/3}$ = 1.7, 2.3 and 2.8 s, overtopping a vertical structure fronted by 1:10 and 1:30 sloping foreshores. Incident wave heights were estimated with a technique to resolve incident and reflected waves using two simultaneous wave records. The overtopping rate was obtained as the average of three measurements, each for two hundred waves.

The original dataset comprised consisted of 205 tests with conditions at the toe varying from shallow to emergent, where the toe of the structure was initially dry ($h_{toe} \leq 0$). Here, we analyse a subset of these tests with $h_{toe}/H_{m0,deep} \leq 1$ (DS-802, Table 4.3).

Goda et al. (1975) noted that during the physical tests the amplitude of the IG waves (estimated at the time using Equation 4.1) and the level of wave-induced setup were higher than typically observed at a real coast. This was attributed to the re-reflection of waves between the vertical wall and the wave generation paddle, the magnitude of which varied depending on $\tan m$ and $h_{toe}/H_{m0,deep}$. This modification was based on engineering judgement, not measurements.

To compensate for this, Goda et al. (1975) increased the measured $h_{toe}$—and by relation reduced $R_c$—by the values shown in Table 4.4 based on engineering judgement, not measurements. These corrected values were then used to derive the design diagrams presented in Goda (2000) which have since been adopted in the technical standard for the design of port and harbour facilities in Japan. To be consistent with this analysis, we have applied the same correction to the original data here.

**Table 4.4.** *Correction to $h_{toe}$ and $R_c$ in cm as proposed by Goda et al. (1975).*

<table>
<tr><td></td><td colspan="3">tan(m) = 1/30</td><td colspan="3">tan(m) = 1/10</td></tr>
<tr><td>$h_{toe}$ (cm)</td><td>$T_{1/3}$ = 1.7 s</td><td>$T_{1/3}$ = 2.3 s</td><td>$T_{1/3}$ = 2.8 s</td><td>$T_{1/3}$ = 1.7 s</td><td>$T_{1/3}$ = 2.3 s</td><td>$T_{1/3}$ = 2.8 s</td></tr>
<tr><td>22.5</td><td colspan="3" rowspan="4">1.5</td><td colspan="3" rowspan="3">1.5</td></tr>
<tr><td>15.0</td></tr>
<tr><td>10</td></tr>
<tr><td>5</td><td>1.5</td><td>2</td><td>2</td></tr>
<tr><td>0</td><td rowspan="2">2</td><td colspan="2" rowspan="2">2.5</td></tr>
<tr><td>-5</td><td colspan="3">1.5</td></tr>
<tr><td>-10</td><td>-</td><td>-</td><td>-</td><td></td><td></td><td></td></tr>
</table>

### *4.2.2.2 Lashley et al. (2020b) Dataset*

After verifying the numerical model's ability to accurately simulate wave transformation under very shallow conditions, Lashley et al. (2020b) (Chapter 2) carried out 672 simulations in prototype scale—using the XBeach non-hydrostatic numerical model (Kingsday release)—of irregular waves (JONSWAP-type with peak enhancement factor of 3.3) propagating over an idealized structure-foreshore profile (Figure 4.1). In these simulations, $H_{m0,deep}$, $T_p$, wave directional spreading, $h_{toe}$, $m$, bottom friction, width of vegetated cover and structure slope ($\alpha$) were systematically varied, following a one-[factor]-at-a-time (OAT approach). In the present study, we analyse part of this dataset, without the influence of vegetation, directional spreading, bottom friction or wave reflection (i.e. with the structure removed). In each simulation, $H_{m0,toe}$, $T_{m-1,0,toe}$, wave-induced setup at the structure toe ($\bar{\eta}$)

and the relative magnitude of the IG waves, defined as the ratio of IG to sea and swell waves at the structure toe ($H_{m0,IG,toe}$ /$H_{m0,SS,toe}$) were assessed.

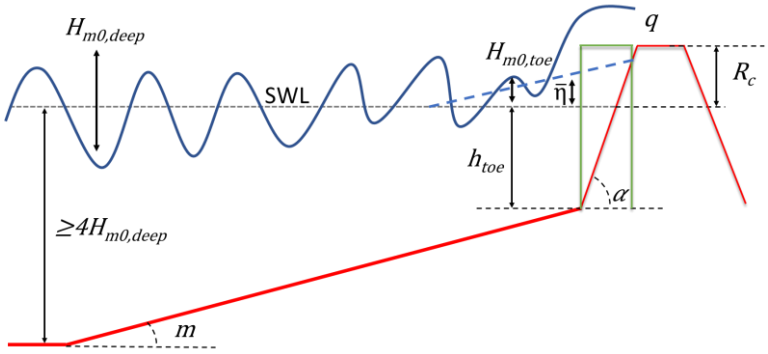


**Figure 4.1.** *Schematic vertical (green) and sloping structures with very shallow foreshores, highlighting key variables.*

In each simulation, the offshore water depth was set to 4 times $H_{m0,deep}$, in line with the definition of deep water proposed by Hofland et al. (2017). The numerical model was configured such that the numerical parameter governing the maximum breaking wave steepness was set to 0.5; a smooth flume bottom was represented using a Manning roughness coefficient of 0.012 s/m$^{1/3}$; and a cross-shore grid spacing varying from a maximum of 100 grid cells per deep-water wavelength (offshore) to 1 m at the toe.

### 4.2.3 PERFORMANCE METRICS

In order to assess the performance of the empirical model for relative wave height at the toe ($H_{m0,toe}/H_{m0,deep}$), the Scatter Index ($SCI$) objective function was applied as a normalized measure of error (Equation 10):

$$SCI_{\Psi} = \frac{\sqrt{\frac{1}{n}\sum_{i=1}^{N}\left(\Psi_{pred}^{i} - \Psi_{meas}^{i}\right)^{2}}}{\frac{1}{n}\sum_{i=1}^{N}\Psi_{meas}^{i}}, \tag{4.13}$$

where $\Psi$ represents $H_{m0,toe}/H_{m0,deep}$, in a sample size $N$; and subscripts $pred$ and $meas$ refer to the empirical predictions and measurements, respectively. Lower $SCI$ values (< 0.2) indicate accurate model predictions.

Following Altomare et al. (2016), the geometric mean ($\bar{x}_G$ [-]) is applied assess the accuracy of the overtopping formulae:

$$\bar{x}_G = \exp\left[\frac{1}{N}\sum_{i=1}^{N} \ln x_i\right], \tag{4.14}$$

with $x_i = q_{pred,i}/q_{meas,i}$, where N is the number of data points, $q_{pred,i}$ and $q_{meas,i}$ are the $i$th modelled (empirically) and observed mean overtopping discharges, respectively. An $\bar{x}_G$ value of 1 indicates no bias, while values greater than and less than 1 indicate tendencies to over- and underestimate $q$, respectively. Similarly, the geometric standard deviation associated with the mean is applied to assess the level of scatter– and general accuracy—of the empirical formulae:

$$\sigma(\bar{x}_G) = \exp\left\{\left[\frac{1}{N}\sum_{i=1}^{N} ((\ln x_i)^2 - (\ln \bar{x}_G)^2)\right]^{0.5}\right\}. \tag{4.15}$$

If the data is assumed to be normally distributed, 90 % of the data will fall within 1.65 standard deviations, with lower bound, $\bar{x}_G \cdot [\sigma(\bar{x}_G)^{-1.65}]$ and the upper bound, $\bar{x}_G \cdot [\sigma(\bar{x}_G)^{1.65}]$.

## 4.3 RESULTS AND DISCUSSIONS

### 4.3.1 FORESHORE EFFECT ON NEARSHORE CONDITIONS

In order to establish accurate wave overtopping formulae based on deep-water wave characteristics, the effects of shallow foreshores on wave conditions at the toe of the structure need to be accurately parameterised. In this section, we demonstrate that the foreshore effects on nearshore conditions can be accurately modelled as functions of $h_{toe}/H_{m0,deep}$, $\tan m$ and $s_{om-1,0}$. The nearshore processes considered are namely: i) the change in significant wave height due to shoaling and breaking; ii) the increase in static and dynamic wave setup (i.e. the magnitude of IG waves).

#### *4.3.1.1 Significant Wave Height*

Under very shallow conditions ($h_{toe}/H_{m0,deep} \leq 1$) two trends in Figure 4.2 become evident: i) $H_{m0,toe}/H_{m0,deep}$ decreases linearly as $h_{toe}/H_{m0,deep}$ decreases; and ii) $H_{m0,toe}/H_{m0,deep}$ increases as $\cot(m)$ becomes steeper (visible by the marker colours in Figure 4.2). The area where $1 < h_{toe}/H_{m0,deep} \leq 1.5$ appears to be a transition region where the foreshore—represented by $h_{toe}/H_{m0,deep}$ and $\tan(m)$—shows a minor influence on $H_{m0,toe}/H_{m0,deep}$.

In addition, Figure 4.3 indicates that the influence of the deep-water wave steepness ($s_{om-1,0}$) on $H_{m0,toe}/H_{m0,deep}$ decreases as $h_{toe}/H_{m0,deep}$ decreases, made evident by the reduced scatter at lower $h_{toe}/H_{m0,deep}$ values. Note that $s_{om-1,0}$ is used here in place of $s_{op}$ in accordance with the current standard, where $T_{m-1,0}$ is used in place of $T_p$ or $T_{1/3}$ (EurOtop, 2018); for conversion we take $T_{m-1,0} = T_p/1.1$ .

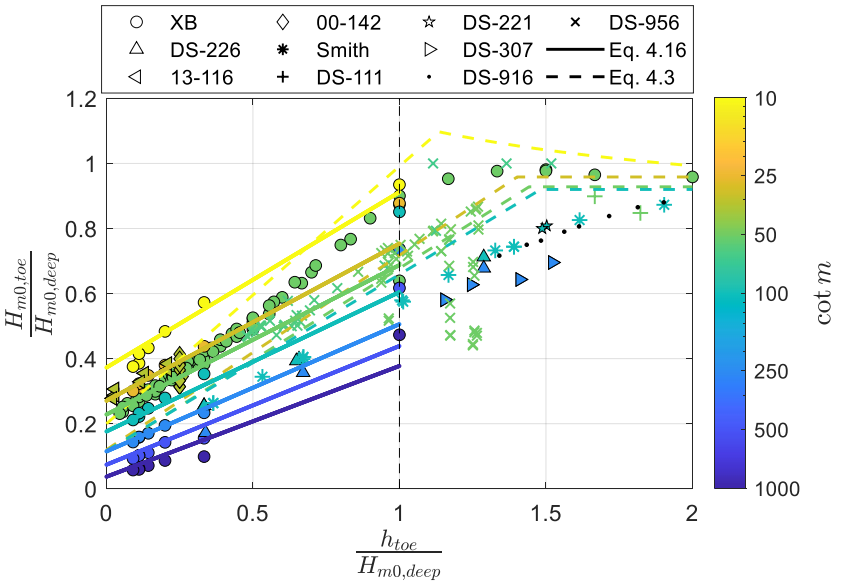


**Figure 4.2.** *Variation in relative wave height at the toe ($H_{m0,toe}$ /$H_{m0,deep}$) with relative water depth at the toe ($h_{toe}$ /$H_{m0,deep}$) and foreshore slope ($cot(m)$) (see colorscale) for data with 0.030 < wave steepness ($s_{om-1,0}$)< 0.042. Solid and dashed lines represent Equation 4.16 and 4.3, respectively, for $s_{om-1,0}$ = 0.036.*

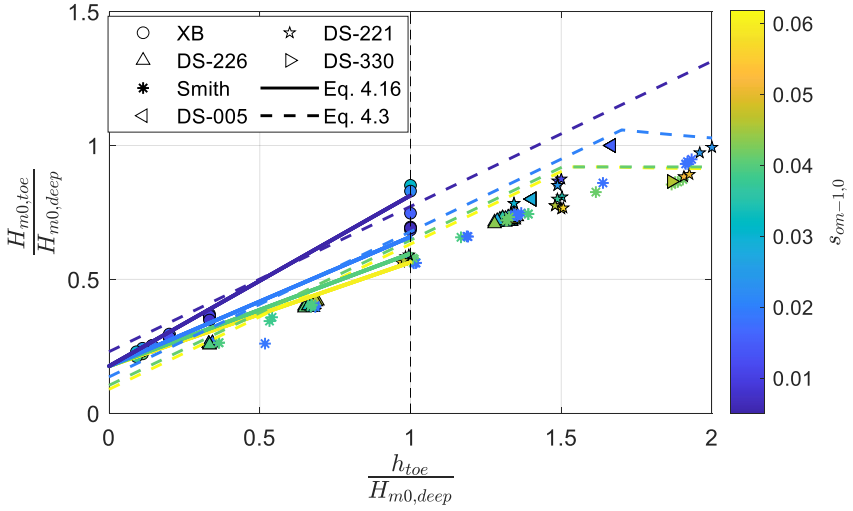


**Figure 4.3.** *Variation in relative wave height at the toe ($H_{m0,toe}$ /$H_{m0,deep}$) with relative water depth ($h_{toe}$ /$H_{m0,deep}$) and wave steepness ($s_{om-1,0}$) (see colorscale) for data with foreshore slope ($cot(m)$) = 100. Solid lines represent Equation 4.16.*

For conditions where $h_{toe}/H_{m0,deep} \leq 1$, the following expression holds with $R^2$ = 0.84 and $SCI$ = 0.18 (Figure 4.4):

$$\frac{H_{m0,toe}}{H_{m0,deep}} = M \cdot \frac{h_{toe}}{H_{m0,deep}} + C \tag{4.16}$$



where,

$$M = 0.35 \cdot \frac{\tan(m)^{0.10}}{s_{om-1,0}{}^{0.20}} \tag{4.17}$$

and,

$$C = 0.95 \cdot \tan(m)^{0.15} - 0.30 \tag{4.18}$$

Equations 4.16 to 4.18 were derived based on the observed linear relationship between $H_{m0,toe}/H_{m0,deep}$ and $h_{toe}/H_{m0,deep}$ where the slope ($M$[-]) and intercept ($C$ [-]) of the relationship are dependent on $\tan(m)$ and $s_{om-1,0}$. The exponents of each term were then obtained using a trial-and-error approach to minimize scatter in the data (Table 4.1). It should be highlighted that $H_{m0,toe}/H_{m0,deep} \neq 0$ when $h_{toe}/H_{m0,deep}$ = 0 due to the influence of static and dynamic setup (IG waves), discussed in Section 4.3.1.2 and also highlighted by Goda (2000). However, experience suggests that care should be taken for cases with $h_{toe}/H_{m0,deep}$ = 0, as the bed may intermittently become dry resulting in an inconsistent time series and inaccurate estimates of $H_{m0,toe}$.

As noted in Section 4.2.2, some scatter in Figure 4.4 is to be expected due to model effects and differences in measurement techniques between datasets. In particular, the low frequency cut-off used to calculate $H_{m0}$ could significantly influence results under very shallow conditions where IG waves dominate.

Through Equation 4.16, the wave height at the structure may be estimated using parameters that are usually either known or estimated without difficulty: the offshore wave height, offshore steepness, foreshore slope and relative water depth at the structure toe. This is also directly in line with the work of Hofland et al. (2017) who showed that the relative wave period at the toe ($T_{m-1,0,toe}/T_{m-1,0,deep}$) can be empirically modelled, with reasonable accuracy, as a function of $h_{toe}/H_{m0,deep}$ and $\tan(m)$. The main disadvantage of such an empirical approach, is the assumption of a straight (uniform) foreshore slope. However, this disadvantage is seen as minor compared to the use of numerical models that do not include IG waves in very shallow water, e.g. SWAN.

Given the differences in the approach of Goda (2000)—namely the use of $H_{1/3}$ and not $H_{m0}$; and the treatment of the IG waves as an increase in mean water level versus directly including

them in the wave height estimate, as done here—our comparison of Equations 4.3 and 4.16 is purely qualitative. Both equations capture the linear relationship between $h_{toe}/H_{m0,deep}$ and $H_{m0,toe}/H_{m0,deep}$ and the increase in $H_{m0,toe}/H_{m0,deep}$ with steeper slopes. The main difference between the two approaches is the treatment of the deep-water wave steepness ($s_{om-1,0}$). Equation 4.3 shows parallel lines for different values of $s_{om-1,0}$ while Equation 4.16 converges as $h_{toe}/H_{m0,deep}$ decreases (Figure 4.3). This convergence was observed in the data (Figure 4.3) and is due to the depth-limited nature of shallow water waves. That is, as the water depth becomes shallower, the influence of $s_{om-1,0}$ decreases and the magnitude of $H_{m0,toe}$ is now governed by $h_{toe}$.

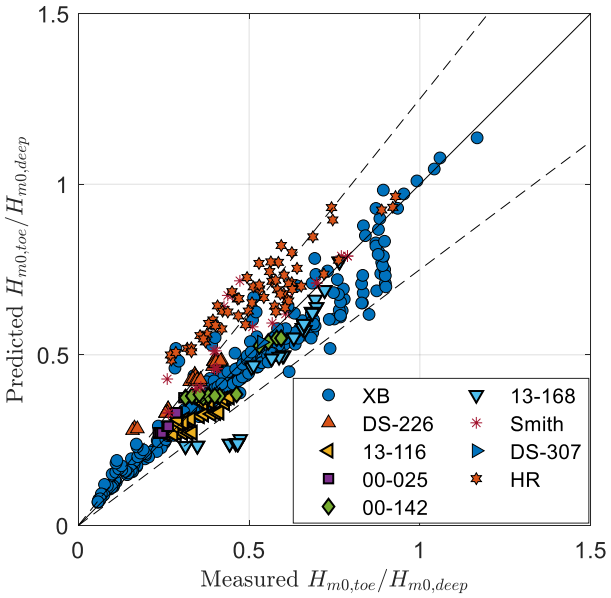


**Figure 4.4.** *Predicted (using Equation 4.16) versus measured $H_{m0,toe}/H_{m0,deep}$ for data (Table 4.1 and Table 4.2) with $h_{toe}/H_{m0,deep} \leq 1$. Solid line indicates perfect agreement. Dashed lines indicate +/- 25% error.*

Given the differences in the approach of Goda (2000)—namely the use of $H_{1/3}$ and not $H_{m0}$; and the treatment of the IG waves as an increase in mean water level versus directly including them in the wave height estimate, as done here—our comparison of Equations 4.3 and 4.16 is purely qualitative. Both equations capture the linear relationship between $h_{toe}/H_{m0,deep}$ and $H_{m0,toe}/H_{m0,deep}$ and the increase in $H_{m0,toe}/H_{m0,deep}$ with steeper slopes. The main difference between the two approaches is the treatment of the deep-water wave steepness ($s_{om-1,0}$). Equation 4.3 shows parallel lines for different values of $s_{om-1,0}$ while Equation 4.16 converges as $h_{toe}/H_{m0,deep}$ decreases (Figure 4.3). This convergence was observed in the data (Figure 4.3) and is due to the depth-limited nature of shallow water waves. That is,

as the water depth becomes shallower, the influence of $s_{om-1,0}$ decreases and the magnitude of $H_{m0,toe}$ is now governed by $h_{toe}$.

The observed convergence is also supported by *linear wave theory* which states that waves become less (frequency) dispersive as the water depth becomes shallower—that is, the influence of the wave period (and by extension $s_{om-1,0}$) on nearshore wave conditions decreases as $h_{toe}/H_{m0,deep}$ decreases. This is also made evident in Figure 4.5 by the decrease in scatter with shallower water depths. Of particular note is the correspondence between $h_{toe}/H_{m0,deep} \leq 1$ and the definition of shallow water according to linear wave theory, where the ratio of the local water depth to wavelength ($h_{toe}/L_{toe}$) < 1/20 (Figure 4.5); and $L_{toe}$ is obtained by solving the well-known dispersion relationship.



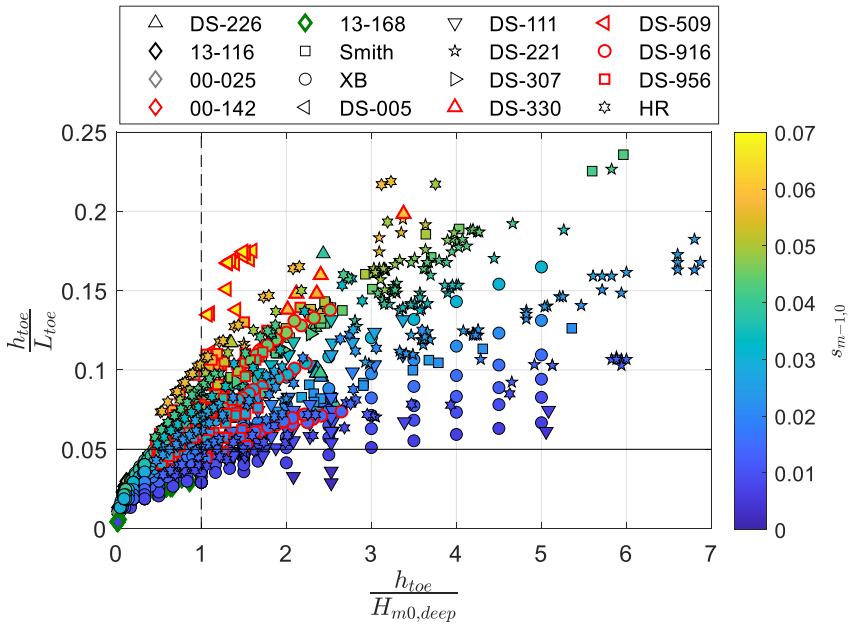


**Figure 4.5.** *Variation in ratio of local water depth to local wavelength—obtained by solving the well-known dispersion relationship—with relative water depth. Horizontal line indicates the transition to "shallow water" according to linear wave theory. Dashed vertical line indicates transition to very shallow conditions ($h_{toe}/H_{m0,deep}$ = 1) according to Hofland et al. (2017).*

#### *4.3.1.2 Static and Dynamic Wave Setup*

In addition to the relative wave height and period at the toe, $h_{toe}/H_{m0,deep}$ and $\tan(m)$ serve as descriptors for both the magnitude of relative (static) wave setup ($\bar{\eta}\ /H_{m0,deep}$, Figure 4.6a) and the dynamic wave setup—represented by the relative magnitude of the IG waves at the toe ($H_{m0,IG,toe}\ /H_{m0,SS,toe}$, Figure 4.6b)—generated due to SS waves shoaling and breaking over the foreshore. Furthermore, both quantities appear to reach their maximum as

$h_{toe}/H_{m0,deep}$ approaches zero (Figure 4.6). The trend in $\bar{\eta}/H_{m0,deep}$ is also supported by the work of Goda (2000) which was obtained by digitizing and interpolating between the curves of Figure 3.25 of the same reference; though, the XBeach predictions are consistently lower than that of Goda (2000). These differences are likely due to the definition of $\bar{\eta}$: Goda (2000) refers to $\bar{\eta}$ at the shoreline, i.e. the mean water level in the swash zone (where $\bar{\eta}$ reaches its maximum); while the XBeach estimates of $\bar{\eta}$ were taken in the surf zone (Lashley et al., 2020b).

As Equation 4.1 does not consider the influence of the foreshore slope, it is more valuable to assess the best-fit trend of $H_{m0,IG,toe}$—predicted using Equations 4.1 and 4.2—normalised by $H_{m0,SS,toe}$ (predicted by XBeach). Remarkably, the best-fit trend of Equations 4.1 and 4.2 agrees well with the XBeach model results (Figure 4.6b).

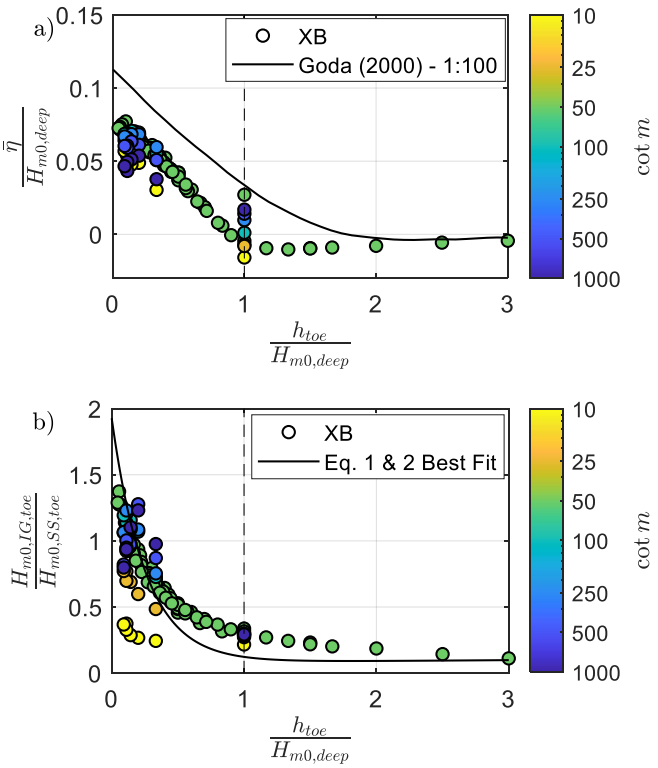


**Figure 4.6.** *Variation in: a) relative wave setup ($\bar{\eta}/H_{m0,deep}$) and b) relative magnitude of infragravity waves ($H_{m0,IG,toe}/H_{m0,SS,toe}$) with relative water depth ($h_{toe}/H_{m0,deep}$) and foreshore slope ($cot(m)$), for data with 0.030 < wave steepness ($s_{om-1,0}$)< 0.042; as modelled numerically using XBeach Nonhydrostatic. Solid line in panel 'a' is based on $s_{om-1,0}$= 0.036.*

One important takeaway, is that the influence of the foreshore only becomes significant once $h_{toe}/H_{m0,deep} \leq 1$; that is, all of the nearshore processes considered here: change in wave height (Figure 4.2 and Figure 4.3), change in wave period (Hofland et al., 2017), wave setup (Figure 4.6a) and shift in energy to low frequencies (Figure 4.6b), show high correlations with $h_{toe}/H_{m0,deep}$ and $\tan m$ when $h_{toe}/H_{m0,deep} \leq 1$. So, in short, if $h_{toe}/H_{m0,deep} > 1$, then the foreshore may be neglected in the analysis and the EurOtop (2018) approach is practical. However, if $h_{toe}/H_{m0,deep} \leq 1$, wave shoaling and breaking become significant and a more accurate approach would be that of Goda et al. (1975).

### 4.3.2 DEVELOPMENT OF OVERTOPPING FORMULAE

In Section 4.3.1, we demonstrated and discussed how the effects of the foreshore on nearshore conditions can be accurately represented as functions of $h_{toe}/H_{m0,deep}$ and $\tan(m)$. This suggests that wave overtopping, which is typically estimated as a function of nearshore parameters (at the toe of the structure), may actually be represented as a function of deep-water parameters when $h_{toe}/H_{m0,deep} \leq 1$. In line with the Goda et al. (1975) approach, also published in Goda (2000), we propose the following for vertical structures:

$$\frac{q}{\sqrt{g \cdot H_{m0,deep}{}^3}} = \mathrm{f}\left(\frac{h_{toe}}{H_{m0,deep}}, \frac{R_c}{H_{m0,deep}}, s_{om-1,0}, \tan m\right). \tag{4.19}$$

Likewise, for sloping structures:

$$\frac{q}{\sqrt{g \cdot H_{m0,deep}{}^3}} = \mathrm{f}\left(\frac{h_{toe}}{H_{m0,deep}}, \frac{R_c}{H_{m0,deep}}, s_{om-1,0}, \tan(m), \tan(\alpha)\right). \tag{4.20}$$

#### *4.3.2.1 Vertical Structures*

The datasets listed in Table 4.3 show a negative exponential relationship between relative discharge and relative freeboard (Figure 4.7 and Figure 4.8). This typical relationship is evident by the linear increase in $q \,/\sqrt{g \cdot H_{m0,deep}{}^3}$ (logarithmic y-axis) with decreasing freeboard (linear colour axis). On the other hand, $q \,/\sqrt{g \cdot H_{m0,deep}{}^3}$ shows a positive and much more dynamic relationship with $h_{toe}/H_{m0,deep}$ (Figure 4.7 and Figure 4.8). Visual inspection of the data and original Goda et al. (1975) design diagrams revealed three distinct regimes: i) a very shallow regime ($0.5 \leq h_{toe}/H_{m0,deep} \leq 1$), where a steep linear relationship exists between $\log q \,/\sqrt{g \cdot H_{m0,deep}{}^3}$ and $h_{toe}/H_{m0,deep}$; ii) an extremely shallow or emergent regime ($h_{toe}/H_{m0,deep} \leq 0.1$), where the relationship is much gentler—suggesting a reduced dependence; and iii) a transition region between the two regimes ($0.1 <$

$h_{toe}/H_{m0,deep}$ < 0.5), where the rate of reduction $q \,/\, \sqrt{g \cdot H_{m0,deep}{}^3}$ with change in $h_{toe}/H_{m0,deep}$ is maximum. Notably, this transition region is centred on the threshold between very and extremely shallow water, $h_{toe}/H_{m0,deep}$ = 0.3 (Hofland et al., 2017).

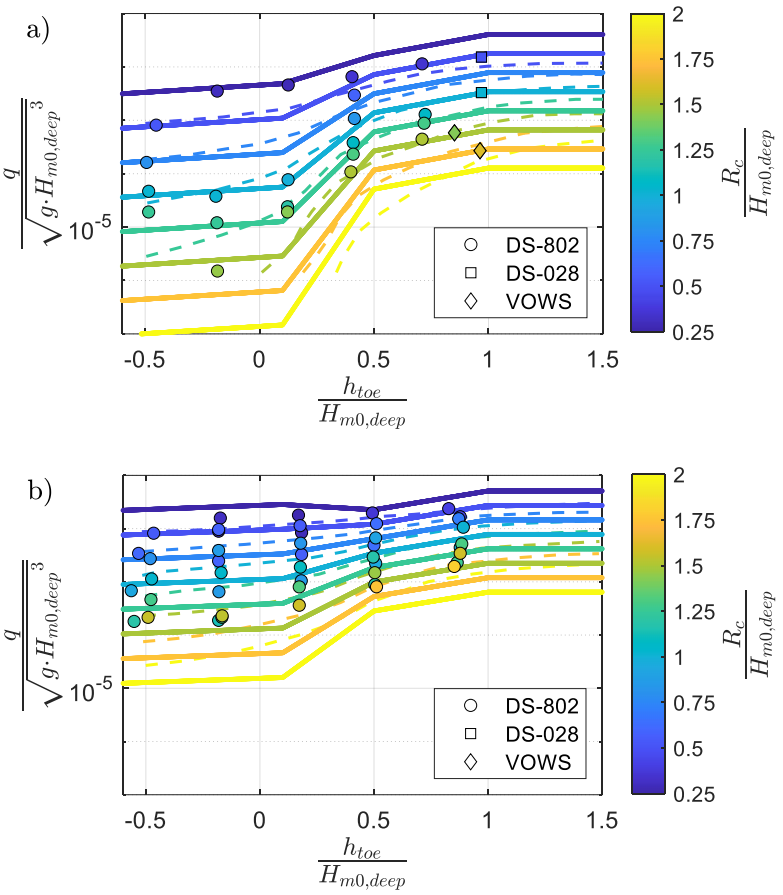


**Figure 4.7**. *Variation in relative discharge, $q \,/\, \sqrt{g \cdot H_{m0,deep}{}^3}$, with relative water depth ($h_{toe}\,/H_{m0,deep}$) and relative freeboard ($R_c\,/H_{m0,deep}$) for vertical structures (Table 4.3) with wave steepness ($s_{om-1,0}$) = a) 0.044 and b) 0.015 for a foreshore slope (cot m) = 10. Solid lines represent Equations 4.21 to 4.28; while dashed lines represent the digitized design curves of Goda et al. (1975).*

As noted in Section 4.3.1 and Figure 4.6, both static wave setup and dynamic setup—that is, the slow periodic variations in mean water level due to IG waves—increase considerably as $h_{toe}/H_{m0,deep}$ decreases. These static and periodic changes in mean water level equate to a reduction in $R_c/H_{m0,deep}$ which results in higher-than-expected overtopping for cases with $h_{toe}/H_{m0,deep} \leq 0.1$, as also observed by Goda et al. (1975).

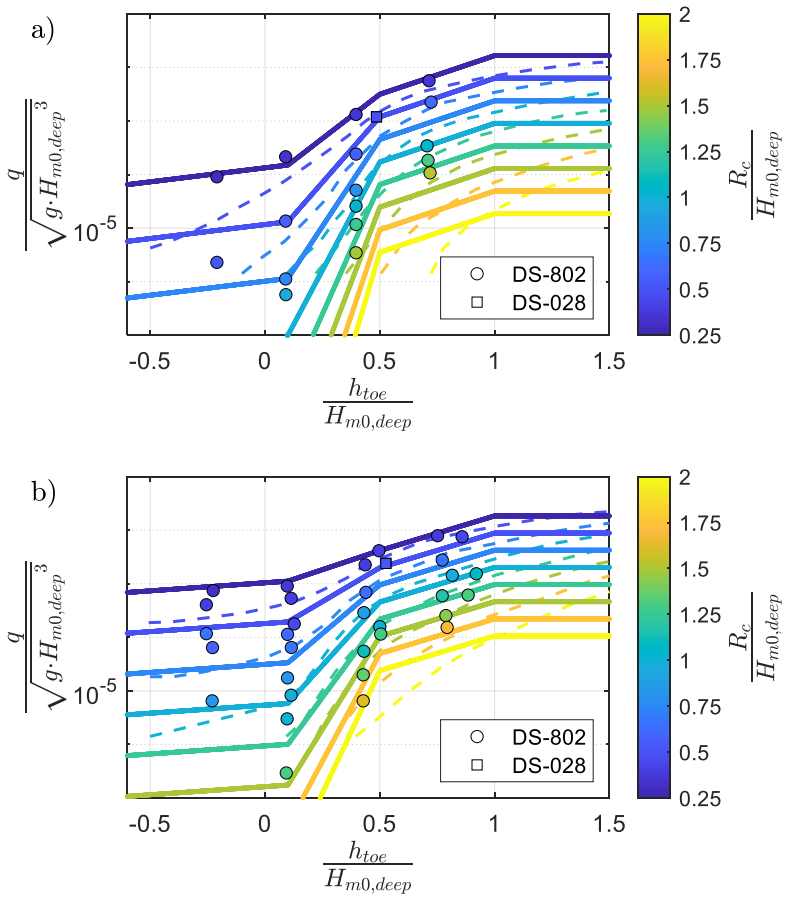


**Figure 4.8.** *Variation in relative discharge, $q/\sqrt{g \cdot H_{m0,deep}{}^3}$, with relative water depth ($h_{toe}/H_{m0,deep}$) and relative freeboard ($R_c/H_{m0,deep}$) for vertical structures (Table 4.3) with wave steepness ($s_{om-1,0}$) = a) 0.044 and b) 0.015, for a foreshore slope (cot m) = 30. Solid lines represent Equations 4.21 to 4.28; while dashed lines represent the digitized design curves of Goda et al. (1975).*

Based on the above-mentioned trends, the proposed formulae for vertical structures each have the following basic form:

$$\frac{q}{\sqrt{g \cdot H_{m0,deep}{}^3}} = a \cdot \exp\left(-b \cdot \frac{R_c}{H_{m0,deep}} + c \cdot \frac{h_{toe}}{H_{m0,deep}}\right), \tag{4.21}$$

where the coefficients $a$, $b$ and $c$ are each a function of $s_{om-1,0}$ and $m$. For very shallow cases (regime 1), with $0.5 \leq h_{toe}/H_{m0,deep} \leq 1$:

$$a_1 = 0.90 \cdot \frac{\tan(m)^{2.05}}{{s_{om-1,0}}^{0.20}}; \tag{4.22}$$

$$b_1 = 5.10 \cdot \frac{{s_{om-1,0}}^{0.25}}{\tan(m)^{0.15}}; \tag{4.23}$$

and,

$$c_1 = 0.70 \cdot \frac{{s_{om-1,0}}^{0.10}}{\tan(m)^{0.55}}. \tag{4.24}$$

For extremely shallow or emergent cases (regime 2), with $h_{toe}/H_{m0,deep} \leq 0.1$ :

$$a_2 = 0.09 \cdot \frac{\tan(m)^{2.35}}{{s_{om-1,0}}^{1.25}}; \tag{4.25}$$

$$b_2 = 5.40 \cdot \frac{{s_{om-1,0}}^{0.30}}{\tan(m)^{0.45}}; \tag{4.26}$$

and,

$$c_2 = 0.75 \cdot \frac{{s_{om-1,0}}^{0.50}}{\tan(m)^{0.60}}. \tag{4.27}$$

For the transition between the two regimes ($0.1 < h_{toe}/H_{m0,deep} < 0.5$), the user should interpolate exponentially:

$$y_3 = y_2 \cdot \left(\frac{y_1}{y_2}\right)^{(x_3 - x_2)/(x_1 - x_2)}, \tag{4.28}$$

where $x$ and $y$ are stand-ins for $h_{toe}/H_{m0,deep}$ and $q/\sqrt{g \cdot {H_{m0,deep}}^3}$, respectively; and the subscripts 1, 2 and 3 refer to the first, second and transition (third) regimes, respectively.

Qualitatively speaking, Equations 4.21 to 4.28 match both the data and the original Goda et al. (1975) design curves—which were obtained by digitizing the diagrams as presented in (Goda, 2000) (Figure 4.7 and Figure 4.8). Additionally, though Equations 4.21 to 4.28 were developed for conditions where $h_{toe}/H_{m0,deep} \leq 1$, the overtopping discharge for cases with $1 < h_{toe}/H_{m0,deep} \leq 1.5$ may also be well-estimated by taking the predicted maximum of Equations 4.21 to 4.28 (i.e. for $h_{toe}/H_{m0,deep} = 1$) (Figure 4.7 and Figure 4.8). It should also be noted that most of the data used to derive the EurOtop (2018) formulae for vertical structures starts in this shallow range and extend to deeper conditions ($h_{toe}/H_{m0,deep} > 1$). This further highlights the significance of the Goda et al. (1975) dataset and the need for formulae—such as Equations 4.21 to 4.28—for shallower conditions.

Quantitatively, Equations 4.21 to 4.28 are unbiased with minor scatter, yielding a $\bar{x}_G$ value of 1.02 and $\sigma(\bar{x}_G)$ of 1.68. If we consider wave overtopping to be normally distributed, then 90% of the predicted overtopping discharge would be located within a range of values between 0.43 and 2.40 times the measured overtopping discharge. Furthermore, Figure 4.9 shows that the ratio of the predicted (using Equations 4.21 to 4.28) to measured overtopping discharge ( $q_{pred}/q_{meas}$ ) is relatively uniform for varying values of $R_c\ /H_{m0,deep}$ , $h_{toe}\ /H_{m0,deep}$ , $\tan(m)$ and $s_{om-1,0}$ . This condition, referred to as homoscedasticity, suggests that the accuracy of Equations 4.21 to 4.28 is not dependent on any single parameter. Figure 4.9 also shows the parameter ranges used in the derivation of Equations 4.21 to 4.28; and hence, the ranges within which they can be reliably applied.

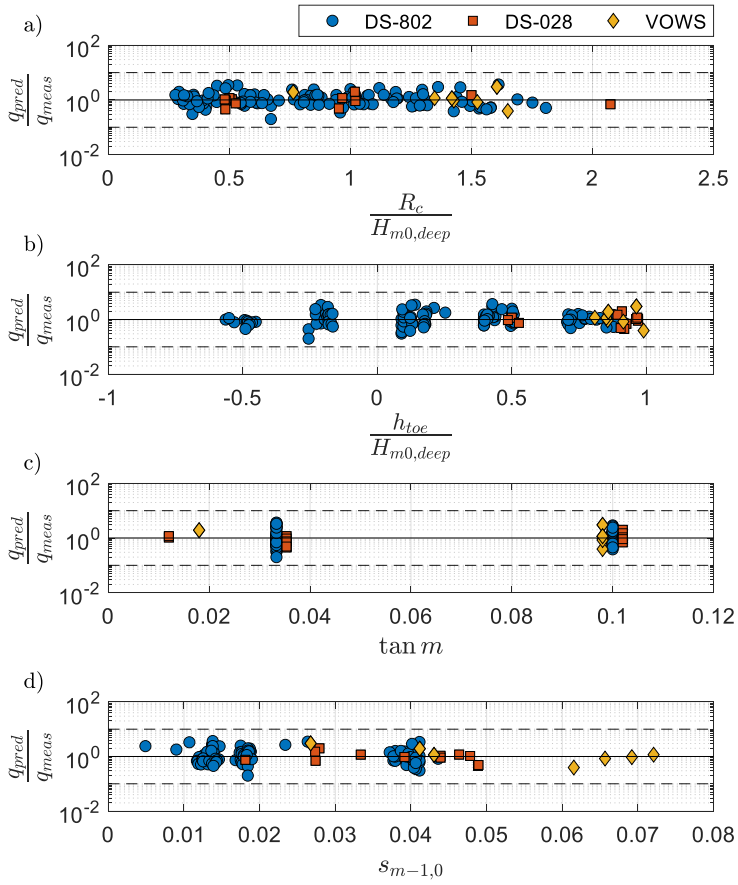


**Figure 4.9**. *Ratio of predicted (Equations 4.21 to 4.28) to measured overtopping discharge versus: a) relative freeboard ($R_c\ /H_{m0,deep}$) , b) relative water depth ($h_{toe}\ /H_{m0,deep}$), c) foreshore slope ($\tan(m)$), and d) wave steepness ($s_{om-1,0}$), for vertical structures (Table 4.3). Solid line indicates perfect agreement. Dashed lines represent predictions that are a factor of 10 higher/lower than measurements. Note that the data in panel 'c' are slightly offset to make all points visible.*

#### *4.3.2.2 Sloping Structures*

Using the same approach as outlined in Section 4.3.2.1 and the datasets listed in Table 4.2, the formulae derived for sloping structures with shallow foreshores follow:

$$\frac{q}{\sqrt{g \cdot {H_{m0,deep}}^3}} = d \cdot \exp\left(-e \cdot \frac{R_c}{H_{m0,deep}} + f \cdot \frac{h_{toe}}{H_{m0,deep}}\right). \tag{4.29}$$

For very shallow cases (regime 1), with $0.5 \leq h_{toe}/H_{m0,deep} \leq 1$:

$$d_1 = 1.90 \cdot {s_{om-1,0}}^{1.15}; \tag{4.30}$$

$$e_1 = 7.40 \cdot \frac{{s_{om-1,0}}^{0.60}}{\tan(m)^{0.25} \cdot \tan(\alpha)^{0.60}}; \tag{4.31}$$

and,

$$f_1 = 0.70 \cdot \frac{\tan(m)^{0.80}}{{s_{om-1,0}}^{0.80}}. \tag{4.32}$$

For extremely shallow or emergent cases (regime 2), with $h_{toe}/H_{m0,deep} \leq 0.1$ :

$$d_2 = 1.35 \cdot \tan(m)^{0.35} \cdot {s_{om-1,0}}^{0.85}; \tag{4.33}$$

$$e_2 = 3.75 \cdot \frac{{s_{om-1,0}}^{0.70}}{\tan(m)^{0.70} \cdot \tan(\alpha)^{0.60}}; \tag{4.34}$$

and,

$$f_2 = 0.20 \cdot \frac{{s_{om-1,0}}^{0.35}}{\tan(m)^{1.30}}. \tag{4.35}$$

with exponential interpolation between the two regimes ($0.1 < h_{toe}\ /H_{m0,deep} < 0.5$).

Equations 4.29 to 4.35 agree reasonably well with the data for sloping structures (Figure 4.10) which show similar trends to those observed for vertical structures (Figure 4.8). Figure 4.11 and Figure 4.12 also show no trend of increasing (or decreasing) scatter with changes in $R_c\ /H_{m0,deep}$ , $h_{toe}\ /H_{m0,deep}$ , $\tan(m)$ , $s_{0m-1,0}$ or $\tan(\alpha)$ , suggesting that homoscedasticity is maintained. It should be noted that due to the very small scale of the Tamada et al. (2002) data—with 0.027 m $\leq H_{m0,deep} \leq$ 0.068 m—there is larger inherent scatter in the observed overtopping discharge, compared to the other datasets (Figure 4.11 and Figure 4.12). Nevertheless, the Tamada et al. (2002) dataset has been considered reliable as it was previously used to derive overtopping formulae (Goda, 2009, Mase et al., 2013, Yuhi et al., 2020) and draw design diagrams (see Figures 5.8 to 5.10 in Goda (2010)).

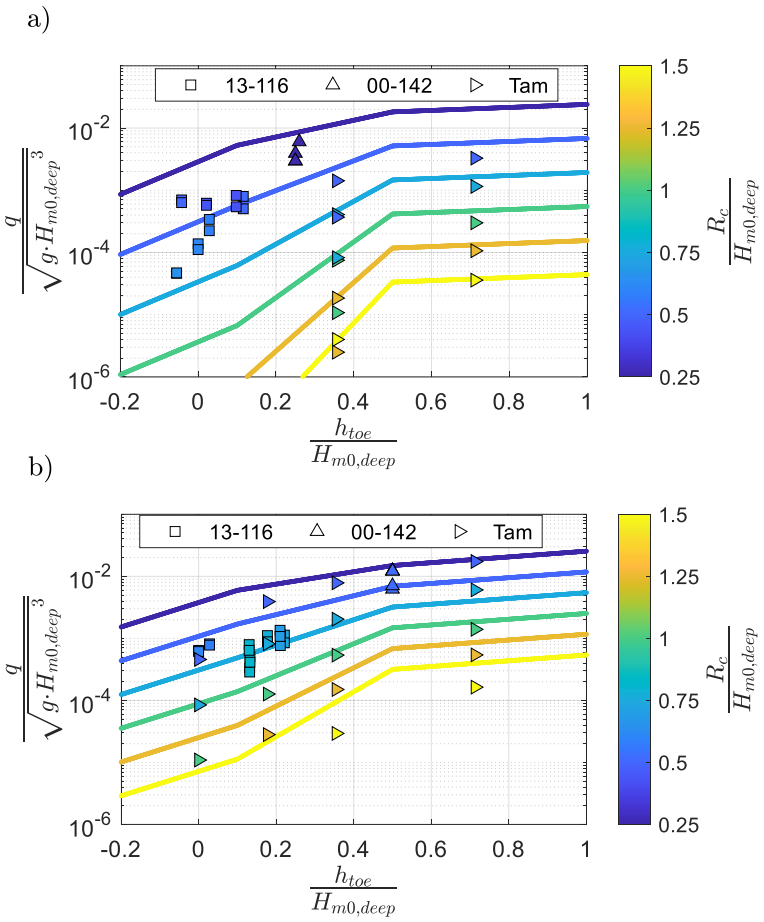


**Figure 4.10**. *Variation in relative discharge, $q / \sqrt{g \cdot H_{m0,deep}{}^3}$, with relative water depth ($h_{toe} / H_{m0,deep}$) and relative freeboard ($R_c / H_{m0,deep}$) for sloping structures (Table 4.2) with wave steepness ($s_{om-1,0}$) = a) 0.041 and b) 0.018, for foreshore slopes ($cot(m)$) = 30 and 35 and structure slope ($cot(\alpha)$) = 3. Solid lines represent Equations 4.29 to 4.35 with $cot\, m$ = 32.5.*

Compared to the existing EurOtop (2018) approach (Equations 4.7 to 4.11), Equations 4.29 to 4.35 show higher accuracy and a wider range of applicability. With $\bar{x}_G$ = 1.01 and $\sigma(\bar{x}_G)$ = 1.90, Equations 4.29 to 4.35 may be considered both accurate and unbiased; and if we consider wave overtopping to be normally distributed, then 90% of the predicted overtopping discharge would be located within a range of values between 0.35 and 2.92 times the measured overtopping discharge. On the other hand, the EurOtop (2018) formulae show a negative bias ($\bar{x}_G$ = 0.68) and much larger scatter ($\sigma(\bar{x}_G)$ = 3.84)—scatter which increases as the foreshore slope becomes steeper (Figure 4.13). This is to be expected since the formulae were derived mainly for relatively mild foreshore slopes (Altomare et al., 2016). If we only

consider the cases with $\cot(m) \geq 35$, the accuracy of Equations 4.7 to 4.11 increases significantly ($\bar{x}_G$ =1.11 and $\sigma(\bar{x}_G)$ = 2.11); thereby, confirming their inapplicability to steeper foreshore slopes.

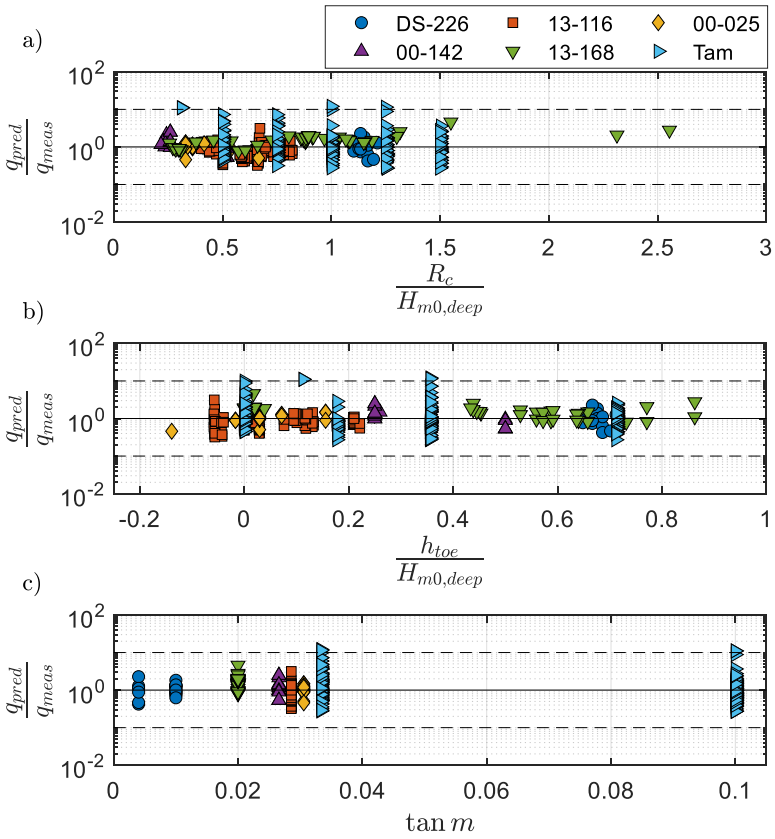


**Figure 4.11.** *Ratio of predicted (Equations 4.29 and 4.35) to measured overtopping discharge versus: a) relative freeboard ($R_c$ /$H_{m0,deep}$), b) relative wate depth ($h_{toe}$ /$H_{m0,deep}$) and c) foreshore slope ($\tan m$) for sloping structures (Table 4.2). Solid line indicates perfect agreement. Dashed lines represent predictions that are a factor of 10 higher/lower than measurements. Note that the data for $\tan m$ = 0.029 (1:35 slope) are slightly offset to make all points visible.*

The new formulae proposed here (Equations 4.29 to 4.35) may therefore be seen as an attractive alternative to Equations 4.7 to 4.11, when obtaining nearshore parameters is either impractical or would otherwise result in unwanted uncertainty. Furthermore, as the existing EurOtop (2018) formulae were mainly developed for relatively mild slopes ($\cot(m) \geq 35$); Equations 4.29 to 4.35— which consider foreshore slopes as steep as 1:10—may prove further advantageous.

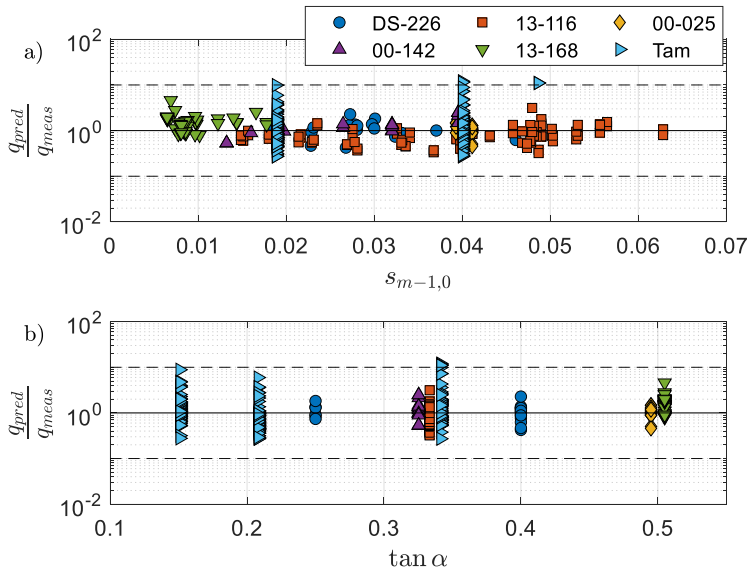


**Figure 4.12**. *Ratio of predicted (Equations 4.29 and 4.35) to measured overtopping discharge versus: a) wave steepness ($s_{om-1,0}$) and b) structure slope ($tan(\alpha)$), for sloping structures (Table 4.2). Solid line indicates perfect agreement. Dashed lines represent predictions that are a factor of 4 higher/lower than measurements. Note that the data for $tan(\alpha)$ = 0.33 and 0.5 are slightly offset to make all points visible.*

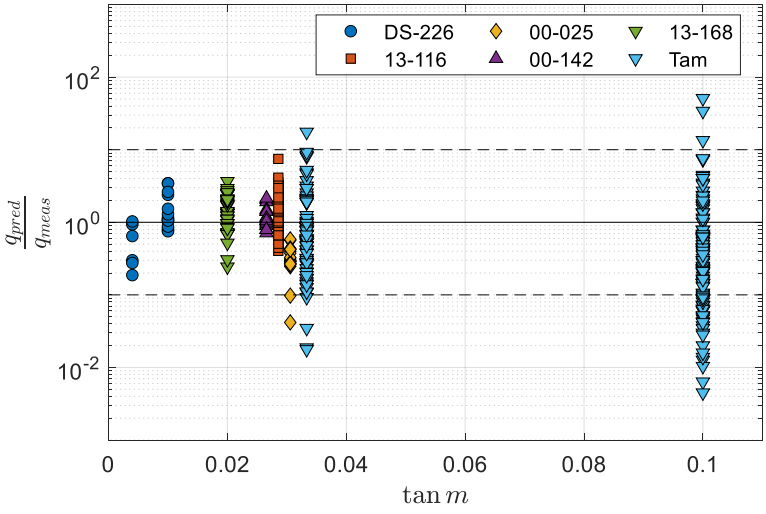


**Figure 4.13.** *Ratio of predicted (Equations 4.7 to 4.11 (EurOtop, 2018)) to measured overtopping discharge versus foreshore slope ($tan(m)$) for sloping structures (Table 4.2). Solid line indicates perfect agreement. Dashed lines represent predictions that are a factor of 10 higher/lower than measurements. Note that the data for $tan(m)$ = 0.029 (1:35 slope) are slightly offset to make all points visible.*

#### 4.3.2.3 Physical Explanation of the Proposed Empirical Coefficients

The coefficients of Equations 4.21 to 4.35 were established based on the observed influence of $s_{om-1,0}$, $\tan\alpha$ and $\tan m$ on the mean overtopping discharge; while the values of their exponents were obtained using a trial-and-error approach to minimize scatter. Though the coefficients were the result of empirical fitting, their functional forms are in-line with existing approaches which make use of a breaker parameter—which combines $s_{om-1,0}$, with either $\tan(\alpha)$ (Van Gent, 1999) or $\tan(m)$ (Bruce et al., 2004). The main difference here is the direct inclusion of both $\tan(m)$ and $\tan(\alpha)$ compared to existing approaches which use a single imaginary or "equivalent" slope (Altomare et al., 2016, Mase et al., 2013).

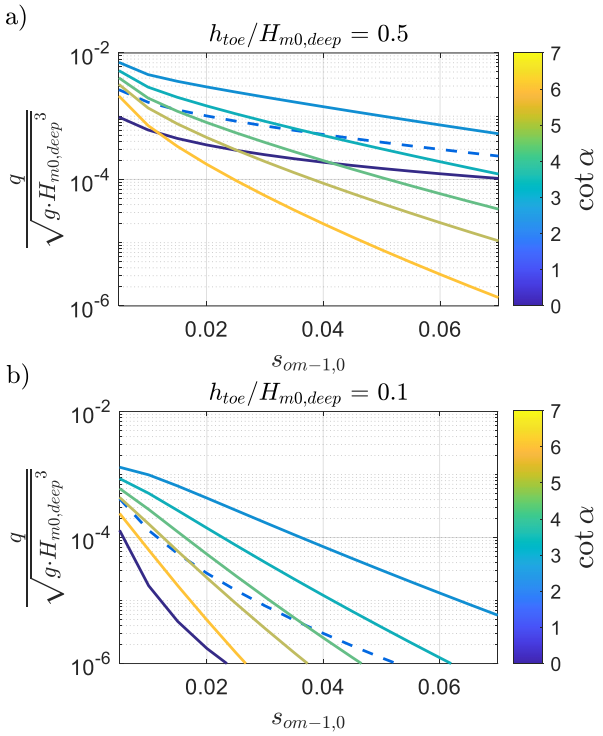


**Figure 4.14.** *Relationship between relative discharge, $q/\sqrt{g \cdot H_{m0,deep}{}^3}$, modelled using Equations 4.21 to 4.35 and wave steepness ($s_{om-1,0}$) for (a) very shallow conditions ($h_{toe}/H_{m0,deep}$ = 0.5) and (b) extremely shallow conditions ($h_{toe}/H_{m0,deep}$ = 0.1) , for different structure slopes ($\cot\alpha$), with $R_c/H_{m0,deep}$ = 1 and foreshore slope (m = 1:30). Dashed line for $\cot\alpha$ = 1 was obtained by interpolating between formulae for vertical walls ($\cot\alpha$ = 0) and sloping structures ($\cot\alpha$ = 2).*

Equations 4.21 to 4.35 show that $q/\sqrt{g \cdot H_{m0,deep}{}^3}$ increases as $s_{om-1,0}$ decreases (Figure 4.14), consistent with the notion that longer waves yield larger overtopping volumes

(EurOtop, 2018). Likewise, the formulae also show that $q \,/\, \sqrt{g \cdot H_{m0,deep}{}^3}$ increases as the foreshore and structure slopes become steeper (Figure 4.15), consistent with the early findings of Goda et al. (1975) and Owen (1980), respectively.

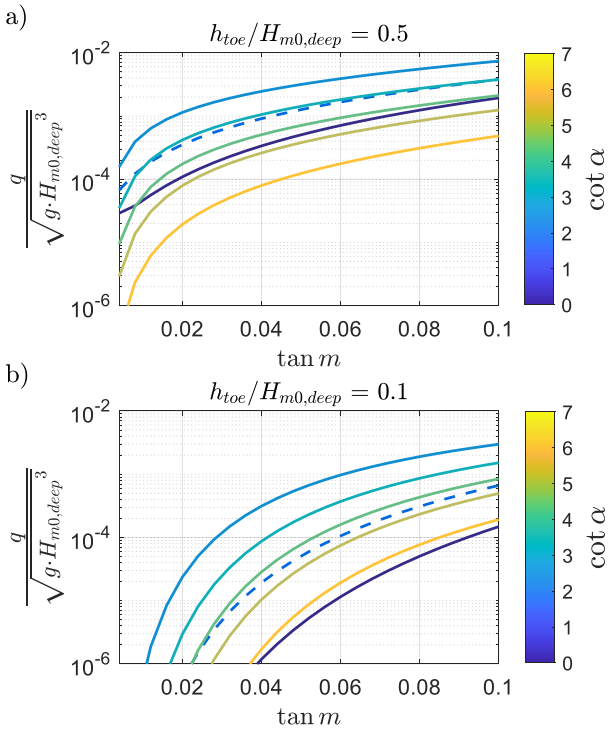


**Figure 4.15**. *Relationship between relative discharge, $q \,/\, \sqrt{g \cdot H_{m0,deep}{}^3}$, modelled using Equations 4.21 to 4.35 and foreshore slope ($\tan(m)$) for (a) very shallow conditions ($h_{toe}/H_{m0,deep}$ = 0.5) and (b) extremely shallow conditions ($h_{toe}/H_{m0,deep}$ = 0.1) , for different structure slopes ($\cot(\alpha)$), with $R_c/H_{m0,deep}$ = 1 and wave steepness ($s_{om-1,0}$) = 0.03. Dashed line for $\cot \alpha$ = 1 was obtained by interpolating between formulae for vertical walls ($\cot(\alpha)$ = 0) and sloping structures ($\cot(\alpha)$ = 2).*

Considering the full range of structure slopes considered ($2 \leq \cot(\alpha) \leq 7$, Table 4.2), Figure 4.14 and Figure 4.15 show that $q \,/\, \sqrt{g \cdot H_{m0,deep}{}^3}$ is maximum at $\cot(\alpha) = 2$; but then reduces significantly for vertical structures ($\cot(\alpha) = 0$). Based on the work of Victor and Troch (2012), also Section 5.3.3 of EurOtop (2018), for less shallow water—who found that $q$ indeed decreased from $\cot(\alpha) = 2$ to $\cot(\alpha) = 0$—interpolation between the formulae for vertical structures (Equations 4.21 to 4.28) and those for sloping structures (Equations 4.29 to 4.35) is recommended for very steep sloping structures ($0 < \cot(\alpha) < 2$). Curves for $\cot(\alpha) = 1$, obtained using this approach, are also shown in Figure 4.14 and Figure 4.15.

### 4.3.3 LIMITATIONS OF THE APPROACH

One notable limitation of the approach taken in the present study, is the lack of data for validation. As data with shallow foreshores was limited, all of the available data was used to derive the expressions herein. Therefore, the accuracy of the formulae for conditions outside of the range used to derive them is unknown.

Secondly, while the approach based on deep-water wave characteristics has significant advantages, one drawback of this approach is the assumption of uniform foreshore slope. In reality, foreshores may be very irregular with strong local variations, such as bars or ridges. Therefore, the formulae proposed here should be used with caution if applied to cases with highly irregular bathymetry.

## 4.4 CONCLUSIONS

A comprehensive collection of physical and numerical datasets was applied to: i) assess the influence of the foreshore on nearshore wave conditions; and ii) based on this assessment, derive empirical overtopping formulae for very shallow water up to emergent (initially dry) toes. In line with the work of Goda et al. (1975), we have shown that the effects of the foreshore can be well-represented by two foreshore parameters: $h_{toe}\,/H_{m0,deep}$ and $\tan(m)$. As such, it was possible to derive accurate overtopping formulae—for both vertical and sloping structures—which directly incorporate $h_{toe}\,/H_{m0,deep}$ and $\tan(m)$ to account for the changes that occur as a result of shallow foreshores. Findings suggest that relative magnitudes of wave-induced setup and infragravity waves at the toe of structures built on land or in extremely shallow water can be considerable, resulting in higher-than-expected overtopping.

The formulae developed for vertical structures (Equations 4.21 to 4.28) provide an alternative to the original Goda et al. (1975) design diagrams for very shallow conditions ($h_{toe}/H_{m0,toe} \leq 1$), where such a graphical approach may prove tedious or time-consuming. For sloping structures, the EurOtop (2018) approach is considered attractive from deep to shallow water ($h_{toe}/H_{m0,toe} > 1$)—where spectral wave models provide accurate estimates at the structure toe with little computational effort. However, Equations 4.29 to 4.35 provide an accurate and convenient alternative for very shallow conditions, where predicting wave parameters at the toe becomes highly uncertain or impractical (e.g. in the case of emergent toe conditions) without the use of computationally-demanding, high-resolution numerical models.

While Equations 4.21 to 4.35 performed reasonably well here, their accuracy outside the range of conditions used to derive them has not been assessed (see Figure 4.9, Figure 4.11 and Figure 4.12 for overview of parameter ranges). Furthermore, a drawback with formulae developed using deep-water wave parameters, is the assumption of a uniform foreshore slope. Therefore, care should be taken when applying Equations 4.21 to 4.35 to cases with highly irregular bathymetry and numerical wave models (e.g. BOSZ (Lashley et al., 2020a)) should

be used to verify results. Future work should extend the approach here by considering a wider range of foreshore slopes in the case of vertical structures, and to even shallower (negative) water depths for sloping structures. Finally, more physical model tests focused on assessing wave setup and the magnitude of IG waves at the toe of structures built on land ($h_{toe}$ /$H_{m0,deep} \leq 0$) are needed to further support the findings presented here.

# 5

# INFLUENCE OF IG WAVES ON SAFETY ALONG THE DUTCH WADDEN SEA COAST*


## ABSTRACT

Many coastlines around the world are protected by coastal structures (e.g. dikes or seawalls) fronted by wide, shallow foreshores, such as the saltmarshes and mudflats. These foreshores attenuate storm waves and are expected to reduce the likelihood of waves overtopping the dikes behind them. However, most of the studies to-date that sought to quantify their effectiveness have excluded the influence of infragravity (IG) waves, which often dominate in shallow water. In this chapter, a modular and adaptable framework is proposed to estimate the probability of coastal dike failure by overtopping waves ($P_f$ [year$^{-1}$]). The influence of IG waves on wave overtopping is included using the empirical approach developed in Chapter 2, which is validated against observations made during two recent storms at the Dutch Wadden coast (2015 and 2017). The framework is applied to the Dutch Wadden Sea coast, which is protected by dikes, to compare the $P_f$ with and without the influence of IG waves. Findings show that including IG waves results in 1.1 to 1.6 times higher $P_f$ values, suggesting that safety may be overestimated when they are neglected. This is attributed to the influence of the IG waves on the design wave period, and to a lesser extent the wave height, at the toe of the dike. Additionally, the spatial variation in this effect, observed for the case considered, highlights its dependence on local bathymetric and offshore forcing conditions—with IG waves showing greater influence at locations with larger offshore waves and shallower water depths. Finally, the change in $P_f$ due to the IG waves varied significantly


*This chapter is currently under review as: Lashley, C. H., Jonkman, S. N., Van der Meer, J., Bricker, J. D., and Vuik, V.: The Influence of Infragravity Waves on the Safety of Coastal Defences: A Case Study of the Dutch Wadden Sea, Nat. Hazards Earth Syst. Sci. Discuss., 2021, 1-40, 10.5194/nhess-2021-211, 2021.

depending on the empirical wave overtopping model selected, emphasizing the importance of tools developed specifically shallow foreshore environments.

This chapter is organized as follows: Section 5.1.3 describes the geographic area that will be the focus of this study. Section 5.2 provides a detailed description of the dike-foreshore system under consideration and the probabilistic framework applied, including descriptions of the numerical and empirical models therein. Section 5.2 also describes the field dataset used to validate the empirical approach for the inclusion of IG waves. In Section 5.3, the results of the validation are presented, followed by the application of the framework to the wider Wadden Sea coast. Section 5.4 discusses the results and their implications for practice; and Section 5.5 concludes the paper by addressing the overall research objective, stating limitations and identifying areas for future work.



## 5.1 INTRODUCTION

### 5.1.1 BACKGROUND

Coastal defences (e.g. dikes or seawalls), fronted by wide, shallow foreshores, protect many coastlines around the world. Examples include the sandy foreshores along the Belgian coast (Altomare et al., 2016), the wide shelfs of the Mekong Delta, Vietnam (Nguyen et al., 2020) and the intertidal flats of the Wadden Sea along the north coast of the Netherlands (Vuik et al., 2016). These bodies of sediment reduce the water depth in front of the structure such that large incident waves are forced to break. This reduced wave load at the structure is then expected to improve safety by reducing the likelihood of the structure failing. If vegetation is present, the drag forces exerted by stems, branches and leaves further enhance this attenuation effect.

Several studies sought to quantify the hazard mitigation potential of shallow foreshores, with and without vegetation, including physical model tests (Möller et al., 2014), numerical simulations (Vuik et al., 2016;Willemsen et al., 2020) and field measurements (Garzon et al., 2019). While these studies assessed the ability of the foreshore to attenuate the height of wind-sea and swell (hereafter, SS) waves—with frequencies typically greater than 0.05 Hz—they neglected the influence of infragravity (hereafter, IG) waves.

Under extreme conditions, with large offshore waves and very shallow local water depths, the shoaling and subsequent breaking of SS waves results in energy transfer to lower frequencies and the growth of IG waves, also referred to in literature as “surfbeat” (Bertin et al., 2018;Van Dongeren et al., 2016). IG waves are widely recognized as the driving force behind coastal erosion and flooding along shallow coastlines. Recent reports of their impact include: unexpectedly high wave run-up at the coast of Banneg island, France (Sheremet et al., 2014); extensive damage and casualties along the coral-reef lined coast in the Philippines during Typhoon Haiyan (Roeber and Bricker, 2015); the erosion and overwash of several

dunes along the west coast of France (Baumann et al., 2017;Lashley et al., 2019); and damage along Seisho Coast of Japan during Typhoon Lan (Matsuba et al., 2020). Despite this knowledge, IG waves are often not considered in the risk assessment of coastal defences. This oversight is linked to the use of phase-averaged wave models—which inherently exclude IG-wave dynamics—to estimate the wave load at the structure. The impact of this neglect on the safety of coastal defences has yet to be thoroughly investigated.



In the Netherlands, coastal defences are typically designed to resist the volume of water expected to pass over the crest of (or overtop) the structure due to wave action during storms associated with a very high return period (2,000 to 10,000 years). This phenomenon, referred to as wave overtopping, is typically represented by a mean discharge per meter width of structure, $q$ [$m^3$/s or l/s per m]. The probability of failure due to wave overtopping is then determined by assessing the likelihood that the actual discharge ($q_a$) exceeds some critical value ($q_c$), which is dependent on the erosion resistance of the grass-covered landward slope. Following a recent policy revision, the safety standard for the coastal defences in the Netherlands is now defined by an (acceptable) probability of failure. For example, typical values for the Dutch Wadden Sea coast—a shallow, intertidal area in the north of the country—are failure probabilities of 1/1000 and 1/3000 per year.

From a design perspective, the presence of IG waves typically results in higher characteristic values of the two main parameters used to estimate $q_a$: namely, the significant wave height and spectral wave period, both assessed at the structure toe (Chapter 2 (Lashley et al., 2020a)). Vuik et al. (2018b) assessed the overtopping failure probability of an idealised the dike-foreshore system, representative of the Dutch Wadden Sea coast, considering the effects of vegetation. This study considered the influence of IG waves on the wave period at the toe using the Hofland et al. (2017) empirical model, but neglected their influence on the wave height. Furthermore, Nguyen et al. (2020) later showed that the Hofland et al. (2017) formulae tend to underestimate the development of longer spectral wave periods on foreshore slopes milder than 1:250 (Nguyen et al., 2020)—which is a typical characteristic of the Wadden Sea. As a result, the true influence of IG waves along the Dutch Wadden Sea coast remains unknown.

Oosterlo et al. (2018) carried out a similar probabilistic assessment of a dike with a sandy foreshore, in the south of the Netherlands, but directly included the IG waves by using the XBeach Surfbeat numerical model to estimate the wave parameters at the toe. The authors found, for the considered case, that accounting for the IG waves resulted in $10^2$ times higher overtopping failure probabilities compared to methods that neglected them. This rather striking finding requires further investigation; particularly, to determine if the large IG-wave influence reported by Oosterlo et al. (2018) holds for other cases as well or if it was merely an artefact of the method used.

Chapter 3 (Lashley et al., 2020b) demonstrated that the influence of IG waves on wave parameters at the toe could be accurately estimated using a combined numerical and empirical approach. In this approach, the phase-averaged wave model (SWAN) is used to simulate the dissipation of SS waves in shallow water; while the IG component is estimated using empirical formulae. Since this approach allows for the accurate representation of IG waves at the dike toe but maintains the utility and speed of phase-averaged wave modelling, it can be applied on a large scale with little computational effort. In the present study, this approach is extended and used as a key component to assess the influence of IG waves on the probability of dike failure along the Dutch Wadden Sea coast.

### 5.1.2 OBJECTIVE AND APPROACH

Previous studies either neglected the influence of IG waves on the probability of failure by wave overtopping or yielded inconclusive results. Consequently, the influence of IG waves on the safety of coastal defences remains unknown. To remedy this, it is the primary aim of the current paper to investigate the influence of IG waves on the probability of failure due to wave overtopping for coastal defences (dikes) with shallow foreshores. This is achieved by first augmenting the probabilistic framework developed by Vuik et al. (2018b) by incorporating newly validated empirical formulae that capture the influence of IG waves on design parameters, following the approach demonstrated in Chapter 3 (Lashley et al., 2020b). The modified framework is then used to estimate the probability of dike failure by wave overtopping along the Dutch Wadden Sea coast (Figure 5.1).

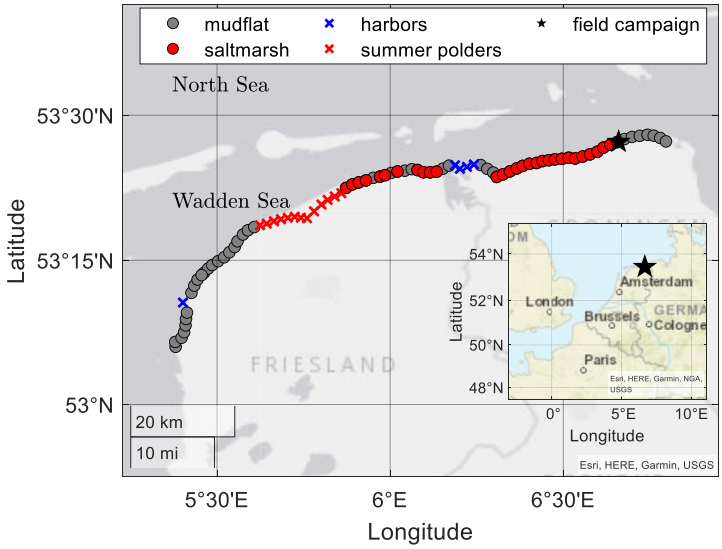


**Figure 5.1** *Location of the Dutch Wadden Sea with reference to wider Europe (inset). Circle markers indicate dikes considered, while 'x' markers highlight those that were excluded from the analysis. Star marker indicates the location of the field site at Uithuizerwad.*

### 5.1.3 STUDY AREA

The Dutch Wadden Sea is a shallow, mildly sloping intertidal zone situated between the Netherlands (mainland) and several barrier islands, which shield the area from large North Sea waves (Figure 5.1). Along the Wadden Sea coast, a system of dikes fronted by saltmarshes and mudflats exists. In the present study, we consider the stretch of dikes with shallow foreshores—that is, with bed levels at the toe either just below or a few meters higher than mean sea level (NAP)—that are typically impacted by North-westerly waves during storms (Figure 5.1). Further information on storm conditions in the study area is presented in Section 5.2.6 and Table 5.1.



The analysis includes the dikes from the city of Harlingen to those west of Eemshaven in the province of Groningen; but it excludes the flood defences in front of harbours and areas referred to as summer polders (Figure 5.1). Summer polders are low-lying, embanked areas situated in front of the dike and are usually dry in the summer months but may flood during winter storms. As these polders extend for several kilometres, the 1 km transect approach taken here would not be representative.

## 5.2 MATERIALS AND METHODS

### 5.2.1 MODEL FRAMEWORK AND SYSTEM DESCRIPTION

The model framework used to compute the probability of flooding due to wave overtopping is presented in Figure 5.2, and is modified after Vuik et al. (2018b) to include the effect of IG waves. Boundary conditions of offshore wave heights, periods and water levels are transformed over the foreshore to the structure toe using SWAN. These SWAN estimates at the toe are then modified using empirical formulae to account for IG waves. These estimates are then used as input to calculate the actual overtopping discharge, $q_a$. The probability of failure by wave overtopping, $P(Z < 0)$ is then obtained using the open-source implementation of the First Order Reliability Method (FORM (Hasofer and Lind, 1974)).

While the framework below (Figure 5.2) follows that of Vuik et al. (2018b), there are noteworthy differences between the two approaches. Firstly, the influence of IG waves on both the wave height and period at the toe is considered—using empirical formulae that are valid for a wide range of foreshore slopes ($10 \leq \cot(m) \leq 1000$). Secondly, the effect of wind on wave transformation is neglected here due to close proximity to the shoreline—within 1 km. Lastly, as it is very likely that almost all vegetation will flatten or break under extreme forcing (Möller et al., 2014;Vuik et al., 2018a), wave attenuation by vegetation is not included in the probabilistic analysis. That said, the effect of vegetation (should it remain standing) is demonstrated for one location (Uithuizerwad field site, Figure 5.1) in Section 5.3.2; and treated as part of the discussion (Section 5.4.1). The individual components of the model framework are described in detail below. A visual representation of the dike-foreshore system, and the various framework components, is provided in Figure 5.3.

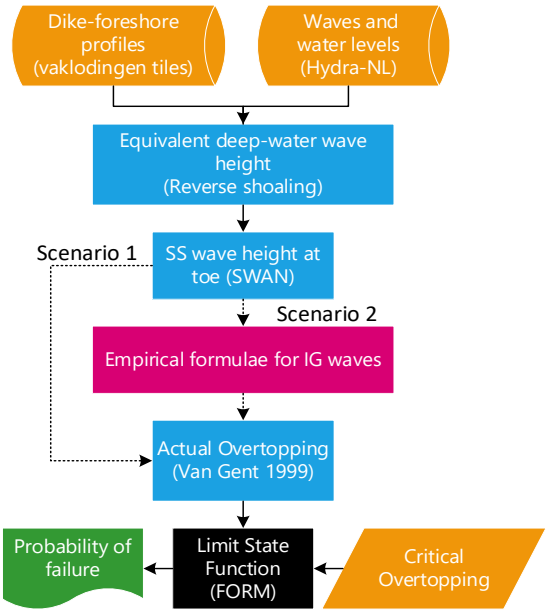


**Figure 5.2** *Model framework highlighting Scenario 1, which considers only the influence of SS waves and Scenario 2, which considers both SS and IG waves. See Section 5.2.5.3 for further scenario descriptions.*

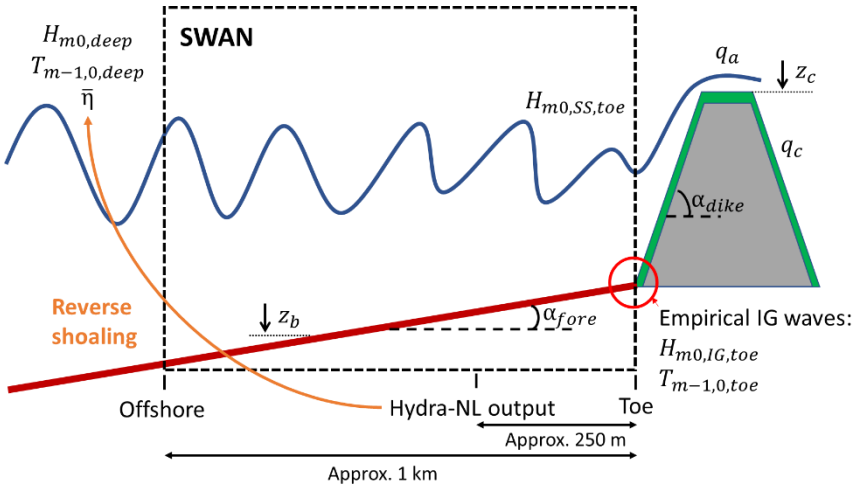


**Figure 5.3** *Schematic representation of the dike-foreshore system showing the areas where key parameters and tools are applied. These parameters and tools are introduced throughout Section 5.2: Methods.*

### 5.2.2 BOUNDARY CONDITIONS

#### *5.2.2.1 Offshore Waves and Water Levels*

To obtain the offshore water levels ($\bar{\eta}$ [m]), wave heights ($H_{m0}$ [m]) and periods ($T_{m-1,0,deep}$ [m]), Hydra-NL (Duits, 2019) was applied—a probabilistic application designed specifically for the assessment and design of flood defences in the Netherlands. It uses statistics of wind speed, wind direction, water level and their respective correlations to find the corresponding wave characteristics in a pre-calculated database, obtained using the phase-averaged numerical model, SWAN. The tool provides estimates along the entire Dutch Wadden coast, every 250 m, a few hundred meters offshore. To reduce the overall computational demand, the output locations were reduced to one every 1.5 km (Figure 5.1).

The wave heights estimated by Hydra-NL were reverse shoaled, using linear wave theory, to an offshore point approximately 1 km from the dike toe. This was done so as to remove the influence of the foreshore, similar to the approach of Van Osselen (2016), to obtain estimates of the offshore wave height ($H_{m0,deep}$ [m]) for use with Equation 5.12. This approach also allowed additional foreshore processes (e.g. vegetation) that were not considered in the original Hydra-NL calculations to be modelled here (see Section 5.2.3.1). Compared to the original Hydra-NL estimates, the average change in significant wave height by reverse shoaling was +2%, with a maximum of +4% and minimum of -9%. As this approach neglects friction, refraction and any local generation or breaking that may occur, it is considered here to be an approximate estimate.

For each location, five exceedance probabilities were considered: 1/100, 1/300, 1/1000, 1/3000 and 1/10000 per year (Table 5.1). Using the $\bar{\eta}$, $H_{m0,deep}$ and $T_{m-1,0,deep}$ estimates for each probability of exceedance, Weibull distribution parameters—namely, scale and shape parameters—were derived to accurately describe the extremes. The range of the scale and shape parameter values is provided in Table B. 1 (Appendix B).

**Table 5.1** *Characteristic values for offshore waves and water levels at the Uithuizerwad field site.*

| Variables | Unit | | | | | |
|---|---|---|---|---|---|---|
| Exceedance probability | 1/year | 1/100 | 1/300 | 1/1000 | 1/3000 | 1/10000 |
| $\bar{\eta}$ | m | 4.29 | 4.62 | 4.95 | 5.26 | 5.59 |
| $H_{m0,deep}$ | | 1.40 | 1.58 | 1.77 | 1.94 | 2.14 |
| $T_{m-1,0,deep}$ | s | 5.02 | 5.55 | 6.04 | 6.52 | 6.99 |

#### *5.2.2.2 Dike-foreshore characteristics*

The bathymetry of the Dutch coast, from dry land up to the 20 m isobath in the North Sea, is continuously measured (at least once every seven years) by the Dutch government

(Rijkswaterstaat). This dataset, referred to as "Vaklodingen" (Wiegmann et al., 2005), covers the Wadden Sea with a 20-m grid resolution (Figure 5.4). Cross-shore transects of approximately 1 km, at intervals corresponding to the Hydra-NL output locations, were extracted considering a NW to SE orientation—in-line with the dominant wind/wave direction during storms (NW) (Vuik et al., 2018b), similar to the approach taken by Willemsen et al. (2020). By aligning the transect with the dominant wind/wave direction, the influence of wave obliqueness on wave propagation and overtopping may be neglected.



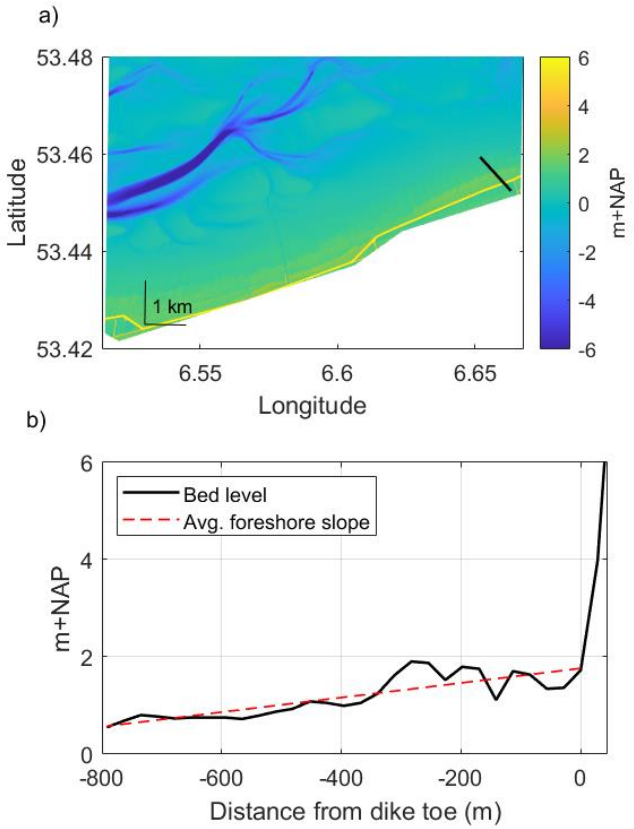


**Figure 5.4** *Subset of the Vaklodingen bathymetry dataset showing a) a NW-SE oriented transect at the field site location, Uithuizerwad (black line) and b) the cross-shore profile of this transect with the estimated average foreshore slope at the field site location.*

For each transect, the mean elevations ($z_b$ [m+NAP]) and average foreshore slopes ($\tan(m)$) were obtained. To account for variations in bathymetry and measurement inaccuracies, $z_b$ was treated as a normally distributed parameter with a standard deviation of 0.2 m. While the actual bathymetry is used for the numerical modelling of the SS waves (Section 5.2.3.1), the estimated $\tan(m)$ is necessary for use with the empirical formulae for the influence of the IG

waves (Section 5.2.3.2). Given the range of validity of the empirical formulae (Equations 5.12 and 5.13), a minimum foreshore slope of 1/1000 is considered here.

Given the significant influence of the dike geometry on the calculated probability of failure (Section 5.3.2.2), the crest level ($z_c$ [m + NAP]) and average dike slope ($\tan(\alpha)$ [-]) are treated here as deterministic parameters with the same values applied to each location. This was done to remove the influence of variations in dike geometry on the calculated failure probabilities and allow the analysis to focus on what occurs over the foreshore. The crest levels were set to 6 m + NAP, corresponding to the required safety level (probability of failure less than 1/1000 per year), but also varied as part of the sensitivity analysis. Similarly, the dike slopes were set to 1/7 to represent the average slope of a typical Wadden Sea dike, which is often characterised by 1:4 upper and lower slopes separated by a mildly sloping berm. Note that an analysis of the sensitivity of the estimated probability of failure to variations in $z_c$, including its treatment as deterministic versus stochastic, is provided in Section 5.3.2.2.



### 5.2.3 WAVE TRANSFORMATION

#### *5.2.3.1 Numerical Model for SS Waves: SWAN*

SWAN is a third-generation, phase-averaged wave model used to estimate the generation (by wind), propagation and dissipation (by depth-induced breaking and bottom friction) of waves from offshore to the structure toe. This includes wave-wave interactions, in both deep and shallow water, and wave-induced setup; but neglects wave-induced currents and the generation or propagation of IG waves. SWAN computes the spectral evolution of wave action density ($A$) in space and time. For stationary 1D simulations, the governing equations follow:

$$\frac{\partial c_x A}{\partial x} = \frac{S_{tot}}{\omega}, \tag{5.1}$$

where $c_x$ is the propagation velocity of wave energy in the x-direction, $\omega$ is the frequency and $S_{tot}$ may include dissipation terms due to depth-limited wave breaking ($\bar{D}_w$), vegetation ($\bar{D}_v$) and bottom friction; and energy transfer terms.

To simulate depth-limited wave breaking, SWAN uses the following parametric dissipation model, by default (Battjes and Janssen, 1978):

$$\bar{D}_w = \frac{\alpha}{4}\rho g f_{mean} Q_b H_{max}^2, \tag{5.2}$$

and $Q_b$ is estimated as:

$$\frac{1 - Q_b}{\ln Q_b} = -8\frac{E_{tot}}{H_{max}^2}, \tag{5.3}$$

where $f_{mean}$ [Hz] is the mean wave frequency, $H_{max} = \gamma_{bj} h$ and $E_{tot}$ is the total wave-energy variance. Here, the breaker parameter ($\gamma_{bj}$) is based on the offshore wave steepness, $s_0 = H_{rms}/L_0$ [-] (Battjes and Stive, 1985):

$$\gamma_{bj} = 0.5 + 0.4 \tanh(33 \cdot s_0), \tag{5.4}$$

where $H_{rms}$ is the root mean square wave height, with $H_{rms} = 8 \cdot E_{tot}$. Following Vuik et al. (2018b), $\gamma_{bj}$ is treated as a normally-distributed parameter with a standard deviation of 0.05.



As recommended by Baron-Hyppolite et al. (2018), the explicit vegetation representation in SWAN—which was implemented by Suzuki et al. (2012)—is applied. This method represents vegetation as rigid cylinders, following the approach of Dalrymple et al. (1984) modified for irregular waves by Mendez and Losada (2004). In this approach, the mean rate of energy dissipation per unit horizontal area due to wave damping by vegetation ($\epsilon_v$) is given by:

$$\overline{D}_v = \frac{1}{2g\sqrt{\pi}} \rho C_D b_v N_v \left(\frac{gk}{2f_{mean}}\right)^3 \frac{\sinh^3 kh_v + 3\sinh kh_v}{3k\cosh^3 kh} {H_{rms}}^3, \tag{5.5}$$

where $\rho$ is the density of water, $g$ [m/s$^2$] is the gravitational acceleration, $k$ [m$^{-1}$] is the mean wave number, $h$ [m] is the water depth, $C_D$(0.4) is the drag coefficient, $b_v$ (3 mm) is the stem diameter, $N_v$ (1200 stems/m$^2$) is the vegetation density and $h_v$ (0.3 m) is the vegetation height; where the values in parentheses are representative of saltmarshes in the Netherlands (Vuik et al., 2016).

Deep-water processes such as white-capping, wind and quadruplet wave-wave interactions were disabled. All other model parameters were kept at their default values. For all simulations, a constant grid spacing of 2.5 m was applied. This corresponded to approximately 15-20 grid cells per deep-water wavelength.

#### *5.2.3.2 Empirical Formulae for the Influence of IG Waves*

The influence of the IG waves may be represented by an increase in the design parameters, namely: the total significant wave height ($H_{m0,toe}$ [m]) and spectral wave period ($T_{m-1,0,toe}$ [s]) at the toe based on incident waves, where:

$$H_{m0} = \sqrt{{H_{m0,SS}}^2 + {H_{m0,IG}}^2}, \tag{5.6}$$

$$H_{m0,SS} = 4\sqrt{\int_{0.05}^{1} C_{\eta\eta}\, df}, \tag{5.7}$$

$$H_{m0,IG} = 4\sqrt{\int_{0.005}^{0.05} C_{\eta\eta}\, df}, \tag{5.8}$$

where $C_{\eta\eta}(f)$ [m$^2$/Hz] is the wave energy density and 0.05 Hz is the frequency separating SS and IG motions. It should be noted that for conditions with a single, clearly-defined peak frequency ($f_p$), the frequency separating IG and SS motions is typically taken as $f_p/2$. However, as wave spectra in the Dutch Wadden Sea typically show multiple peaks, a separation frequency of 0.05 Hz is typically used to avoid contaminating the IG signal with that of swell (with periods around 10 s or 0.1 Hz). This choice of split frequency is consistent with previous studies in the area (Engelstad et al., 2017;De Bakker et al., 2014) and coincides with the minimum in spectral density in the observed wave spectra at the field site (Appendix C, Figure C.1).



$$T_{m-1,0} = \frac{m_{-1}}{m_0}, \tag{5.9}$$

where,

$$m_n = \sqrt{\int_{0.005}^{1} C_{\eta\eta} \cdot f^n\, df}. \tag{5.10}$$

### Influence on Significant Wave Height at Toe

In Chapter 2 (Lashley et al., 2020a), the influence of various dike-foreshore parameters on wave conditions at the dike toe was investigated using the XBeach non-hydrostatic numerical model (Kingsday release) in both 1D and 2D mode. In each simulation, the offshore wave height ($H_{m0,deep}$), offshore spectral wave period ($T_{m-1,0,deep}$), wave directional spreading ($\sigma_{dir}$ [°]), water depth at the toe ($h_{toe}$), foreshore slope ($m$ [°]), width of vegetated cover ($W_{veg}$) and structure slope ($\alpha$) were systematically varied, following a one-[factor]-at-a-time (OAT approach). From the resulting dataset of 672 different numerical estimates of $T_{m-1,0,toe}$, $H_{m0,IG,toe}$ and $H_{m0,SS,toe}$, the following formula for $H_{m0,IG,toe}$ was derived:

$$H_{m0,IG,toe} = \widetilde{H}_{IG} \cdot H_{m0,SS,toe}, \tag{5.11}$$

where the relative magnitude of the IG waves,

$$\widetilde{H}_{IG} = 0.36 \cdot {H_{m0,deep}}^{0.5} \cdot \bar{\gamma}_\sigma \cdot \bar{\gamma}_h \cdot \bar{\gamma}_f \cdot \bar{\gamma}_v \cdot \bar{\gamma}_d, \tag{5.12}$$

where $\bar{\gamma}_\sigma, \bar{\gamma}_h, \bar{\gamma}_f, \bar{\gamma}_v, \bar{\gamma}_d$ are influence factors for wave directional spreading, water depth at the toe, foreshore slope, vegetated cover and structure slope, respectively; see Lashley et al. (2020a) for further details on how each influence factor is determined. However, it should be noted that the influence of vegetation on IG waves was assessed for very shallow conditions

($h_{toe}/h_v$ = 3.3); therefore, the performance of Equation 5.12 for vegetation with larger water depth to stem height ratios is yet to be verified. For the probabilistic analysis, Equation 5.12 is multiplied by normally distributed factor ($f_{IG}$ [-]) with a mean (0.99) and standard deviation (0.18) based on the bias and scatter observed during its derivation, respectively (Lashley et al., 2020a).



The above approach accounts for IG-wave generation by: i) bound-wave shoaling over mildly-sloping bathymetry; and ii) the temporal variation in the location of breaking waves, known as the break-point forcing mechanism (Battjes, 2004). However, it does not account for IG waves that may be refractively trapped, known as edge waves or those reflected from a distant coast, known as leaky waves (Elgar et al., 1992;Bertin et al., 2018;Reniers et al., 2021).

### Influence on Spectral Wave Period at Toe

The existing method to estimate the increase in spectral wave period at the toe due to IG waves in shallow water, developed by Hofland et al. (2017), was based on laboratory tests with foreshore slopes, 35 < $\cot(m)$ < 250. While the method proved accurate within this range, as shown by (Lashley et al., 2020b), it tended to underestimate $T_{m-1,0,toe}$ for slopes gentler than 1:250 (Nguyen et al., 2020). As foreshores in the Wadden Sea are typically 1:500 and gentler, a new formulation for $T_{m-1,0,toe}$ is derived here—using the above-mentioned numerical dataset (Lashley et al., 2020a).

Since $T_{m-1,0,toe}$ and $\widetilde{H}_{IG}$ both describe the amount of energy in the IG band compared to the SS band, it stands to reason that a simple relation should exist between the two parameters. From the Lashley et al. (2020a) numerical dataset with 10 < $\cot(m)$ < 1000, the following relationship between $T_{m-1,0,toe}/T_{m-1,0,deep}$, $\widetilde{H}_{IG}$ and $\cot\alpha_{fore}$ was found ($R^2$ = 0.92):

$$\frac{T_{m-1,0,toe}}{T_{m-1,0,deep}} = \begin{cases} 1.59 \cdot \widetilde{H}_{IG}^{\ 0.69} \cdot \cot(m)^{\ 0.17} & \dfrac{h_{toe}}{H_{m0,deep}} \leq 1 \\ 1 & \dfrac{h_{toe}}{H_{m0,deep}} > 1 \end{cases}, \tag{5.13}$$

Further details on the derivation of Equation 5.13 and its performance in comparison to the Hofland et al. (2017) model are provided in Appendix D. For the probabilistic analysis, Equation 5.13 is multiplied by normally distributed factor ($f_{Tm}$) with a mean (0.99) and standard deviation (0.17) based on the bias and scatter observed during its derivation, respectively.

### 5.2.4 WAVE OVERTOPPING

#### *5.2.4.1 Empirical Formulae for Actual Wave Overtopping*

In the present study, the overtopping formula proposed by Van Gent (1999) (Equation 5.14) is applied. This formula was chosen because it was developed specifically for shallow foreshores, considers the influence of both SS and IG waves and is considered valid for a wide range of breaker parameter ($\xi_{m-1,0}$ ) values.



$$\frac{q_a}{\sqrt{g \cdot H_{m0,toe}^3}} = 10^c \cdot \exp\left(-\frac{R_c}{H_{m0,toe} \cdot \left(0.33 + 0.022 \cdot \xi_{m-1,0}\right)}\right), \tag{5.14}$$

where,

$$\xi_{m-1,0} = \frac{\tan(\alpha)}{\sqrt{H_{m0,toe} / L_{m-1,0}}}, \tag{5.15}$$

$$L_{m-1,0} = \frac{g \cdot T_{m-1,0,toe}^2}{2\pi}, \tag{5.16}$$

where $g$ is the gravitational constant of acceleration, $\alpha$ is the dike slope, $\xi_{m-1,0}$ is the Iribarren number (also referred to as the breaker parameter) and $L_{m-1,0}$ is a fictitious wavelength based on the spectral wave period at the toe. It is important to note that $H_{m0,toe}$ and $T_{m-1,0,toe}$ in the above equations are based on the incident waves (i.e. without the influence of wave reflection at the structure). The empirical coefficient ($c$) is a normally-distributed parameter with a mean of -0.92 and a standard deviation of 0.24.

Here, Equation 5.14 here is applied to all locations, regardless of $\xi_{m-1,0}$ value. However, it should be noted that this approach does not coincide with the current standard (EurOtop, 2018). EurOtop (2018) recommends that different formulae be applied depending on the $\xi_{m-1,0}$ value (Van der Meer and Bruce, 2014;Altomare et al., 2016). However, due to the gentle dike (1:7) and foreshore slopes (1:600, on average) considered here, applying the EurOtop (2018) approach proved challenging. This is discussed in detail in Section 5.4.2.

Note that the empirical formulae developed in Chapter 4, based on deep-water wave parameters, could be used as an alternative approach to calculating the actual overtopping discharge for cases with $h_{toe}/H_{m0,deep}$. However, as the formulae developed in Chapter 4 directly include the influence of IG waves, it would be impossible to obtain overtopping estimates without IG waves (which are needed to assess their impact). As a result, those formulae were not applied here.

#### 5.2.4.2 Critical Wave Overtopping

The erosion resistance of the grass-covered landward slope of the dike is described by a critical or tolerable overtopping discharge ($q_c$). Given the significant influence of this parameter on the probability of dike failure by wave overtopping (Section 5.3.2.2), it is treated here as a deterministic parameter with a value of 50 l/s/m for each location. In this way, the influence of other parameters, such as those linked to the IG waves, can be better assessed. An analysis of the sensitivity of the estimated probability of failure to changes in $q_c$, is provided in Section 5.3.2.2. This analysis also demonstrates how the probability of failure would change if $q_c$ were instead treated as a stochastic parameter.



### 5.2.5 PROBABILISTIC METHODS

#### 5.2.5.1 FORM

The open-source implementation of FORM, part of OpenEarthTools (Van Koningsveld et al., 2010), is used to evaluate the limit state function (LSF) for any possible combination of input variables, which are each described by probability distributions. The following LSF is considered here (Oosterlo et al., 2018):

$$Z = \log q_c - \log q_a, \tag{5.17}$$

where $Z$ is the limit state considering the critical ($q_c$) and actual ($q_a$) overtopping discharges, which represent the resistance and load, respectively; and the probability of failure by wave overtopping, $P_f = P\ (Z < 0)$ or $P\ (q_a > q_c)$.

FORM simplifies the mathematical problem by linearizing the LSF and transforming all probability distributions to equivalent normal distributions. $P_f$ is then expressed in terms of a reliability index ($\beta$), which represents the minimum distance from the most probable failure point on the limit state surface ($Z = 0$), referred to as the design point, to the origin of the transformed coordinate system (Hasofer and Lind, 1974).

$$\beta = \frac{\mu_z}{\sigma_z}, \tag{5.18}$$

where are the mean and standard deviation of the limit-state function ($Z$); and

$$P_f = \Phi(-\beta), \tag{5.19}$$

where $\Phi$ is the cumulative distribution function for a standard normal variable.

FORM starts in a user-defined position in the probability density functions of all variables (e.g. the mean value). It then uses an iterative procedure to update the design point until convergence is achieved (Vuik et al., 2018b). In each iteration, FORM tests how strong the LSF responds to a perturbation of each individual variable, $X_i$. The response is expressed in

terms of the partial derivative $\partial Z/\partial X_i$, which are then used to calculate sensitivity factors ($\alpha_{sf,i}$):

$$\alpha_{sf,i} = \frac{\partial Z/\partial X_i \cdot \sigma_i}{\sigma_z}, \tag{5.20}$$

where $\alpha_{sf,i}$ represents the relative importance of the uncertainty in each stochastic parameter, such that $\sqrt{\sum_{i=1}^{n} \alpha_{sf,i}{}^2}$ = 1. Uncertainties in parameters with large $\alpha_{sf}$-values—that is, values closer to 1—are considered to be significant, such that a small change in the uncertainty of that parameter would result in a relatively large change in the reliability index ($\beta$). However, the uncertainty in parameters with $\alpha_{sf}$-values close to zero have minor relative importance and those parameters may be treated as deterministic (Kjerengtroen and Comer, 1996).



#### 5.2.5.2 Dependencies

The following (Gaussian) dependencies between variables are imposed (Table 5.2); all other variables are considered independent:

**Table 5.2** *Pearson correlation coefficients (ρ) for Gaussian dependence between boundary conditions ($\bar{\eta}$, $H_{m0,deep}$ and $T_{m-1,0,deep}$).*

| Variables | | $\rho$ | Source |
|---|---|---|---|
| $\bar{\eta}$ | $H_{m0,deep}$ | 0.97 | Vuik et al. (2018b) |
| $\bar{\eta}$ | $T_{m-1,0,deep}$ | 0.96 | |
| $H_{m0,deep}$ | $T_{m-1,0,deep}$ | 0.99 | |

#### 5.2.5.3 Foreshore Scenarios

In order to investigate the effect of IG waves on the $P_f$, we consider the following two scenarios:

1) SS wave breaking: where the influence of the foreshore bathymetry on incident SS waves is considered but IG waves are neglected; and
2) SS wave breaking and IG waves: where the influence of the foreshore bathymetry on both SS and IG waves are considered.

In the Netherlands, Scenario 1 represents standard practice, as the influence of IG waves are typically not considered during safety assessments. By assessing the difference in $P_f$ between Scenario 1 and 2—hereafter, referred to as $P_{f1}$ and $P_{f2}$, respectively—the influence of the IG waves may be quantified. Note that in both scenarios vegetation is assumed to be flattened, broken or not present (mudflats) in the analysis of the wider Wadden Sea coast. However,

the influence of standing vegetation on the $P_f$ is demonstrated for a single case at the Uithuizerwad location in Section 5.3.2.

### 5.2.6 FIELD DATA FOR MODEL VALIDATION

The performance of the combined numerical and empirical wave modelling approach is assessed by comparing estimates to storm data measured at Uithuizerwad, the Dutch Wadden Sea (Figure 5.1)—where the dike is fronted by vegetated foreshore with an average foreshore slope of 1:600. In this way, the ability of the approach to accurately represent the processes occurring over the foreshore is verified, namely: i) the decrease in SS waves due to depth-induced breaking over the foreshore and ii) the increase in wave height and period at the toe due to IG waves. This dataset is described below:



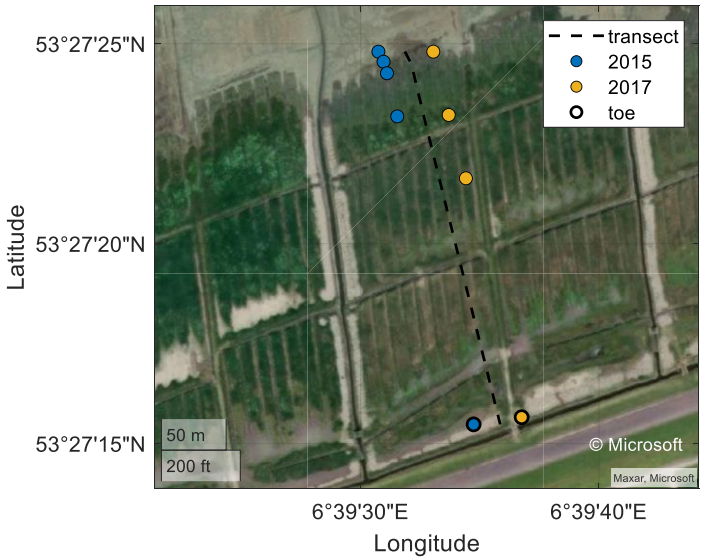


**Figure 5.5** *Wave gauges locations for the January 2015 and January 2017 field campaigns at Uithuizerwad (corresponding to the star in Figure 5.1).*

Two field campaigns were carried out in winter 2014/2015 and 2016/2017 at Uithuizerwad (Figure 5.1), capturing severe storms on January 11, 2015 and January 13, 2017, both with exceedance probabilities of 1/5 per year (Zhu et al., 2020). Here, we consider two transects of wave gauges that captured the change in wave conditions from the marsh edge to dike toe (Figure 5.5). In January 2015, a transect of 5 pressure gauges (Ocean Sensor Systems, Inc., USA) was deployed nearshore, each sampling at 5 Hz over a period of 7 minutes, every 15 minutes (Figure 5.5a). In January 2017, the set-up of the experiment was slightly altered with four gauges deployed, each sampling continuously at 5 Hz (Figure 5.5b).

The pressure signal from each gauge was translated into time series of surface elevations, using linear wave theory to adjust for attenuation of the pressure signal with depth. After that, a Fourier transform was performed, to transform the data from the time domain to the frequency domain (Hann window, 50% overlap). To improve the frequency resolution of the resulting wave spectra, measurements from two successive bursts were combined into a single time record. For the 2015 dataset, this yielded spectra with 19 degrees of freedom and a frequency resolution of 0.011 Hz; while the analysis of the 2017 dataset yielded spectra with 31 degrees of freedom and a frequency resolution of 0.0089 Hz. The measured wave and water level conditions at the marsh edge for the 2015 and 2017 winter storms are summarized in Table 5.3.



**Table 5.3** *Measured wave and water level conditions at the marsh edge during the 2015 and 2017 winter storms at the Uithuizerwad field site.*

| Variables | Unit | | |
|---|---|---|---|
| Year | | 2015 | 2017 |
| $\bar{\eta}$ | m | 3.12 | 3.25 |
| $H_{m0,deep}$ | | 0.71 | 0.84 |
| $T_{m-1,0,deep}$ | s | 5.02 | 5.31 |

## 5.3 RESULTS

### 5.3.1 VALIDATION OF WAVE MODELLING

In this section, the comparison between the combined numerical (Section 5.2.3.1) and empirical (Section 5.2.3.2) modelling approach for wave transformation and the field measurements (Section 5.2.6) is presented.

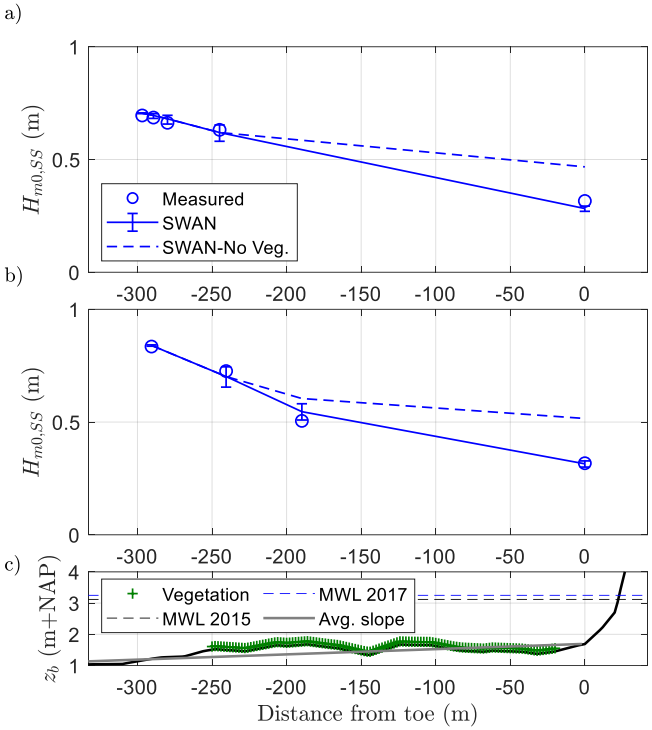


**Figure 5.6** *Comparison of measured and modelled significant wave heights in the SS bands ($H_{m0,SS}$) at the peaks of the a) January 2015 and b) January 2017 storms at Uithuizerwad (see Figure 5.5 for gauge locations). Error bars represent the uncertainty in the estimates based on the standard deviation of Equation 5.4. Panel 'c' shows the bed level and vegetated cover.*

For both the 2015 and 2017 storms, SWAN is setup as a transect (1D) in line with wave sensors (Figure 5.5). In each simulation, the numerical model is forced at its boundary with the measured wave spectra at the most offshore wave sensor. SWAN is able to capture the dissipation of SS waves due to the combined effects of the shallow bathymetry and vegetation (Figure 5.6). In 2015, the modelled SS-wave attenuation from the most offshore gauge to the dike toe was 56%, half of which (28%) was due to depth-induced wave breaking over the shallow bathymetry alone. Similarly, modelled SS-wave attenuation in 2017 was 63% with 39% due to depth-induced wave breaking alone.

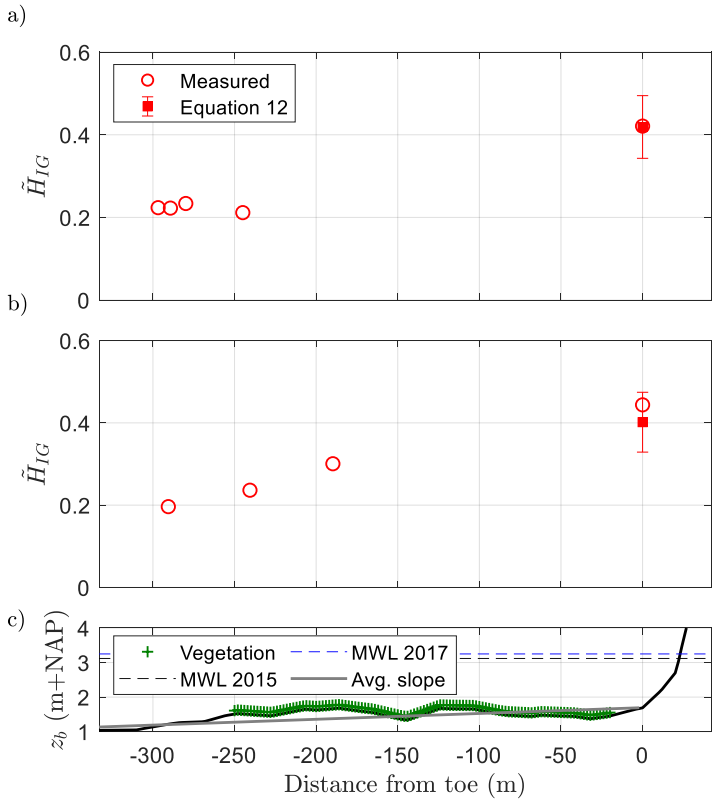


**Figure 5.7** *Comparison of measured and modelled relative magnitude of the IG waves ($\tilde{H}_{IG}$) at the peaks of the a) January 2015 and b) January 2017 storms at Uithuizerwad (see Figure 5.5 for gauge locations). Error bars represent the uncertainty in the estimates based on the standard deviation of Equation 5.12. Panel 'c' shows the bed level and vegetated cover.*

At the toe of the dike, Equations 5.12 and 5.13 are used to estimate the increase in the relative magnitude of the IG waves, $\tilde{H}_{IG}$ (Figure 5.7) and the associated increase in spectral wave period relative to its deep-water value, $T_{m-1,0,toe}/T_{m-1,0,deep}$ (Figure 5.8), respectively. Compared to the measurements at the toe, Equation 5.12 produced an average error of -5%. In Figure 5.8, estimates of $T_{m-1,0,toe}/T_{m-1,0,deep}$ made by SWAN and the Hofland et al. (2017) formula are also presented for comparison. For the two storms, SWAN produced an average error of -48% compared to Equation 5.13 with 11%; thus indicating the relevance of IG waves. Similarly, the Hofland et al. (2017) formula produced an average error of -55%. As the Hofland et al. (2017) formula is based on tests with $35 \leq \cot(m) \leq 250$, these results further indicate that it should not be applied outside of this range and highlights the added value of Equation 5.13—which considers slopes as gentle as 1:1000.

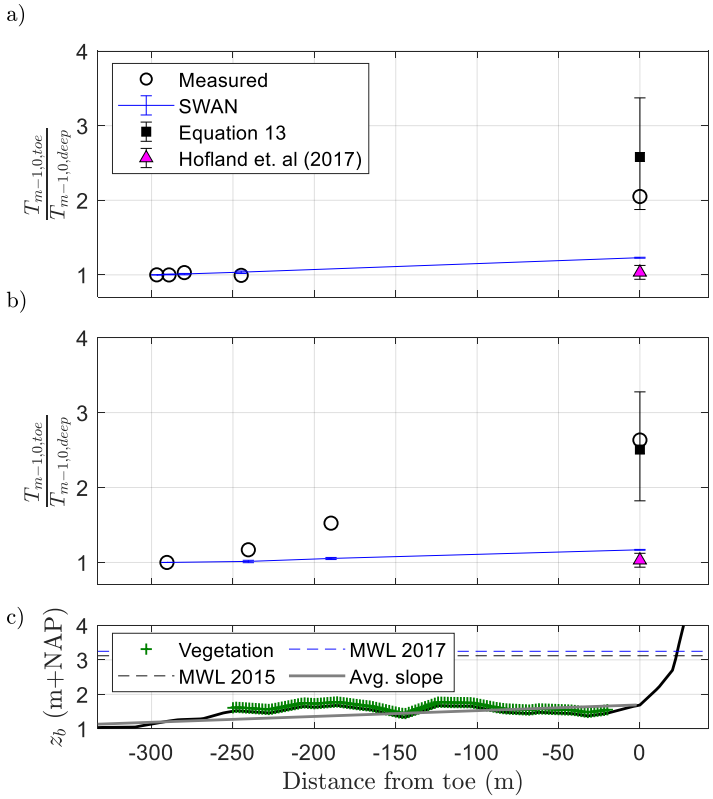


**Figure 5.8** *Comparison of measured and modelled relative spectral wave period ($T_{m-1,0,toe}/T_{m-1,0,deep}$) at the peaks of the a) January 2015 and b) January 2017 storms at Uithuizerwad (see Figure 5.5 for gauge locations). Error bars represent the uncertainty in the estimates based on the standard deviations of Equations 5.12, 5.13 and the Hofland et al. (2017) formula (Appendix D). Panel 'c' shows the bed level and vegetated cover.*

### 5.3.2 PROBABILITY OF FAILURE: UITHUIZERWAD CASE

#### *5.3.2.1 Influence of IG waves on Probability of Failure*

Using the modified probabilistic framework (Section 5.2.1), the annual probabilities of failure due to wave overtopping ($P_f$) at Uithuizerwad are presented in Figure 5.9a for the two scenarios considered and an additional scenario to assess the influence of standing vegetation. The calculated $P_f$ is presented alongside estimates of the wave height and period at the toe for a proxy storm with an exceedance probability of 1/3000 per year (Figure 5.9b), which is in line with the safety standard.

Scenario 2 (SS + IG) results in a $P_f$ 1.3 times larger than that of scenario 1 (SS) (Figure 5.9a). An increase which corresponds well with the increase in the spectral wave period at the toe ($T_{m-1,0,toe}$), and to a lesser extent, the increase in wave height at the toe ($H_{m0,toe}$) due to IG waves (Figure 5.9b). If the effects of standing vegetation are considered (SS + IG + Veg), the

$P_f$ is reduced by one order of magnitude (Figure 5.9a). This is due to the wave attenuation effect of the vegetation, which reduces both $H_{m0,toe}$ and $T_{m-1,0,toe}$ compared to scenario 2 (SS + IG) alone (Figure 5.9b).

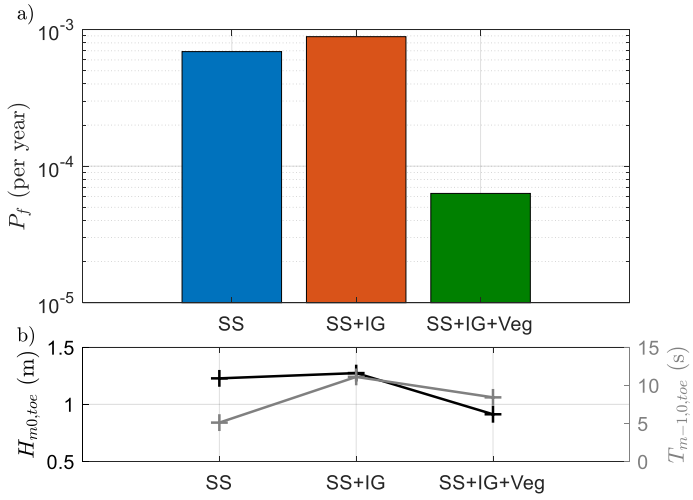


**Figure 5.9** *Relationship between a) annual failure probabilities at Uithuizerwad for the two scenarios considered and b) physical parameters for a proxy storm with an exceedance probability of 1/3000 per year and a still water level of 5.26 m + NAP. Crest level of 6 m + NAP and dike slope of 1:7 considered. Note that the influence of vegetation may be overestimated (see Section 5.4.1).*

### *5.3.2.2 Influence of Parameter Values and Uncertainty on the Probability of Failure*

The influence of the dike crest level ($z_c$) on the calculated $P_f$ is presented in Figure 5.10a. It can be seen that the influence of the IG waves increases with increasing $z_c$ value. This is because the large load ($q_a$) needed for failure of a higher dike is reached earlier when IG waves are included. On the other hand, the difference between scenario 1 and scenario 2 remains rather constant with varying values for the critical wave overtopping discharge, $q_{crit}$ while the magnitude of the calculated $P_f$ decreases by a factor of $O(10)$ when $q_{crit}$ is increased by the same magnitude (Figure 5.10b).

With respect to the stochastic parameters, the sensitivity of the calculated $P_f$ to uncertainties in each parameter is assessed using the FORM $\alpha_{sf}$-values (Section 5.2.5.1, Figure 5.11). Negative $\alpha_{sf}$-values represent variables that contribute to the load by increasing the actual overtopping discharge ($q_a$). In both scenarios, the uncertainty in the offshore water level ($\bar{\eta}$) dominates the probability of failure with $\alpha \leq$ -0.96. This is expected since the dike is unlikely to fail without extreme water levels (i.e. a severe storm). In scenario 1 (Figure 5.11a), the variables that also contribute to the load are: the empirical wave overtopping coefficient ($c$)—

since larger $c$ values increase $q_a$ (Section 5.2.4.1); the SWAN breaker parameters ($\gamma_{BJ}$), which controls the magnitude of breaking waves, such that higher $\gamma_{BJ}$ lead to larger wave heights at the structure toe and thus larger $q_a$; and the offshore wave forcing parameters ($H_{m0,deep}$ and $T_{m-1,0,deep}$).



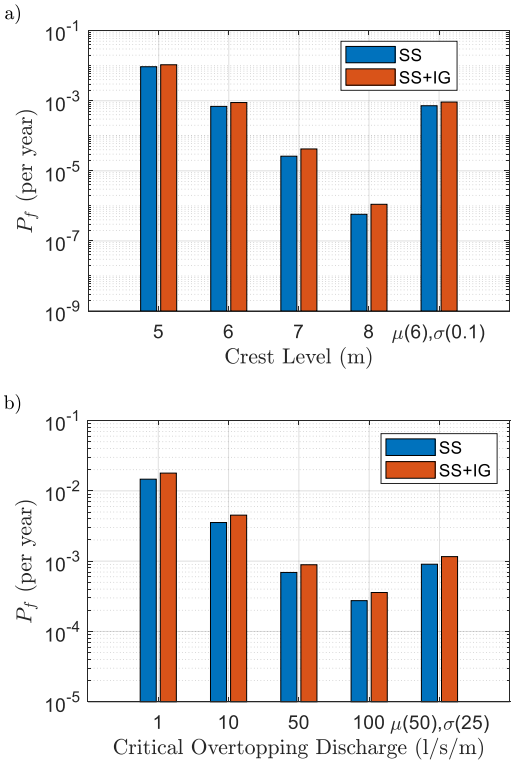


**Figure 5.10** *Annual failure probabilities for the two scenarios considered for: a) different dike crest levels with a fixed critical overtopping discharge of 50 l/s/m; and b) different critical overtopping discharges with a fixed crest level of 6 m + NAP. A dike slope of 1:7 is considered.*

As expected, when the influence of the IG waves is included in the analysis (scenario 2, Figure 5.11b) the uncertainty in factors for the relative IG-wave height, $f_{IG}$ ($\alpha$ = -0.03) and spectral wave period, $f_{TM}$ ($\alpha$ = -0.02) also contribute to the load, as larger $H_{m0,toe}$ and $T_{m-1,0,toe}$ values increase $q_a$. This suggests that the calculated $P_f$ is indeed sensitive to the accuracy of Equations 5.12 and 5.13. The uncertainty in bed level ($z_b$) also contributes to the load due to its influence on the water depth at the toe, which directly influences the relative magnitude of the IG waves at the dike toe ($\widetilde{H}_{IG}$).

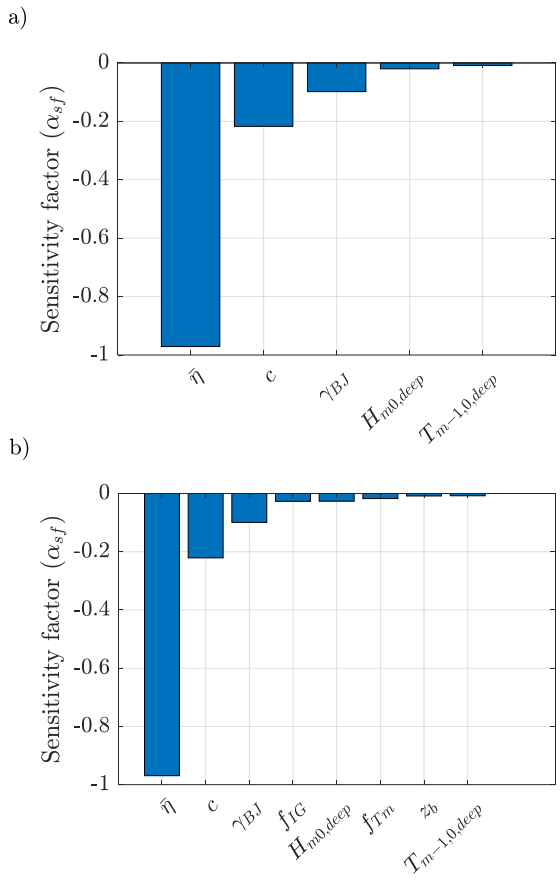


**Figure 5.11** *Sensitivity factors ($\alpha_{sf}$) ranked from left to right in order of importance, for a) scenario 1: SS and b) scenario 2: SS + IG. Negative values indicate load parameters.*

Overall, the results of the validation suggest that Equations 5.12 and 5.13 may be applied to the area with reasonable accuracy. Likewise, the results of the application of the model framework to the case at Uithuizerwad are in line with expectations. The calculated failure probability for scenario 1 (SS) are similar to the assumed safety standard (less than 1/1000 per year) and the differences observed between the scenarios show clear relationships with physical wave parameters at the dike toe, namely the significant wave height and spectral wave period that determine the magnitude of wave overtopping Figure 5.9b. With confidence in the model framework, it is applied to the wider Wadden Sea area (Figure 5.1) for a spatial analysis of the $P_f$.

### 5.3.3 PROBABILITY OF FAILURE FOR THE WIDER WADDEN SEA AREA

As a next step, the dikes of the wider Wadden Sea area are considered from the city of Harlingen to those west of Eemshaven in the city of Groningen. Again, we apply the

assumption of a constant dike height of 6 m (above NAP) and a slope 1:7 for all the dikes in the area. For scenario 1, the probability of failure due to wave overtopping ($P_{f1}$) ranges from 1.1 x $10^{-4}$ to 3.1 x $10^{-2}$ per year with an average value of 4.6 x $10^{-3}$ per year (Figure 5.12a). These variations in $P_{f1}$ are due to: i) the level of exposure—where areas behind inlets are exposed to higher values of $H_{m0,deep}$ and $T_{m-1,0,deep}$ compared to those behind the barrier islands; ii) variations in the mean water level ($\bar{\eta}$), where values in the West can be approximately 0.5 m lower than those in the East for the same return period event; and iii) the amount of wave dissipation that occurs due to depth-induced wave breaking over the foreshore—where attenuation is greater at locations with higher foreshore elevations.

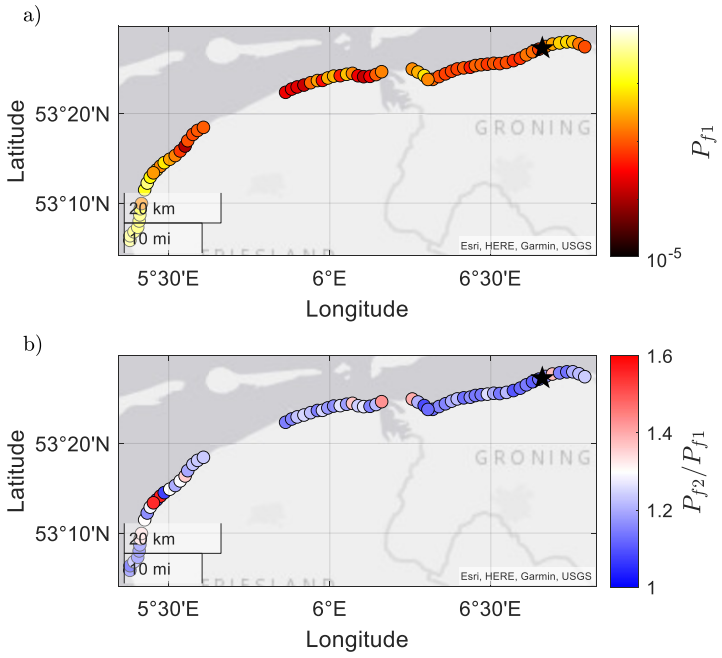


**Figure 5.12** *Spatial variation in the probability of dike failure by wave overtopping for a) scenario 1: SS ($P_{f1}$) and b) scenario 2: SS + IG relative to scenario 1 ($P_{f2}/P_{f1}$) across the wider Dutch Wadden Sea area for dikes with identical crest heights ($z_c$ = 6m) and dike slopes ($cot\ (\alpha)$ = 7).*

To demonstrate this, we examine the variations in $P_{f1}$ against physical parameters for a proxy storm with an exceedance probability of 1/3000 per year. In Figure 5.13a, an offshore forcing parameter ($H_{m0,deep}^2 T_{m-1,0,deep}$), which is proportional to the offshore energy flux, is used to represent the combined influence of $H_{m0,deep}$ and $T_{m-1,0,deep}$.

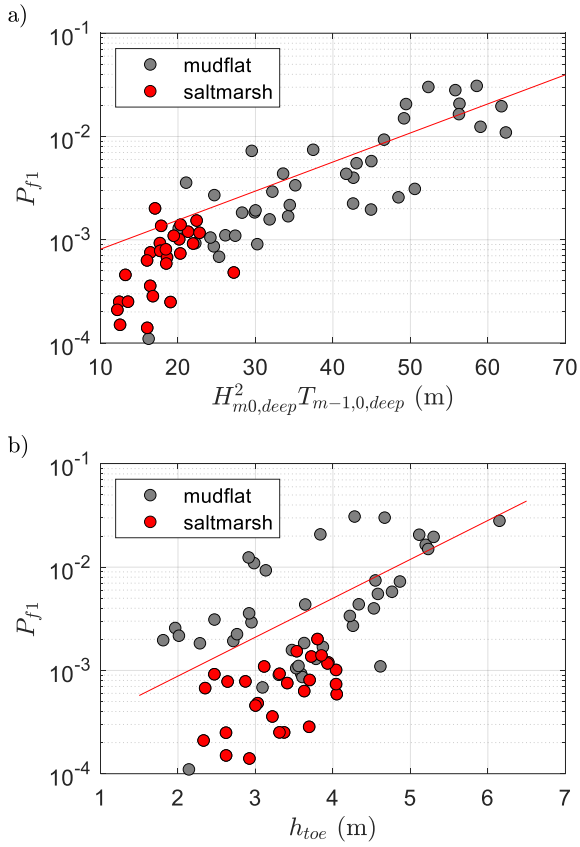


**Figure 5.13** *Relationship between probability of failure for scenario 1 (SS) and a) an offshore forcing parameter (and b) the water depth at the dike toe ($h_{toe}$), across the wider Dutch Wadden Sea area. Lines indicate best-fit through the data.*

In Figure 5.13b, the influence of variations in $\bar{\eta}$ and the bed level at the toe ($z_{b,toe}$) are represented by $h_{toe} = \bar{\eta} - z_{b,toe}$. The calculated $P_{f1}$ shows a strong positive relationship with $H^2_{m0,deep}T_{m-1,0,deep}$ ($R^2$= 0.65), meaning that higher forcing results in higher failure probabilities. Though the correlation with $h_{toe}$ is lower ($R^2$ = 0.43), there is a trend of increasing $P_{f1}$ with increasing $h_{toe}$. This is because larger $h_{toe}$ values lead to higher wave heights at the toe due to less wave breaking. Likewise, higher water levels ($\bar{\eta}$) associated with larger $h_{toe}$ values, also lead to lower freeboards which results in higher overtopping volumes. Figure 5.13 also highlights that dikes fronted by mudflats typically have higher $P_{f1}$-values than those with saltmarshes, as saltmarshes accrete higher bed levels which in-turn promote more SS-wave attenuation by breaking.

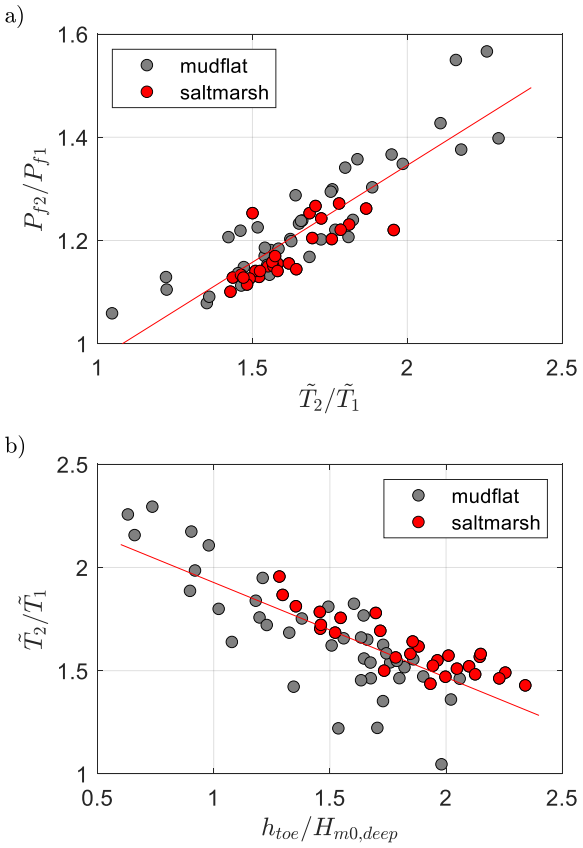


**Figure 5.14** *a) Relationship between the change in probability of failure due to IG waves ($P_{f2}/P_{f1}$) and the increase in relative spectral wave period at the toe ($\tilde{T}_2/\tilde{T}_1$); and b) relationship between $\tilde{T}_2/\tilde{T}_1$ and the relative water depth ($h_{toe}/H_{m0,deep}$), across the wider Wadden area. Note that $\tilde{T}$ is a stand-in for $T_{m-1,0,toe}/T_{m-1,0,deep}$. Subscripts 1 and 2 refer to scenarios 1 and 2, respectively.*

In order to identify the influence of the IG waves, the probability of failure by wave overtopping in scenario 2 relative to that of scenario 1 ($P_{f2}/P_{f1}$) is assessed. Figure 5.12b shows that $P_{f2}/P_{f1}$ ranges from 1.1 to 1.6, with an average value of 1.2. This increase in $P_f$ is due predominantly to the increase in $T_{m-1,0,toe}/T_{m-1,0,deep}$ (at the design point) between scenario 2 and scenario 1—represented by $\tilde{T}_2/\tilde{T}_1$ (Figure 5.14), where $\tilde{T} = T_{m-1,0,toe}/T_{m-1,0,deep}$ and subscripts 1 and 2 represent scenarios 1 and 2, respectively. Figure 5.14a shows a strong positive relationship between $P_{f2}/P_{f1}$ and $\tilde{T}_2/\tilde{T}_1$ ($R^2$ = 0.76), where a factor 2 increase in spectral wave period ($\tilde{T}_2/\tilde{T}_1$) corresponds to a 1.5 times increase in the failure probability ($P_{f2}/P_{f1}$). On the other hand, the increase in wave height at the toe (due to the

IG waves) between the two scenarios was negligible (0.5 to 4.5%) compared to the increase in wave period.

As $T_{m-1,0,toe}/T_{m-1,0,deep}$ depends largely on the offshore wave height, water depth at the toe and foreshore slope (Equation 5.13), the spatial variations in $P_{f2}/P_{f1}$ (Figure 5.12b) are due to variations in local bathymetric and forcing conditions. This is further demonstrated in Figure 5.14b by examining the relationship between the increase in spectral wave period ($\tilde{T}_2/\tilde{T}_1$) and the relative water depth under proxy storm conditions (1/3000 per year). The relative water depth parameter, which takes into account the variations in both local water depth ($h_{toe}$) and offshore wave height ($H_{m0,deep}$), shows a clear negative relationship with $\tilde{T}_2/\tilde{T}_1$ ($R^2$ = 0.61). Therefore, areas with low water depths at the toe and/or large offshore waves are expected to have a greater IG-wave influence on $T_{m-1,0,toe}$. It should be noted that the increase in spectral wave period due to IG waves is also sensitive to the estimated foreshore slope (Equation 5.13). However, as the foreshores in the Wadden Sea can all be considered very gentle (1:600, on average), the foreshore slope showed little correlation with $\tilde{T}_2/\tilde{T}_1$ ($R^2 < 0.1$).



## 5.4 DISCUSSION

### 5.4.1 MODELLING APPROACH

The combined numerical and empirical approach to wave transformation proved accurate when compared to the 2015 and 2017 storm data at Uithuizerwad, also highlighting the growth of $\widetilde{H}_{IG}$ (Figure 5.7) and the associated increase in $T_{m-1,0}/T_{m-1,0,deep}$ (Figure 5.8) as the water depth becomes shallower. Of particular note, is the difference in $T_{m-1,0,toe}/T_{m-1,0,deep}$ calculated by the phase-averaged wave model SWAN compared to measurements. While the measurement data is likely contaminated by IG waves reflected from the dike, leading to longer wave periods, there is still a gross underestimation of $T_{m-1,0,toe}/T_{m-1,0,deep}$ by SWAN due to its exclusion of IG-wave dynamics (Lashley et al., 2020b). Despite this, SWAN was able to accurately model SS-wave transformation over the foreshore (Figure 5.6). Likewise, the growth of $\widetilde{H}_{IG}$ (Figure 5.7) and $T_{m-1,0}/T_{m-1,0,deep}$ (Figure 5.8) at the dike toe are accurately captured using Equations 5.12 and 5.13, respectively.

The probabilistic method FORM was able to compute the $P_f$ within 20 to 30 iterations with a computation time of under 10 minutes per dike section. Other methods, such as Crude Monte Carlo or Numerical Integration are known to be much more computationally demanding. However, other approaches such as Adaptive Directional Importance Sampling (Den Bieman et al., 2014) may also prove to be equally suitable for this application. This short computation time is also attributed to the use of a phase-averaged wave model (SWAN),

which is roughly 100 times faster than its phase-resolving counterparts (e.g. SWASH or XBeach Nonhydrostatic) (Lashley et al., 2020b).

As the dike characteristics (crest level, slope and critical overtopping discharge) typically dominate the probabilistic analysis, their treatment as deterministic variables here allowed the analysis to focus on the influence of foreshore parameters. Furthermore, by treating the influence of the IG waves as a separate module (Section 5.2.3.2), calculations with and without IG waves could be easily performed. Such a modular approach allows the framework to be easily modified or adapted to varying conditions. For example, the module to calculate the actual overtopping discharge could be extended with the formulae of Lashley et al. (2021) for environments where the conditions at the structure toe are extremely shallow, or in the case of vertical seawalls rather than sloping structures. Likewise, another numerical or empirical model more suited to the specific area of application could replace the model used here for SS-wave transformation (SWAN). This makes the overall approach easily adaptable and applicable to other coastlines where IG waves may play a critical role, such as the Belgian coast (Altomare et al., 2016), Japanese coast (Mase et al., 2013) and north and south coasts of Vietnam (Nguyen et al., 2020).



### 5.4.2 APPLICABILITY OF FORMULAE FOR THE ACTUAL OVERTOPPING DISCHARGE

In the present study, the original overtopping formula of Van Gent (1999) (Equation 5.14) was applied to all locations. This formula was selected because it was developed specifically for shallow foreshores considering the influence of both SS and IG waves and is considered valid for a wide range of breaker parameter ($\xi_{m-1,0}$ ) values.

However, applying Equation 5.14 here—to locations with $\xi_{m-1,0}$ < 5 at the design point—does not coincide with the current standard (EurOtop, 2018). In EurOtop (2018), different formulae are applied depending on $\xi_{m-1,0}$ value (Van der Meer and Bruce, 2014;Altomare et al., 2016). An analysis of the different approaches revealed the following points:

- For $\xi_{m-1,0}$ < 1.8, which is typical for $\cot(\alpha)$ = 7, the spectral wave period showed a considerable influence on the overtopping discharge ($q_a$) calculated using the EurOtop (2018) approach. Figure 5.15a shows that a 1.5 times increase in wave period (due to IG waves) ($\tilde{T}_2/\tilde{T}_1$), resulted in an order of magnitude increase the $P_f$ using the EurOtop (2018) approach. Since the EurOtop (2018) formula for $\xi_{m-1,0}$ < 1.8 (Van der Meer and Bruce, 2014) was not derived for shallow foreshore conditions (with IG waves), this significant increase in the $P_f$ is likely incorrect and requires further research.
- For 1.8 < $\xi_{m-1,0}$ < 5, which is typical for $\cot(\alpha)$ = 3, the wave period no longer influences the EurOtop (2018) calculation, as a maximum $q_a$ is reached. This is

evident in Figure 5.15b as no clear trend between $\tilde{T}_2/\tilde{T}_1$ and $P_{f2}/P_{f1}$ is visible for the EurOtop (2018) calculations. In these cases, the differences between EurOtop (2018) and the original Van Gent (1999) calculations are much smaller (Figure 5.15b) compared to Figure 5.15a.

- For $\xi_{m-1,0}$ > 7 or wave steepness at the toe < 0.01, the modified version of the Van Gent (1999) formula (Altomare et al., 2016), described in EurOtop (2018) are valid for foreshore slopes steeper than or equal to 1:250. However, the modified approach, based on an equivalent slope concept (Altomare et al., 2016), is only applicable to foreshore slopes steeper than 1:250. As the foreshore slopes of the Wadden Sea are typically gentler than 1:500, the modified formulae could not be used here. Therefore, locations meeting these criteria were excluded for the EurOtop (2018) calculations.
- The results using the original Van Gent (1999) formula were of the same order of magnitude for both dike slopes considered (Figure 5.15), suggesting that the formula was not very sensitive to changes in $\xi_{m-1,0}$. However, it should be noted that this formula was derived using a limited dataset with $\cot(\alpha)$ = 2.5 and 4 and $\cot(m)$ = 100 and 250. Therefore, future studies should verify its performance for conditions with $\cot(\alpha)$ > 4 and $\cot(m)$ > 250.



The above findings suggest that the EurOtop (2018) approach may be incorrect for shallow foreshore conditions with gentle dike slopes (e.g. 1:7), which often have $\xi_{m-1,0}$ < 1.8. The source of this uncertainty lies in the sensitivity of the formulae to $T_{m-1,0,toe}$, a parameter whose magnitude increases proportionally with the magnitude of the IG waves (Appendix D).

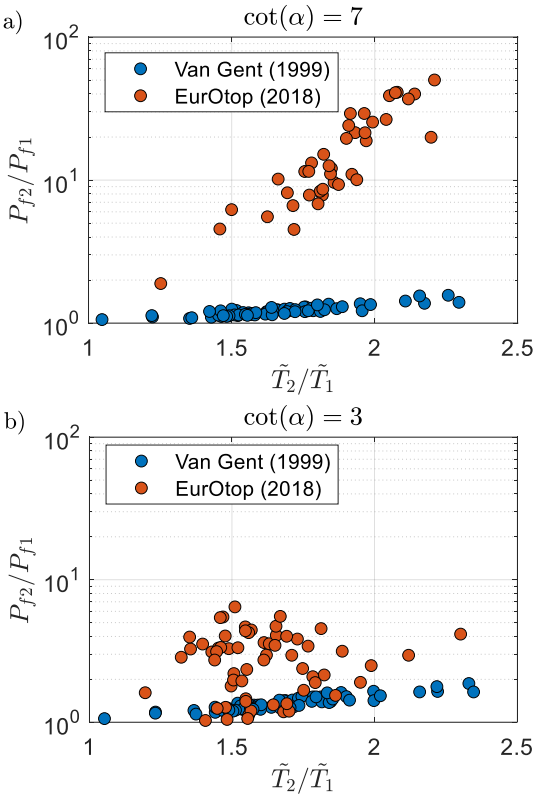


**Figure 5.15** *Relationship between the change in probability of failure due to IG waves ($P_{f2}/P_{f1}$) and the increase in relative spectral wave period at the toe ($\tilde{T}_2/\tilde{T}_1$) calculated using the original Van Gent (1999) and EurOtop (2018) approaches for the actual overtopping discharge. Note that cases with wave steepness at the toe < 0.01 were excluded from the EurOtop (2018) calculations since the equivalent slope concept could not be applied (Section 5.4.2).*

### 5.4.3 INFLUENCE OF IG WAVES ON DESIGN PARAMETERS

The influence of IG waves may be represented as an increase in the magnitude of both design parameters ($H_{m0,toe}$ and $T_{m-1,0,toe}$), compared to a situation where the IG waves are neglected. This was demonstrated in Chapter 3 (Lashley et al., 2020b), where the relative magnitude of the IG waves ($\tilde{H}_{IG} = H_{m0.IG,toe}/H_{m0,SS,toe}$) > 0.5 and the IG waves had a notable influence on both parameters.

In the present study, $\tilde{H}_{IG}$ was much lower, ranging from 0.14 to 0.35 with a mean value of 0.19 (considering proxy storm conditions with 1/3000 per year exceedance probability). As a result, the impact of the IG waves on the total wave height at the toe was negligible (0.5 to 4.5%), since $H_{m0,toe} = \sqrt{H_{m0,IG,toe}^2 + H_{m0,SS,toe}^2}$. That said, there was still a notable increase

in $T_{m-1,0,toe}$. This is attributed to: i) the sensitivity of $T_{m-1,0}$ to wave energy density at low frequencies, by definition (Equation 5.9); and ii) the influence of the foreshore slope on the shape of the wave spectrum at the toe—where gentler foreshore slopes lead to wider surf zones and more energy transfer to lower frequencies. This is demonstrated in Figure 5.16 using the results of two numerical simulations (XBeach Nonhydrostatic). The increase in $T_{m-1,0,toe}$ due to IG waves is larger for the 1:500 foreshore slope than the 1:50, despite having similar $\widetilde{H}_{IG}$ values (Figure 5.16, Table 5.4). Table 5.4 also shows that while the influence of the IG waves on $T_{m-1,0,toe}$ is noteworthy, their influence on the total wave height at the toe ($H_{m0,toe}$) is negligible.

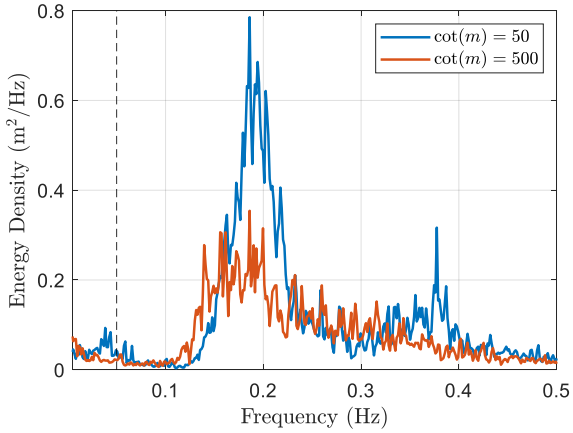


**Figure 5.16** *Results of XBeach numerical simulations showing wave spectra at the dike toe for a 1:50 and 1:500 foreshore slope, under the same offshore forcing conditions ($H_{m0,deep}$ = 1 m, $T_{m-1,0,deep}$ = 4.54 s and $h_{toe}$ = 1 m). Dashed vertical line indicates the frequency separating IG and SS wave motions.*

**Table 5.4** *Results of XBeach Nonhydrostatic simulations taken at the dike toe for two different foreshore slopes under the same offshore forcing conditions ($H_{m0,deep}$ = 1 m, $T_{m-1,0,deep}$ = 4.54 s and $h_{toe}$ = 1 m).*

| $\cot(m)$ | $H_{m0,toe}$ | $H_{m0,SS,toe}$ | $H_{m0,IG,toe}$ | $\widetilde{H}_{IG}$ | $T_{m-1,0,toe}$ (SS only) | $T_{m-1,0,toe}$ (SS + IG) |
|---|---|---|---|---|---|---|
| 50 | 0.98 m | 0.97 m | 0.15 m | 0.16 | 4.61 s | 5.98 s |
| 500 | 0.80 m | 0.79 m | 0.14 m | 0.17 | 4.80 s | 7.22 s |

The main takeaway here is that while IG waves may have a negligible influence on the design wave height at the structure, their influence on the design wave period can be considerable and should therefore not be neglected, particularly on gentle foreshore slopes.

### 5.4.4 INFLUENCE OF SALTMARSH VEGETATION

Another discussion point is the influence of saltmarsh vegetation and whether its effects should be considered for very high return period events. Figure 5.9 suggests that safety could be significantly improved by standing saltmarsh vegetation; however, these findings must be interpreted with caution. In their analysis based on dikes with foreshores in the Wadden Sea, (Vuik et al., 2018b) included a stem-breakage model and concluded that it was very likely that almost all vegetation would break under extreme forcing—resulting in $P_f$ values similar to that of a non-vegetated foreshores. This flattening and breaking of saltmarsh vegetation under storm conditions was also reported by Möller et al. (2014) who conducted large-scale flume experiments with transplanted Wadden Sea vegetation.

Moreover, though the vegetation component of Equation 5.12 was able to capture the influence of vegetation on IG waves for the two storms considered here (Figure 5.6 to Figure 5.8), its performance for more extreme events requires further validation. This is due to the low stem height to water depth ratio ($h_{toe}/h_v$ = 3.3) considered in its derivation. As a result, Equation 5.12 may overestimate the influence of vegetation for high return-period events with $h_{toe}/h_v \approx 13$. Thus, the influence of saltmarsh vegetation on coastal safety under extreme forcing remains an important issue for future research.

### 5.4.5 IMPLICATIONS FOR PRACTICE

Including the effects of IG waves (scenario 2) increases the $P_f$ by up to two times, compared to scenario 1 (Figure 5.9 and Figure 5.12b). This effect is considerably smaller than that reported by Oosterlo et al. (2018), where including the IG waves increased the $P_f$ by two orders of magnitude. This means that the findings of Oosterlo et al. (2018) were indeed case-specific and due to the (potentially inappropriate) use of empirical overtopping formulae that were not formulated specifically for situations with IG waves (Van der Meer, 2002), as discussed in Section 5.4.2.

But what does the presence of IG waves mean for practice? In general, the reliability of the existing defences may be overestimated since IG waves are largely neglected in their assessment. By interpolating the results of Figure 5.10 logarithmically, the required crest level at Uithuizerwad for a fixed target probability of failure can be determined. For a target annual failure probability of 1/1000 per year (which corresponds to the safety standard), a crest level of 6.3 m (+ NAP) is needed for scenario 1 (SS). For scenario 2 (SS + IG), the required crest level is 6.5 m. Therefore, the influence of the IG waves may be alternatively seen as an increase in the required crest level of around 0.2 m with a cost in the order of magnitude of M€1/per km (Jonkman et al., 2013). If the influence of the IG waves on the $P_f$ were one order of magnitude larger, as suggested by the EurOtop (2018) formula (Figure 5.15a), then the increase in the required crest level would be around 0.8 m with an order of magnitude increase in cost (M€10/per km).

This increase in $P_f$ is attributed to the growth of $T_{m-1,0,toe}$ due to the IG waves and the well-known relationship between wave overtopping and wave period, where longer waves (larger $T_{m-1,0,toe}$ values) result in more overtopping (Section 5.2.4.1) and, by extension, higher $P_f$ values. These findings suggest that attention should also be given to changes in wave period, and not on wave height attenuation alone, when considering the influence of shallow foreshores on safety. However, it is important to stress that this effect is highly dependent on local conditions, as $T_{m-1,0,toe}/T_{m-1,0,deep}$ (Equation 5.13) is dependent on the offshore wave height, the water depth at the toe and the estimated foreshore slope. Therefore, it should be assessed on a case-by-case basis rather than assumed constant over a large area. This spatial variability is demonstrated in Figure 5.12b.

Additionally, the calculated $P_{f2}$ was found to be sensitive to the uncertainty in Equations 5.12 and 5.13 (Figure 5.11), which are based primarily on numerical simulations since field and physical model data are lacking. Future studies should carry out experiments to further validate and improve the empirical formulations presented here and, if possible, reduce the uncertainty (scatter) in their estimates.

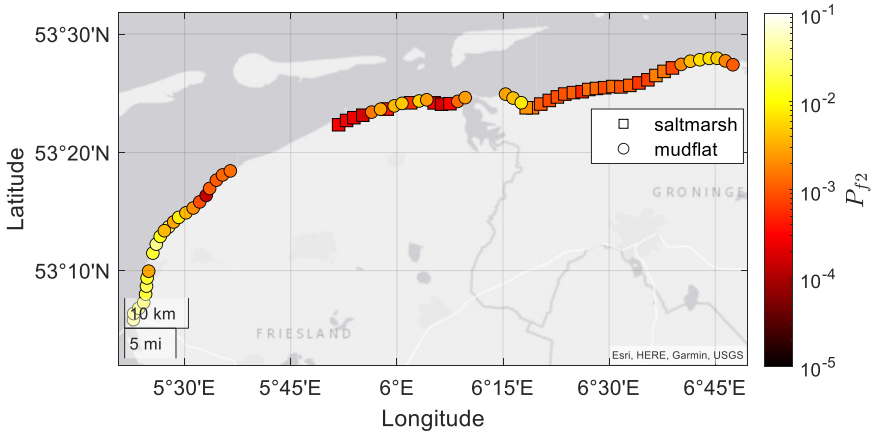


**Figure 5.17** *Influence of raised bed levels due to saltmarshes on the spatial variation in the probability of dike failure by wave overtopping for scenario 2: SS + IG waves ($P_{f2}$) across the wider Dutch Wadden Sea area for dikes with identical crest heights ($z_c$ = 6m) and dike slopes ($cot\ (\alpha)$ = 7).*

Even though vegetation itself was neglected in the probabilistic analysis of the wider Wadden Sea area, findings here advocate the importance of maintaining saltmarshes; as (higher) saltmarsh platforms attenuate more SS waves than lower mudflats, which results in lower $P_f$ values—even when IG waves are taken into account (Figure 5.17). These findings support the arguments of Zhu et al. (2020) for the net positive impact of shallow foreshores on coastal safety. However, the estimated increase in safety due to the foreshore may be reduced when

IG waves are included in the analysis—in particular where wave overtopping is concerned. In planning and implementing foreshore systems, it is therefore important to consider the effects of IG waves on safety as well.

## 5.5 CONCLUSION



In this paper insight has been given into the influence of infragravity (IG) waves on the probability of failure by wave overtopping ($P_f$) for dikes fronted by shallow foreshores. This was achieved by incorporating an empirical expression for the IG-wave height at the toe (Equation 5.12 (Lashley et al., 2020a)) and a newly derived expression for the spectral wave period at the toe (Equation 5.13) into a probabilistic framework (Vuik et al., 2018b). The combined numerical and empirical wave modelling approach was first validated using data collected at Uithuizerwad, during two storms with an exceedance probability of 1/5 per year. It was able to reproduce the wave transformation processes associated with shallow foreshores under extreme conditions with reasonable accuracy, namely: i) the dissipation of incident SS waves by depth-induced breaking; ii) the increase in the relative magnitude of the IG waves ($\widetilde{H}_{IG}$); and iii) the increase in the relative spectral wave periods ($T_{m-1,0}/T_{m-1,0,deep}$).

For the Uithuizerwad case, it has been shown that $P_f$ increases by 1.3 times if IG waves are included. This was attributed to the increase in wave period ($T_{m-1,0,toe}$) and, to a lesser extent, wave height ($H_{m0,toe}$) at the toe, which in turn leads to larger values of wave overtopping. The probabilistic framework was then applied to several locations along the Dutch Wadden Sea for a spatial analysis. Overall, including the influence of IG waves increased the $P_f$ across all locations with the magnitude of the increase ($P_{f2}/P_{f1}$) varying from 1.1 to 1.6. Findings indicate that 76% of this variation is explained by the increase in $T_{m-1,0,toe}$, as larger values lead to an increase in overtopping discharge. This increase is due to the IG waves and is highly dependent on the water depth and offshore wave height at each location.

The sensitivity of the calculated $P_f$ to changes in $T_{m-1,0,toe}$ (Figure 5.13a) compared to changes in $H_{m0,toe}$ also suggests that wave height attenuation alone is not a sufficient metric to evaluate the influence of shallow foreshores on safety. It is recommended that future studies assess changes in both wave height and period over the foreshore, which can be estimated using the empirical formulations proposed in Chapter 2 (Lashley et al., 2020a) and this chapter, respectively.

The main conclusion of the present work is that IG waves can have a negative effect on safety. The magnitude of the impact varied considerably depending on the empirical wave overtopping formula applied—where a maximum increase of 1.6 times the $P_f$ was found

with the Van Gent (1999) formula compared to an 88 times increase when EurOtop (2018) was applied. Here, the Van Gent (1999) formula was considered more appropriate since both SS and IG waves were considered in its derivation. It is thus important that coastal engineers, dike managers and decision makers consider this when assessing coastal flood risk. The methods proposed in this paper can aid in this by allowing practitioners to quickly identify areas where IG waves—and therefore tools which account for them—should be included in the analysis. Furthermore, given the modular characteristic of the approach, it could be easily fitted with different tools or adapted to other coastlines where IG waves may play a significant role.



The generalisability of these results is however subject to certain limitations. For instance, the analyses were conducted assuming a fixed dike height with a constant slope at each location. Therefore, it is recommended that the analyses be repeated using the actual dike geometries. Likewise, in this study we have validated and applied the framework to the Dutch Wadden Sea, but it is recommended that the framework be further applied at tested for other sites where IG waves play a role. Examples of such sites include the sandy foreshores along the Belgian coast (Altomare et al., 2016), the wide shelfs of the Mekong Delta, Vietnam (Nguyen et al., 2020) and the steep foreshores found in Japan (Mase et al., 2013). It must also be noted that the current study did not consider edge or leaky (free) IG waves (Reniers et al., 2021). Therefore, additional field campaigns focused on measuring IG waves would provide much needed insight into IG-wave dynamics in the Dutch Wadden Sea and provide more data to validate the tools implemented here; particularly, for more extreme conditions. It is also very important that the applicability of the existing empirical formulae for wave overtopping to conditions with IG waves be critically assessed given the sensitivity of the formulae to the presence of IG waves. Finally, while vegetation had a notable influence on wave attenuation for storms with relatively high probability of exceedance (1/5 per year, Figure 5.6), it was assumed to be flattened or broken under more extreme conditions (Vuik et al., 2018a). Further research is required to assess the attenuation effects of saltmarsh vegetation under extreme water level and wave forcing.

# 6

# CONCLUSIONS AND RECOMMENDATIONS

This chapter concludes the dissertation by readdressing the research aim (Section 6.1) and explaining the scientific and practical implications of the findings (Section 6.2). The limitations of the research are also acknowledged in Section 6.3 along with recommendations for future research.

## 6.1 CONCLUSIONS

Coastal defences around the world are typically designed to resist the volume of water that may overtop them due to wave action during storms. While the methods used in current practice are able to accurately estimate the impact of wind-sea and swell (SS) waves, they do not explicitly address infragravity (IG) waves, which often dominate at shallow coasts. As a result, the influence of IG waves on safety along coasts protected by structures with shallow foreshores remained unknown. In light of this, this dissertation aimed to:

> *Develop new methods to estimate the influence of IG waves on the safety of coastal defences with shallow foreshores against wave overtopping.*

This aim was achieved by analysing numerical model, physical model and field data in order to derive new empirical formulae that account for the influence of IG waves. The newly-derived formulae accurately captured the effects of IG waves on the design wave height (Chapter 2) and period at the structure (Chapter 5), and the magnitude of the wave overtopping discharge. For wave overtopping, two methods were proposed: the first augments the traditional approach, where phase-averaged numerical modelling is first used to estimate wave parameters at the toe, followed by an empirical estimate of the wave overtopping (Chapter 3); while the second approach, which is fully empirical, uses deep-water wave parameters as input and directly accounts for IG waves (Chapter 4). These tools were then assembled into a probabilistic framework capable of quantifying the impact of IG waves on safety along the Dutch Wadden Sea coast.

The general conclusion of the dissertation is that IG waves can have an important impact on safety. Moreover, findings indicate that the safety of existing coastal defences with shallow

foreshores may be overestimated, since IG waves are largely neglected in the current practice for their design and assessment. The specific conclusions and major findings of the research are detailed below as answers to the research questions (RQ's) formulated in Section 1.3:

**RQ1. Under what conditions do IG waves dominate wave conditions at the toe of the dike?**



To answer this RQ, a parameter representing the significance of the IG waves at the structure toe was established. It was based on the ratio of the significant IG to SS wave heights at the structure. IG-wave dominance was then defined as the condition where the significant IG wave height exceeds that of the SS waves. The response of this parameter to varying environmental conditions was then assessed by means of numerical (XBeach) simulations.

It was evident from the numerical simulations and limited physical model tests (Chapter 2) that higher[1], directionally narrow-banded (long-crested)[2] offshore waves; shallower foreshore water depths[3]; milder foreshore slopes[4]; and reduced vegetated cover [5] give rise to IG-wave dominance. These findings are summarised in Figure 6.1. Results also indicated that IG waves experience near-complete reflection at the structure, resulting in IG waves becoming even larger at the structure toe[6].

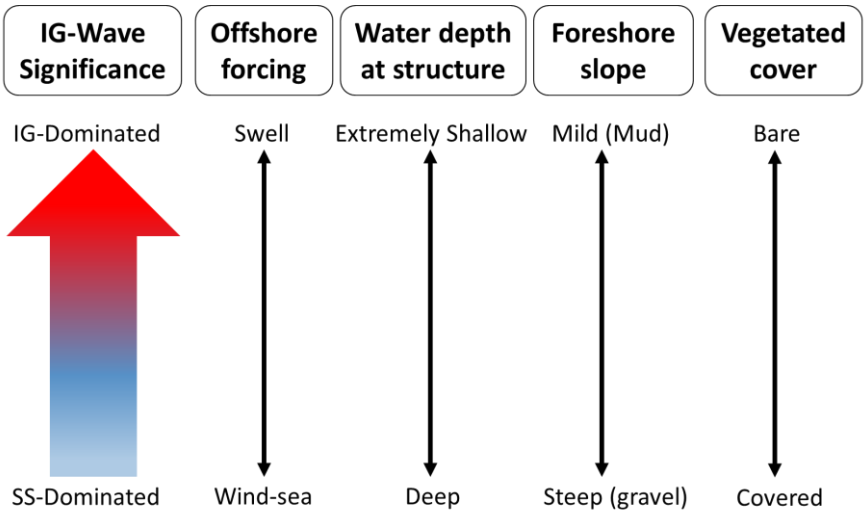


**Figure 6.1**: *Diagram describing when and where IG waves are expected to be significant based on the findings of Chapter 2.*

[1] Figure 2.9
[2] Figure 2.12
[3] Figure 2.14
[4] Figure 2.17
[5] Figure 2.20
[6] Figure 2.4c

In addition, an empirical method—based on the numerical dataset produced—was developed to estimate the relative magnitude (or significance) of the IG waves based on the above-mentioned environmental parameters (Figure 6.2).

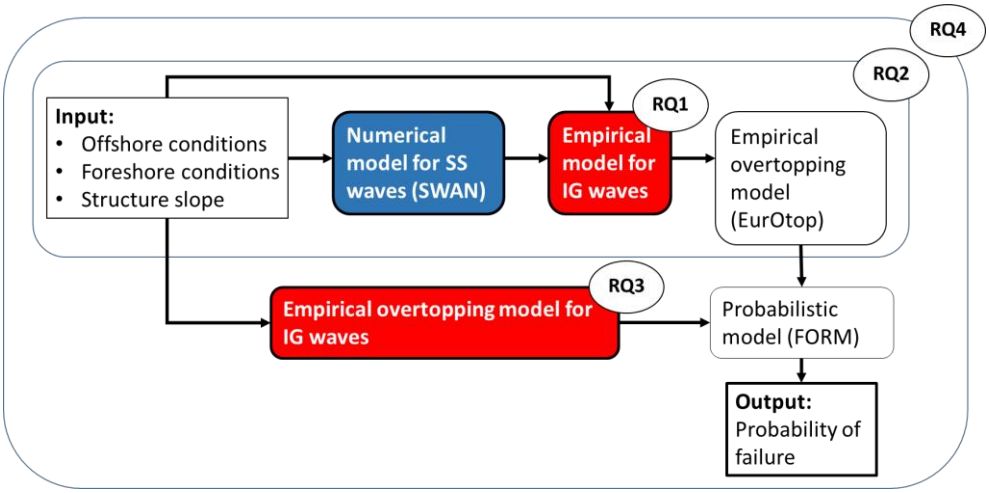


**Figure 6.2***: Framework developed in this dissertation to estimate the safety and probability of failure by wave overtopping, including the effects of IG waves (RQ4, Chapter 5), showing: the empirical method for the relative magnitude of the IG waves (RQ1, Chapter 2), the combined numerical and empirical method to estimate the overtopping discharge (RQ2, Chapter 3); and the alternative approach based on deep-water wave parameters (RQ3, Chapter 4).*

**RQ2. Is there a trade-off between numerical model accuracy and the computational load required to simulate wave overtopping in IG-wave dominated environments?**

The accuracy and computational demand of six, widely-used numerical approaches to estimating wave overtopping were assessed and compared. The analysis included models that calculated wave overtopping directly (OpenFOAM, SWASH, XBeach Non-hydrostatic and XBeach Surfbeat) and SWAN, which must be combined with overtopping formulae (e.g. (EurOtop, 2018)). The accuracy of each model was determined by comparing their predictions to measurements of wave overtopping made during physical model tests—under IG-wave dominant conditions. The associated simulation time for each model was also recorded and used to assess computational demand.

The results highlighted an important point, that using more computationally-demanding models does not guarantee improved accuracy in the prediction of nearshore wave parameters or overtopping discharge[7]. Phase-averaged models (e.g. SWAN) are typically the least computationally demanding but they inherently exclude IG-wave dynamics. This makes

[7] Figure 3.16

them very attractive computationally but inaccurate for IG-wave dominated environments. However, in this dissertation it is shown that SWAN can perform on par, if not better, than more complex models in the prediction of mean overtopping discharge. This is made possible by combining SWAN with the empirical model developed in Chapter 2 to account for IG waves and the (EurOtop, 2018) overtopping formulae (Figure 6.2).

**RQ3. How can empirical estimates of wave overtopping be improved to account for very shallow foreshores where IG waves dominate?**



Given the difficulty in obtaining accurate estimates of wave parameters at the dike toe under IG-wave dominant conditions, there was need for an empirical overtopping model based on deep-water parameters, which are typically obtained easily and with high-accuracy. This was achieved by revisiting the Goda et al. (1975) graphical approach for vertical structures—where the overtopping discharge was modelled as a function of the following deep-water parameters: relative water depth, relative freeboard, foreshore slope and deep-water wave steepness. By combining this approach with new datasets and trend analyses, new overtopping formulae for both vertical and sloping structures were formulated for very to extremely shallow conditions. These formulae proved more accurate and wide-ranging than the existing method[8] and may serve as alternatives to the more common approach, which require wave parameters at the toe as input. This deep-water parameter approach is particularly useful as it removes the need for additional numerical modelling (Figure 6.2). Despite this advancement, the new formulae are still limited to a 1D assumption, as capturing the 2D effects of the foreshore on wave overtopping remains a challenge.

**RQ4. What is the influence of IG waves on the probability of dike failure by wave overtopping along the Dutch Wadden Sea coast?**

In Chapter 5, the approaches developed in Chapters 2 to 4 were combined with the First Order Reliability Method (FORM) to estimate the probability of dike failure by wave overtopping along the shallow Dutch Wadden Sea coast. By using a modular approach, where the IG waves are treated as a separate component (RQ1 in Figure 6.2), the failure probability with and without the IG waves could be easily determined.

Including the IG waves resulted in 1.1 to 1.6 times higher failure probabilities for the Dutch Wadden Sea coast, suggesting that coastal safety may be overestimated when they are neglected. This was attributed to the influence of the IG waves on the wave period and, to a lesser extent, the wave height at the structure toe. Additionally, the spatial variation in this effect observed for the Dutch Wadden Sea highlights its dependence on local bathymetric

[8] Figure 4.7 to Figure 4.13

and offshore forcing conditions—with IG waves having greater influence on the failure probability for cases with larger offshore waves and shallower water depths.

The effect of the IG waves on safety varied considerably depending on the empirical wave overtopping formula applied—where a maximum increase of 1.6 times the $P_f$ was found with the Van Gent (1999) formula compared to an 88 times increase when EurOtop (2018) was applied. As the Van Gent (1999) formula was derived specifically for shallow foreshores considering IG waves, it was considered more appropriate to quantify the impact of the IG waves here. It is thus important that coastal engineers and dike managers use appropriate tools, such as Van Gent (1999) and those developed in Chapter 4, when assessing wave overtopping at dikes with shallow and very shallow foreshores, respectively.



## 6.2 RECOMMENDATIONS FOR PRACTICE

The findings of this dissertation provide insights not only for scientists (as outlined above in the answers to the research questions) but also for practitioners in the field of coastal defence reliability. For practitioners, the main question follows: should they be concerned with IG waves? Using the empirical methods developed in this dissertation, the answer to this question may be obtained rather quickly. The empirical method developed in Chapter 2 (RQ1) should be applied first for a quick estimate of the relative magnitude of the IG waves for design conditions at the location being considered. If the calculation indicates that IG waves are significant, then the methods of Chapters 3 (RQ2) or 4 (RQ3) should be used to estimate the actual overtopping discharge. Finally, the combined framework of Chapter 5 (RQ4) can be used to estimate the probability of dike failure, considering the spatial and temporal variability in the offshore forcing and dike resistance parameters.

Whether or not IG waves are expected to be significant depends on the environmental conditions at the specific location under consideration. For example, it is expected that IG waves will play a more critical role at a structure with a wide and shallow mudflat foreshore, exposed to large swell compared to a beach with a steeper sandy foreshore exposed to smaller, locally-generated wind waves and deeper water (Chapter 2 and Figure 6.1). However, it should be noted that IG waves do not need to dominate conditions at the toe—where their amplitude exceeds that of the SS waves—in order to affect coastal safety, as seen for the Dutch Wadden Sea coast where the ratio of IG to SS waves at the toe was around 0.15 (Chapter 5). This is due to the sensitivity of wave overtopping to the spectral wave period at the dike toe, which is very sensitive wave motions at IG frequencies (discussed in Chapters 3 and 4).

Therefore, it is recommended that IG waves always be considered when assessing wave overtopping at structures with shallow foreshores. The approach developed here proved accurate when compared to field data at one location along the Dutch Wadden Sea coast. However, additional field campaigns focused on measuring IG waves would provide much

needed insight into IG-wave dynamics in the Dutch Wadden Sea and provide more data to validate the tools implemented here; particularly, for more extreme conditions. These campaigns should form transects of at least 1 km, at different locations across the Dutch Wadden Sea (from say Harlingen to Eemshaven) and measure not only surface elevations but also current velocities (e.g. using Acoustic Doppler Current Profilers (ADCPs)) with measurement durations sufficiently long (≥ 20 minutes) to accurately capture the IG waves.



While the presence of IG waves leads to higher-than-expected wave overtopping discharges, shallow foreshores still have a net positive impact on the magnitude of wave overtopping at coastal structures (Chapter 5). This is also discussed in Chapter 4, where the overtopping discharge continues to decrease as the water depth becomes shallower; however, the rate of that decrease is reduced due to the influence of the IG waves. Therefore, the accurate design and implementation of foreshores as part of mitigating coastal flood risk requires consideration of IG waves.

Towards that goal, this dissertation provides practitioners with a suite of tools to quantify to influence of IG waves on the safety of coastal defences with shallow foreshores against wave overtopping (Figure 6.2). Thereby, reducing the uncertainty in the overall the impact of shallow foreshores and allowing dike managers to make more informed decisions when considering hazard mitigation strategies.

## 6.3 LIMITATIONS AND RECOMMENDATIONS FOR FUTURE WORK

The generalisability of these results is subject to certain limitations. For instance:

- The scope of this dissertation was limited to IG waves generated by either the breakpoint forcing (which dominates steeper slopes) or the bound wave shoaling (dominates milder slopes) mechanisms (both discussed Chapter 2). It therefore did not consider the influence of free IG waves generated from distant sources (leaky waves) or long-shore propagating IG waves (edge waves). Future studies should investigate the relevance of leaky and edge waves, especially along the Dutch Wadden Sea coast.

- Likewise, this dissertation focused on time-averaged wave parameters, such as mean overtopping discharge, significant wave height and spectral wave period. It therefore did not consider individual wave overtopping volumes. As the flow properties of individual overtopping events are equally important for safety (Altomare et al., 2020, Sandoval and Bruce, 2018, Suzuki et al., 2020). Future work should assess the influence of IG waves on individual overtopping volumes.

- The approach adopted here to identify the conditions that promote IG waves considered the influence of each parameter independently and then combined them

into a single empirical formula. While this simple approach proved accurate, the dependencies between parameters (if any) were not considered. Future studies should investigate this further by making use of multi-variate approaches such as machine learning (Passarella et al., 2018) or Bayesian networks (Pearson et al., 2017).

- While the empirical methods derived here performed reasonably well, their accuracy outside of the conditions considered in their derivation has not be assessed. Future work should aim to validate/extend their applicability for conditions outside of those considered in this dissertation. Example conditions include vegetation other than saltmarshes or saltmarshes with submergence depths significantly greater than 3 times the vegetation height for the magnitude of the IG waves; and structure slopes gentler than 1:7 or relative freeboards greater than 2.5 for wave overtopping. The specific ranges considered for each parameter are detailed in Chapter 2 and Chapter 4 for the empirical models developed.

- Though the empirical formulae based on deep-water wave parameters have significant advantages, one major drawback is the assumption of a uniform foreshore slope with no reflection or 2-D effects. In reality, foreshores are often very irregular with strong local variations such as bars or ridges. In the future, these formulae should be validated for cases with irregular bathymetry.

- While the Dutch Wadden Sea coast was considered the central case study of this dissertation, the tools developed herein are considered applicable to coastlines outside of the Netherlands. Future studies should consider areas with differing environmental conditions to further validate the methods.

- The influence of vegetation considered here was based on numerical simulations (SWAN and XBeach Nonhydrostatic) with very limited data for validation. Future work should investigate the influence of saltmarsh vegetation on IG waves under storm conditions; particularly, when the vegetation is deeply submerged.

- Future work should also investigate the influence of the various numerical schemes implemented in the respective numerical models considered here, as this was not within the scope of the present work.

- In general, a greater focus on IG waves in physical model tests and field campaigns would produce much needed data to validate the findings and methods developed here.

- In Chapter 4, new empirical overtopping formulae were developed for very to extremely shallow foreshores (with water depth to offshore wave height ratios less than one), where IG waves are expected to be significant. For deeper conditions, it was assumed that the existing EurOtop (2018) formulae would apply. However, Chapter 5 revealed that this may not be the case for gentle dike slopes (1:7) and less shallow conditions where IG waves do not dominate but still influence conditions at the dike toe. It is therefore very important that the applicability of the EurOtop (2018) formulae, for conditions with some IG waves, be critically assessed given the sensitivity of the formulae to the presence of IG waves (Chapter 5).

# REFERENCES


Akbar, M., and Aliabadi, S. (2013). "Hybrid numerical methods to solve shallow water equations for hurricane induced storm surge modeling." *Environmental Modelling & Software*, 46, 118-128

Altomare, C., Domínguez, J. M., Crespo, A. J. C., Suzuki, T., Caceres, I., and Gómez-Gesteira, M. (2015). "Hybridization of the Wave Propagation Model SWASH and the Meshfree Particle Method SPH for Real Coastal Applications." *Coastal Engineering Journal*, 57(04), 1550024

Altomare, C., Suzuki, T., Chen, X., Verwaest, T., and Kortenhaus, A. (2016). "Wave overtopping of sea dikes with very shallow foreshores." *Coastal Engineering*, 116, 236-257

Altomare, C., Tagliafierro, B., Dominguez, J. M., Suzuki, T., and Viccione, G. (2018). "Improved relaxation zone method in SPH-based model for coastal engineering applications." *Applied Ocean Research*, 81, 15-33

Altomare, C., Suzuki, T., and Verwaest, T. (2020a). "Influence of directional spreading on wave overtopping of sea dikes with gentle and shallow foreshores." *Coastal Engineering*, 157, 103654

Altomare, C., Gironella, X., Suzuki, T., Viccione, G., and Saponieri, A. (2020b). "Overtopping Metrics and Coastal Safety: A Case of Study from the Catalan Coast." *Journal of Marine Science and Engineering*, 8(8), 556

Baldock, T. "Long wave generation by the shoaling and breaking of transient wave groups on a beach." *Proc., Proceedings of the Royal Society of London A: Mathematical, Physical and Engineering Sciences*, The Royal Society, 1853-1876

Baldock, T. E., Huntley, D. A., Bird, P. A. D., O'Hare, T., and Bullock, G. N. (2000). "Breakpoint generated surf beat induced by bichromatic wave groups." *Coastal Engineering*, 39(2), 213-242

Baldock, T. E., and Huntley, D. A. (2002). "Long-wave forcing by the breaking of random gravity waves on a beach." *Proceedings of the Royal Society A: Mathematical, Physical and Engineering Sciences*, 458(2025), 2177-2201

Baldock, T. E. (2012). "Dissipation of incident forced long waves in the surf zone—Implications for the concept of “bound” wave release at short wave breaking." *Coastal Engineering*, 60, 276-285

Baron-Hyppolite, C., Lashley, C. H., Garzon, J., Miesse, T., Ferreira, C., and Bricker, J. D. (2018). "Comparison of Implicit and Explicit Vegetation Representations in SWAN Hindcasting Wave Dissipation by Coastal Wetlands in Chesapeake Bay." *Geosciences*, 9(1), 8

Battjes, J., and Stive, M. (1985). "Calibration and verification of a dissipation model for random breaking waves." *Journal of Geophysical Research: Oceans*, 90(C5), 9159-9167

Battjes, J. A., and Janssen, J. "Energy loss and set-up due to breaking of random waves." *Proc., 16th Conference on Coastal Engineering*, ASCE, 569-587

Battjes, J. A. (2004). "Shoaling of subharmonic gravity waves." *Journal of Geophysical Research*, 109(C2)

Baumann, J., Chaumillon, E., Bertin, X., Schneider, J. L., Guillot, B., and Schmutz, M. (2017). "Importance of infragravity waves for the generation of washover deposits." *Marine Geology*, 391, 20-35

Bertin, X., De Bakker, A., Van Dongeren, A., Coco, G., André, G., Ardhuin, F., Bonneton, P., Bouchette, F., Castelle, B., Crawford, W. C., Davidson, M., Deen, M., Dodet, G., Guérin, T., Inch, K., Leckler, F., McCall, R., Muller, H., Olabarrieta, M., Roelvink, D., Ruessink, G., Sous, D., Stutzmann, É., and Tissier, M. (2018). "Infragravity waves: From driving mechanisms to impacts." *Earth-Science Reviews*, 177, 774-799

Booij, N., Ris, R. C., and Holthuijsen, L. H. (1999). "A third-generation wave model for coastal regions - 1. Model description and validation." *J Geophys Res-Oceans*, 104(C4), 7649-7666

Brocchini, M., and Dodd, N. (2008). "Nonlinear shallow water equation modeling for coastal engineering." *J Waterw Port C-Asce*, 134(2), 104-120

Bruce, T., Pearson, J., and Allsop, W. "Violent overtopping of seawalls-extended prediction methods." *Proc., Breakwaters, coastal structures and coastlines: Proceedings of the international conference organized by the Institution of Civil Engineers and held in London, UK on 26-28 September 2001*, Thomas Telford Publishing, 245-255

Bruce, T., Pearson, J., and Allsop, W. (2004). "Violent wave overtopping-extension of prediction method to broken waves." *Coastal Structures 2003*, 619-630.

Buckley, M., Lowe, R., and Hansen, J. (2014). "Evaluation of nearshore wave models in steep reef environments." *Ocean Dynamics*, 64(6), 847-862

Buckley, M. L., Lowe, R. J., Hansen, J. E., Van Dongeren, A. R., and Storlazzi, C. D. (2018). "Mechanisms of Wave-Driven Water Level Variability on Reef-Fringed Coastlines." *Journal of Geophysical Research: Oceans*, 123(5), 3811-3831

Cavaleri, L., Alves, J. H. G. M., Ardhuin, F., Babanin, A., Banner, M., Belibassakis, K., Benoit, M., Donelan, M., Groeneweg, J., Herbers, T. H. C., Hwang, P., Janssen, P. A. E. M., Janssen, T., Lavrenov, I. V., Magne, R., Monbaliu, J., Onorato, M., Polnikov, V., Resio, D., Rogers, W. E., Sheremet, A., McKee Smith, J., Tolman, H. L., van Vledder, G., Wolf, J., and Young, I. (2007). "Wave modelling – The state of the art." *Progress in Oceanography*, 75(4), 603-674

Coates, T., Jones, R., and Bona, P. (1997). "Wind/swell seas and steep approach slopes, Hydraulic Research Institute Wallingford." Technical Report on wave flume studies, TR24.

Conde, J. J. R. d. E. T. (2019a). "Comparison of different methods for generation and absorption of water waves." 18(1), 71-77

Conde, J. M. P. (2019b). "Comparison of Different Methods for Generation and Absorption of Water Waves." *Revista de Engenharia Térmica*, 18(1), 71-77

Contardo, S., and Symonds, G. (2013). "Infragravity response to variable wave forcing in the nearshore." *Journal of Geophysical Research: Oceans*, 118(12), 7095-7106

Cox, N., Dunkin, L. M., and Irish, J. L. (2013). "An empirical model for infragravity swash on barred beaches." *Coastal Engineering*, 81, 44-50

Crespo, A. J. C., Domínguez, J. M., Rogers, B. D., Gómez-Gesteira, M., Longshaw, S., Canelas, R., Vacondio, R., Barreiro, A., and García-Feal, O. (2015). "DualSPHysics: Open-source parallel CFD solver based on Smoothed Particle Hydrodynamics (SPH)." *Computer Physics Communications*, 187, 204-216

Dally, W. R. (1992). "Random breaking waves: Field verification of a wave-by-wave algorithm for engineering application." *Coastal Engineering*, 16(4), 369-397

Dalrymple, R. A., Kirby, J. T., and Hwang, P. A. (1984a). "Wave Diffraction Due to Areas of Energy Dissipation." *Journal of Waterway, Port, Coastal, and Ocean Engineering*, 110(1), 67-79

Dalrymple, R. A., Kirby, J. T., and Hwang, P. A. (1984b). "Wave Diffraction Due to Areas of Energy-Dissipation." *J Waterw Port C-Asce*, 110(1), 67-79

De Bakker, A., Tissier, M., and Ruessink, B. (2014a). "Shoreline dissipation of infragravity waves." *Continental Shelf Research*, 72, 73-82

De Bakker, A. T. M., Tissier, M. F. S., and Ruessink, B. G. (2014b). "Shoreline dissipation of infragravity waves." *Continental Shelf Research*, 72(Supplement C), 73-82

De Ridder, M. (2018). "Non-hydrostatic wave modelling of coral reefs with the addition of a porous in-canopy model." MSc, Delft University of Technology, Retrieved from http://resolver.tudelft.nl/uuid:4f738968-be52-4484-af1d-60a0e74fdbab.

Den Bieman, J. P., Stuparu, D. E., Hoonhout, B. M., Diermanse, F. L. M., Boers, M., and Van Geer, P. F. C. (2014). "Fully Probabilistic Dune Safety Assessment Using an Advanced Probabilistic Method." *Coastal Engineering Proceedings*, 1(34)

Duits, M. (2019). "Hydra-NL: Gebruikershandleiding versie 2.7." Rijkswaterstaat.

Elgar, S., Herbers, T., Okihiro, M., Oltman-Shay, J., and Guza, R. (1992). "Observations of infragravity waves." *Journal of Geophysical Research: Oceans*, 97(C10), 15573-15577

Engelstad, A., Ruessink, B. G., Wesselman, D., Hoekstra, P., Oost, A., and Van der Vegt, M. (2017). "Observations of waves and currents during barrier island inundation." *Journal of Geophysical Research: Oceans*, 122(4), 3152-3169

EurOtop (2018). "Manual on wave overtopping of sea defences and related structures. An overtopping manual largely based on European research, but for worldwide application." J. Van der Meer, N. Allsop, T. Bruce, J. De Rouck, A. Kortenhaus, T. Pullen, H. Schuttrumpf, P. Troch, and B. Zanuttigh, eds.Retrieved from www. overtopping-manual. com.

Garzon, J. L., Maza, M., Ferreira, C. M., Lara, J. L., and Losada, I. J. (2019). "Wave Attenuation by Spartina Saltmarshes in the Chesapeake Bay Under Storm Surge Conditions." *Journal of Geophysical Research: Oceans*, 124(7), 5220-5243

Goda, Y. (1970). "Estimation of the rate of irregular wave overtopping of seawalls." *Rep. Port Harbour Res., Inst.*, 9(4), 3-41. (in Japanese)

Goda, Y. (1975a). "Irregular wave deformation in the surf zone." *Coastal Engineering in Japan*, 18(1), 13-26

Goda, Y., Kishara, Y., and Kamiyama, Y. (1975). "Laboratory investigation on the overtopping rate of seawalls by irregular waves." *Report of the Port Harbour Research Institute*, 14(4), 3-44. (in Japenese)

Goda, Y. (1975b). "Deformation of irregular waves due to depth-controlled wave breaking." *Report of the Port Harbour Research Institute*, 14(3), 59-106

Goda, Y. (1985). "Random Seas and Design of Maritime Structures." 1st Edition,University of Tokyo Press.

Goda, Y. (2000). "Random Seas and Design of Maritime Structures." 2nd Edition, *Advanced Series on Ocean Engineering*, 15, World Scientific Publishing, 464.

Goda, Y. (2009). "Derivation of unified wave overtopping formulas for seawalls with smooth, impermeable surfaces based on selected CLASH datasets." *Coastal Engineering*, 56(4), 385-399

Goda, Y. (2010). "Random Seas and Design of Maritime Structures." 3rd Edition, 33, World Scientific Publishing.

Gomes da Silva, P., Medina, R., González, M., and Garnier, R. (2018). "Infragravity swash parameterization on beaches: The role of the profile shape and the morphodynamic beach state." *Coastal Engineering*, 136, 41-55

Gourlay, M. R. (1996). "Wave set-up on coral reefs. 1. Set-up and wave-generated flow on an idealised two dimensional horizontal reef." *Coastal Engineering*, 27(3), 161-193

Gruwez, V., Altomare, C., Suzuki, T., Streicher, M., Cappietti, L., Kortenhaus, A., and Troch, P. (2020). "Validation of RANS Modelling for Wave Interactions with Sea Dikes on Shallow Foreshores Using a Large-Scale Experimental Dataset." 8(9), 650

Guza, R., Thornton, E., and Holman, R. (1984). "Swash on steep and shallow beaches." *Coastal Engineering 1984*, 708-723.

Guza, R. T., and Thornton, E. B. (1982). "Swash oscillations on a natural beach." *Journal of Geophysical Research: Oceans*, 87(C1), 483-491

Hasofer, A. M., and Lind, N. C. (1974). "Exact and invariant second-moment code format." *Journal of the Engineering Mechanics division*, 100(1), 111-121

Henderson, S. M., and Bowen, A. J. (2002). "Observations of surf beat forcing and dissipation." *Journal of Geophysical Research: Oceans*, 107(C11), 14-11-14-10

Henderson, S. M., Guza, R. T., Elgar, S., Herbers, T. H. C., and Bowen, A. J. (2006). "Nonlinear generation and loss of infragravity wave energy." *Journal of Geophysical Research: Oceans*, 111(C12), n/a-n/a

Herbers, T., Elgar, S., and Guza, R. (1999). "Directional spreading of waves in the nearshore." *Journal of Geophysical Research: Oceans*, 104(C4), 7683-7693

Herbert, D. (1993). "Wave overtopping of vertical walls."

Higuera, P., Lara, J. L., and Losada, I. J. (2013). "Simulating coastal engineering processes with OpenFOAM®." *Coastal Engineering*, 71, 119-134

Hirt, C. W., and Nichols, B. D. (1981). "Volume of fluid (VOF) method for the dynamics of free boundaries." *Journal of Computational Physics*, 39(1), 201-225

Hofland, B., Chen, X., Altomare, C., and Oosterlo, P. (2017). "Prediction formula for the spectral wave period T m-1,0 on mildly sloping shallow foreshores." *Coastal Engineering*, 123(Supplement C), 21-28

Holman, R. A., and Sallenger, A. H. (1985). "Setup and swash on a natural beach." *Journal of Geophysical Research: Oceans*, 90(C1), 945-953

Holthuijsen, L. H., Booij, N., and Herbers, T. H. C. (1989). "A prediction model for stationary, short-crested waves in shallow water with ambient currents." *Coastal Engineering*, 13(1), 23-54

Inch, K., Davidson, M., Masselink, G., and Russell, P. (2017). "Observations of nearshore infragravity wave dynamics under high energy swell and wind-wave conditions." *Continental Shelf Research*, 138, 19-31

Jacobsen, N. G., Fuhrman, D. R., and Fredsøe, J. (2012). "A wave generation toolbox for the open-source CFD library: OpenFoam®." *International Journal for Numerical Methods in Fluids*, 70(9), 1073-1088

Janssen, T. T., Battjes, J. A., and Van Dongeren, A. R. (2003). "Long waves induced by short-wave groups over a sloping bottom." *Journal of Geophysical Research: Oceans*, 108(C8)

Jasak, H., Jemcov, A., and Tukovic, Z. (2007). "OpenFOAM: A C++ library for complex physics simulations." *Proc., International workshop on coupled methods in numerical dynamics*, IUC Dubrovnik, Croatia, 1-20

Jonkman, S., Kok, M., Van Ledden, M. k., and Vrijling, J. (2009). "Risk-based design of flood defence systems: a preliminary analysis of the optimal protection level for the New Orleans metropolitan area." *Journal of Flood Risk Management*, 2(3), 170-181

Jonkman, S. N., Hillen, M. M., Nicholls, R. J., Kanning, W., and Van Ledden, M. (2013). "Costs of adapting coastal defences to sea-level rise—new estimates and their implications." *Journal of Coastal Research*, 29(5), 1212-1226

Kazolea, M., and Ricchiuto, M. (2018). "On wave breaking for Boussinesq-type models." *Ocean Modelling*, 123, 16-39

Kirby, J. T., Wei, G., Chen, Q., Kennedy, A. B., and Dalrymple, R. A. (1998). "FUNWAVE 1.0: fully nonlinear Boussinesq wave model-Documentation and user's manual." *research report NO. CACR-98-06*

Kjerengtroen, L., and Comer, J. (1996). "Probabilistic Methods in Design: An Overview of Current Technologies." *SAE transactions*, 244-251

Klopman, G., and Van der Meer, J. W. (1999). "Random Wave Measurements in Front of Reflective Structures." *Journal of Waterway, Port, Coastal, and Ocean Engineering*, 125(1), 39-45

Koftis, T., Prinos, P., and Stratigaki, V. (2013). "Wave damping over artificial Posidonia oceanica meadow: A large-scale experimental study." *Coastal Engineering*, 73, 71-83

Lara, J. L., Ruju, A., and Losada, I. J. (2011). "Reynolds averaged Navier–Stokes modelling of long waves induced by a transient wave group on a beach." *Proceedings of the Royal Society A: Mathematical, Physical and Engineering Science*, 467(2129), 1215-1242

Larsen, B. E., Fuhrman, D. R., and Roenby, J. (2019). "Performance of interFoam on the simulation of progressive waves." *Coastal Engineering Journal*, 61(3), 380-400

Lashley, C. H., Roelvink, D., Van Dongeren, A., Buckley, M. L., and Lowe, R. J. (2018). "Nonhydrostatic and surfbeat model predictions of extreme wave run-up in fringing reef environments." *Coastal Engineering*, 137, 11-27

Lashley, C. H., Bricker, J. D., van der Meer, J., Altomare, C., and Suzuki, T. (2019a). "Infragravity-Wave Dominance at Sea-Dikes Fronted by Very and Extremely Shallow Foreshores." *The 29th International Ocean and Polar Engineering Conference*International Society of Offshore and Polar Engineers, Honolulu, Hawaii, USA, 7.

Lashley, C. H., Bertin, X., Roelvink, D., and Arnaud, G. (2019b). "Contribution of Infragravity Waves to Run-up and Overwash in the Pertuis Breton Embayment (France)." *Journal of Marine Science and Engineering*, 7(7), 205

Lashley, C. H., Bricker, J. D., van der Meer, J., Altomare, C., and Suzuki, T. (2020a). "Relative Magnitude of Infragravity Waves at Coastal Dikes with Shallow Foreshores: A Prediction Tool." *Journal of Waterway, Port, Coastal, and Ocean Engineering*, 146(5)

Lashley, C. H., Zanuttigh, B., Bricker, J. D., Van der Meer, J., Altomare, C., Suzuki, T., Roeber, V., and Oosterlo, P. (2020b). "Benchmarking of numerical models for wave overtopping at dikes with shallow mildly sloping foreshores: Accuracy versus speed." *Environmental Modelling & Software*, 130, 104740

Lashley, C. H., Van der Meer, J., Bricker, J. D., Altomare, C., Suzuki, T., and Hirayama, K. (2021). "Formulating Wave Overtopping at Vertical and Sloping Structures with Very Shallow Foreshores Using Deep-water Wave Characteristics." *Journal of Waterway, Port, Coastal, and Ocean Engineering*, 147

List, J. H. (1992). "A model for the generation of two-dimensional surf beat." *Journal of Geophysical Research: Oceans*, 97(C4), 5623-5635

Longuet-Higgins, M. S., and Stewart, R. W. (1962). "Radiation stress and mass transport in gravity waves, with application to 'surf beats'." *Journal of Fluid Mechanics*, 13(4), 481-504

Lowe, R. J., Falter, J. L., Koseff, J. R., Monismith, S. G., and Atkinson, M. J. (2007). "Spectral wave flow attenuation within submerged canopies: Implications for wave energy dissipation." *Journal of Geophysical Research: Oceans*, 112(C5)

Lowe, R. J., Buckley, M. L., Altomare, C., Rijnsdorp, D. P., Yao, Y., Suzuki, T., and Bricker, J. D. (2019). "Numerical simulations of surf zone wave dynamics using Smoothed Particle Hydrodynamics." *Ocean Modelling*, 144, 101481

Lynett, P. J., Gately, K., Wilson, R., Montoya, L., Arcas, D., Aytore, B., Bai, Y., Bricker, J. D., Castro, M. J., Cheung, K. F., David, C. G., Dogan, G. G., Escalante, C., González-Vida, J. M., Grilli, S. T., Heitmann, T. W., Horrillo, J., Kânoğlu, U., Kian, R., Kirby, J. T., Li, W., Macías, J., Nicolsky, D. J., Ortega, S., Pampell-Manis, A., Park, Y. S., Roeber, V., Sharghivand, N., Shelby, M., Shi, F., Tehranirad, B., Tolkova, E., Thio, H. K., Velioğlu, D., Yalçıner, A. C., Yamazaki, Y., Zaytsev, A., and Zhang, Y. J. (2017). "Inter-model analysis of tsunami-induced coastal currents." *Ocean Modelling*, 114, 14-32

Ma, G., Shi, F., and Kirby, J. T. (2012). "Shock-capturing non-hydrostatic model for fully dispersive surface wave processes." *Ocean Modelling*, 43-44, 22-35

Mase, H., and Kirby, J. T. (1993). "Hybrid Frequency-Domain KdV Equation for Random Wave Transformation." *Coastal Engineering 1992*, 474-487.

Mase, H., Tamada, T., Yasuda, T., Hedges, T. S., and Reis, M. T. (2013). "Wave Runup and Overtopping at Seawalls Built on Land and in Very Shallow Water." *Journal of Waterway, Port, Coastal, and Ocean Engineering*, 139(5), 346-357

Masselink, G. (1995). "Group bound long waves as a source of infragravity energy in the surf zone." *Continental Shelf Research*, 15(13), 1525-1547

Matsuba, Y., Shimozono, T., and Sato, S. (2020). "Infragravity wave dynamics on Seisho Coast during Typhoon Lan in 2017." *Coastal Engineering Journal*, 62(2), 299-316

McCall, R. T., Masselink, G., Poate, T. G., Roelvink, J. A., and Almeida, L. P. (2015). "Modelling the morphodynamics of gravel beaches during storms with XBeach-G." *Coastal Engineering*, 103, 52-66

Mendez, F. J., and Losada, I. J. (2004). "An empirical model to estimate the propagation of random breaking and nonbreaking waves over vegetation fields." *Coastal Engineering*, 51(2), 103-118

Möller, I., Kudella, M., Rupprecht, F., Spencer, T., Paul, M., Van Wesenbeeck, B. K., Wolters, G., Jensen, K., Bouma, T. J., and Miranda-Lange, M. J. N. G. (2014). "Wave attenuation over coastal salt marshes under storm surge conditions." 7(10), 727-731

Nairn, R. B., Roelvink, J., and Southgate, H. N. (1990). "Transition zone width and implications for modelling surfzone hydrodynamics." *Proc., 22nd International Conference on Coastal Engineering*, ASCE, 68-81

Nguyen, T.-H., Hofland, B., Dan Chinh, V., and Stive, M. (2020). "Wave Overtopping Discharge for Very Gently Sloping Foreshores." 12(6), 1695

Nwogu, O. (1993). "Alternative Form of Boussinesq Equations for Nearshore Wave-Propagation." *J Waterw Port C-Asce*, 119(6), 618-638

Nwogu, O., and Demirbilek, Z. (2010). "Infragravity wave motions and runup over shallow fringing reefs." *Journal of waterway, port, coastal, and ocean engineering*, 136(6), 295-305

Okihiro, M., Guza, R. T., and Seymour, R. J. (1993). "Excitation of seiche observed in a small harbor." *Journal of Geophysical Research*, 98(C10), 18201-18211

Oosterlo, P., McCall, R., Vuik, V., Hofland, B., Van der Meer, J., and Jonkman, S. (2018). "Probabilistic Assessment of Overtopping of Sea Dikes with Foreshores including Infragravity Waves and Morphological Changes: Westkapelle Case Study." *Journal of Marine Science and Engineering*, 6(2), 48

Owen, M. (1980). "Design of seawalls allowing for wave overtopping." *Report Ex*, 924, 39

Passarella, M., Goldstein, E. B., Muro, S. D., and Coco, G. (2018). "The use of genetic programming to develop a predictor of swash excursion on sandy beaches." *Natural Hazards and Earth System Sciences*, 18(2), 599-611

Pearson, S. G., Storlazzi, C. D., Van Dongeren, A. R., Tissier, M. F. S., and Reniers, A. J. H. M. (2017). "A Bayesian-Based System to Assess Wave-Driven Flooding Hazards on Coral Reef-Lined Coasts." *Journal of Geophysical Research: Oceans*, 122(12), 10099-10117

Pomeroy, A., Lowe, R., Symonds, G., Van Dongeren, A., and Moore, C. (2012). "The dynamics of infragravity wave transformation over a fringing reef." *J Geophys Res-Oceans*, 117(C11)

Power, H. E., Hughes, M. G., Aagaard, T., and Baldock, T. E. (2010). "Nearshore wave height variation in unsaturated surf." 115(C8)

Pullen, T., and Allsop, N. (2004). "Final report on laboratory measurements Samphire Hoe." *CLASH WP4 D36*

Reniers, A. J. H. M., Naporowski, R., Tissier, M. F. S., de Schipper, M. A., Akrish, G., and Rijnsdorp, D. P. (2021). "North Sea Infragravity Wave Observations." 9(2), 141

Rijnsdorp, D. P., Smit, P. B., Zijlema, M., and Reniers, A. J. H. M. (2017). "Efficient non-hydrostatic modelling of 3D wave-induced currents using a subgrid approach." *Ocean Modelling*, 116, 118-133

Roeber, V., Cheung, K. F., and Kobayashi, M. H. (2010). "Shock-capturing Boussinesq-type model for nearshore wave processes." *Coastal Engineering*, 57(4), 407-423

Roeber, V., and Cheung, K. (2012). "BOSZ (Boussinesq Ocean and Surf Zone model)." *Proc., 2011 NTHMP Model Benchmarking Workshop*, NOAA,

Roeber, V., and Bricker, J. D. (2015). "Destructive tsunami-like wave generated by surf beat over a coral reef during Typhoon Haiyan." *Nat Commun*, 6, 7854

Roelvink, D., Reniers, A., Van Dongeren, A., Van Thiel de Vries, J., McCall, R., and Lescinski, J. (2009). "Modelling storm impacts on beaches, dunes and barrier islands." *Coastal Engineering*, 56(11-12), 1133-1152

Roelvink, D., Van Dongeren, A., McCall, R., Hoonhout, B., Van Rooijen, A., Van Geer, P., De Vet, L., Nederhoff, K., and Quataert, E. (2015). "XBeach Technical Reference: Kingsday Release." Delft, The Netherlands: Deltares, Technical report, 141p.

Roelvink, D., McCall, R., Mehvar, S., Nederhoff, K., and Dastgheib, A. (2018). "Improving predictions of swash dynamics in XBeach: The role of groupiness and incident-band runup." *Coastal Engineering*, 134, 103-123

Roelvink, D., and Costas, S. (2019). "Coupling nearshore and aeolian processes: XBeach and duna process-based models." *Environmental Modelling & Software*, 115, 98-112

Roelvink, J. A., and Stive, M. J. F. (1989). "Bar-generating cross-shore flow mechanisms on a beach." *Journal of Geophysical Research: Oceans (1978–2012)*, 94(C4), 4785-4800

Roelvink, J. A. (1993). "Dissipation in random wave groups incident on a beach." *Coastal Engineering*, 19(1), 127-150

Romano, A., Bellotti, G., Briganti, R., and Franco, L. (2015). "Uncertainties in the physical modelling of the wave overtopping over a rubble mound breakwater: The role of the seeding number and of the test duration." *Coastal Engineering*, 103, 15-21

Ruessink, B. G., Kleinhans, M. G., and Van Den Beukel, P. G. L. (1998). "Observations of swash under highly dissipative conditions." *Journal of Geophysical Research: Oceans*, 103(C2), 3111-3118

Ruggiero, P., Holman, R. A., and Beach, R. A. (2004). "Wave run-up on a high-energy dissipative beach." *Journal of Geophysical Research: Oceans*, 109(C6), n/a-n/a

Sallenger, A. H., and Holman, R. A. (1985). "Wave energy saturation on a natural beach of variable slope." *Journal of Geophysical Research: Oceans*, 90(C6), 11939-11944

Sandoval, C., and Bruce, T. (2018). "Wave overtopping hazard to pedestrians: video evidence from real accidents." *Coasts, Marine Structures and Breakwaters 2017: Realising the Potential*, ICE Publishing, 501-512.

Sheremet, A., Guza, R., Elgar, S., and Herbers, T. (2002). "Observations of nearshore infragravity waves: Seaward and shoreward propagating components." *Journal of Geophysical Research: Oceans*, 107(C8)

Sheremet, A., Staples, T., Ardhuin, F., Suanez, S., and Fichaut, B. (2014). "Observations of large infragravity wave runup at Banneg Island, France." *Geophysical Research Letters*, 41(3), 976-982

Shimozono, T., Tajima, Y., Kennedy, A. B., Nobuoka, H., Sasaki, J., and Sato, S. (2015a). "Combined infragravity wave and sea-swell runup over fringing reefs by super typhoon Haiyan." *Journal of Geophysical Research: Oceans*, 120(6), 4463-4486

Shimozono, T., Tajima, Y., Kennedy, A. B., Nobuoka, H., Sasaki, J., and Sato, S. (2015b). "Combined infragravity wave and sea-swell runup over fringing reefs by super typhoon Haiyan." *J Geophys Res-Oceans*, 120(6), 4463-4486

Sierra, J. P., González-Marco, D., Mestres, M., Gironella, X., Oliveira, T. C. A., Cáceres, I., and Mösso, C. (2010). "Numerical model for wave overtopping and transmission through permeable coastal structures." *Environmental Modelling & Software*, 25(12), 1897-1904

Simarro, G., Orfila, A., and Galan, A. (2013). "Linear shoaling in Boussinesq-type wave propagation models." *Coastal Engineering*, 80, 100-106

Smagorinsky, J. (1963). "General Circulation Experiments with the Primitive Equations." *Monthly Weather Review*, 91(3), 99-164

Smit, P., Stelling, G., Roelvink, J., Van Thiel de Vries, J., McCall, R., Van Dongeren, A., Zwinkels, C., and Jacobs, R. (2010). "XBeach: Non-hydrostatic model: Validation, verification and model description." *Delft Univ. Technol*

Smit, P., Zijlema, M., and Stelling, G. (2013). "Depth-induced wave breaking in a non-hydrostatic, near-shore wave model." *Coastal Engineering*, 76, 1-16

Smith, G., Wallast, I., and van Gent, M. R. (2003). "Rock slope stability with shallow foreshores." *Coastal Engineering 2002: Solving Coastal Conundrums*, World Scientific, 1524-1536.

Smith, J. M., Sherlock, A. R., and Resio, D. T. (2001). "STWAVE: Steady-state spectral wave model user's manual for STWAVE, Version 3.0." ENGINEER RESEARCH AND DEVELOPMENT CENTER VICKSBURG MS COASTAL AND HYDRAULICSLAB.

Smith, R. A. E., Bates, P. D., and Hayes, C. (2012). "Evaluation of a coastal flood inundation model using hard and soft data." *Environmental Modelling & Software*, 30, 35-46

St-Germain, P., Nistor, I., Readshaw, J., and Lamont, G. (2014). "Numerical Modeling of Coastal Dike Overtopping Using Sph and Non-Hydrostatic Nlsw Equations." *Coastal Engineering Proceedings*, 1(34)

Stelling, G., and Zijlema, M. (2003). "An accurate and efficient finite-difference algorithm for non-hydrostatic free-surface flow with application to wave propagation." *International Journal for Numerical Methods in Fluids*, 43(1), 1-23

Stockdon, H. F., Holman, R. A., Howd, P. A., and Sallenger, A. H. (2006). "Empirical parameterization of setup, swash, and runup." *Coastal Engineering*, 53(7), 573-588

Suzuki, T., Zijlema, M., Burger, B., Meijer, M. C., and Narayan, S. (2012). "Wave dissipation by vegetation with layer schematization in SWAN." *Coastal Engineering*, 59(1), 64-71

Suzuki, T., Altomare, C., Veale, W., Verwaest, T., Trouw, K., Troch, P., and Zijlema, M. (2017). "Efficient and robust wave overtopping estimation for impermeable coastal structures in shallow foreshores using SWASH." *Coastal Engineering*, 122(Supplement C), 108-123

Suzuki, T., Hu, Z., Kumada, K., Phan, L. K., and Zijlema, M. (2019). "Non-hydrostatic modeling of drag, inertia and porous effects in wave propagation over dense vegetation fields." *Coastal Engineering*, 149, 49-64

Suzuki, T., Altomare, C., Yasuda, T., and Verwaest, T. (2020). "Characterization of Overtopping Waves on Sea Dikes with Gentle and Shallow Foreshores." *Journal of Marine Science and Engineering*, 8(10), 752

Svendsen, I. A. (1984). "Wave heights and set-up in a surf zone." *Coastal Engineering*, 8(4), 303-329

Symonds, G., Huntley, D. A., and Bowen, A. J. (1982). "Two-dimensional surf beat: Long wave generation by a time-varying breakpoint." *Journal of Geophysical Research: Oceans*, 87(C1), 492-498

Takayama, T., Nagai, T., and Nishida, K. (1982). "Decrease of wave overtopping amount due to seawalls of low crest types." *Report of the Port Harbour Research Institute*, 21(2), 151-205. (in Japanese)

Tamada, T., Inoue, M., and T, T. "Experimental studies on diagrams for the estimation of wave overtopping rate on gentle slope-type seawalls and these reduction effectd on wave overtopping." *Proc., Proc. Coastal Eng., JSCE*, 641-645. (in Japanese)

Tamada, T., Mase, H., and Yasuda, T. (2015). "Integrated Formula of Wave Overtopping and Runup Modeling for Vertical Seawalls Based on CLASH Datasets." *Journal of Japan Society of Civil Engineers, Ser. B2 (Coastal Engineering)*, 71(2), 847-852. (in Japanese)

Thomson, J., Elgar, S., Raubenheimer, B., Herbers, T. H. C., and Guza, R. T. (2006). "Tidal modulation of infragravity waves via nonlinear energy losses in the surfzone." *Geophysical Research Letters*, 33(5)

Van der Meer, J., and De Waal, J. (1993). "Waterbeweging op taluds: invloed van berm, ruwheid, ondiep voorland en scheve lang-en kortkammige golfaanval." (in Dutch)

Van der Meer, J. (2002). "Technical report wave run-up and wave overtopping at dikes." *TAW report (incorporated in the EurOtop manual)*

Van der Meer, J., and Bruce, T. (2014). "New physical insights and design formulas on wave overtopping at sloping and vertical structures." *Journal of Waterway, Port, Coastal, Ocean Engineering* 140(6), 04014025

Van Dongeren, A., Reniers, A., Battjes, J., and Svendsen, I. (2003). "Numerical modeling of infragravity wave response during DELILAH." *Journal of Geophysical Research: Oceans*, 108(C9)

Van Dongeren, A., Battjes, J., Janssen, T., Van Noorloos, J., Steenhauer, K., Steenbergen, G., and Reniers, A. (2007). "Shoaling and shoreline dissipation of low-frequency waves." *Journal of Geophysical Research: Oceans*, 112(C2), n/a-n/a

Van Dongeren, A., De Jong, M., Van der Lem, C., Van Deyzen, A., and Den Bieman, J. (2016). "Review of Long Wave Dynamics over Reefs and into Ports with Implication for Port Operations." *Journal of Marine Science and Engineering*, 4(1), 12

Van Dongeren, A. R., and Svendsen, I. A. (1997). "Quasi 3-D modeling of nearshore hydrodynamics." Delaware Univ. Newark Center for App. Coast. Research.

Van Gent, M. (1999). "Physical model investigations on coastal structures with shallow foreshores: 2D model tests with single and double-peaked wave energy spectra." *Hydraulic Engineering Reports*,Delft.

Van Gent, M. R. A. (2001). "Wave Runup on Dikes with Shallow Foreshores." *Journal of Waterway, Port, Coastal, and Ocean Engineering*, 127(5), 254-262

Van Koningsveld, M., De Boer, G., Baart, F., Damsma, T., Den Heijer, C., Van Geer, P., and De Sonnevile, B. "OpenEarth-inter-company management of: data, models, tools & knowledge." *Proc., Proceedings WODCON XIX Conference: Dredging Makes the World a Better Place, 9-14 September 2010, Beijing, China*

Van Osselen, K. (2016). "Foreshores in the Wadden Sea."

Van Rooijen, A., McCall, R., Van Thiel de Vries, J., Van Dongeren, A., Reniers, A., and Roelvink, J. (2016). "Modeling the effect of wave-vegetation interaction on wave setup." *Journal of Geophysical Research: Oceans*, 121(6), 4341-4359

Vanneste, D. F. A., Altomare, C., Suzuki, T., Troch, P., and Verwaest, T. (2014). "Comparison of Numerical Models for Wave Overtopping and Impact on a Sea Wall." *Coastal Engineering Proceedings*, 1(34)

Verbrugghe, T., Domínguez, J. M., Crespo, A. J. C., Altomare, C., Stratigaki, V., Troch, P., and Kortenhaus, A. (2018). "Coupling methodology for smoothed particle hydrodynamics modelling of non-linear wave-structure interactions." *Coastal Engineering*, 138, 184-198

Victor, L., and Troch, P. (2012). "Wave Overtopping at Smooth Impermeable Steep Slopes with Low Crest Freeboards." 138(5), 372-385

Vuik, V., Jonkman, S. N., Borsje, B. W., and Suzuki, T. (2016). "Nature-based flood protection: The efficiency of vegetated foreshores for reducing wave loads on coastal dikes." *Coastal Engineering*, 116(Supplement C), 42-56

Vuik, V., Van Vuren, S., Borsje, B. W., van Wesenbeeck, B. K., and Jonkman, S. N. (2018a). "Assessing safety of nature-based flood defenses: Dealing with extremes and uncertainties." *Coastal Engineering*, 139, 47-64

Vuik, V., Heo, H. Y. S., Zhu, Z., Borsje, B. W., and Jonkman, S. N. (2018b). "Stem breakage of salt marsh vegetation under wave forcing: A field and model study." *Estuarine, Coastal and Shelf science*, 200, 41-58

Vyzikas, T., and Greaves, D. (2018). "Numerical Modelling." *Wave and Tidal Energy*, John Wiley & Sons, Ltd, 289-363.

Warren, I. R., and Bach, H. K. (1992). "MIKE 21: a modelling system for estuaries, coastal waters and seas." *Environmental Software*, 7(4), 229-240

Wiegmann, E., Perluka, R., Oude Elberink, S., and Vogelzang, J. (2005). "Vaklodingen: De inwintechnieken en hun combinaties." Report AGI-2005-GSMH-012 (in Dutch). Rijkswaterstaat, Adviesdienst ….

Willemsen, P. W., Borsje, B. W., Vuik, V., Bouma, T. J., and Hulscher, S. J. (2020). "Field-based decadal wave attenuating capacity of combined tidal flats and salt marshes." *Coastal engineering*, 156, 103628

Yang, S. L., Shi, B. W., Bouma, T. J., Ysebaert, T., and Luo, X. X. (2012). "Wave Attenuation at a Salt Marsh Margin: A Case Study of an Exposed Coast on the Yangtze Estuary." *Estuaries and Coasts*, 35(1), 169-182

Yao, Y., Huang, Z., Monismith, S. G., and Lo, E. Y. M. (2013). "Characteristics of Monochromatic Waves Breaking over Fringing Reefs." *Journal of Coastal Research*, 94-104

Yuhi, M., Mase, H., Kim, S., Umeda, S., and Altomare, C. (2020). "Refinement of integrated formula of wave overtopping and runup modeling." *Ocean Engineering*, 108350

Zhang, S. J., Zhu, L. S., and Zou, K. (2019). "A Comparative Study of Numerical Models for Wave Propagation and Setup on Steep Coral Reefs." *China Ocean Eng*, 33(4), 424-435

Zhu, Z., Vuik, V., Visser, P. J., Soens, T., van Wesenbeeck, B., van de Koppel, J., Jonkman, S. N., Temmerman, S., and Bouma, T. J. (2020). "Historic storms and the hidden value of coastal wetlands for nature-based flood defence." *Nature Sustainability*, 3(10), 853-862

Zijlema, M., and Stelling, G. S. (2008). "Efficient computation of surf zone waves using the nonlinear shallow water equations with non-hydrostatic pressure." *Coastal Engineering*, 55(10), 780-790

Zijlema, M., Stelling, G., and Smit, P. (2011). "SWASH: An operational public domain code for simulating wave fields and rapidly varied flows in coastal waters." *Coastal Engineering*, 58(10), 992-1012

# LIST OF SYMBOLS

The following symbols were used in this dissertation:

$A$= Envelope of the sea and swell waves (m);

$a$= Fitted coefficient in the prediction of $\widetilde{H}_{IG}$ ($m^{-1}$);

$a_h$= Vegetation height (m);

$b_v$= Vegetation stem diameter (m);

$C_D$= Drag coefficient (-);

$C_{\eta\eta}$= Wave energy density ($m^2$/Hz);

$c$= Wave speed (m/s);

$c_f$= Bed friction factor (-);

$c_g$= Wave-group velocity (m/s);

$c_{in}$= Incoming wave speed (m/s);

$c_{out}$= Outgoing wave speed (m/s);

$F_D$= Drag force (N/m);

$F_v$= Depth-averaged vegetation force (N);

$f_{low}$= Mean frequency of the IG wave at breakpoint (Hz);

$f_{node}$= Nodal frequency of standing wave (Hz);

$f_p$= Peak frequency (Hz);

$\widetilde{H}_{IG}$= Relative magnitude of the infragravity waves at the dike toe (-);

$H_{m0}$= total significant wave height (m);

$H_{m0,deep}$= Total significant wave height offshore in deep water (m);

$H_{m0,IG}$= Significant wave height in the infragravity frequency band (m);

$H_{m0,IG,toe}$= Significant wave height in the infragravity frequency band, at the dike toe (m);

$H_{m0,SS}$= Significant wave height in the sea and swell frequency band (m);

$H_{m0,SS,toe}$= Significant wave height in the sea and swell frequency band, at the dike toe (m);

$h$= Local water depth (m);

$h_b$= Water depth at break-point (m);

$h_{toe}$= Initial water depth at the dike toe (m);

$k$= Wave number (rad/m);

$L$= Local wave length (m);

$L_0$= Wave length in deep water (m);

$m$= Foreshore slope angle (°);

$m_n$= n$^{th}$ moment of spectrum;

$m_{node}$= Mode of the dike-foreshore system (standing wave) (-);

$N_v$= Vegetation stem density (stems/m$^2$);

$n$= Manning roughness coefficient (s/m$^{1/3}$);

$q$ = mean overtopping discharge (l/s/m or m3/s/m)

$\bar{q}$= Depth-averaged dynamic (non-hydrostatic) pressure normalised by the density (-);

$q_a$ = actual mean overtopping discharge (l/s/m or m3/s/m);

$q_c$ = critical mean overtopping discharge (l/s/m or m3/s/m);

$q_{mod}$ = modelled mean overtopping discharge (l/s/m or m3/s/m);

$q_{obs}$ = observed mean overtopping discharge (l/s/m or m3/s/m);

$Rel.bias$= Relative Bias (-);

$R_{\eta A}$= Cross-correlation coefficient (-);

$R^2$= Coefficient of determination (-);

$s$= User-defined directional spreading factor (XBeach) (-);

$s_0$= $s_{0p}$= Deep-water wave steepness (-);

$SCI$= Scatter Index (-);

$T_{m-1,0}$= Spectral wave period (s);

$T_{m-1,0,deep}$= Spectral wave period offshore in deep water (s);

$T_{m-1,0,toe}$= Spectral wave period at toe of structure (s);

$T_p$= Peak wave period in deep water (s);

$u$= Depth-averaged cross-shore velocity (m/s);

$v_h$= Horizontal viscosity ($m^2/s$);

$W_{veg}$= Width of vegetated cover (m);

$x$= Cross-shore location (m);

$x_b$= Cross-shore breakpoint location (m);

$x_{dike}$= Cross-shore dike location (m);

$\alpha$= Dike slope angle (°);

$\beta_b$= Normalized bed slope (-);

$\Delta x$= Cross-shore grid spacing (m);

$\Delta y$= Alongshore grid spacing (m);

$\eta$= Surface elevation (m);

$\bar{\eta}$= Mean water level relative to the dike toe (m);

$\eta^{IG}$= Low-pass filtered surface elevation (m);

$\eta_{in}^{IG}$= Incoming low-pass filtered surface elevation (m);

$\eta_{out}^{IG}$= Outgoing low-pass filtered surface elevation (m);

$\eta^{SS}$= High-pass filtered surface elevation (m);

$\bar{\gamma}$= Influence factor (-);

$\gamma_{bj}$ = breaker parameter for Battjes and Janssen (1978) dissipation model (-)

$\Omega$= Ratio of breaking waves to water depth (-);

$\omega$= Angular frequency (rad/s);

$\rho$= Density of water ($kg/m^3$);

$\sigma$= Directional spreading (°);

$\sigma_A$= Standard deviation of the wave envelope time series (m);

$\sigma_\eta$= Standard deviation of the low-pass filtered surface elevation time series (m);

$\xi_0$= Breaker index (Iribarren number) based on peak wave period (-).

$\xi_{m-1,0}$= Breaker index (Iribarren number) based on spectral wave period (-).

$\zeta_{rms}$ = amplitude of the IG waves (m)

# APPENDIX A: XBEACH NONHYDROSTATIC SENSITIVTY ANALYSIS

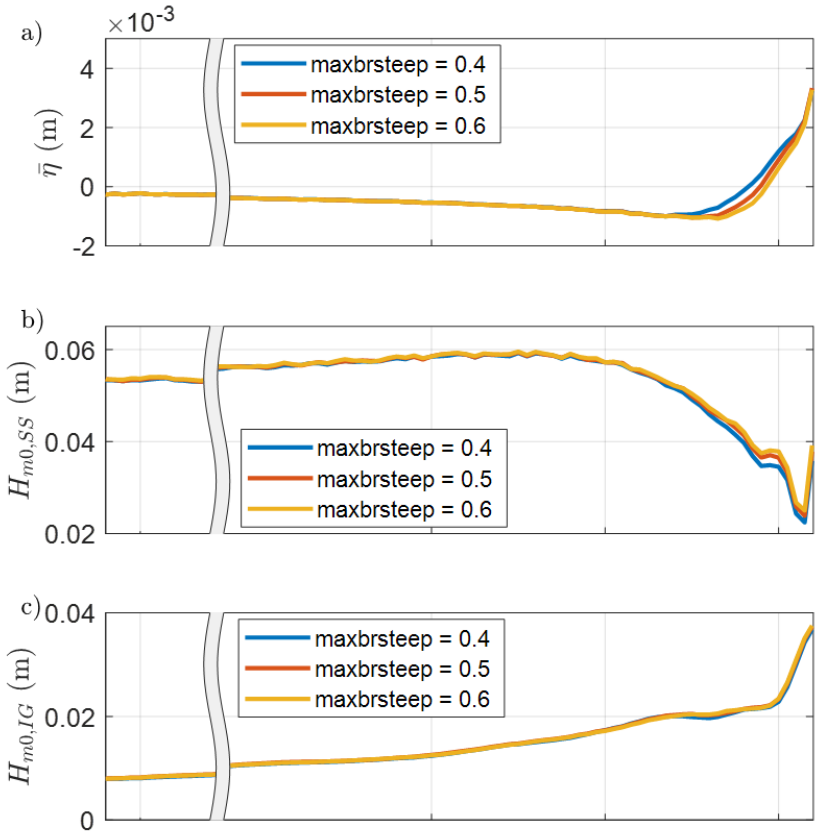


***Figure A. 1*** *Sensitivity of modelled a) wave setup ($\bar{\eta}$), b) sea-swell wave height ($H_{m0,SS}$) and c) infragravity wave height ($H_{m0IG}$) to changes in maximum breaking wave steepness parameter (maxbrsteep) in XBeach Non-hydrostatic.*

# APPENDIX B: OVERVIEW OF STOCHASTIC VARIABLES

**Table B. 1** *Extreme parameters for offshore wave and water level characteristics (Weibull distributions). Note that the scale (sc) and shape (sh) parameters, derived from Hydra-NL estimates, are dependent on location along the Wadden coast; the range of values is provided here.*

| Variable | Symbol | Units | Parameters | |
|---|---|---|---|---|
| | | | $sc$ | $sh$ |
| Offshore significant wave height | $H_{m0}$ | m | 0.31 – 1.11 | 1.21 – 3.01 |
| Offshore spectral wave period | $T_{m-1,0}$ | s | 1.81 – 3.91 | 1.81 – 3.51 |
| Offshore mean water level | $\bar{\eta}$ | m+NAP | 2.51 – 2.71 | 2.81 – 3.31 |

**Table B. 2** *Normally distributed foreshore parameters. Note that the mean value ($\mu^*$) is dependent on location along the Wadden coast.*

| Variable | Symbol | Units | Parameters | |
|---|---|---|---|---|
| | | | $\mu$ | $\sigma$ |
| Foreshore bed level | $z_b$ | m+NAP | $\mu^*$ | 0.2 |
| Factor for relative magnitude of IG waves at toe | $f_{IG}$ | - | 0.99 | 0.18 |
| Factor for relative magnitude of spectral wave period at toe | $f_{Tm}$ | - | 0.99 | 0.17 |
| Empirical overtopping coefficients | $c$ | - | -0.92 | 0.24 |

# APPENDIX C: WAVE SPECTRA AT UITHUIZERWAD DURING 2015 AND 2017 STORMS

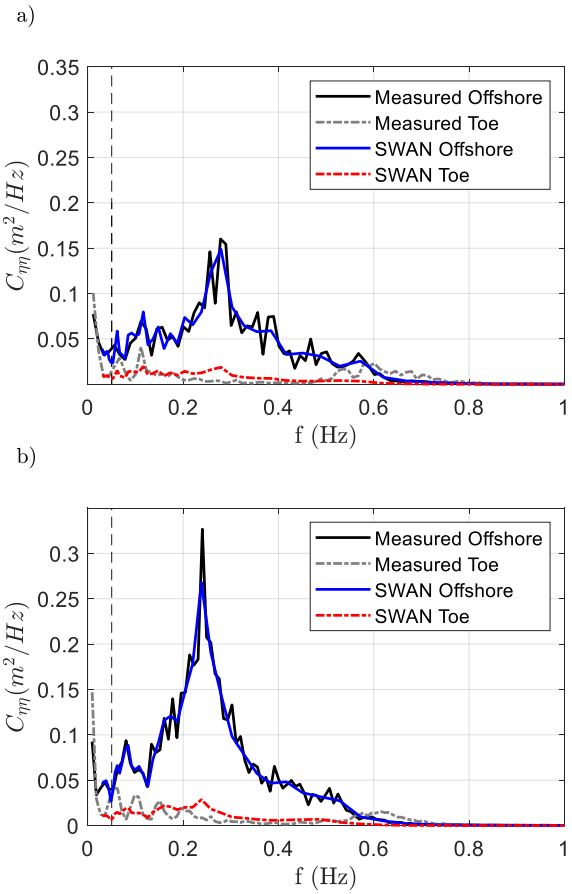


**Figure C. 1** *Comparison of observed and modelled wave spectra for a) January 2015 and b) January 2017. Dashed vertical lines separate SS and IG frequencies. (See Figure 5.5 for reference to instrument locations).*

# APPENDIX D: DERIVATION OF FORMULA FOR SPECTRAL WAVE PERIOD AT TOE

Hofland et al. (2017) showed that the ratio of spectral wave period at the structure toe to its deep-water equivalent ($T_{m-1,0,toe}/T_{m-1,0,deep}$) may be empirically modelled as a function of relative water depth and foreshore slope (Equations D.1 to D.3). For long-crested waves (no directional spreading):

$$\frac{T_{m-1,0,toe,in}}{T_{m-1,0,deep}} - 1 = 6 \cdot \exp\left(-4\tilde{h}\right) + \exp\left(-\tilde{h}\right), \qquad (D.1)$$

and for cases with short-crested waves:

$$\frac{T_{m-1,0,toe,in}}{T_{m-1,0,deep}} - 1 = 6 \cdot \exp\left(-6\tilde{h}\right) + 0.25 \cdot \exp\left(-0.75\tilde{h}\right), \qquad (D.2)$$

where,

$$\tilde{h} = \frac{h_{toe}}{H_{m0,deep}} \left(\frac{\cot \alpha_{fore}}{100}\right)^{0.2}. \qquad (D.3)$$

However, as Equations D.1 to D.3 were based on tests with $35 \leq \cot \alpha_{fore} \leq 250$, they tend to over- and under-estimate $T_{m-1,0,toe}$ for steep ($\cot \alpha_{fore} < 35$) and very gentle slopes ($\cot \alpha_{fore} > 250$), respectively—with $R^2$ = 0.30 when applied to the numerical dataset (Figure D. 1). This inaccuracy, particularly for very gentle slopes ($\cot \alpha_{fore}$ > 250), has also been reported by Nguyen et al. (2020) and suggests that a new formulation is required for application to the Dutch Wadden Sea—where foreshore slopes are typically 1:500 or gentler.

Since both $T_{m-1,0,toe}$ and $\widetilde{H}_{IG}$ both describe the amount of energy in the IG band compared to the SS band, it stands to reason that a simple relation should exist between the two parameters. From the numerical dataset developed in Chapter 2 (Lashley et al., 2020), it can be seen that $T_{m-1,0,toe}/T_{m-1,0,deep}$ increases with increasing $\widetilde{H}_{IG}$ ($R^2$ = 0.76), but with scatter related to the foreshore slope (Figure D. 2a). Based on these trends, the following relation is proposed:

$$\frac{T_{m-1,0,toe}}{T_{m-1,0,deep}} = \begin{cases} 1.59 \cdot \widetilde{H}_{IG}{}^{0.69} \cdot (\cot \alpha_{fore})^{0.17} & \frac{h_{toe}}{H_{m0,deep}} \leq 1 \\ 1 & \frac{h_{toe}}{H_{m0,deep}} > 1 \end{cases}, \qquad (D.4)$$

where the exponents were determined empirically, by minimizing scatter. Including the foreshore slope term significantly reduces the scatter in the data ($R^2$ = 0.92, Figure D. 2b) and gives a better representation for mild slopes. This is due to the influence of the foreshore slope, not only on the relative magnitude of the IG waves but also on the spectral shape. As the area over which shoaling occurs increases with gentler foreshore slopes, energy transfer by nonlinear (difference) triad interactions occurs over a longer duration than on steeper slopes. This causes the spectral peak to migrate to lower frequencies and results in larger values of $T_{m-1,0,toe}$ for gentler foreshore slopes (Battjes, 2004), despite having similar $\widetilde{H}_{IG}$-values.

It should also be noted that for deep-water cases, where $h_{toe}/H_{m0,deep} > 1$, $T_{m-1,0,toe}/T_{m-1,0,deep} \approx 1$ and is independent of the foreshore slope and $\widetilde{H}_{IG}$ parameters (Figure D. 2b). This is consistent with the findings of Chapter 4 which suggest that the foreshore's influence only becomes significant for cases with $h_{toe}/H_{m0,deep} \leq 1$.

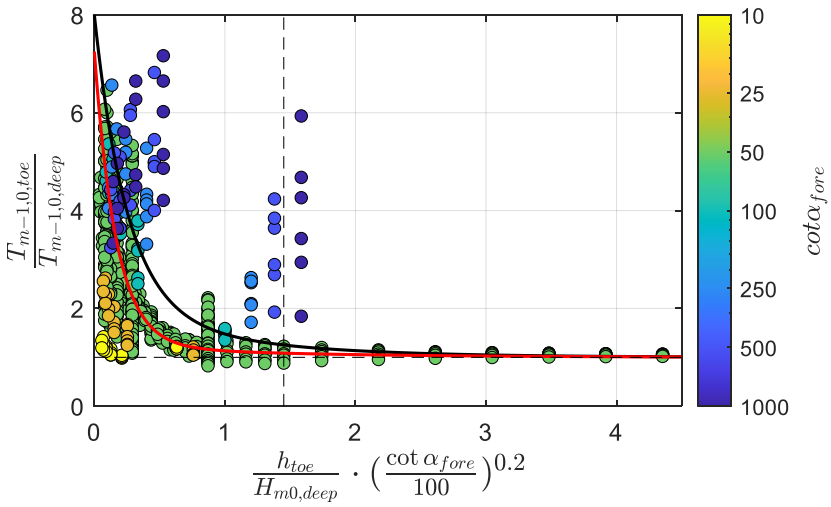


**Figure D. 1** *Numerically modelled realtive spectral wave period as a function of relative water depth and foreshore slope, following Hofland et al. (2017). Black and red lines represent Equations C.1 and C.2, respectively.*

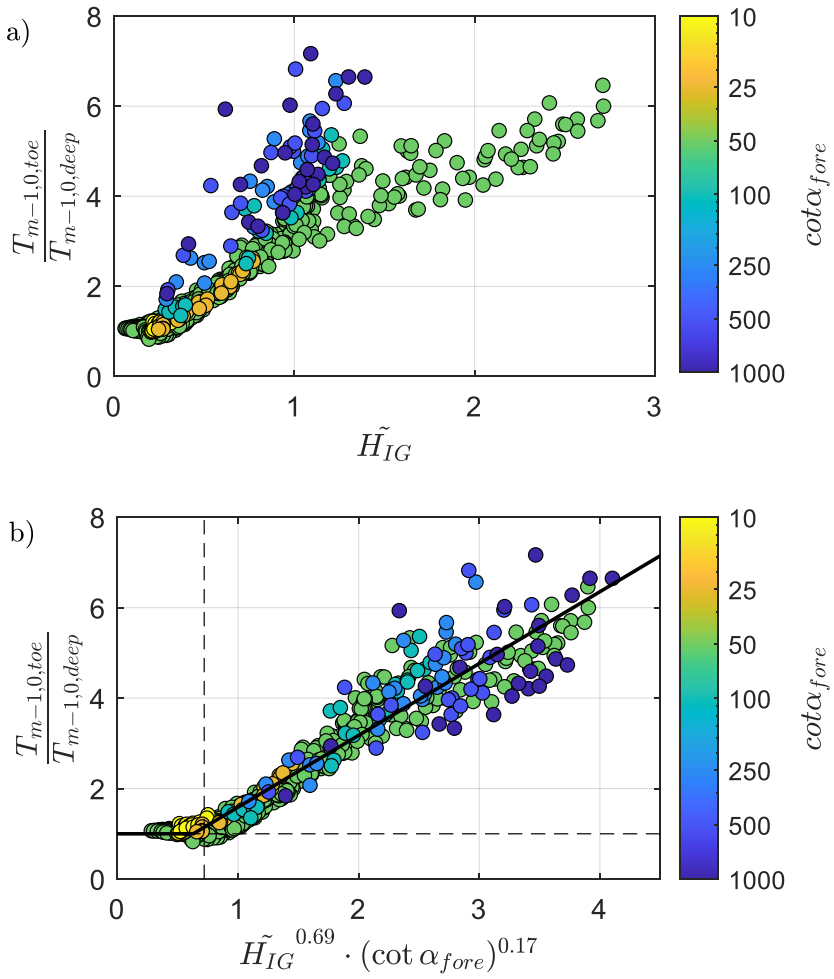


**Figure D. 2** *Numerically modelled realtive spectral wave period as a function of a) $\tilde{H}_{IG}$ alone; and b) $\tilde{H}_{IG}$ and an additional foreshore-slope term. Solid line represents Equation D.4. Dashed vertical line indicates $h_{toe}/H_{m0,deep}$ = 1 and dashed horizontal line represents the deep-water limit where $T_{m-1,0,toe}/T_{m-1,0,deep} \approx 1$.*

# Christopher H. Lashley, M.Sc.

Dept. of Hydraulic Engineering (Waterbouwkunde)
PO Box 5048, 2600GA, Delft, the Netherlands
Email: c.h.lashley@tudelft.nl; clashley@udel.edu


**Education**

| | |
|---|---|
| 2021 | Ph.D. in Hydraulic Engineering, Delft University of Technology |
| 2017 | MSc. in Coastal Engineering & Port Development, IHE-Delft (Distinction) |
| 2013 | MSc. Building & Construction Management, University of the West Indies (Distinction) |
| 2011 | BSc. Civil Engineering, University of the West Indies (First Class Honors) |

**Work History**

| | |
|---|---|
| 2021-present | Post-doctoral Researcher, Center for Applied Coastal Research, University of Delaware, Newark, DE, USA |
| 2017-present | PhD Candidate, Department of Hydraulic Engineering, Delft University of Technology, Delft, the Netherlands |
| 2016-2017 | Student/Intern, Deltares, the Netherlands |
| 2014-2017 | Project Management Subject Expert, TenStep East Caribbean, Barbados |
| 2013-2017 | Director of Projects, HE&W Consulting, Barbados |
| 2011-2013 | Junior Project Engineer, Rotherley Construction, Barbados |

**Peer-reviewed Papers in International Journals**


Lashley, C. H., Jonkman, S. N., Van der Meer, J., Bricker, J. D., and Vuik, V.: The Influence of Infragravity Waves on the Safety of Coastal Defences: A Case Study of the Dutch Wadden Sea, Nat. Hazards Earth Syst. Sci. Discuss., 2021, 1-40, 10.5194/nhess-2021-211, 2021.

Lashley, C. H., Van der Meer, J., Bricker, J. D., Altomare, C., Suzuki, T., and Hirayama, K.: Formulating Wave Overtopping at Vertical and Sloping Structures with Shallow Foreshores Using Deep-Water Wave Characteristics, Journal of Waterway, Port, Coastal, and Ocean Engineering, 147, 10.1061/(asce)ww.1943-5460.0000675, 2021.

Lashley, C. H., Bricker, J. D., Van der Meer, J., Altomare, C., and Suzuki, T. (2020). Relative Magnitude of Infragravity Waves at Coastal Dikes with Shallow Foreshores: A Prediction Tool. *Journal of Waterway, Port, Coastal, and Ocean Engineering.*

Lashley, C. H., Zanuttigh, B., Bricker, J. D., van der Meer, J., Altomare, C., Suzuki, T., Roeber, V., and Oosterlo, P. (2020). Benchmarking of numerical models for wave overtopping at dikes with shallow mildly sloping foreshores: Accuracy versus speed. *Environmental Modelling & Software*, 104740.

Lashley, C. H., Bertin, X., Roelvink, D., and Arnaud, G. (2019). Contribution of Infragravity Waves to Run-up and Overwash in the Pertuis Breton Embayment (France). *Journal of Marine Science and Engineering*, 7(7), 205.

Lashley, C. H., Roelvink, D., van Dongeren, A., Buckley, M. L., and Lowe, R. J. (2018). Nonhydrostatic and surfbeat model predictions of extreme wave run-up in fringing reef environments. *Coastal Engineering*, 137, 11-27.

Baron-Hyppolite, C., Lashley, C. H., Garzon, J., Miesse, T., Ferreira, C., and Bricker, J. D. (2018). Comparison of Implicit and Explicit Vegetation Representations in SWAN Hindcasting Wave Dissipation by Coastal Wetlands in Chesapeake Bay. *Geosciences*, 9(1),

8.

**Conference Proceedings**

Lashley, C. H., Bricker, J. D., van der Meer, J., Altomare, C., and Suzuki, T. (2019). Infragravity-Wave Dominance at Sea-Dikes Fronted by Very and Extremely Shallow Foreshores. *The 29th International Ocean and Polar Engineering Conference*, International Society of Offshore and Polar Engineers, Honolulu, Hawaii, USA, 7.

Lashley, C. H., Bertin, X., and Roelvink, D. (2018) Field Measurements and Numerical Modelling of Wave Run-up and Overwash in the Pertuis Breton Embayment, France. *Proc., Coastlab.*

**Other Publications**

Lashley, C. H. (2016). Barbados: Collaboration and enforcement - the missing pieces of the puzzle in managing the Graeme Hall Swamp (#477). Global Water Partnership.

Phillips II, G. W., Husein, R. E., and Lashley, C. H. (2014). "Model National Recovery Framework." CDEMA.

**Courses Taught**

2014-2017 Project Management Professional Prep, developer & primary instructor

**Supervision experience**

MSc students at TU Delft: 4 graduated (committee and/or supervisor)
MSc students at IHE-Delft: 2 graduated
Fulbright scholars at TU Delft: 1

**Professional Service**

Organizer of the "14th IHE-PHD Symposium - 2020" virtual event entitled, "Collaboration for Sustainability: Inter- and trans-disciplinary research to solve water-related issues".

Student Member of the Coasts, Oceans, Ports, and Rivers Institute of the American Society of Civil Engineers.

Graduate Member of the Barbados Association of Professional Engineers

Volunteer with the Project Management Institute Southern Caribbean Chapter – Barbados Branch

**Professional Training**

2018 Assessing and Supervising Master Projects – Delft University of Technology

**Licenses**

2015 Scrum Product Owner Certified (SPOC)
2012-present Project Management Professional (PMP) Qualification
2012-2018 Leadership in Energy and Environmental Design (LEED) Green Associate

**Languages** English (native), Dutch (B1)